

Copyright

by

Adenike O. Tokan-Lawal

2015

**The Thesis Committee for Adenike O. Tokan-Lawal
Certifies that this is the approved version of the following thesis:**

**Understanding fluid flow in rough-walled fractures using x-ray
microtomography images**

**APPROVED BY
SUPERVISING COMMITTEE:**

Supervisor:

Peter Eichhubl

Co-Supervisor:

Maša Prodanović

M. Bayani Cardenas

William L. Fisher

**Understanding fluid flow in rough-walled fractures using x-ray
microtomography images**

by

Adenike O. Tokan-Lawal, B.S.Comp.E.; B.S.E.E.; M.E.

Thesis

Presented to the Faculty of the Graduate School of

The University of Texas at Austin

in Partial Fulfillment

of the Requirements

for the Degree of

Master of Science in Geological Sciences

The University of Texas at Austin

August 2015

Dedication

This thesis is dedicated to all who contributed to the success of it.

Acknowledgements

Once a dream, now a reality; this journey would not have been possible without the grace of God, the support of my family, professors and mentors, and friends. To my family, thank you for encouraging me in all of my pursuits and inspiring me to follow my dreams, even when they took me thousands of miles away from you. I am especially grateful to my parents, who supported me emotionally and financially. I always knew that you believed in me and wanted the best for me. Thank you for teaching me that the best gift I can offer myself, in life, is to learn, to be happy, and to know and understand myself. Thank you to my brothers and sister for guiding and challenging me to accomplish my dreams.

I would like to give special thanks to my thesis committee. I owe a debt of gratitude to my advisors, Dr. Maša Prodanović and Dr. Peter Eichhubl, for their time, careful attention to detail, and encouraging me to pursue this degree. I am thankful for their untiring support, encouragement and guidance throughout this journey. To Dr. M. Bayani Cardenas and Dr. William L. Fisher, I am grateful for your time, for being on my thesis committee and for all the feedback you provided me.

To my friends, thank you for listening, offering me advice, and supporting me through this entire process. Special thanks to my office mates and colleagues especially: Yaser Alzayer, Owen Callahan, Dr. Andras Fall, Soheil Ghanbarzadeh, Jonathan (Jon) Major, Canalp Ozkul, and Dr. Esti Ukar. I appreciate all the time you spent editing drafts of this work. My sincere thanks to: Kathryn Fry, Müge (Susan) Ergene, and Dr. Kitty

Milliken, for their help with the Petrographic sections of this work. To my friends scattered around the world, thank you for your thoughts, well-wishes/prayers, phone calls, e-mails, texts, visits, editing advice, and being there whenever I needed a friend.

I am most grateful to the industry associates of the Fracture Research and Application Consortium (FRAC), the Shell University of Texas at Austin Unconventional Research (SUTUR) and the friends of Jackson School of Geosciences for providing the funds for my education and the research contained in this thesis. To Dr. Jessie Masiano, thank you for tirelessly working on my CT Scans and ensuring that the images were sufficient for the analyses I needed them for. To Dr. Christopher L. Landry, Dr. Zuleima Karpyn, Dr. Julia Gale, Dr. Stephen Laubach, and Dr. Randall Marrett I am grateful for the samples you provided for my work, and also for the advice and support you have given me throughout this journey.

Above all, I owe all my gratitude to God; all that I am and ever hope to be, I owe it all to Thee.

Abstract

Understanding fluid flow in rough-walled fractures using x-ray microtomography images

Adenike O. Tokan-Lawal, M.S.Geo.Sci.

The University of Texas at Austin, 2015

Supervisor(s): Peter Eichhubl and Maša Prodanović

Natural fractures provide fluid flow pathways in otherwise low permeability reservoirs. These fractures are usually lined or completely filled with mineral cements. The presence of these cements causes very rough fracture walls that can constrict flow and hinder the connectivity between the fracture and matrix/fracture pores thereby reducing porosity, permeability and matrix/fracture transfer.

In order to accurately predict fluid transport in the unconventional reservoirs, I study the influence of diagenesis (cementation and compaction in particular) and fracture roughness on flow in artificial (fractured polyethylene) and naturally fractured carbonate (Niobrara Formation outcrop) and tight gas sandstones (Torridonian outcrop and Travis Peak reservoir in particular). X-ray microtomography imaging provides information on fracture geometry. Image analysis and characterization of the connectivity and geometric tortuosity of the pore space and individual fluid phases at different saturations is performed via ImageJ and 3DMA Rock software. I also use a combination of the level-set-method-based progressive-quasistatic algorithm (LSMPQS software), and lattice Boltzmann simulation (Palabos software) to characterize the capillary dominated displacement properties and the relative permeability of the naturally cemented fractures within. Finally, I numerically investigate the effect of (uniform) cementation on the

fracture permeability as well as the tortuosity of the pore space and the capillary pressure-water saturation (P_c - S_w) relationship in the Niobrara.

Permeability estimates in the different formations vary by several orders of magnitude with the different correlations that currently exist in the literature for all samples studied. The presence of cements increases the geometric tortuosity of the pore space and capillary pressure while reducing the permeability and porosity. Contrary to our expectation, the tortuosity of either wetting or non-wetting phase and their respective relative permeabilities show no clear correlation. Overall, pore scale methods provide an insight to flow characteristics in rough walled fractures at micron scale that are not well represented by existing correlations. The measured properties can be used as input in reservoir simulators.

Table of Contents

List of Tables	xiii
List of Figures	xiv
Chapter 1: Introduction	1
Chapter 2: Fluid Flow in Porous Media	6
Wettability	8
Capillary Pressure	10
Capillary pressure-saturation relationship in a porous medium	12
Saturation	13
Permeability	14
Relative Permeability	15
Tortuosity	16
Chapter 3: Fluid Flow in Fractured Porous Media	21
Naturally Fractured Reservoirs	22
Cemented Fractures	24
Estimates of Fracture Permeability	31
Modifications	32
Tortuosity in fractures	33
Relative Permeability in Fractures	35
Chapter 4: Methodology	39
Image Analysis	39
3D Medial Axis	40
Level Set Method Progressive Quasistatic (LSMPQS) Algorithm	41
Cementation of the fracture pore space	45
Lattice Boltzmann Method	46
Palabos software	52

Chapter 5: Fractured Polyethylene.....	53
Sample Description.....	53
Image characterization.....	53
Fluid configurations.....	60
Permeability.....	64
Discussion.....	66
Conclusion.....	69
Chapter 6: Torridonian Sandstone.....	72
Sample Description.....	72
Petrography.....	75
Visual inspection of the thin section.....	75
Method.....	77
Point Count.....	78
Porosity.....	79
Grain types and Distribution.....	81
Quartz.....	81
Feldspars.....	82
Lithic Fragments.....	82
Cement.....	84
Other Grains.....	85
Fracture.....	86
Diagenetic mineral phases.....	88
Statistical Analysis.....	88
Image characterization.....	93
Fluid configurations.....	94
Permeability.....	101
Conclusion.....	103
Chapter 7: A comparative analysis of fracture fluid-flow properties of Torridonian and Travis Peak sandstones.....	104
Geologic Setting.....	104

Petrography	107
Image characterization	111
Fluid configurations	118
Permeability	121
Discussion	123
Comparison to published fracture flow models	123
Comparison of fracture flow between Travis Peak and Torridonian sandstones	124
Conclusion	131
Chapter 8: Niobrara Carbonate	133
Sample Description	133
Image characterization and manipulation	134
Absolute Permeability	139
Fluid Configurations and Relative Permeability	139
Discussion	144
Conclusion	146
Chapter 9: Summary	147
Appendix A: Methods	150
Image characterization	150
Segmentation in ImageJ	150
Medial axis extraction and tortuosity analysis in 3DMA-Rock	156
Modeling of fluid flow in imaged porous media	175
Capillary dominated fluid displacement in LSMPQS	175
Tortuosity of fluid phases in 3DMA	177
Permeability computation with Palabos	181
Appendix B: Subsampling in the Niobrara	193
Appendix C: Monterey	200
Petrology	201
Analysis of the fracture space	206

Cementation in the Monterey.....	209
References.....	214
Vita	226

List of Tables

Table 5.1:	Summary of pore space geometry and fracture characteristics used in Landry and Karpyn (2012).....	66
Table 5.2:	Summary of pore space geometry and fracture characteristics from our analysis.....	67
Table 5.3:	Summary of lattice Boltzmann (LB) permeability measurements and fracture permeability estimates (after Landry and Karpyn, 2012)....	67
Table 5.4:	Summary of permeability measurements and fracture permeability estimates.....	68
Table 6.1:	QFL composition in the sample.....	78
Table 6.2:	Sandstone composition from point count (% of whole rock).	80
Table 6.3:	Point count estimated porosity and porosity losses.	80
Table 6.4:	Summary of Statistical Analysis.....	91
Table 6.5:	Summary of feldspar and quartz comparisons.....	92
Table 6.6:	Summary of Data Analysis of the feldspar and quartz in the sample as measured from JMicroVision.	92
Table 6.7:	Porosity and the sizes of the different media shown in Figure 6.21.	100
Table 7.1:	Summary of pore space geometry and fracture characteristics for the Travis Peak and Torridonian sandstones	126
Table 7.2:	Summary of permeability measurements and fracture permeability estimates for the Travis Peak and Torridonian sandstones.....	127
Table 8.1:	Summary of the mean aperture, porosity and permeability values for the Niobrara samples	139
Table A.1:	Location of data files used in this thesis	191

List of Figures

Figure 2.1:	Schematic drawing of a porous medium filled with one or more fluids (Bastian, 2010).....	6
Figure 2.2:	The presence of unbalanced forces of liquid molecules at the surface causes surface tension (Yuan and Lee, 2013).....	10
Figure 2.3:	Geometry of the interfacial element of area between the wetting and non-wetting fluid phases. R_1 and R_2 are principal curvatures.....	11
Figure 2.4:	Advancing, θ_a , and receding, θ_r , contact angles. Advancing contact angle ($\theta_a > \theta_r$) is always larger than or equal to the receding contact angle.....	12
Figure 2.5:	Typical capillary pressure-saturation curves illustrating hysteresis (taken from (Prodanovic, 2005) and created after (Dullien, 1979)). Hysteresis is the capillary pressure difference that exists between the drainage and imbibition curves. The magnitude of capillary pressure depends on the saturation and the direction of saturation change.	14
Figure 2.6:	Schematic of possible (a) hydraulic (length L_h) and (b) geometric (length L_g) flow pathway in a saturated porous medium (Ghanbarian et al., 2013).....	18
Figure 3.1:	Naturally fractured reservoir classification system Type G represents unconventional fractured gas reservoirs such as coal-bed methane (CBM), and fractured gas condensate reservoirs. Type M reservoirs have high matrix porosity and permeability; hence open fractures can enhance permeability while natural fractures act as barriers (Bratton et al., 2006).	23

Figure 3.2: An array of linked (open) en echelon fractures (Photograph by Peter Eichhubl).....	26
Figure 3.3: Striated surface from a slickenside (Photograph by Owen Callahan).	27
Figure 3.4: Completely filled mineralized fracture (Photograph by Owen Callahan).	28
Figure 3.5: Partially mineralized fractures showing visible pore space (Photograph by Owen Callahan).	29
Figure 3.6: Vuggy bed-parallel fractures (Photograph by Peter Eichhubl).....	30
Figure 3.7: Flow between parallel plates with aperture, b , plate heights, H , and plates width, W (Klimczak et al., 2010).	32
Figure 3.8: Illustration of channel tortuosity in an open fracture (Chen et al., 2004)	34
Figure 4.1: Overview of image analysis steps typical in the detailed analysis of pore scale images of porous media (Tokan-Lawal et al., 2013).	40
Figure 4.2: (a) 1D interface embedded as a zero level set ($\phi = 0$) of a real valued level set function, ϕ , defined on the entire 2D domain (b) Schematic of ϕ from which (a) is obtained. The surface shows ϕ at a particular time; the level set function evolves with time according to equation 4.1 (c) Comparison of the location of the interface at time t^* , to its initial condition. Reprinted from Prodanović and Bryant (2009)	44
Figure 4.3: The cross-section of a sandstone sample showing original grain space (gray) and the pore space (white). After uniform cementation, the pore grain interface has moved to the new location inside the pore space. Reprinted from Prodanović et al. (2013).	46

Figure 4.4: Lattice links for the D3Q19 lattice Boltzmann method. Reprinted from De et al. (2009).	49
Figure 4.5: Bounce-back node with perfect reflection from the wall (solid).	52
Figure 5.1: Pore-grain surface of the polyethylene: top-down view. For surface creation purposes, sides of image were padded with a layer of grain space.....	54
Figure 5.2: Pore-grain surface of the polyethylene: side view. For surface creation purposes, sides of cube were padded with a layer of grain space.....	55
Figure 5.3: (a) Pore-grain surface (b) pore-grain surface trimmed down to the medial axis. The coloring represents the distance from the closest grain voxel (i.e. red is the closest while purple is furthest).....	56
Figure 5.4: Shortest paths across the polyethylene sample. (a), (b) and (c) represent the shortest paths in the x, y and z directions respectively.	57
Figure 5.5: Cumulative distribution function (CDF) of tortuosity in the x-, y- and z-directions.....	58
Figure 5.6: Probability distribution function for the aperture of the pore spaces in the polyethylene sample. The sample has a mean aperture of 0.5873 mm; a standard deviation of 0.1762 mm; and a range of 0.1762 – 1.6073 mm.	59
Figure 5.7: Aperture field distribution (measured in y-direction) of the polyethylene. The aperture ranges from 0.1289 mm to 2.1182 mm.	60
Figure 5.8: Curvature versus wetting phase (water) saturation during drainage and imbibition for the polyethylene sample.	61

Figure 5.9: (a) Residual wetting phase at the end of drainage (b) Residual non-wetting phase at the end of imbibition (before last bit of non-wetting phase is pushed out).....	63
Figure 5.10: Tortuosity of the wetting and non-wetting phases versus water saturation during drainage and imbibition for the polyethylene sample.	64
Figure 5.11: Relative permeability versus saturation of the wetting and non-wetting phases for the polyethylene sample. The non-wetting phase percolated through the fracture on the first drainage step (~70% S_w) thus significantly reducing the drainage wetting phase permeability.....	65
Figure 6.1: Torridonian sandstone from the Moine Thrust Belt, NW Scotland (Photograph by Peter Eichhubl).....	73
Figure 6.2: Map of Applecross Formation (Torridon Group) exposures in NW Scotland (modified from Ellis et al., 2012).....	74
Figure 6.3: Sample showing the abundance of chlorite between the grains (PPL).	76
Figure 6.4: Normalized representation of sandstone composition (QFL).....	78
Figure 6.5: Errors from the point count based on a 95% confidence interval following Howarth (1998).	79
Figure 6.6: Sample showing the abundance of quartz and feldspars (XPL).	81
Figure 6.7: Sub-rounded beta quartz grain (PPL).	82
Figure 6.9: Muscovite contained within lithic fragments (XPL).	84
Figure 6.10: Detrital chlorite in the lithic fragments (XPL).....	85
Figure 6.11: Granitic lithic with altered feldspar (XPL).	86
Figure 6.12: Opening mode fracture containing blocky quartz and locally preserved porosity (PPL).....	87
Figure 6.13: Fracture containing blocky quartz and secondary pores (PPL).	87

Figure 6.14: Cumulative distribution function (cdf) of grain diameter in (a) mm (b) phi scale (ϕ).	89
Figure 6.15: Grain size histogram with normal distribution fit overlain (a) mm (b) phi scale (ϕ). The Skewness shows that the grains are moderately well sorted in both the mm and phi scales. The average grain size is 0.28 mm with a standard deviation of 0.12 mm and a range between 0.08 – 0.62 mm.	90
Figure 6.16: Microtomographic slice of (a) scan A – voxel length 6.31 μm (b) voxel length 3.16 μm . Images are 5.2 mm in diameter.	94
Figure 6.17: (a) Pore-grain surface and (b) medial axis (pore space skeleton) (450x200x200 voxels). The medial axis is colored according to their distance to the grain surface.....	94
Figure 6.18: (a) Scan A aperture field distribution (measured in z-direction). (b) Probability density function (based on imaged data) of apertures for both scans. Note that only positive apertures are shown, Median and average values (for the positive values) of aperture are 0.2576mm and 0.2021mm for scan B. As expected, with increased resolution, the smallest bin frequency reduces.	96
Figure 6.19: (a) Residual water configuration surface at the drainage end point for scan A. (b) Scan A at the end of imbibition. The pore/grain surface of the Torridonian pore is shown as transparent, and the trapped non-wetting phase (blue) in the pore space.....	97
Figure 6.20: (a) Curvature-saturation plots for drainage and imbibition for both Torridonian scans. (b) Matching tortuosity saturation curves for NW phase during drainage and imbibition.....	98

Figure 6.21: (a) Cumulative distribution function of x-direction tortuosity in different media (see Table 6.1). (b) Influence of cementation on tortuosity. Cement was numerically added to all grain surfaces of Castlegate sandstone until porosity reduced to 10%.	99
Figure 6.22: (a) Relative permeability curves for drainage and imbibition of the two Torridonian scans. (b) Relative permeability curves computed based on correlations from Chen and Horne (2006).	102
Figure 7.1: Map showing the location of the Travis Peak Ashland SFOT No. 1 well (red star) (Davies et al., 1993)	106
Figure 7.2: Scanning-electron-microscope-based-cathodoluminescence (SEM-CL) image (with a UV-blue filter) of the Travis Peak sample. The fracture contains euhedral quartz crystals. Lateral cement grows on the crack seal bridge. Presence of transgranular micro-fractures relating to the crack seal	108
Figure 7.3: Sample showing the abundance of quartz and feldspars, and evidence of grain dissolution in the Travis Peak (XPL).....	109
Figure 7.4: Sample showing the presence of carbonate cement in the fracture space, lithic fragments and grain dissolution (PPL).	110
Figure 7.5: Microtomographic slice of Travis Peak sample. Voxel length = 5.97 μm . Image is ~4.2mm in diameter. Fracture pore contains quartz and carbonate cement bridges.....	112
Figure 7.6: Fracture-grain surface for (a) TP1 (b) TP2. TP1 has a similar structure to the Torridonian fracture described in Chapter 6 and in Tokan-Lawal et al. (2013). In comparison, TP2 fracture space is more connected.	113

Figure 7.7: Aperture field distribution (measured in z-direction): (a) TP1 (b) TP2. The apertures in TP2 are wider (with a mean of 0.1214 mm) than those in TP1 (mean 0.0863 mm)	115
Figure 7.8: Probability distribution function of aperture for TP1 and TP2. The apertures in TP2 are wider (with a mean of 0.1214 mm) than those in TP1 (mean 0.0863 mm).	116
Figure 7.9: Medial axis (pore space skeleton) for (a) TP1 and (b) TP2. The medial axis voxels are colored according to the distance of the pore to the grain surface (red is the closest, and purple is the furthest). Both samples contain 400x400x175 voxels.	117
Figure 7.10: Cumulative distribution function (CDF) of x-direction tortuosity for samples TP1 and TP2. The paths in TP1 (mean tortuosity = 2.4190) are more tortuous than those in TP2 (mean tortuosity = 1.8582).	118
Figure 7.11: Curvature-Saturation plots for the Travis Peak sandstones.	119
Figure 7.12: (a) Residual wetting phase at the drainage end point for TP1 (b) Trapped non-wetting phase of TP1 at the end of imbibition. TP1 has more trapped either phase and is shown here; TP2 shows less trapping but the configurations are similar and thus not shown.	120
Figure 7.13: Drainage and imbibition relative permeability plots for the Travis peak samples. Drain-nw: drainage of non-wetting fluid, drain-w: drainage of wetting fluid, imbibe-w: imbibition of wetting fluid and imbibe-nw: imbibition of non-wetting fluid.....	122
Figure 7.14: Relative permeability curves (drainage) computed based on correlations from Chen and Horne (2006). Drain-nw: drainage of non-wetting fluid, drain-w: drainage of wetting fluid.	123

Figure 7.15: Plot of permeability vs porosity for the Torridonian and Travis Peak samples. ACL = Alternate Cubic Law; WWIG = Witherspoon et al. (1980) and ZKS = Zhang et al. (1996).....	125
Figure 7.16: Probability distribution function (PDF) of the aperture in the Travis Peak and Torridonian sandstones. The aperture in the sandstones decreases with increasing depth with the Torridonian having average apertures of 0.2576 mm (A) and 0.2021 mm (B).	129
Figure 7.17: Cumulative distribution function (CDF) of the x-direction tortuosity in the Torridonian and Travis Peak. The Torridonian A and B have narrower tortuosities than TP1 and TP2 due to less cement constrictions.	130
Figure 7.18: Curvature-Water Saturation plot of the Travis Peak and Torridonian sandstones. Torridonian A and TP1 show bypassed fluid phases during drainage and imbibition due to constricted geometry.....	131
Figure 8.1: (a) Core plug containing a partially cemented fracture in limestone of the Niobrara Formation, Lyons, Colorado. Core plug is 1 inch (2.5 cm) in diameter (b) Tomographic image slice, 1 inch (2.5 cm) in diameter, imaged at UTCT with voxel length = 29.69 μm	133
Figure 8.2: Transmitted light petrographic images of partially calcite-cemented (cc) fracture in Niobrara Formation. Host rock composed of micritic carbonate. (a) Plain-polarized, (b) cross-polarized image of twinned calcite growing into residual fracture pore space	134

Figure 8.3: (a) Fracture-solid surface of the imaged fracture before numerical cementation (b) fracture-solid surface after numerical cementation (c) side/aperture view of the fracture surface (d) the fracture pore space thinned down to the medial axis skeleton. The coloring reveals the distance to the closest grain voxel, i.e. red is the closest while blue is farthest from the closest grain voxel.136

Figure 8.4: Change in aperture (a) and porosity (b) during simulated fracture cement growth in ~ 0.1 mm increments on the imaged fracture pore space. 137

Figure 8.5: Aperture field for (a) the imaged fracture, $h_{\max}=2.32$ mm, $h_{\text{ave}}=1.26$ mm and (b) the fracture after numerically adding 0.5 mm of cement. Note large white/blue islands indicating contact areas that appear after cementation. (c) Probability Density Function (PDF) of z-direction aperture for the original and cemented samples. PDF shows that the aperture distribution in the Niobrara shifts to the left after cementation.138

Figure 8.6: (a) Curvature-saturation curves for drainage for the original and numerically cemented Niobrara fracture. (b) Matching tortuosity saturation curves for the non-wetting (nw) phase during drainage. Tortuosity values have been divided by the average tortuosity values shown in Table 8.1.140

Figure 8.7: Trapped wetting phase at the end of drainage for (a) the original (b) cemented Niobrara fracture.141

Figure 8.8: (a) Drainage relative permeability plots for the original and cemented fractures. D-nw: drainage of non-wetting fluid, d-w: drainage of wetting fluid. (b) Non-wetting (in red) and wetting (in green) fluid configurations for cemented sample for the third drainage step. Interlocked configuration reduces relative permeability to both fluids.143

Figure 8.9: CDF of the x-direction tortuosity in the Torridonian and Travis Peak.145

Figure A.1: (Top left) Tomographic image – slice of Berea sandstone. (Top right) White (black) voxels are identified as phase 0 (1) through the threshold T_0 (T_1). Yellow (red) voxels are identified as phase 0 (1) via kriging. (Bottom left) result after the indicator kriging segmentation. (Bottom Right) Histogram with superimposed attenuation coefficient. Indicator kriging thresholds are indicated as light vertical lines (3DMA-ROCK website - http://www.ams.sunysb.edu/~lindquis/3dma/3dma_rock/3dma_rock_05_primer/primer.html)151

Figure A.2: Importing the image sequence152

Figure A.3: Selecting the region of interest using the rectangular selection (yellow)153

Figure A.4: Image slice after the unwanted voxels have been cleared out.154

Figure A.5: Histogram of the 800 image slices.....155

Figure B.1: Aperture field distribution (measured in y-direction) of the 000 Niobrara subsample. The aperture ranges from 0.0990 mm to 2.0550 mm.193

Figure B.2: Aperture field distribution (measured in y-direction) of the 010 Niobrara subsample. The aperture ranges from 0 mm to 2.3456 mm.....	194
Figure B.3: Aperture field distribution (measured in y-direction) of the 100 Niobrara subsample. The aperture ranges from 0.1303 mm to 2.3456 mm.	195
Figure B.4: Aperture field distribution (measured in y-direction) of the 100 Niobrara subsample. The aperture ranges from 0 mm to 2.5816 mm.....	196
Figure B.5: CDF of x-direction tortuosity in the 4 Niobrara subsamples.....	197
Figure B.6: Aperture distribution in the 4 subsamples.	198
Figure B.7: Curvature – Saturation plot for the 4 Niobrara subsamples.....	199
Figure C.1: Monterey sample showing the fracture with pores and quartz cement.	200
Figure C.2: Full scan of the thin-section of the Monterey sample. Scan shows the matrix as well as the fracture containing mineral cements and pores. .	200
Figure C.3: The matrix-fracture boundary in the Monterey sample. Scale bars (yellow and red respectively) are 200 microns in both images. Top: Plain polarized light (PPL) image: boundary shows two types of calcite in the matrix, which appears to be a mixture of oxidized and non- oxidized calcite. Bottom: The cross-polarized image (XPL; of a similar region) confirms existence of the “calcite mixture” boundary and shows different quartz cements on top of it.....	201
Figure C.4: The non-oxidized calcite along the matrix-fracture boundary shows varying thickness. The scale bar is 500 microns.....	202

Figure C.5: The presence of calcite along the matrix-fracture boundary is not continuous (PPL). The scale bar is 500 microns.....	203
Figure C.6: PPL image of fracture pore space with quartz bridges. The scale bar is 500 microns.....	204
Figure C.7: XPL image of a matrix/fracture boundary showing microfractures in between different layers with some variation in composition. This indicates different timing for different layers. The scale bar is 500 microns.....	205
Figure C.8: Probability distribution function (PDF) of the fracture aperture. Aperture in the fracture ranges from 0 to ~4.8mm	206
Figure C.9: Z-direction of the fracture aperture showing the distribution	207
Figure C.10: Curvature – Saturation plot for drainage and imbibition.	208
Figure C.11: Porosity vs. Cement thickness in the Monterey.....	210
Figure C.12: Aperture vs. Cementation thickness in the Monterey.....	211
Figure C.13: Aperture distribution field after 5mm of cement has been numerically added to the fracture space.....	212
Figure C.14: Probability distribution function of the aperture in the cemented Monterey sample after the addition of 5mm thick cement.	213

Chapter 1: Introduction

In petroleum reservoirs of low matrix permeability including unconventional reservoirs, natural fractures are considered to control fluid flow and hence production (Gale et al., 2007; Walton and McLennan, 2013). Fractures are mechanical discontinuities. Where they have remained unfilled with mineral cement, they tend to form conductive channels for flow (Witherspoon et al., 1980; Philip et al., 2005; Agosta et al., 2010). Flow through fractured rock can vary widely depending on fracture parameters that include fracture density, hydraulic aperture, degree of fracture cement infill, and roughness or tortuosity (Brown, 1987, 1989; Pyrak-Nolte et al., 1988; Brown et al., 1995; Méheust and Schmittbuhl, 2001; Crandall et al., 2010). In order to predict reserves and production from these reservoirs, it is important to understand how the fractures and their inter-connectivity control fluid flow and geophysical reservoir properties.

Fractures present both challenges and opportunities for exploration and production from petroleum reservoirs. Opening-mode fractures often act as conduits for fluid flow in reservoirs; however, this flow is often localized (Cooke, 1997; Laubach, 2003; Olson et al., 2009). In such cases, the fractures are usually important for their influence on permeability rather than porosity. Matrix porosity stores the hydrocarbons, while fractures provide permeable pathways for the transport of hydrocarbons to producing wells.

Reservoir models for production history are used in the oil and gas industry to

understand and predict future well performance. These models generally do not take into account the complex geometry of real fracture systems which can vary from one grid-block to another, and sometimes even within a single grid-block (Jolley et al., 2007). Limitations in properly accounting for fracture network geometry and fracture flow properties, including the flow properties of single fractures, add significant uncertainty to reservoir flow models (Kalantari-Dahaghi and Mohaghegh, 2009). Hence, an understanding of fluid flow in fractures at the pore scale is important for the development of predictive reservoir models.

Permeability is one of the most important properties to describe fluid flow in fractures. Commonly, flow in fractures is modeled using the cubic law which relates the fluid flow rate through a fracture to its aperture; it is valid for laminar flow between parallel plates (Lomize, 1951; Snow, 1965; Witherspoon et al., 1980). The cubic law fails to account for surface roughness and tortuosity and thus may incorrectly predict reservoir permeability for fractured reservoirs (Louis, 1967). Hence, there has been considerable research centered on developing modifications for the cubic law to account for these parameters (Witherspoon et al., 1980; Walsh and Brace, 1984; Zimmerman and Bodvarsson, 1996; Oron and Berkowitz, 1998). Despite these modifications, it has been found that the cubic law still does not adequately predict the permeability of fractures with small apertures (Brown et al., 1995; Mourzenko et al., 1995; Dijk and Berkowitz, 1999; Kim et al., 2003; Eker and Akin, 2006).

The study of flow through rough fractures can be difficult to observe and quantify experimentally, hence, investigators have turned to pore-scale fluid flow models, and

computational fluid dynamics (CFD) to numerically simulate flows in complex pore spaces (Landry and Karpyn, 2012). Numerical tools for determining space-resolved fluid flow characteristics are based on the Navier–Stokes for natural or synthetically generated fracture geometries and matrix pores. Natural fracture geometries can be imaged using X-ray computed tomography (Ketcham and Carlson, 2001; Wildenschild et al., 2002) and synthetic fractures can be computed by a suite of numerical models (Brown, 1995; Glover et al., 1998; Méheust and Schmittbuhl, 2001, 2003; Ogilvie et al., 2006; Neuville et al., 2010, 2011). The solutions of the Navier–Stokes equation for these geometries are calculated by a variety of numerical techniques, such as lattice Boltzmann methods (LBM) (Arns et al., 2004; Sukop and Thorne, 2006; Narváez et al., 2010; and Khan et al., 2011), finite element methods (Wang et al., 2003), or finite difference methods (Al-Omari and Masad, 2004).

In this study, fluid flow in fractured reservoirs is analyzed using a combination of the level-set-method-based progressive-quasistatic algorithm (LSMPQS software), and Lattice Boltzmann simulation to characterize the capillary-dominated displacement properties and relative permeability of the natural fractures that are lined or partially filled with mineral cement. The geometry of the residual fracture space was acquired from x-ray computed microtomography (μ CT) scans. μ CT scans are capable of capturing the micron- to millimeter-scale aperture and roughness of the fracture surfaces in three dimensions, well below the resolution of well logging tools. I quantified the influence of mineral cement on the capillary pressure, tortuosity, and absolute and relative permeability of the fluid flow through natural and induced fractures. This work is, to my

knowledge, the first that studies the influence of partial cementation on fluid flow properties in fracture geometries true to the micron scale 3D geometry. I hypothesize that natural fractures provide the most direct paths across the medium when compared to other porous media. The presence of constrictions inhibits the flow through the fracture, however, fluids will still move through the open parts of the fracture. Additionally, I postulate that the presence of mineral cement in the fracture increases tortuosity and capillary pressure, while pore-filling cement reduces the permeability and porosity of the medium.

Chapter 2 gives an overview of fluid flow in porous media. It begins with a definition of porous media, their flow properties, and motivation for studying flow through porous media. Chapter 3 develops Chapter 2 further by relating it to fluid flow in fractured porous media. The chapter begins with an overview of fractures, including how they differ from unfractured porous media, their flow properties, and my motivation for studying flow through fractures.

Chapter 4 discusses the methods used to characterize the fracture void space. Simulation of capillary dominated fluid displacement and permeability calculations are also described. Chapters 5-8 contain the results of the analysis completed using the methods described in Chapter 4. Chapter 5 discusses the analysis of a fracture within Polyethylene, used as an analog material. Chapter 6 applies this analysis to fractures in Torridonian sandstone (Applecross Formation of the Torridon Group) of NE Scotland. This work has been published as Tokan-Lawal et al. (2013). In addition, chapter 6 includes a petrographic analysis on the Torridonian sandstone. Chapter 7 compares an

outcrop sample from the Applecross Formation (Torridonian sandstone) to a core sample of the Travis Peak Formation a tight-gas sandstone reservoir in East Texas. Although the Torridonian and Travis Peak sandstones have different compositions, age, and burial and exposure histories, they are both sandstones tightly cemented by quartz thus representative of a wide range of unconventional oil and gas sandstone reservoirs. Finally, Chapter 8, investigates the influence of mineral cement on fluid flow in the fractured carbonate of the Niobrara Formation of Colorado. In this published work (Tokan-Lawal et. al., 2014), cement was numerically grown in the fracture space, and the influence of the cement growth on fluid flow was studied. Chapter 9 provides an overall summary.

In the following chapters I will demonstrate that pore scale methods provide valuable insight into the flow characteristics of rough-walled fractures at the micron scale. I will show that the presence of mineral cement occludes some flow paths in fractures thereby reducing their porosity and permeability. Despite this reduction in permeability, these partially cemented fractures provide the narrowest tortuosity when compared to the porous host medium and thus provide the most direct path across the medium. Fluid phases are more disconnected as cementation increases, hence relative permeability reduces as cementation increases. Permeability and porosity reduce with increasing depth, while geometric tortuosity increases with increasing depth.

Chapter 2: Fluid Flow in Porous Media

A porous medium is a body composed of a persistent solid phase, called solid matrix, and void or pore space that can be filled with one or more fluid phases such as water, oil, hydrocarbon condensate, natural gas, CO₂, or air (Figure 2.1). The geometry of the pore space describes the shapes and sizes of its pores and or fractures and their surface roughness, whereas the topology describes how the pores and fractures are connected to one another (Dullien, 1979; Vogel, 1997). Pore geometry and topology both affect the flow properties and other physical properties of the rock mass, such as the elastic and electric properties. The simplest upscaled (or effective) property of a porous medium is porosity, ϕ , which is the volume fraction of pores and fractures.

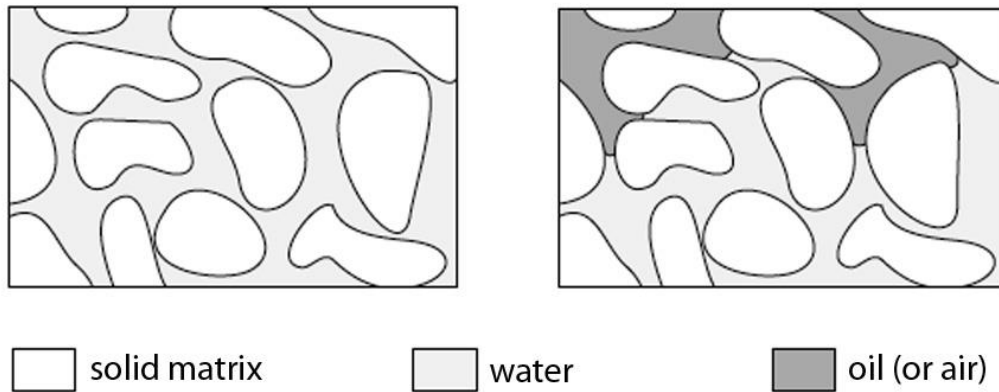


Figure 2.1: Schematic drawing of a porous medium filled with one or more fluids (Bastian, 2010)

The basic law governing single-phase flow of fluids in porous media, such as sediment and sedimentary rocks and unconsolidated granular media, is Darcy's law. The theoretical framework for Darcy's law follows the principle that flux is proportional to

the gradient in hydraulic potential. In 1856, Henry Darcy, a French civil engineer, developed Darcy's law while he was investigating the downward flow of water through sand filters for water purification. The law states that the velocity of fluid flow is proportional to the hydraulic gradient:

$$q = \frac{Q}{A} = -K \frac{\Delta h}{\Delta L} = -K \frac{\partial h}{\partial L} \quad (2.1)$$

where, q is the flux (specific discharge or discharge velocity), Q is the volumetric flow rate, A is the cross-sectional area normal to the flow, K is the hydraulic conductivity, Δh is the hydraulic head, ΔL is the length over which the hydraulic gradient is applied.

Although Darcy's law was initially derived from experiments on water flowing through sand, and it is valid for most granular media as long as the flow is laminar, i.e. the rate of the flowing fluid is sufficiently low to be directly proportional to the potential gradient (Hubbert, 1956). The physical meaning of Darcy's law is that fluid flow is driven towards regions of lower potential energy and not, except in the special case of horizontal flow, from higher to lower pressure (Hubbert, 1956; Gudmundsson, 2011).

When Darcy's law is applied to fluids other than water, permeability is used instead of hydraulic conductivity. When the fluid properties are known, hydraulic conductivity can be written in terms of permeability, as:

$$K = \frac{k\rho g}{\mu} \quad (2.2)$$

At any point, within the flow system, characterized by elevation, z , and manometer height, h , the pressure is given by the hydrostatic equation:

$$P = \rho g(h - z) \quad (2.3)$$

Hence, Darcy's law can be re-written as:

$$q = -\frac{k \Delta P}{\mu \Delta L} = -\frac{k}{\mu} \frac{dP}{dx} \quad (2.4)$$

where, $\frac{dP}{dx}$ is the pressure gradient in the direction of flow, k is the permeability of the porous rock, μ is the viscosity of the flowing fluid, ΔP is the change in pressure, ΔL is the change in length of the medium, and x is the positive distance in the direction of flow. Permeability is understood to be a function of the porous medium geometry and of topology only. In a more general vector formulation of equation (2.4), k is a tensor and implies directional dependence.

WETTABILITY

Wettability is defined as the tendency of one fluid to adhere to a solid surface in the presence of other immiscible fluids (De Gennes, 1985). Fluids are regarded as *immiscible* if a distinct sharp interface is maintained between them. Basic reservoir properties like relative permeability, capillary pressure, and resistivity depend strongly on wettability (Owens, 1971). Wettability is usually quantified at the pore scale by the local contact angle. Contact angle is the angle, θ , that the interface between two fluid phases makes with the solid measured through the denser phase (Good, 1992). The fluid, which adheres more readily to the surface, is termed the *wetting phase*. More specifically, a contact angle less than 90° indicates that wetting of the surface is favorable, and the fluid

will spread over a large area on the surface; while contact angles greater than 90° generally means that wetting of the surface is unfavorable so the fluid will minimize its contact with the surface and form a compact liquid droplet (Dullien, 1979; De Gennes, 1985; Good, 1992). The wetting phase tends to reside in the smallest areas of the pore space such as small pores, the corners of larger pores, as well as connected films residing in the roughness of the solid surface (Dullien, 1979). Conversely, the other fluid, the *non-wetting phase*, which adheres less easily, resides in the largest areas of the pore space, principally in the centers of large pores.

In the absence of other forces, the shape of a liquid droplet is determined solely by the surface tension of the liquid (De Gennes, 1985; Good, 1992; Yuan and Lee, 2013). In a liquid, each molecule in the bulk is pulled equally in every direction by neighboring liquid molecules, resulting in a net force of zero. However, the molecules exposed at the surface do not have neighboring molecules in all directions to provide a balanced net force (Yuan and Lee, 2013). Instead, they are pulled inward by the neighboring molecules (Figure 2.2), creating an internal pressure. As a result, the liquid voluntarily contracts its surface area to maintain the lowest surface free energy. This intermolecular force to contract the surface is called the *surface tension*, and it is responsible for the shape of liquid droplets (De Gennes, 1985; Good, 1992; Yuan and Lee, 2013).

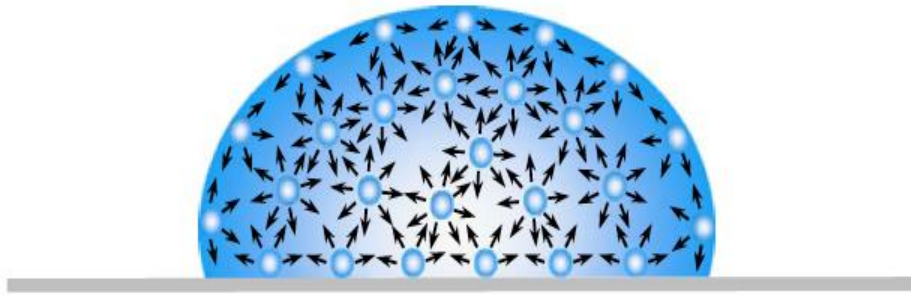


Figure 2.2: The presence of unbalanced forces of liquid molecules at the surface causes surface tension (Yuan and Lee, 2013)

The wettability of a reservoir system can be categorized water-wet, oil-wet, or neutrally wet. Spotty (fractional) wettability and mixed wettability describe systems with non-uniform wetting properties, in which portions of the solid surface are wet by one phase, and other portions are wet by the other phase (Brown, 1956; Fatt, 1959 Salathiel, 1973; Good, 1992). Mixed wettability, as proposed by Salathiel (1973) describes a special type of fractional wettability in which the oil-wet surfaces form continuous paths through the largest pores. Salathiel (1973) hypothesized that the initial trapping of oil in a reservoir is a primary drainage process, as water (the wetting phase) is displaced by non-wetting oil. Then, those portions of the pore structure that experience intimate contact with the oil phase become coated with hydrocarbon compounds and change to oil-wet.

CAPILLARY PRESSURE

Capillary pressure is the difference (discontinuity) in pressure across the interface of two immiscible fluid phases in contact. This discontinuity in pressure depends on the curvature of the interface separating the two fluids (Clark, 1960; Dullien, 1979). The

capillary pressure is given by the Laplace equation (also referred to as the Young-Laplace equation) as:

$$P_c = P_{nw} - P_w = \sigma \kappa \quad (2.5)$$

where, P_c is the capillary pressure, σ is the interfacial tension, and κ is twice the mean curvature of the interface:

$$\kappa = 2\kappa_m = \frac{1}{R_1} + \frac{1}{R_2} \quad (2.6)$$

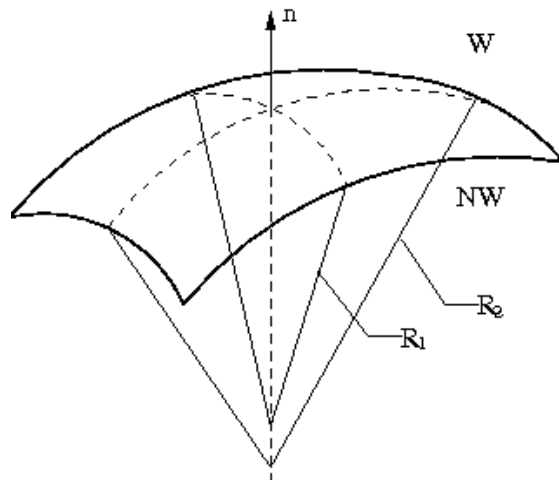


Figure 2.3: Geometry of the interfacial element of area between the wetting and non-wetting fluid phases. R_1 and R_2 are principal curvatures

Radii R_1 and R_2 are the principal radii of curvature and are measured in mutually perpendicular directions. The principal radii can be negative (e.g. saddle-like interfaces).

In two-dimensions, the (mean) curvature is an inverse of the only possible radius of

curvature. In three dimensions, however, there is an infinite number of principal curvature pairs that sum up to a given mean curvature value.

Capillary pressure-saturation relationship in a porous medium

Two processes characterize the immiscible fluid displacement in a porous medium: drainage and imbibition, and they are both quantified through capillary pressure-saturation relationship.

Drainage is the process in which the non-wetting fluid displaces the wetting fluid. In order for the non-wetting fluid to enter the saturated medium, a critical entry pressure, P_b , must exist. The entry pressure is determined by the size of the largest pore throats connected to the surface of the medium (Dullien, 1979).

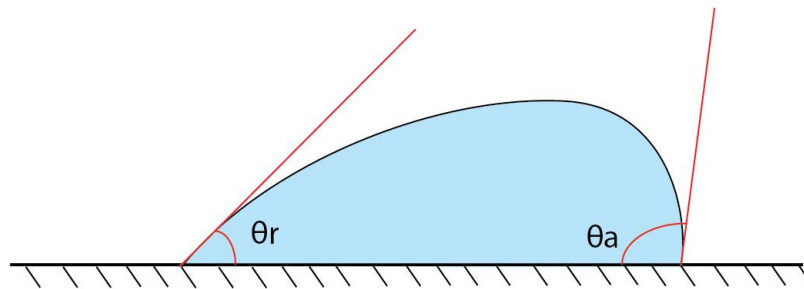


Figure 2.4: Advancing, θ_a , and receding, θ_r , contact angles. Advancing contact angle ($\theta_a > \theta_r$) is always larger than or equal to the receding contact angle.

Drainage continues through rapid local advances of the fluid interface with local pressure exceeding the critical entry pressure value of the largest accessible throat constriction. As

the pressure of the non-wetting fluid is increased, the non-wetting fluid invades the smaller pores (Lenormand et al., 1983). The saturation of the wetting fluid decreases until the fluid becomes discontinuous and can no longer be displaced from the medium by increasing the capillary pressure. During drainage, the wetting fluid recedes from the porous medium (solid) forming a *receding* (minimal) contact angle.

Imbibition is the process in which the wetting fluid displaces the non-wetting fluid. If the non-wetting fluid saturates the rock, introducing the wetting fluid at the surface can start a spontaneous imbibition process (Lenormand et al., 1983). During imbibition, the wetting fluid advances into the porous medium and the contact angle is the *advancing* (maximal) contact angle.

The difference between the advancing and receding angles is called contact angle hysteresis. Contact angle is generally attributed to: surface roughness; surface heterogeneity; solution impurities adsorbing on the surface; or swelling (Dullien, 1979; Yuan and Lee, 2013).

Saturation

The saturation of any fluid is the fraction of the pore space it occupies. Idealized capillary pressure-saturation relationships ($P_c = P_c(S_w)$) are commonly used to describe the drainage-imbibition process. The difference between an *advancing* and a *receding* contact angle as well as the pore geometry and topology (and the thermodynamic instabilities in interface advancement they cause, see Morrow, 1970) result in differences

(hysteresis) in the capillary pressure curves for drainage and imbibition, as shown in Figure 2.5.

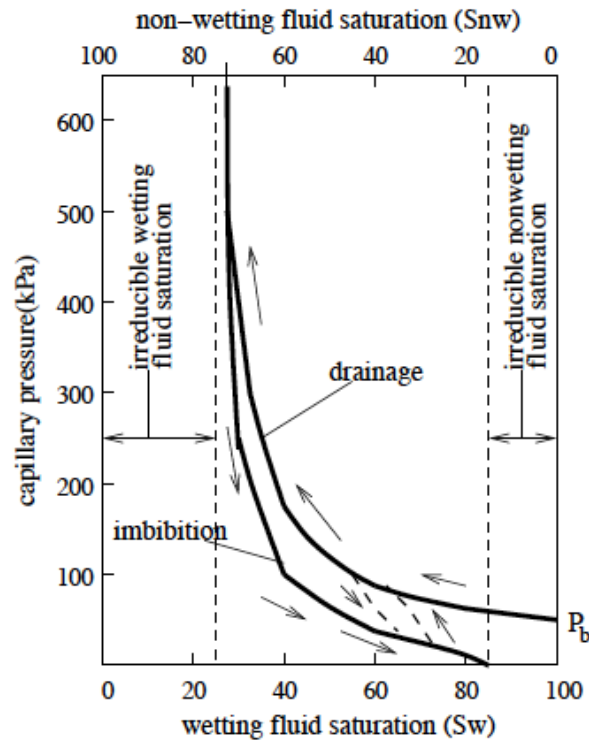


Figure 2.5: Typical capillary pressure-saturation curves illustrating hysteresis (taken from (Prodanovic, 2005) and created after (Dullien, 1979)). Hysteresis is the capillary pressure difference that exists between the drainage and imbibition curves. The magnitude of capillary pressure depends on the saturation and the direction of saturation change.

PERMEABILITY

In addition to being porous, a good reservoir rock must be permeable. Permeability is the ease with which fluids can move through rock. The pores in a porous rock may be interconnected or disconnected; in addition, the presence of multiple non-miscible fluids inhibits the flow of one fluid relative to the others. The permeability of a

rock depends on the degree of connectivity between the pores. Grain size, grain shape, grain size distribution, grain packing, and the distribution of diagenetic mineral phases all affect porosity and pore space connectivity, which controls permeability.

Reservoirs can have primary and secondary porosity. In clastic sedimentary rocks, primary porosity is interstitial pore space between grains. Secondary porosity results from grain dissolution during burial diagenesis, and the formation of open fractures (Archie, 1950; Ehrenberg, 1989). Compaction and cementation reduce permeability; fracturing and dissolution tend to increase it (Ehrenberg, 1989; Gudmundsson, 2011). In unconventional clastic reservoirs and low-porosity carbonates, secondary permeability often provides the main flow conduit for fluid migration.

RELATIVE PERMEABILITY

Permeability as defined in equation (2.4) is also known as the absolute permeability that is applicable to porous media that are completely saturated by a single-phase, non-reactive fluid. In petroleum reservoirs, it is possible for two or more fluids to flow simultaneously. When multiple fluids flow at the same time (multiphase flow), the absolute permeability is no longer sufficient to calculate the flow of each fluid type in the presence of the other fluids (Collins, 1976). The permeability of one fluid in the presence of the other fluid becomes important. This permeability is known as the effective permeability of the fluid (Dullien, 1979). While the effective permeability is sufficient to make predictions for a fluid, it is more convenient to work with a dimensionless quantity, the relative permeability. The relative permeability of a fluid is the effective permeability

of the fluid divided by the absolute permeability of the porous medium; hence it is a number between 0 and 1.

TORTUOSITY

Natural porous media constitute a broad range of complex systems at different scales. Their pore spaces tend to be irregular, with tortuous and meandering paths for fluid flow. These paths are usually longer than the straight path between the inlet and outlet of the porous medium. The term used to describe the ratio of the flow path to the straight path is called *tortuosity*. Tortuosity is defined as either a geometric parameter, or one that is related to the hydraulic, electrical or diffusive properties (Scheidegger, 1974; Sahimi, 1993; Clennell, 1997; Matyka et al., 2008; Ghanbarian et al., 2013). Tortuosity has no simple or universal definition: different measures of tortuosity are employed by geologists, engineers and chemists to describe the resistive and retarding effects of the pore structure on a range of conduction, advection, and diffusion processes. The following briefly summarizes definitions available in literature.

Geometric tortuosity, τ_g , is the ratio of the average length $\langle L_g \rangle$ of the geometric flow paths through the medium to the length of the sample, L_s , across the medium, hence τ_g is always greater than 1:

$$\tau_g = \frac{\langle L_g \rangle}{L_s} \quad (2.7)$$

Tortuosity can also be defined as the ratio of the shortest pathway (L_{\min}) to the length of the sample, L_s (Alder, 1992; Ghanbarian et al., 2013). Geometric tortuosity coefficient

may be expressed as the inverse of equation (1.6) i.e. $T_g = \frac{1}{\tau_g}$, where $T_g < 1$ (Hillel, 2004).

Hydraulic tortuosity, τ_h , is the square of the ratio of the flux-weighted average path length for hydraulic flow, $\langle L_h \rangle$, to the length of the sample, L , (Clennel, 1997).

$$\tau_h = \left(\frac{L}{\langle L_h \rangle} \right)^2 \quad (2.8)$$

Clennel (1997) and Ghanbarian et al (2013) argue that geometric and hydraulic tortuosity are not the same because L_g takes shortcuts that cross streamlines, thus L_g is shorter than L_h , (Figure 2.3). Hence, $\tau_g < \tau_h$, since hydraulic flow paths are smooth curves rather than straight lines or close tangents to the solid particles.

Bear (1972) defined (hydraulic) tortuosity as the square of the ratio of the true flow path length, L_f , to the length, L , along the major flow axis of the medium (the inverse of τ_h). Following Bear's definition, electric tortuosity, τ_e , can be defined as the square of the ratio of the average path length for electric flow, $\langle L_e \rangle$, to the straight line length (Childs, 1969; Tindall et al., 1999; Wong, 1999):

$$\tau_e = \left(\frac{\langle L_e \rangle}{L_s} \right)^2 \quad (2.9)$$

Electrical tortuosity is also defined as the product of the porosity of the medium, ϕ , and the formation resistivity factor, F (Wyllie, 1957; Schopper, 1966; Dullien, 1979, Coleman and Vassilicos, 2008),

$$\tau_e = \phi F \quad (2.10)$$

where F is the quotient of the electrical resistivity of the saturated porous medium and the resistivity of the saturating fluid (Ghanbarian et al., 2013).

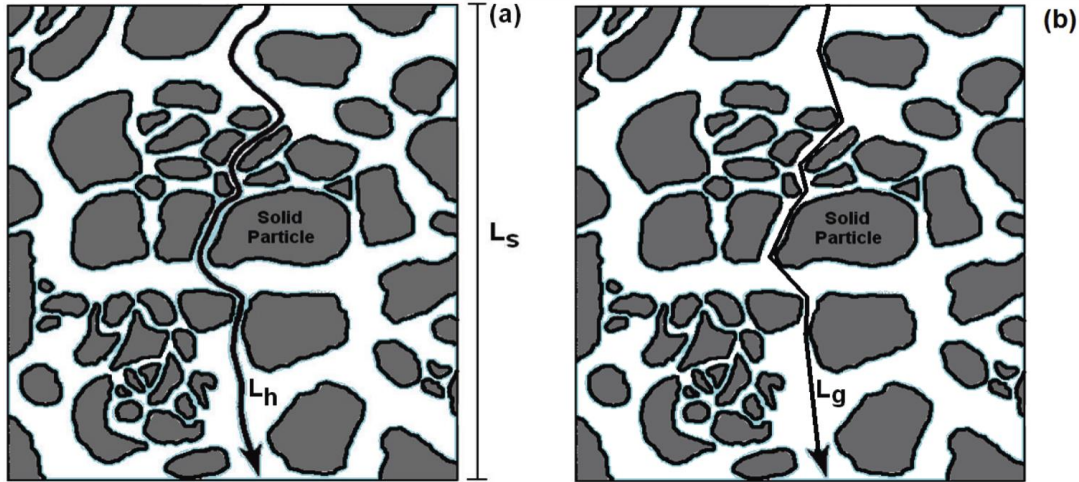


Figure 2.6: Schematic of possible (a) hydraulic (length L_h) and (b) geometric (length L_g) flow pathway in a saturated porous medium (Ghanbarian et al., 2013).

Formation factor is a dimensionless quantity whose value is always > 1 in the absence of solid and/or surface conduction. In such cases, its value is supposedly determined uniquely by the pore geometry (Dullien, 1979) although pore topology (connectivity) must also be relevant (Ghanbarian et al., 2013).

In most laboratory experiments, equations (2.8) and (2.9) are combined to obtain the following relation

$$\phi F = \left(\frac{\langle L_e \rangle}{L_s} \right)^\eta \quad (2.11)$$

where η is a correlation constant, which ranges from 1.7 to 2.

Carman (1937) introduced the concept of tortuosity based on the permeability of a bundle of capillary tubes (Dullien, 1979). The model represents the pores as parallel tubes of length equal to the sample length and of a range of radii. This single-phase permeability model (known as the Carman-Kozeny or Kozeny-Carman equation),

developed for packings of equal spherical grains, relates the absolute permeability, k , to porosity, tortuosity (as defined by Bear, 1972), and grain size d as

$$k = \frac{\phi^3}{\beta\tau^2(1-\phi)^2S_0^2} \quad (2.12)$$

where, β is the shape factor and S_0 is the specific surface area

$$S_0 = \frac{\phi}{r_h} \quad (2.13)$$

and, r_h is the hydraulic radius, defined as

$$r_h = \frac{\text{cross-sectional area normal to flow}}{\text{wetted perimeter of the flow channels}} \quad (2.14)$$

In evaluating tortuosity, it is important to note that the shortest path through the medium does not necessarily coincide with the path of maximized flux.

In contrast to the Carman-Kozeny's formulation for τ_h (used in the permeability equation, equation (2.12)), the electric tortuosity τ_e does not account for the influence of pore size distribution on electric conductivity. Lorenz (1961) demonstrated that the geometric tortuosity τ_g of flow lines accounting for both sinuosity and converging-diverging pore geometry was smaller than the electric tortuosity i.e. $\tau_g < \tau_e = \phi F$ (Ghanbarian et al., 2013).

Diffusive tortuosity is defined, analogous to electrical tortuosity (Epstein, 1989), as:

$$\tau_d = \left(\frac{\langle L_d \rangle}{L_s} \right)^2 \quad (2.15)$$

where $\langle L_d \rangle$ is the average length of a molecular diffusive path. τ_d can also be defined as the diffusion coefficient of the diffusing species in the free fluid, d_f , relative to its value

in the porous medium, d_p (Satterfield and Sherwood, 1963; Greenkorn, 1983; Clennell, 1997; Shen and Chen, 2007; Sahimi, 1993, 2011)

$$\tau_d = \frac{d_f}{d_p} \quad (2.16)$$

Equation (2.13) includes a direct porosity effect on tortuosity. If fluid configuration is near the percolation threshold, then tortuosity is large and, the relationship between tortuosity and porosity diverges. An analogous relation to equation (2.13), common in soil science, removes porosity from the tortuosity value (Curie, 1960; Epstein, 1989; Moldrup et al., 2001; Hillel, 2004; Kirkham, 2005)

$$\tau_d = \phi \frac{d_f}{d_p} \quad (2.17)$$

The inverse of equation (2.14) is sometimes called the pore continuity equation in the gas diffusion literature (Moldrup et al., 2001).

In this thesis I will use equation (2.12) to estimate permeability in fractures, with the hydraulic radius, r_h replaced by the fracture aperture, b .

Chapter 3: Fluid Flow in Fractured Porous Media

Fractures are structural discontinuities resulting from mechanical failure in response to changes in stress conditions (Golf-Racht, 1982; Nelson, 2001; Singhal and Gupta, 2010). Such changes in stress conditions may result from natural processes such as tectonic movement, thermal stresses, lithostatic pressure changes, or changes in pore fluid pressure, or through human activities such as hydraulic fracturing or explosions (Golf-Racht, 1982; Nelson, 2001). In geological terms, a fracture is any planar or curvilinear discontinuity that results from the process of brittle deformation in the Earth's crust.

Natural fractures or fracture systems may range in size from continent scale such as plate boundary faults to microfractures observable only with the aid of a microscope (Aguilera, 1980; Golf-Racht, 1982; Nelson, 2001; Laubach et al., 2009; Singhal and Gupta, 2010). They may be limited or confined to a single layer or extend across multiple layers (Aguilera, 1980; Golf-Racht, 1982).

Fractures are important in engineering, geotechnical, and hydrogeological practice because they provide pathways for fluid flow (Aguilera, 1980; Golf-Racht, 1982; Lee and Farmer, 1993; Nelson, 2001; Singhal and Gupta, 2010). Many economically significant petroleum, geothermal, and water supply reservoirs exist in fractured rocks (Aguilera, 1980; Golf-Racht, 1982; Nelson, 2001). Fracture systems control the dispersion of chemical contaminants into and through the subsurface (Aguilera, 1980; Golf-Racht, 1982; Nelson, 2001). They also affect the stability of engineered structures and

excavations (Aguilera, 1980; Golf-Racht, 1982; Lee and Farmer, 1993; Nelson, 2001). Fractures may have either a positive or negative impact on fluid flow depending on the degree of mineralization (Aguilera, 1980; Nelson, 2001). The influence of mineralization on fluid flow is the main focus of this work.

NATURALLY FRACTURED RESERVOIRS

Narr et al. (2006) defined a naturally fractured reservoir “as a reservoir in which fractures enhance the permeability field, thereby significantly affecting well productivity and recovery efficiency”. Natural fractures can enhance or hinder fluid flow within the reservoir. The storage capacity of naturally fractured reservoirs varies extensively, depending on the value of the primary porosity and the degree of fracturing in the formation (Aguilera, 1980). Hence natural fractures can enhance or hinder fluid flow within the reservoir. Natural fractures can be divided into different types; however, the most widely used classification is Nelson’s (2001). Nelson (2001) identified four types of naturally fractured reservoirs based on their porosity and permeability:

Type 1: Fractures provide the essential reservoir porosity and permeability.

Type 2: Reservoirs containing these fractures have low porosity and permeability; hence the fractures provide the essential reservoir permeability.

Type 3: Fractures assist permeability in an already producible reservoir.

Type 4: Fractures provide no additional porosity or permeability but create significant reservoir anisotropy and tend to form barriers to fluid flow and partition formation into relatively small blocks.

Secondary recovery can be difficult in Type 2 reservoirs if the communication between the matrix and the fracture is poor. Unconventional fractured gas reservoirs such as coal-bed methane and fractured gas condensate reservoirs have been placed in a different class, Type G. These reservoirs often fall within or near the Type 2 reservoirs (Bratton et al., 2006). Type M reservoirs have high matrix porosity and permeability, but natural fractures often complicate fluid flow in these reservoirs by forming barriers (Bratton et al., 2006). The naturally fractured reservoirs studied in this work are of Types 1-3. These fractures can be open, uncemented, partially, or completely mineralized, and I assume that the matrix provides no additional porosity or permeability.

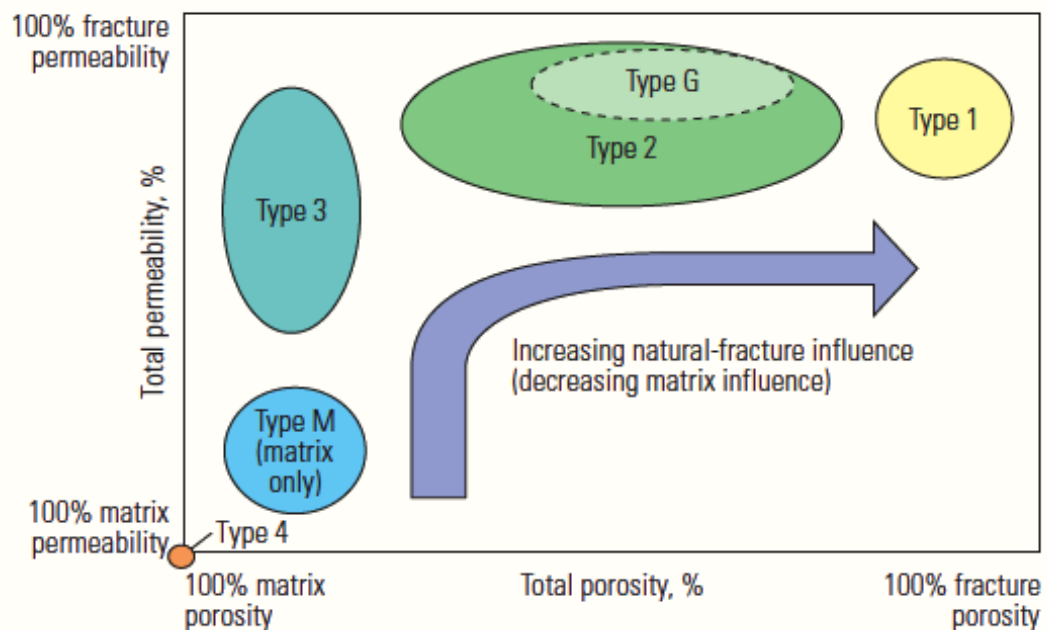


Figure 3.1: Naturally fractured reservoir classification system Type G represents unconventional fractured gas reservoirs such as coal-bed methane (CBM), and fractured gas condensate reservoirs. Type M reservoirs have high matrix porosity and permeability; hence open fractures can enhance permeability while natural fractures act as barriers (Bratton et al., 2006).

CEMENTED FRACTURES

The quality of a reservoir is a function of diagenetic processes that either enhanced or reduced its porosity. Diagenesis describes all chemical and mechanical processes that affect sediments and sedimentary rocks after deposition (Bjørlykke et al., 1989; Worden and Burley, 2003; Laubach, 2003). Diagenesis alters the geometry and chemistry of the pore space as well as the composition of the rock (Hayes, 1979; Laubach, 2003).

Diagenetic processes may have effects at even larger scales: e.g., fracturing or massively cemented zones can affect the “plumbing” at the reservoir scale (Hayes, 1979; Boles et al., 2004). These diagenetic processes alter rock properties and pore pressure, thereby affecting when and how fractures grow (Laubach et al., 2009). Fractures and cement precipitation interact in several ways. For example, cement can line or locally bridge fracture walls, thereby blocking the fracture pore space and impeding flow in the fracture (Laubach et al., 2010). Cement can also influence sandstone mechanical properties, helping to localize fractures in certain depth intervals and rock types (Laubach et al., 2009).

The most common fracture-fill minerals in reservoir rocks are calcite, dolomite and quartz (McBride, 1989; Phillips, 1991; Nelson, 2001; Laubach, 2003; Gale et al., 2007). Fluids moving through fractures can also react with the rock, dissolving fracture walls thereby enlarging their apertures. Fracture filling and morphology types can be described based on the flow potential of the fracture system in the reservoir. The classification is based on degree of both mineralization and deformation along the

fractures (Nelson, 1985, 2001; Laubach, 1988, 2003; Dyke, 1995) and some examples are described below (Figures 3.2 – 3.6):

1. **Open fractures.** These are uncemented and do not contain secondary mineralization of any kind (Figure 3.2). Open fractures significantly enhance permeability parallel to the fracture, but have negligible effect on permeability perpendicular to the fracture.
2. **Deformed fractures.** These are of two types:
 - a. *Slickensides:* a slickenside (Figure 3.3) results from frictional sliding along a fracture or fault plane. This generates striated or polished surfaces that might drastically decrease permeability perpendicular to the fracture while increasing permeability parallel to the fracture, thus causing strong permeability anisotropy.
 - b. *Deformation bands:* these consist of finely abraded material resulting from grinding or sliding motion. Although not fractures, deformation bands can contain slip surfaces that could act as conduits for flow.
3. **Mineral-filled fractures.** Secondary cement mineralization can cause fractures to be:
 - a. *Completely filled* (Figure 3.4), or
 - b. *Partially filled* (Figure 3.5)

Mineral filled fractures are usually permeability barriers, but incomplete filling of a fracture in the form of either vug development or intergranular

porosity can give some measurable increase in permeability to the reservoir (Nelson, 2001)



Figure 3.2: An array of linked (open) en echelon fractures (Photograph by Peter Eichhubl).



Figure 3.3: Striated surface from a slickenside (Photograph by Owen Callahan).

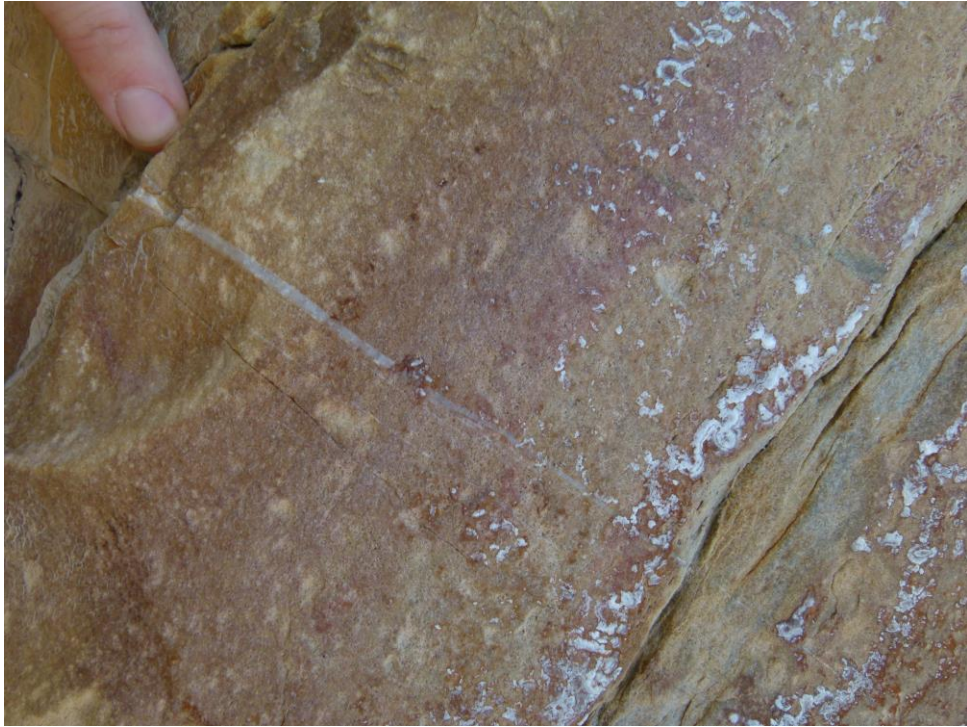


Figure 3.4: Completely filled mineralized fracture (Photograph by Owen Callahan).



Figure 3.5: Partially mineralized fractures showing visible pore space (Photograph by Owen Callahan).

4. **Vuggy fractures** (Figure 3.6). Vugs usually result from percolating acid waters through fractures and can lead to the development of karst. These can provide significant porosity and permeability.



Figure 3.6: Vuggy bed-parallel fractures (Photograph by Peter Eichhubl).

This thesis focuses on examining fluid flow in partial mineral-filled fractures. These mineral-filled fractures contain some measureable pore space within the filling material. The pore space may be primary or secondary in nature, some resulting from a complex diagenetic history of the fracture fill.

ESTIMATES OF FRACTURE PERMEABILITY

While Darcy's law is well established and has been tested for analyzing and predicting flow of fluids in porous media (Bruggeman, 1999), fluid flow in fractured rocks is still a largely unpredictable. Fluid flow through low-permeability rocks usually occurs through interconnected fluid-conducting fractures. The presence of open fractures greatly increases the permeability of the rock. Several authors (Snow, 1969; Wilson, 1970) have modeled fracture planes as smooth parallel plates separated by a constant aperture, b . Thus, fluid flow in the fracture takes place parallel to the fracture's axis, overlooking variations of pressure, velocity or solute concentration across the fracture width (Bear, 1993). This model is described as the parallel plate model, where the volumetric flow rate is proportional to the cube of the aperture. That is,

$$Q = -\left(\frac{Wb^3}{12\mu}\right)\nabla P \quad (3.1)$$

where Q is the volumetric flow rate through the fracture, W is the fracture width, b is the fracture aperture, μ is the dynamic viscosity and ∇P is the pressure gradient (see Figure 3.7). Thus, a small variation in the aperture results in large variations in fluid permeability. If the above relationship is divided by cross-sectional area, and compared to Darcy's law then fracture permeability is defined as:

$$k_f = \frac{b^2}{12} \quad (3.2)$$

Equation (3.2) is a simple approximation of single-phase flow in fractures with impermeable fracture walls and is called the cubic law (Snow, 1969; Witherspoon et al., 1980). The cubic law is the analytical solution to the Stokes equation for viscous flow

through wide smooth parallel plates (no-slip walls). No-slip condition for viscous fluids assumes that at a solid boundary (wall), the fluid will have zero velocity relative to the boundary. The cubic law assumes that the wall is wide enough (width \gg aperture) and the length across which a pressure head is applied is long enough (height $>$ width).

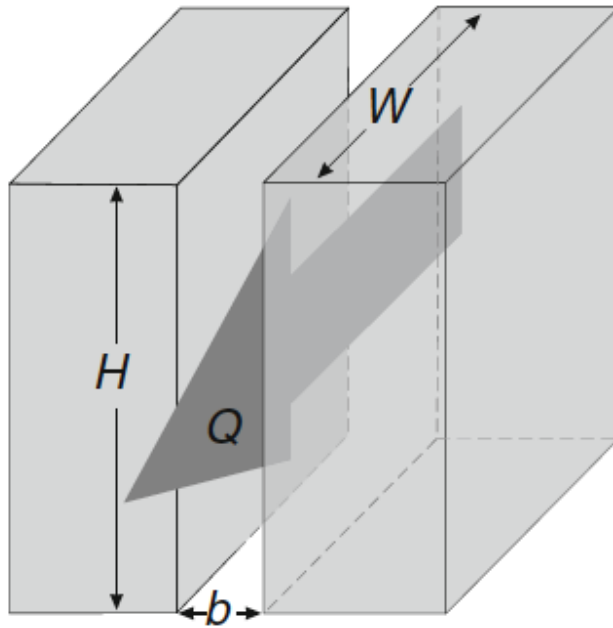


Figure 3.7: Flow between parallel plates with aperture, b , plate heights, H , and plates width, W (Klimczak et al., 2010).

Modifications

Although the cubic law accurately describes single phase flow between smooth-walled plates, natural fractures are almost always rough-walled with some contact between the walls at discrete points (Gangi 1978; Brown & Sholtz, 1985; Brown, 1987; Zimmerman et al., 1992), which decreases total flow. Iwai (1976) added an empirical factor to the cubic law to account for the effects of surface roughness. Engelder and

Scholz (1981) found that their data to agree well with the cubic law modified to account for variable void cross section as a result of applied stress. Other authors (Iwai, 1976; Gale and Raven, 1980; Engelder and Scholz, 1981; Pyrak-Nolte et al., 1987) found that flow through a single fracture under high stress often yielded a relationship between flow and fracture aperture greater than cubic. Walsh (1981) concluded that flow rate depends on two factors: fracture aperture and tortuosity. Modifications to the cubic law have been made to incorporate a correction factor based on fracture roughness (Renshaw, 1995). The accuracy of the cubic law can also be improved by considering explicitly the spatial variability in aperture field that results in the local cubic law (Zimmerman et al., 1991; Mourzenko et al., 1995; Nicholl et al., 1999), which is sometimes called the Reynolds equation.

While the local cubic law has been applied in investigations of fluid flow and reactive solute transport through single fractures, the errors introduced by neglecting tortuosity, roughness, and inertial forces are still unclear.

TORTUOSITY IN FRACTURES

Kranz et al. (1979) observed that the effect of tortuosity could be neglected for fluid flow because aperture dominates flow properties due to the cubic effect. In contrast, a computational study by Tsang (1984) concluded that tortuosity and surface roughness greatly affect the flow especially when contact area is greater than 30%. Natural fractures typically have contact areas and constrictions due to the presence of mineral cements and stress fields. Hence, flow through a single fracture occurs through a few tortuous

channels with variable aperture (Pyrak-Nolte et al., 1985; Bourke et al., 1985; Tsang and Tsang, 1987). Tsang and Tsang (1987) investigated the influence of tortuosity in fluid flow through fractures using fractures from both laboratory (tortuous and intersecting channels) and a hypothetical analytic function. Tsang and Tsang (1987) found that the presence of small apertures in the aperture distribution increased the effect of tortuosity.

Chen et al. (2004) performed air-water flow experiments in smooth-walled fractures and defined a measurable tortuosity coefficient for the channel flow regime, called the channel tortuosity, τ_c (Figure 3.8). The definition of τ_c is based on the smallest bounding rectangle that covers the whole channel for a specific phase (Figure 3.4). The channel tortuosity for gas (air) and water were defined as:

$$\tau_{c,g} = \left(\frac{L_x L_y}{A_c}\right)_g \text{ and } \tau_{c,w} = \left(\frac{L_x L_y}{A_c}\right)_w \quad (3.3)$$

where, A_c is the channel area, L_x and L_y are the length and width of the smallest bounding box, subscripts (g) and (w) denote gas and water respectively.

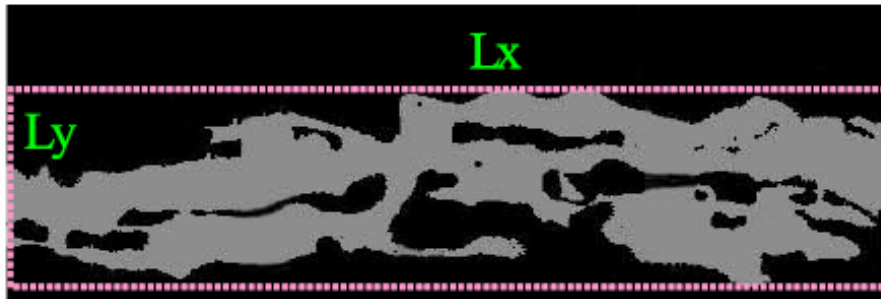


Figure 3.8: Illustration of channel tortuosity in an open fracture (Chen et al., 2004)

Fluid through the channels avoids the constrictions and filled areas of the fracture. Chen et al. (2004) found that the magnitude of channel tortuosity increases when the heterogeneity of fracture surface increases. Hence the presence of mineral cements (fracture filling), which increases the roughness of the fracture surfaces and/or decreases aperture, would increase the tortuosity of pathways and influence the permeability of the medium.

RELATIVE PERMEABILITY IN FRACTURES

The diversity in the geometry of natural fractures and complexity of multiphase flow interactions make it difficult to describe multiphase flow in fractures. Experimental relative permeability studies are limited in the literature and there are no widely accepted correlations between fracture relative permeability and fluid saturation. Pieters and Graves (1994) performed experimental studies and found that fracture relative permeability is not a linear function of saturation. They also concluded that there is a similarity between relative permeability behavior in fractures and porous media.

Capillary forces play a significant role in determining permeability, especially in rough walled fractures with apertures less than a millimeter (Prodanovic et al., 2010). In fractured media, the wetting phase is held preferentially around asperities by the capillary forces due to local aperture variation, whereas the non-wetting phase may be trapped in wider openings surrounded by low-aperture spots (Dullien, 1979). Conversely, the non-wetting phase will occupy the wider parts of the fracture, similar to how it remains in large pores in a granular material. Thus, the configuration of wetting and non-wetting

phases is a function of the spatial distribution of aperture, saturation history, and capillary pressure (Prodanović and Bryant, 2007).

Nicholl et al. (2000) studied the influence of the immobile phase on the relative permeability of the flowing/wetting phase (water) in the saturated condition. They developed a conceptual model that uses the in-place tortuosity induced by the immobile phase as a correction term to decrease the effective hydraulic gradient. The relative permeability of the flowing phase was obtained as:

$$k_{rw} = S_w \tau_{ip} \left[\frac{\langle b_f \rangle^2}{\langle b \rangle^2} \right] \left[\left(1 + \frac{9\sigma_b^2}{\langle b \rangle^2} \right)^{\frac{1}{2}} \left(1 + \frac{9(\sigma_{bf}^2)}{\langle b_f \rangle^2} \right)^{-\frac{1}{2}} \right] \quad (3.4)$$

where, k_{rw} and S_w are the wetting phase relative permeability and saturation respectively, $\langle b \rangle$ and σ_b^2 are the mean and variance of the aperture, $\langle b_f \rangle$ and σ_{bf}^2 are the mean and variance for the aperture field in the region occupied by the flowing phase. τ_{ip} is the in-place tortuosity, which is estimated independently for the measured phase geometries under some assumptions (Nicholl and Glass, 1994) by solving:

$$k_{rw} = S_w \tau_{ip} \frac{\langle b_f \rangle^2}{\langle b \rangle^2} \quad (3.5)$$

Nicholl et al (2000) concluded that in-place tortuosity is the dominant factor controlling the flowing phase relative permeability.

Chen and Horne (2006) modeled two-phase flow in rough-walled fractures. They found that the channel tortuosity (a tortuosity coefficient for the channel flow regime),

and thus, relative permeability, are mainly a function of saturation. The magnitude of channel tortuosity increases when the heterogeneity of the fracture surface increases. The velocity effects on flow structures within the experimental ranges were insignificant. In comparison to the water phase, these authors found that the gas phase relative permeability seems to have less effect with respect to the fracture roughness because of the low viscosity of the gas. The water phase relative permeability, however, demonstrates more phase interference and more residual water saturation as the heterogeneity of the fracture increases. The surface roughness and heterogeneity have a strong effect on the two-phase flow structures that affect the relative permeability. The flow structure approach presented by Chen and Horne (2006) for predicting the corresponding relative permeability in rough-walled fractures was demonstrated to be accurate in comparison with their experimental data. Chen and Horne (2006) proposed tortuous channel model (TCM) as:

$$k_{rw} = 0.74S_w^{*2} + 0.26S_w^* \quad (3.6)$$

$$k_{rg} = 0.43S_g^3 + 0.38S_g^2 + 0.19S_g \quad (3.7)$$

where,

$$S_w^* = \frac{S_w - S_{wr}}{1 - S_{wr}} \quad (3.8)$$

For these equations, k_{rg} is the gas (non-wetting phase) relative permeability, S_g is gas saturation, S_{wr} is residual water saturation, and S_w^* is the normalized water saturation.

In this thesis, fluid flow in fracture reservoirs is explored further. Using natural fractures from three different formations and an artificial polyethylene sample, I explore

the influence of surface roughness on flow through rough-walled fractures. Since natural fractures are usually lined or completely filled with mineral cements, I study the influence of cementation on flow in the fracture. Fracture geometry is acquired from X-ray microtomography (CT) scans, which capture the small-scale roughness of the mineral-lined fractures. The permeability and tortuosity of the fracture profile is determined from simulations of fluid flow through these geometries with impermeable fracture walls.

I use a combination of the level-set-method-based progressive-quasistatic algorithm (LSMPQS software), and Lattice Boltzmann simulation to characterize the capillary-dominated displacement properties and the relative permeability of the naturally cemented fractures within. Finally, I numerically investigate the effect of (uniform) cementation on the fracture permeability as well as the tortuosity of the pore space and the capillary pressure-water saturation (P_c - S_w) relationship.

Chapter 4: Methodology

IMAGE ANALYSIS

In order to understand and simulate flow in partially cemented fractures I imaged fracture and host rock pore structure of core samples non-destructively in 3D using an Xradia 'MicroXCT-400' scanner housed in the University of Texas High-Resolution X-ray CT (UTCT) Facility of the Jackson School of Sciences. Pre-processing involved several steps for noise removal, filtering, and thresholding, carried out using the commercial software Avizo-Fire and the in-house code Blob3D (Ketcham, 2005).

The scanned X-ray micro-tomographic images were first processed to obtain segmented images that classify voxels into fracture (pore) space and solid space. The simplest form of segmentation is simple thresholding, where voxels with grayscale image intensities below a given threshold are classified as one space and above as the other. Only the highest quality tomographic images with a clear threshold can be segmented that way. More sophisticated (in terms of handling noise) image segmentation is done using indicator kriging, which is a single pass method requiring that a subpopulation of voxels of each phase be positively identified before the segmentation procedure (Oh and Lindquist, 1999). I used an intensity window in which values above the upper threshold are assumed to represent solid, and those below the lower threshold to represent pore space. For each of the other voxels, based on its neighborhood, the method finds the probability of the voxel belonging to solid or pore space. The segmented image was then either used in direct flow simulation or further processed to construct the medial axis or skeleton (Lee et al. 1994) and thus to characterize the pore space (see Figure 4.1).

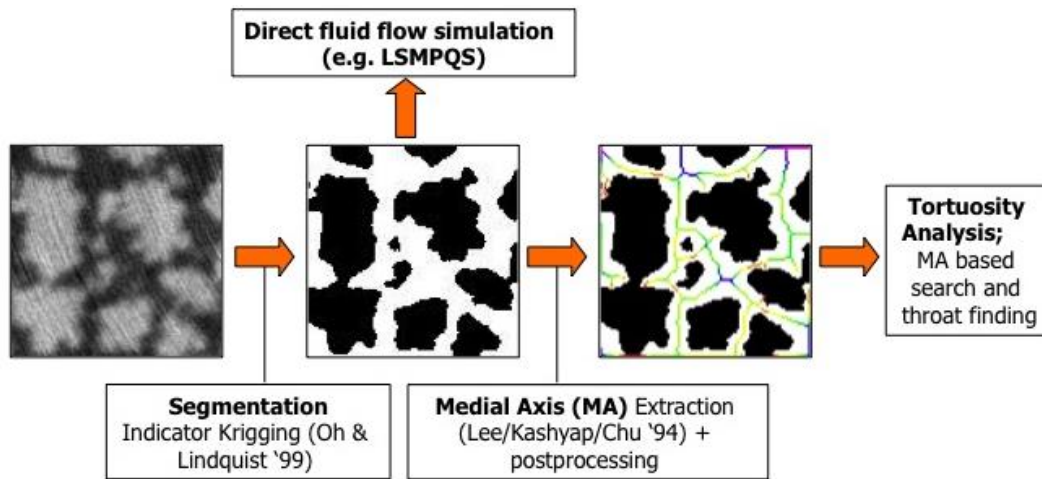


Figure 4.1: Overview of image analysis steps typical in the detailed analysis of pore scale images of porous media (Tokan-Lawal et al., 2013).

3D MEDIAL AXIS

The medial axis of any volume-filling object is intuitively the “spine” of the object running along its geometric middle (Lindquist et. al., 1996). It outlines the inherent shape of the object. The construction of the medial axis starts from the set of all points having more than one closest point on the object’s boundary (also known as medial surface), which is then “thinned” down to a set of digitized paths that retain the connectivity of the original space. For example, the medial axis of a sphere is the center point, for a cylinder it is the axis of rotational symmetry, and for a slab bounded by two infinite parallel planes it is the parallel plane intermediate between the bounding planes (Lindquist et. al., 1996). Medial axis gives basic information concerning the topology and geometry of the void space.

The medial axis skeleton serves both as an easier way to visualize the pore space pathways and their disconnections, and as a starting point for further analyses such as path tortuosity computation and throat finding. The medial axis algorithm is sensitive to surface noise that result in dead-end end paths and isolated pores that need to be removed. These paths are trimmed to remove isolated components that correspond to isolated pores, remove dead end (branch-leaf) paths, reduce “surface remnants”, and merge close clusters. The methodology is implemented within 3DMA-Rock software (Lindquist 2010; Prodanović et al. 2006).

I assume a (trimmed) medial axis has been computed for the pore space inside a rectangular volume and output in medial axis (MA) voxel list format. For each MA voxel i on face a and for each MA voxel j on face b , the algorithm will find the shortest path (if one exists) from i to j through the medial axis network. Let l_{ij} be the length of this shortest path, and d_{ij} be the Euclidean distance between voxel i and j . The geometrical tortuosity t_{ij} of the path is defined as $t_{ij} = \frac{l_{ij}}{d_{ij}}$. In 3DMA-Rock, geometrical tortuosities are computed for the shortest paths between all possible entrance/exit voxel pairs i, j on the MA network and for a better comparison between all of the different voxel pairs, tortuosities are computed using distance between faces a and b instead of d_{ij} . The tortuosity distribution is well described by a gamma distribution.

LEVEL SET METHOD PROGRESSIVE QUASISTATIC (LSMPQS) ALGORITHM

The Level Set Method Progressive Quasistatic (LSMPQS) algorithm simulates capillary dominated fluid displacement in fracture space as defined by segmentation of

the tomographic images. The algorithm is used to find the gas/water configurations during drainage and imbibition cycles. The moving surface of interest is embedded as the zero level set of function $\phi(\vec{x}, t)$ defined on the entire domain. The zero level set is the set of all points \vec{x} such that $\phi(\vec{x}, t) = 0$. Such a representation enables the calculation of various interface properties. For example, the normal to the interface is: $\vec{n} = \frac{\nabla\phi}{|\nabla\phi|}$, where $\nabla\phi = (\phi_x, \phi_y, \phi_z)$ is the spatial gradient of ϕ . The divergence of the normal, $\nabla \cdot \vec{n}$, is twice the mean curvature, κ , which is an important parameter in the Young-Laplace equation for interface equilibria. The time-like parameter, t , tracks the motion of the interface toward an equilibrium position and is not necessarily related to the physical time. The level set function evolves in time according to the following partial differential equation:

$$\phi_t + F|\nabla\phi| = 0 \quad \phi(\vec{x}, 0) \text{ given} \quad (4.1)$$

where F is the speed of the interface in the normal direction. The more general form of this expression is:

$$\phi_t + \vec{u} \cdot \nabla\phi = 0, \quad \phi(\vec{x}, t) \text{ given} \quad (4.2)$$

where \vec{u} is the external velocity field, i.e. if $\vec{u} = F\vec{n} = F \frac{\nabla\phi}{|\nabla\phi|}$, one obtains equation (4.1).

In LSMPQS, capillary forces are assumed to be dominant; hence the equilibrium interface will curve to maintain a balance between interfacial tension and capillary pressure. Incorporating Young-Laplace equation ($p_c = \sigma\kappa$), the appropriate normal

speed model at the core of slow, quasi-static interface movement is:

$$F(\vec{x}, t) = p_c - \sigma\kappa(\vec{x}, t) \quad (4.3)$$

Drainage (imbibition) displacements are modeled as quasistatic processes, in which the meniscus between the wetting and non-wetting phases moves from one equilibrium location to another in response to increments (decrements) in capillary pressure. The drainage fluid interface is initially places a planar or circular interface near the entry of the computational domain (Prodanović and Bryant, 2006). The interface is propagated using a slightly compressible model, which defines the speed F in the evolution, equation 4.1, as (Prodanović and Bryant, 2006):

$$F(\vec{x}, t) = a_0 \exp \left[K \left(1 - \frac{V(t)}{V_m} \right) \right] - b_0 \kappa(\vec{x}, t) \quad (4.4)$$

where, a_0 is the prescribed pressure-like term, V_m is the prescribed non-wetting phase target volume, $V(t)$ is the actual wetting phase volume in the domain at time t , K is the non-wetting phase bulk-modulus, b_0 corresponds to interfacial tension, and $\kappa(\vec{x}, t)$ is twice the mean curvature.

In this work, I model the situation where the wetting fluid is perfectly wetting the solid surface (i.e. contact angle is zero). This is effectively done by describing the solid phase with a separate level set function and implementing a simple penalization if the meniscus enters the solid phase.

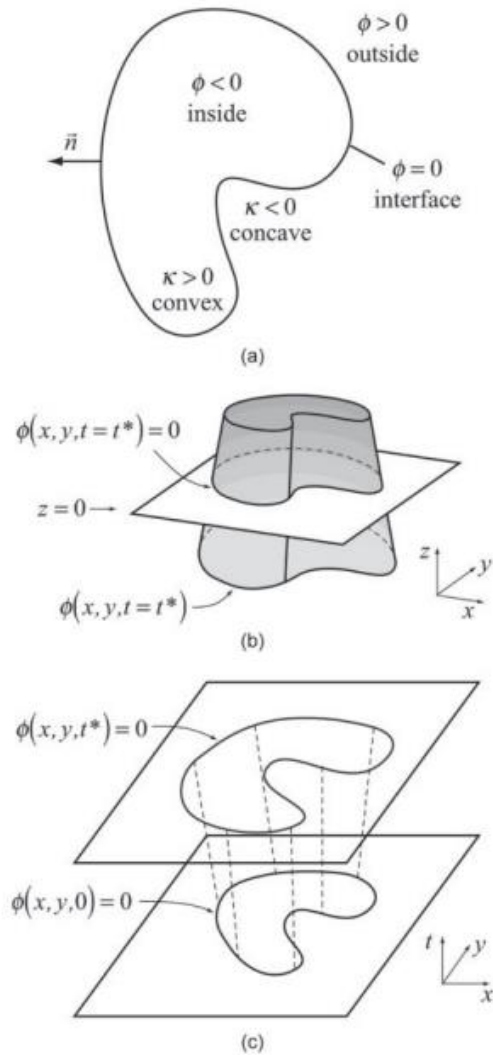


Figure 4.2: (a) 1D interface embedded as a zero level set ($\phi = 0$) of a real valued level set function, ϕ , defined on the entire 2D domain (b) Schematic of ϕ from which (a) is obtained. The surface shows ϕ at a particular time; the level set function evolves with time according to equation 4.1 (c) Comparison of the location of the interface at time t^* , to its initial condition. Reprinted from Prodanović and Bryant (2009)

Cementation of the fracture pore space

I numerically investigate the effect of (uniform) cementation on the fracture permeability as well as the tortuosity of the fracture pore space and the capillary pressure-water saturation (P_c-S_w) relationship using two different methods. Øren and Bakke (2002) introduced process-based reconstruction of sandstone samples based on numerical simulation of geologic processes such as cementation and compaction. Several authors (Mousavi and Bryant, 2007; Motealleh and Bryant, 2009; Torskaya et al., 2007) modified Øren and Bakke's method. These authors started from a model of disordered packing of spherical grains, with grains numerically compacted and diagenetically altered to various degrees. Mousavi and Bryant (2007) used uniform cement overgrowth on a spherical packing, with a possibility of an outside part of the each sphere being ductile (soft) and redistributing itself on the pore space. In an approach that extends these ideas from sphere packings to an arbitrarily complex medium, Prodanović et al. (2013) used a level set method-based cementation method that operates on segmented images of porous media. The speed of cement growth can be uniform (constant in space) or not (in case such information is available). The accurate modeling of cement growth kinetics requires coupled flow and transport equations in a real medium and is currently computationally tractable only in 2D (Tartakovsky et al., 2007; Kang et al., 2009)

In this study, I uniformly cement the Niobrara sample by moving the grain surface into the pore space using simple level set method with constant interface speed. Uniform growth assumes that cement is deposited at the same rate at all grain surfaces, and as it is growing into the pore space the speed, F , is set to a negative constant. For a sketch of

how this works in a general sandstone see Figure 4.3, and for more information on the method see Prodanović et al. (2013).

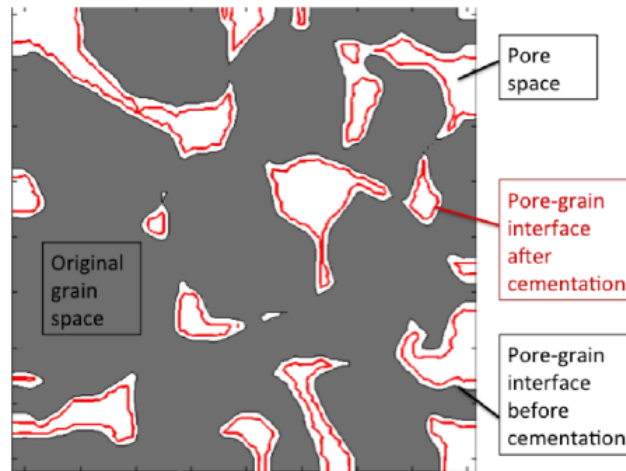


Figure 4.3: The cross-section of a sandstone sample showing original grain space (gray) and the pore space (white). After uniform cementation, the pore grain interface has moved to the new location inside the pore space. Reprinted from Prodanović et al. (2013).

LATTICE BOLTZMANN METHOD

In recent years, the lattice Boltzmann method (LBM) has evolved into an alternative and promising numerical scheme for simulating fluid flows and modeling physics in fluids (Benzi et al., 1992; Shan and Chen, 1993; Chen and Doolen, 1998; Sukop and thorne, 2007, Aidun and Clausen, 2010). Its strength lies in the ability to easily represent complex physical phenomena ranging from multiphase flows to chemical interaction between the fluid and solid. It originates in a molecular description of gas and can directly incorporate physical terms stemming from knowledge of the interaction between molecules. LB models do not track interfaces. Sharp interfaces can be maintained automatically, and macroscopic behaviors such as interface dynamics arise

naturally from the microscopic effects. It is capable of handling complicated boundary conditions (Shan and Chen, 1993; Aidun and Clausen, 2010).

Lattice Boltzmann models are kinetic in origin and fall into the category of mesoscopic models – between microscopic and macroscopic. LBM is based on microscopic models and mesoscopic kinetic equations (Benzi et al., 1992; Shan and Chen, 1993; Chen and Doolen, 1998). Hence, they are capable of capturing microscopic effects as well as reproducing macroscopic behavior. The macroscopic dynamics of fluids are the results of the collective behavior of many microscopic particles in the system hence by developing a simplified (linearized) version of the kinetic equations; one avoids complicated kinetic equations such as the full Boltzmann equation. In this section, a summary of the theoretical background to the LBM is provided; more detailed discussion on the LBM and the boundary conditions is available in Chen and Doolen (1998).

LBM simulates fluid flow problems in terms of a single variable, the particle distribution function, compared to the traditional computational fluid dynamics (CFD) methods that solve the Navier-Stokes equation for macroscopic variables such as continuum pressure and velocity (Shan and Chen, 1993). These variables in LBM are calculated as moments of the density distribution function. The method evolves particle distribution using a finite set of velocities over discrete time steps and kinetic rules obey conservation of mass and energy.

The LBM originated from lattice gas (LG) automata, a discrete particle kinetics utilizing a discrete lattice and discrete time (Shan and Chen, 1993; Chen and Doolen, 1998; Sukop and thorne, 2007, Aidun and Clausen, 2010; Landry and Karpyn, 2012)..

The state of the system is characterized by the discretized one-particle velocity distribution function $n_i(\mathbf{r}, t)$, which describes the number of fluid particles at a lattice node \mathbf{r} , at time t , with a velocity \mathbf{v}_i ; \mathbf{r} , t , and \mathbf{v}_i are discrete, whereas $n_i(\mathbf{r}, t)$ itself is a continuous variable. The mass density $\rho(\mathbf{r}, t)$, and the momentum density $\mathbf{m}(\mathbf{r}, t)$, are defined by moments of this velocity distribution function:

$$\rho(\mathbf{r}, t) = \sum_{i=1}^N n_i(\mathbf{r}, t) \quad (4.5)$$

$$\mathbf{m}(\mathbf{r}, t) = \sum_{i=1}^N \mathbf{v}_i n_i(\mathbf{r}, t) \quad (4.6)$$

Here $\mathbf{m}(\mathbf{r}, t) = \rho(\mathbf{r}, t)\mathbf{u}(\mathbf{r}, t)$, with $\mathbf{u}(\mathbf{r}, t)$ the macroscopic fluid velocity; the summation runs over the complete set of velocities $\{\mathbf{v}_i\}$. The most stable choices are $N=9$ for the two-dimensional lattice model (a.k.a. D2Q9 lattice) and $N=19$ for the three-dimensional lattice model (a.k.a. D3Q19 lattice, Figure 4.4). Both lattices include the center cell of the lattice, describing the particles staying in place, as well as neighboring cells sharing an edge or a face with the central one.

The time evolution of the velocity distribution function in the presence of an externally applied pressure gradient or gravitational force is governed by the discretized Boltzmann equation:

$$n_i(\mathbf{r} + \mathbf{v}_i, t + 1) = n_i(\mathbf{r}, t) + \Omega_i(\mathbf{r}, t) + f_i(\mathbf{r}, t) \quad (4.7)$$

where $\Omega_i(\mathbf{r}, t)$ describes the change in $n_i(\mathbf{r}, t)$ as a result of collisions and $f_i(\mathbf{r}, t)$ incorporates the effect of external forces. Each lattice-Boltzmann update consists of two steps. The first step includes the effects of collisions and external forces: the velocity distribution function after this step is defined as $n_i^*(\mathbf{r}, t)$.

$$n_i^*(\mathbf{r} + \mathbf{v}_i, t + 1) = n_i(\mathbf{r}, t) + \Omega_i(\mathbf{r}, t) + f_i(\mathbf{r}, t) \quad (4.8)$$

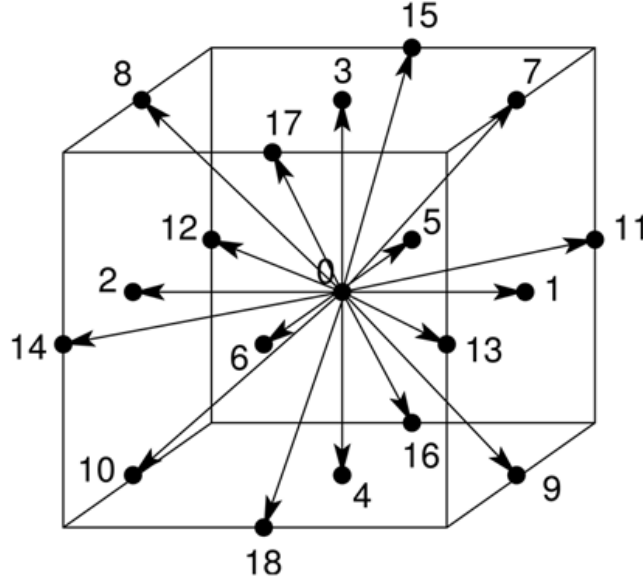


Figure 4.4: Lattice links for the D3Q19 lattice Boltzmann method. Reprinted from De et al. (2009).

The post collision distributions, in the second step, $n_i^*(\mathbf{r}, t)$, are propagated to the neighboring nodes in the direction of their velocities \mathbf{v}_i :

$$n_i(\mathbf{r} + \mathbf{v}_i, t + 1) = n_i^*(\mathbf{r}, t) \quad (4.9)$$

For low-Reynolds-number flows, the equilibrium distribution function $n_i^{eq}(\mathbf{r})$ is only required to linear order in the fluid velocity (Ladd, 1994) i.e.:

$$n_i^{eq}(\mathbf{r}) = \rho(\mathbf{r})[b_0^i + b_1^i \mathbf{v}_i \cdot \mathbf{u}(\mathbf{r})] \quad (4.10)$$

b_0^i and b_1^i are determined by the condition that the shear viscosity is isotropic and that the velocity moments of $n_i^{eq}(\mathbf{r})$ reproduce the correct hydrodynamic fields for low-Reynolds-number flows, i.e., $\sum_i n_i^{eq}(\mathbf{r}) = \rho(\mathbf{r})$, $\sum_i \mathbf{v}_i n_i^{eq}(\mathbf{r}) = \mathbf{m}(\mathbf{r})$ and

$\sum_i \mathbf{v}_i \mathbf{v}_i n_i^{eq}(\mathbf{r}) = c_s \rho(\mathbf{r}) \mathbf{1}$, where c_s is the speed of sound and $\mathbf{1}$ is a unit tensor.

The collision operator $\Omega_i(\mathbf{r}, t)$ can be simplified by linearizing about the equilibrium distribution function (Ladd, 1994):

$$\Omega_i(\mathbf{r}, t) = -[n_i(\mathbf{r}, t) + n_i^{eq}(\mathbf{r})] \quad (4.11)$$

Which is equivalent to the exponential relaxation time model with a relaxation time $\tau = 1$. This choice of collision operator is especially suitable for low-Reynolds-number flows, since the viscosity is not an important parameter in this case.

Incorporating an external pressure gradient, ∇p^{ext} , by applying a uniform force density, $\mathbf{g} = \nabla p^{ext}$ to the fluid, i.e.

$$f_i = b_1^i \mathbf{v}_i \cdot \mathbf{g} \quad (4.12)$$

Thus a constant increment of moment $\Delta \mathbf{m} = \mathbf{g}$ is added to each node at each node at each time step. Combining equations (4.10) – (4.12), the LB equation for low Reynolds number flow in the presence of a uniform force density, can be written as:

$$n_i(\mathbf{r} + \mathbf{v}_i, t + 1) = \sum_{j=1}^N (b_0^i + b_1^i \mathbf{v}_i \cdot \mathbf{v}_j) n_j(\mathbf{r}, t) + b_1^i \mathbf{v}_i \cdot \mathbf{g} \quad (4.13)$$

In order to simulate the interactions between fluid and solid, LBM must be modified to incorporate the boundary conditions imposed on the fluid by the solid phase (Chen and Doolen, 1998; Guo et al., 2002; Sukop and thorne, 2007, Aidun and Clausen, 2010).. Boundary conditions in LBM have been directly adopted from the lattice gas automaton (LGA) method (Shan and Chen, 1993; Chen and Doolen, 1998; Sukop and thorne, 2007, Aidun and Clausen, 2010). For example, a particle (or distribution function) bounce-back scheme is used at walls to obtain no-slip (or zero) velocity conditions. In the

bounce-back scheme, when a particle reaches a wall node, the particle will scatter back to the fluid nodes along its incoming direction. In LGA, the bounce-back operation leads to a mass conservation and zero velocity condition on the wall. The way of handling boundary conditions in LGA and LBM is very simple compared with other numerical schemes, and this makes them a popular choice in porous materials with complex solid boundaries (Ziegler, 1993; Chen and Doolen, 1998; Sukop and Thorne, 2007; Aidun and Clausen, 2010).

The basic argument for the use of the bounce-back scheme to achieve the no-slip boundary condition is as follows: At the wall node, pairing up the incoming particle, we can envisage an imaginary particle inside the wall, which moves in the opposite direction of the incoming particle (Figure 4.5) (Ziegler, 1993; He et al., 1997; Chen and Doolen, 1998). The sum of the momentum of these two particles is zero. The particle collision on the wall nodes simply sends the imaginary particle into the fluid. It has been demonstrated that this bounce-back scheme indeed leads to the zero velocity condition on the wall nodes.

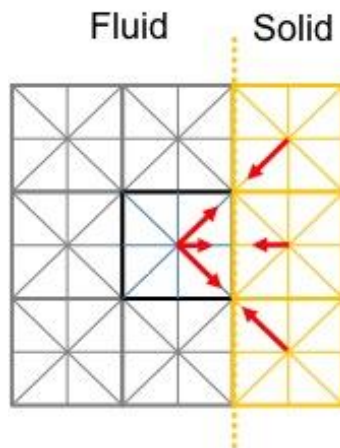


Figure 4.5: Bounce-back node with perfect reflection from the wall (solid).

Palabos software

The permeability of obtained fracture (pore) space (from either numerical model i.e. LSMPQS) was computed using the highly parallelized lattice Boltzmann code, Palabos (www.palabos.org). Palabos is an open source CFD package based on Lattice Boltzmann method implemented in parallel and installed on TACC (Texas Advanced Computing Center) at the University of Texas at Austin. Palabos is written based on Lattice Bhatnagar-Gross-Krook (LBGK) model where momenta of colliding particles will redistribute at some constant rate toward an equilibrium distribution. Permeability is calculated by imposing a constant pressure at the inlet, and a lower pressure at the outlet. The flux is compared with Darcy's law and the resulting constant is permeability.

Chapter 5: Fractured Polyethylene

SAMPLE DESCRIPTION

Porous polyethylene rods of 0.127 cm in diameter, formed by sintering medium/coarse, angular/sub-angular polyethylene grains into rod form, were used as the permeable medium (Landry and Karpyn, 2012). Splitting tools were driven along the desired fracture plane to create a fracture along the sides of the sample. The pore spaces of the fractured sample were imaged using x-ray computed microtomography as described in Chapter 4 and Landry and Karpyn (2012). The polyethylene sample allowed for having matrix and fracture spaces resolved using a single imaging technique. The images were then segmented in the procedure described in Landry and Karpyn (2012).

IMAGE CHARACTERIZATION

Microtomography image scans of the polyethylene sample were taken with voxel length 13.606 μm . I analyzed subvolume image of size 250x250x300 voxel³. The pore and fracture space was analyzed using the 3DMA-Rock software (see Chapter 4). The surface between the pore and solid spaces is shown in Figures 5.1 and 5.2 (top down and side views). Figure 5.3 shows the pore space thinned down to the medial axis skeleton. The coloring reveals the distance to the closest grain voxel (i.e. red is the closest while blue is the furthest). Figure 5.4 shows the shortest paths across the sample in the x-, y- and z-directions found during tortuosity calculation. Figure 5.5 shows the cumulative distribution function of the tortuosity in the x-, y- and z- directions. The z-direction provides the most direct paths across the sample as the fracture is aligned in the z-direction. The x- and y- directions show paths of similar distribution.

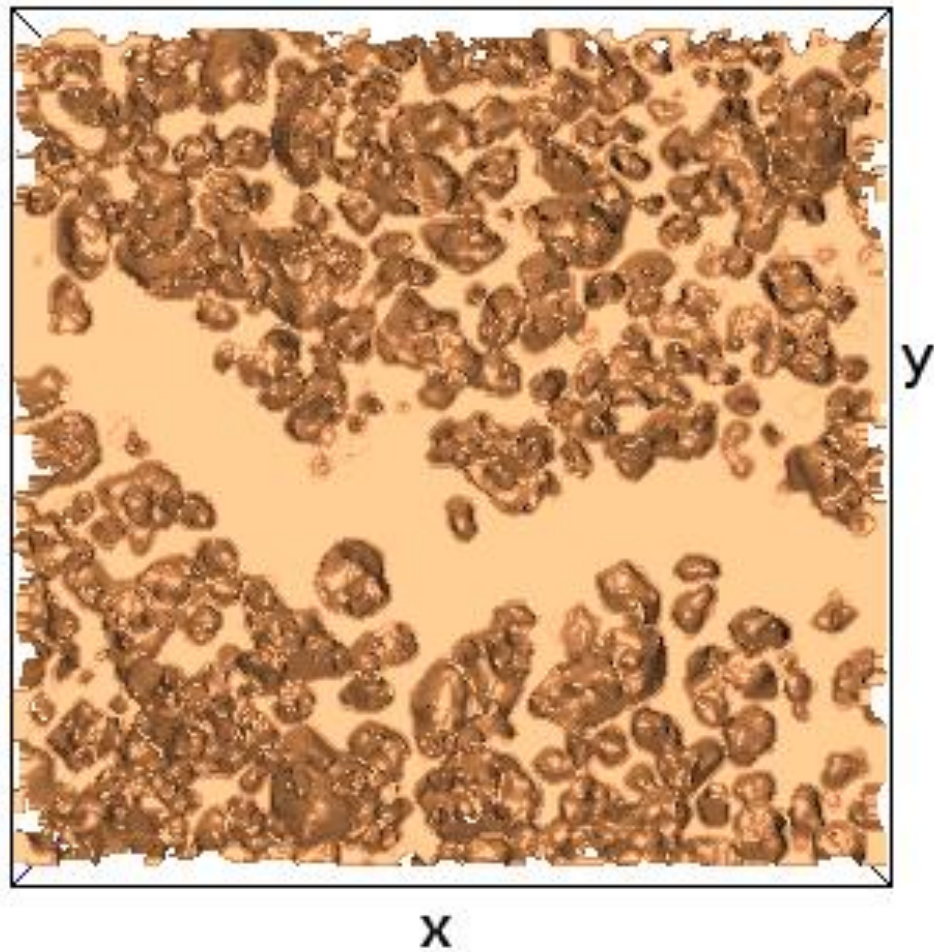


Figure 5.1: Pore-grain surface of the polyethylene: top-down view. For surface creation purposes, sides of image were padded with a layer of grain space.

The segmented images were post-processed to find the aperture in the z direction. The probability distribution function of the aperture of the polyethylene is shown in Figure 5.6, and the aperture field spatial distribution in Figure 5.7. The polyethylene has a mean aperture of 0.5873 mm; a standard deviation of 0.1762 mm; and a range of 0.1762 – 1.6073 mm.

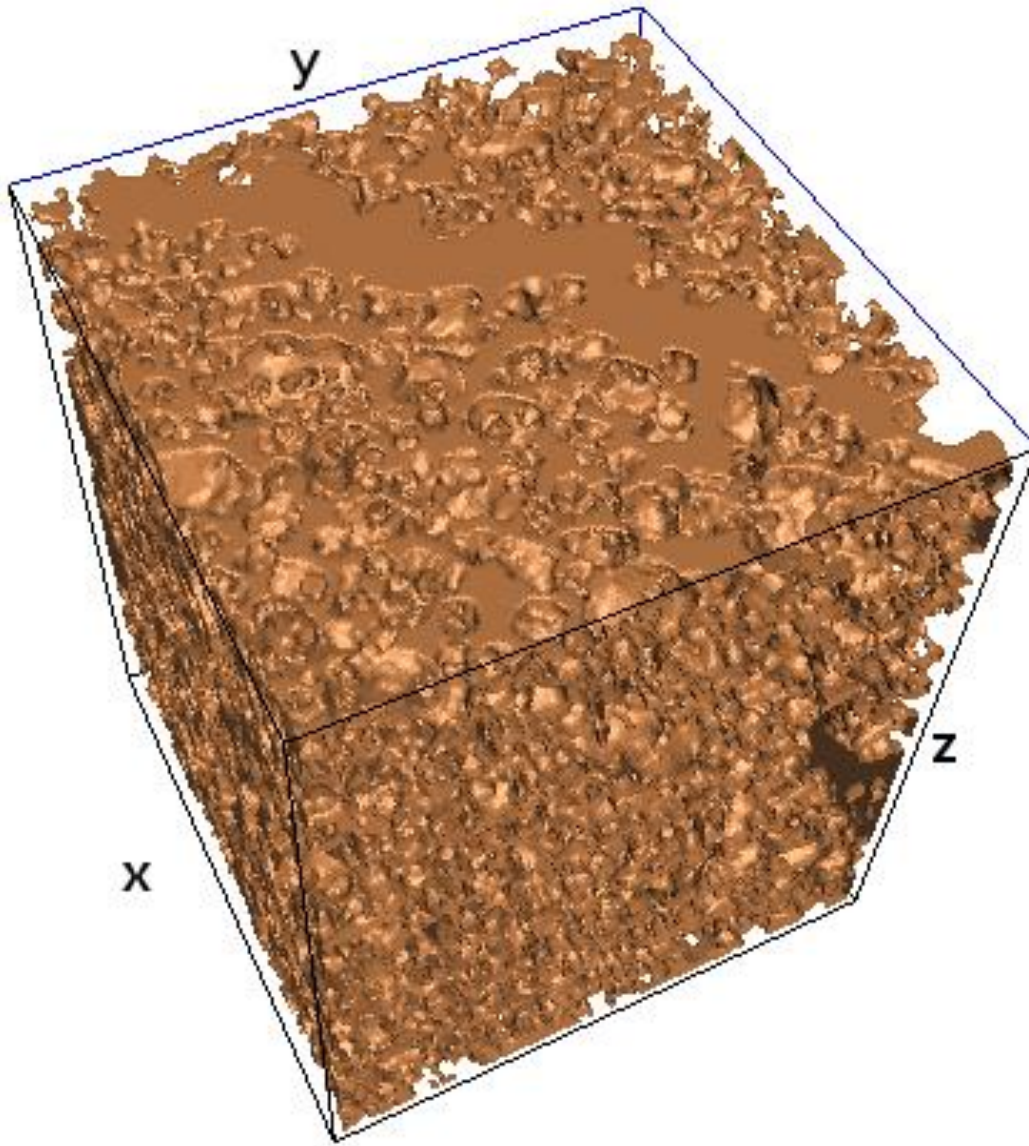
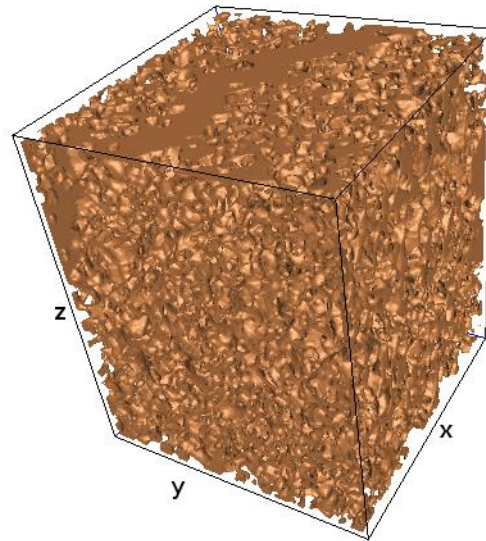
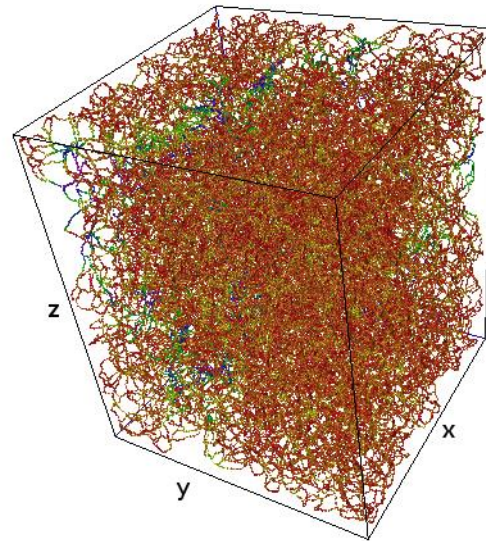


Figure 5.2: Pore-grain surface of the polyethylene: side view. For surface creation purposes, sides of cube were padded with a layer of grain space.



(a)



(b)

Figure 5.3: (a) Pore-grain surface (b) pore-grain surface trimmed down to the medial axis. The coloring represents the distance from the closest grain voxel (i.e. red is the closest while purple is furthest).

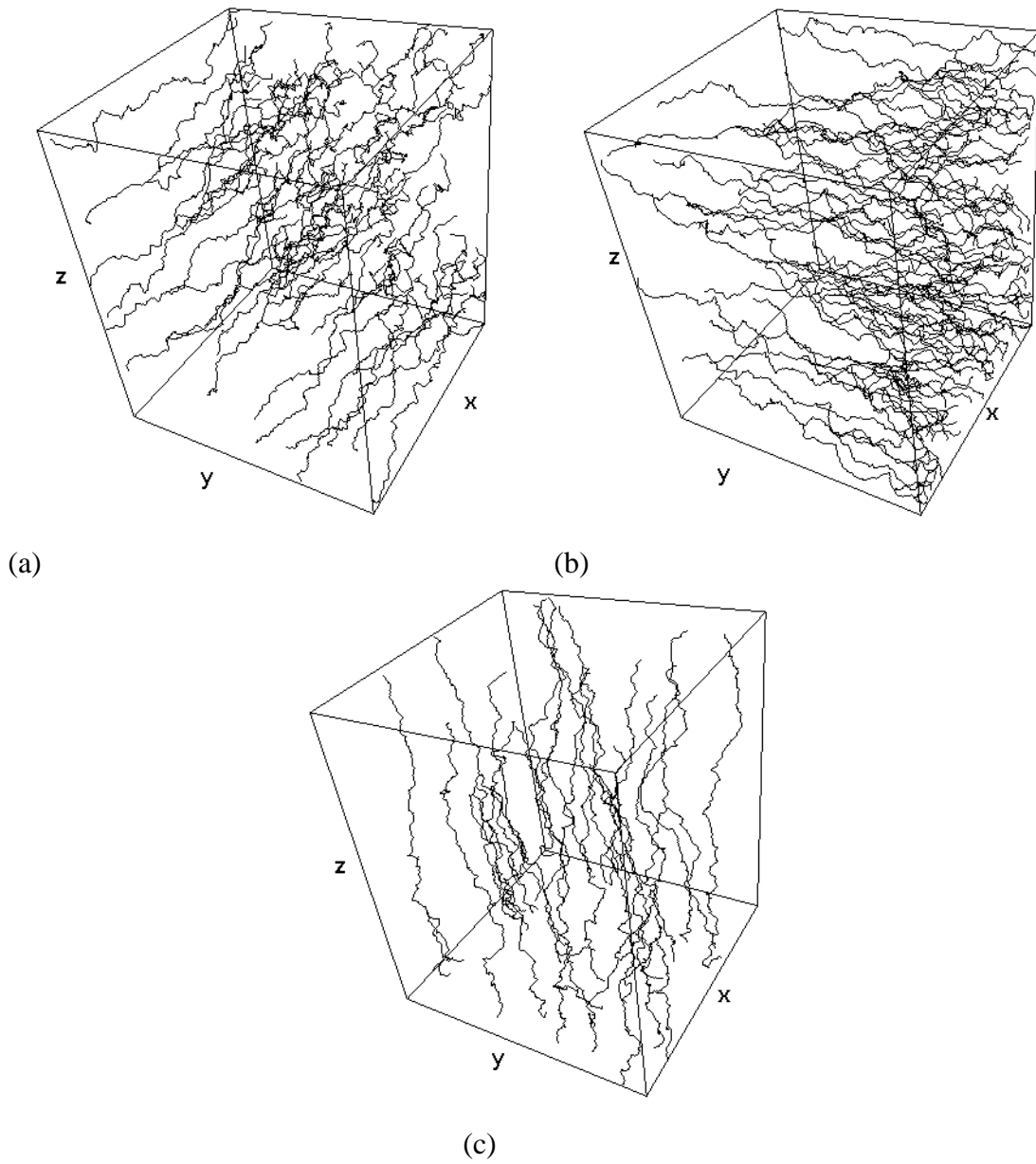


Figure 5.4: Shortest paths across the polyethylene sample. (a), (b) and (c) represent the shortest paths in the x, y and z directions respectively.

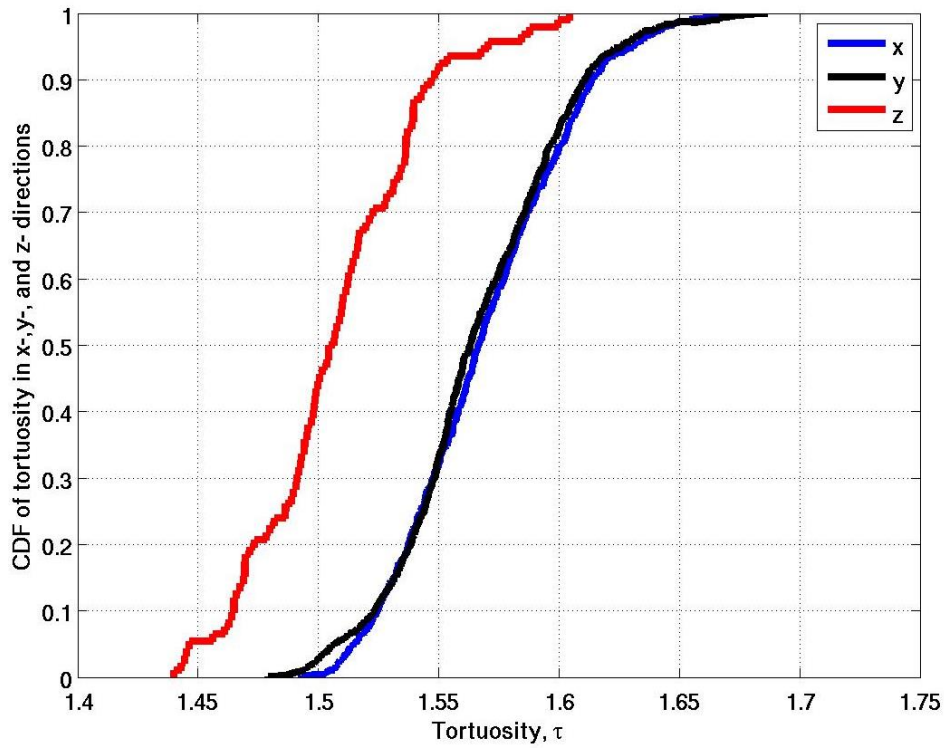


Figure 5.5: Cumulative distribution function (CDF) of tortuosity in the x-, y- and z-directions.

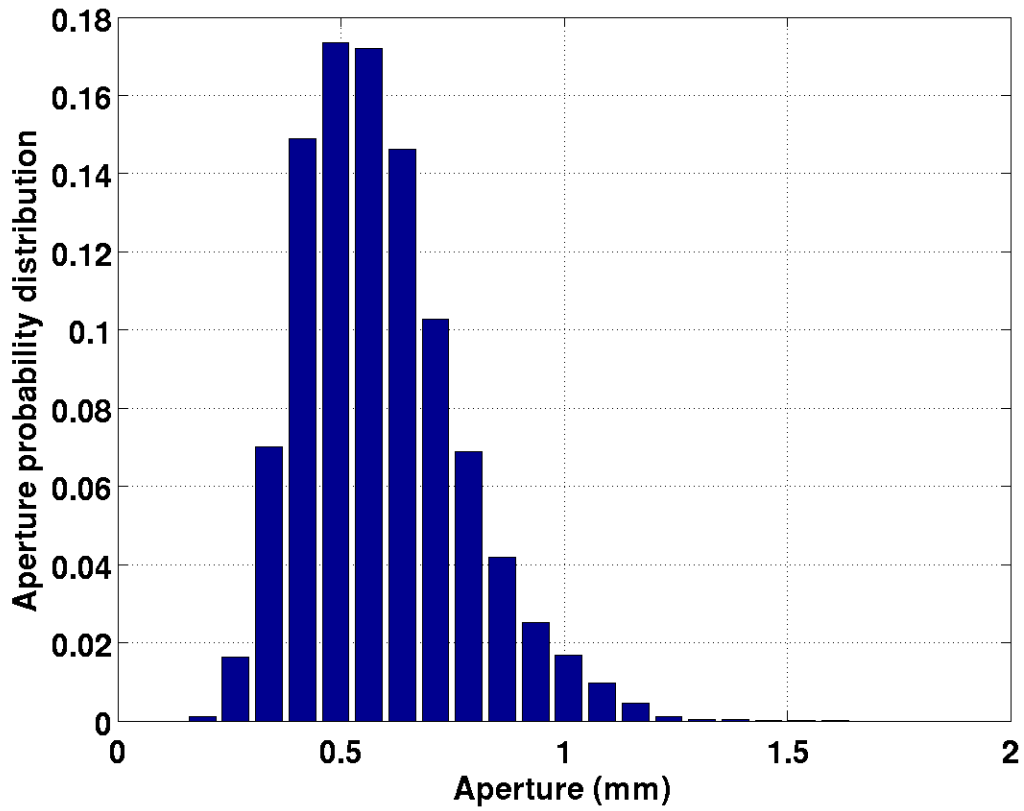


Figure 5.6: Probability distribution function for the aperture of the pore spaces in the polyethylene sample. The sample has a mean aperture of 0.5873 mm; a standard deviation of 0.1762 mm; and a range of 0.1762 – 1.6073 mm.

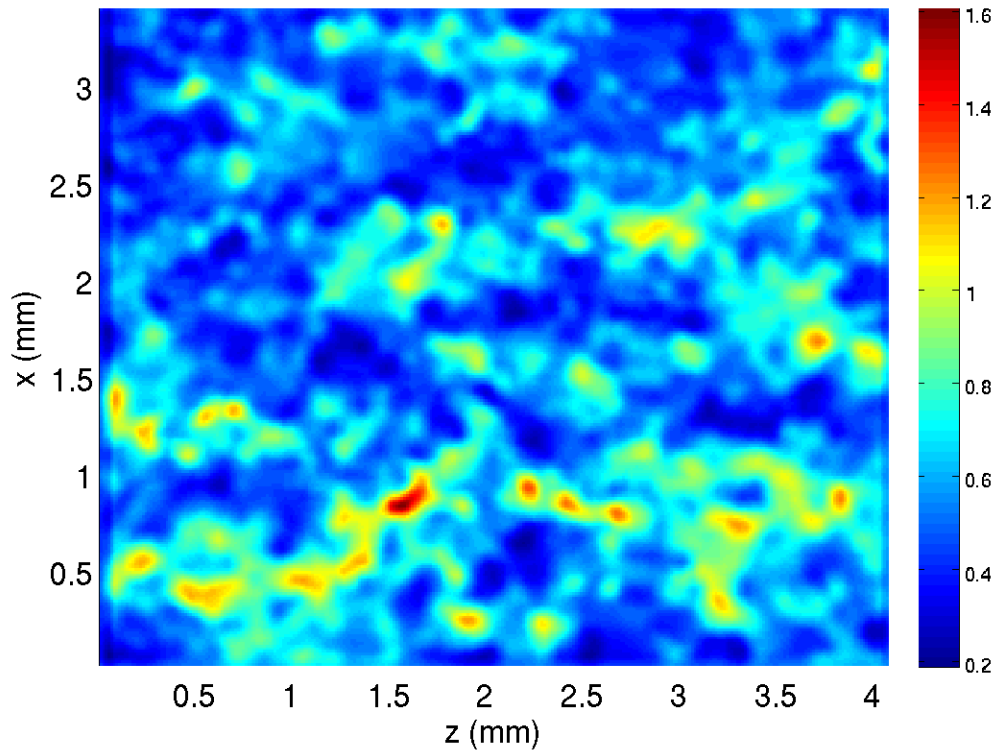


Figure 5.7: Aperture field distribution (measured in y-direction) of the polyethylene. The aperture ranges from 0.1289 mm to 2.1182 mm.

Fluid configurations

The segmented pore (and fracture) spaces were used as input for the LSMPQS simulation. Inlet/outlet volume sides are aligned with x-directions and all others are sealed. The curvature saturation relationship is shown in Figure 5.8.

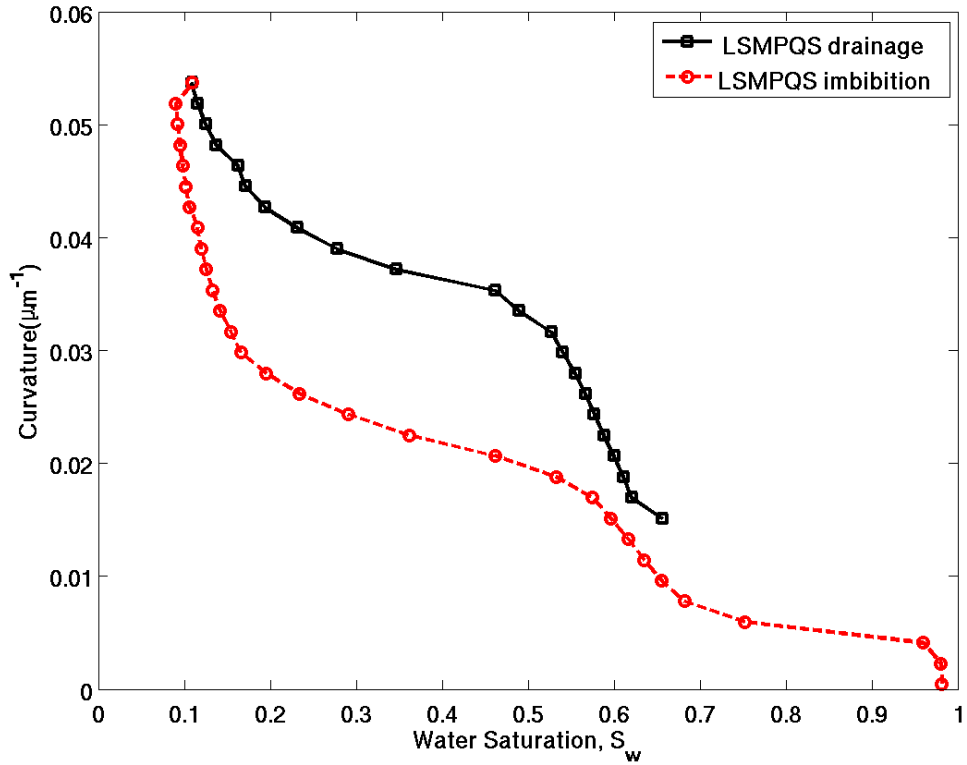


Figure 5.8: Curvature versus wetting phase (water) saturation during drainage and imbibition for the polyethylene sample.

The curvature of the interface is the consequence of preferential wetting of the capillary walls by one of the phases. The wetting phase wets the walls of the capillary, while the non-wetting phase rests on a thin film of the wetting fluid. Curvature can be scaled with surface tension to obtain capillary pressure, as per Young-Laplace equation. During drainage, the non-wetting phase does not penetrate the medium until the curvature exceeds the threshold curvature. Once the threshold curvature is exceeded, the non-wetting phase invades the pore space, pushing out the wetting fluid, until the irreducible water saturation is reached (i.e. until there is no more mobile wetting fluid). The

imbibition capillary pressure (curvature) decreases, and is in general smaller than the drainage capillary pressure for the same saturation, an effect called capillary pressure hysteresis. When the gas pressure is equal to the water pressure ($P_c=0$, which happens at a water saturation $\sim 98\%$), the saturation reaches the spontaneous water imbibition saturation. Increasing the saturation from this point can only be accomplished by forcing the water in through increasing the water pressure above the gas pressure, yielding a negative capillary pressure. An even higher water pressure is required to force the next bit of gas out until the residual gas saturation S_{gr} has been reached.

Figures 5.9(a) and 5.9(b) show wetting and non-wetting fluid configuration at the end of drainage and imbibition, respectively. The wetting phase covers the walls of the pores (apertures) and flows along the walls through thin liquid “sheets”, hence most of the residual wetting phase is either in small nooks and crevices of the pore space (small green blobs), or occupying bypassed parts of the pore space (larger green blobs). The disconnected non-wetting fluid surface is shown in blue and mostly occupies the middle of the pore space.

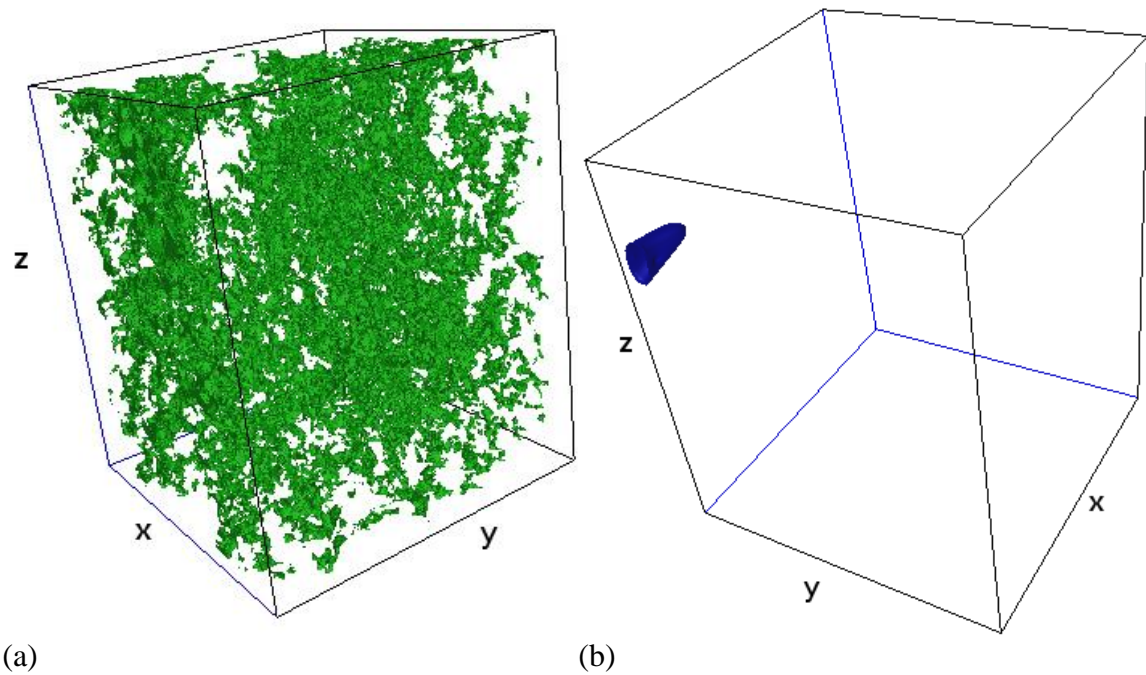


Figure 5.9: (a) Residual wetting phase at the end of drainage (b) Residual non-wetting phase at the end of imbibition (before last bit of non-wetting phase is pushed out).

Figure 5.10 shows tortuosity of NW phase during drainage and imbibition. NW phase is somewhat more tortuous during imbibition than during drainage. As expected, tortuosity is controlled by the saturation of the fluid phases. At very low water saturation during drainage and imbibition; connected pathways for the wetting fluid are non-existent. Likewise, during imbibition, at high water saturation, there are no connected pathways for the non-wetting phases.

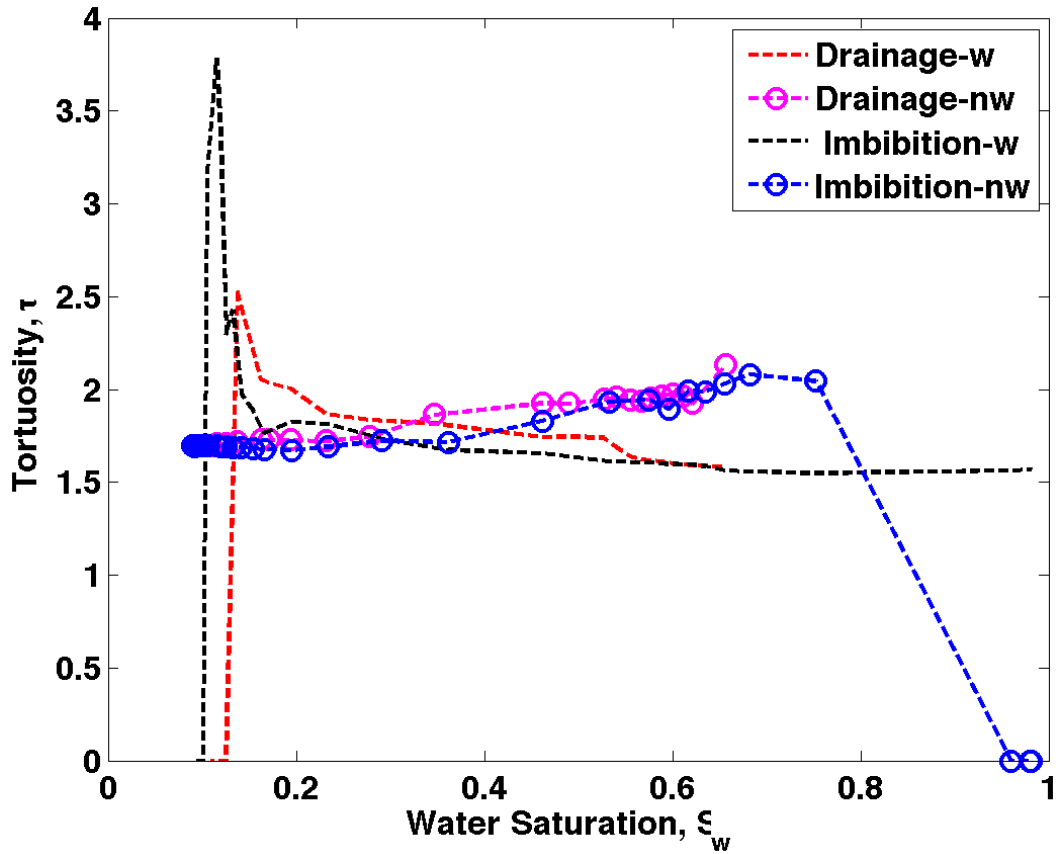


Figure 5.10: Tortuosity of the wetting and non-wetting phases versus water saturation during drainage and imbibition for the polyethylene sample.

Permeability

The absolute permeability of the polyethylene sample was computed as 423.21 D. The sample (fracture and matrix pore space) has a porosity of about 44.54%. Landry and Karpyn (2012) found the matrix porosity and fracture porosity of the pore space to be 32,6% and 24.3% respectively. The volume of the fracture is significant, and the fracture dominates flow. The wetting and non-wetting phase relative permeabilities for the polyethylene were also computed and are shown in Figure 5.10.

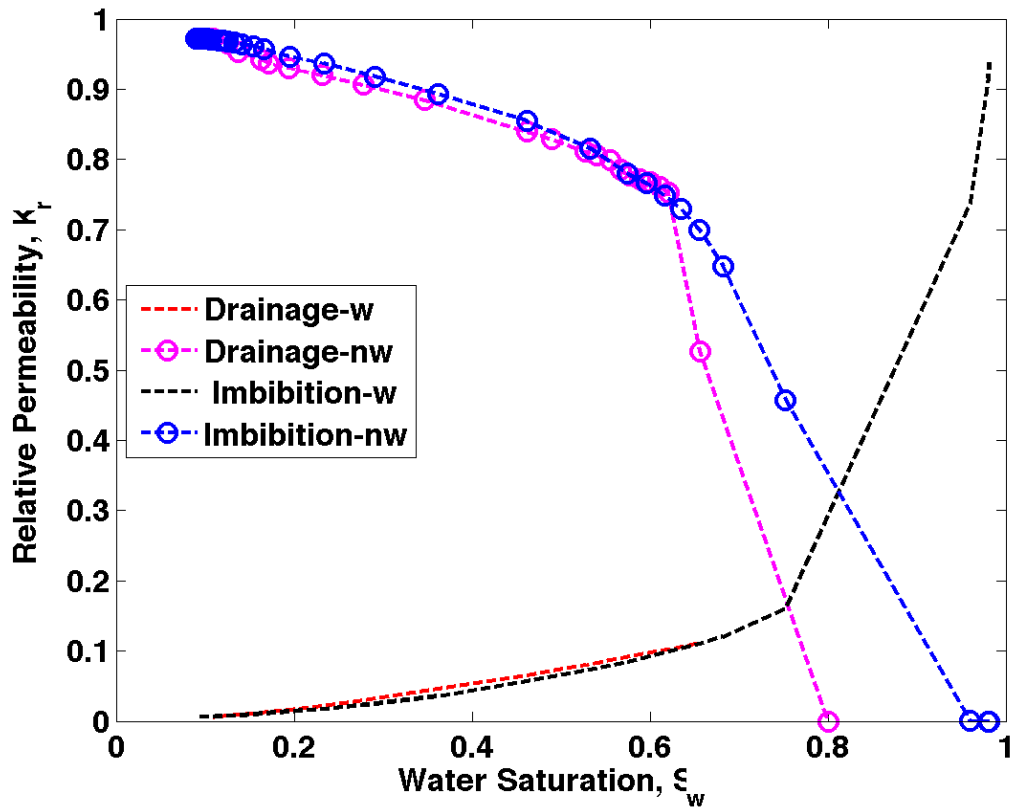


Figure 5.11: Relative permeability versus saturation of the wetting and non-wetting phases for the polyethylene sample. The non-wetting phase percolated through the fracture on the first drainage step ($\sim 70\% S_w$) thus significantly reducing the drainage wetting phase permeability.

At the start of drainage, the sample is 70% saturated with wetting phase, which is mostly located in matrix. The residual water (wetting phase) during drainage is in the matrix only, while the non-wetting phase occupies the fracture and centers of matrix pores. During imbibition, more wetting phase imbibes into the sample and invades the matrix pores first pushing out almost all the non-wetting fluid that may have occupied the pore spaces initially, thus increasing the wetting phase saturation to about 99%.

DISCUSSION

Landry and Karpyn (2012) computed the permeability of the same polyethylene sample. In their paper, they compared their results to those obtained using existing correlations. Table 5.1 shows a summary of the pore space geometry and fracture characteristics used in Landry and Karpyn (2012). These characteristics are also used in this thesis. Landry and Karpyn (2012) compared their work to correlations from Witherspoon et al. (1980); Zhang et al. (1996); Eker and Akin (2006); Zimmerman and Bodvarsson (1996); Nazridoust et al. (2006); Crandall et al. (2010) and the Alternate Cubic Law (ACL). While most of the correlations considered only the fracture permeability the parameters computed for this sample are for both the matrix and fracture (i.e. the entire pore space). Table 5.2 shows the values where they differ from the values in Landry and Karpyn (2012).

Table 5.1: Summary of pore space geometry and fracture characteristics used in Landry and Karpyn (2012).

Pore Space Geometry and Fracture Characteristics	
Specific solid surface area of the matrix pore space (a_m)	11.80 [mm^{-1}]
Fracture contact area fraction (C)	0.220
Average Fracture aperture (\bar{h})	0.651 [mm]
Hurst exponent (ε)	0.612
Fracture tortuosity (θ)	0.523
Fracture aperture standard deviation (σ_h)	0.290 [mm]
Matrix porosity (ϕ_m)	0.326
Fracture porosity (ϕ_f)	0.243

Table 5.2: Summary of pore space geometry and fracture characteristics from our analysis.

Pore Space Geometry and Fracture Characteristics	
Average Fracture aperture (\bar{h})	0.5873 [mm]
Fracture tortuosity (τ)	0.523
Fracture aperture standard deviation (σ_h)	0.1762 [mm]
Matrix and Fracture porosity (ϕ)	0.4454

Table 5.3: Summary of lattice Boltzmann (LB) permeability measurements and fracture permeability estimates (after Landry and Karpyn, 2012).

Method	Permeability Estimate
Fracture permeability (k_f) LK	$3.19 \times 10^{-10} \text{ (m}^2\text{)}$
Effective fracture aperture (h_e) LK	0.1957 (mm)
Alternative Cubic Law	$3.53 \times 10^{-08} \text{ (m}^2\text{)}$
Witherspoon et al. (1980)	$2.14 \times 10^{-08} \text{ (m}^2\text{)}$
Zhang et al. (1996)	$8.29 \times 10^{-10} \text{ (m}^2\text{)}$
Eker and Akin (2006)	$9.64 \times 10^{-07} \text{ (m}^2\text{)}$
Zimmerman and Bodvarsson (1996)	$1.09 \times 10^{-10} \text{ (m}^2\text{)}$
Nazridoust et al. (2006)	$2.80 \times 10^{-10} \text{ (m}^2\text{)}$
Crandall et al.(2010)	$4.75 \times 10^{-10} \text{ (m}^2\text{)}$

Comparing the values in tables 5.3 and 5.4, we see a large variation in the permeability estimates. This is probably due to a variation in the way our apertures are calculated. The largest “pore” spaces are assumed to be the fracture in our case. The alternate cubic law (ACL) determines an estimate of permeability from aperture only, ignoring the influence of fracture geometry and the contribution from the matrix. ACL

overestimates the permeability by a factor ~69. Witherspoon et al. (1980) determined fracture permeability from flow experiment; hence their correlation is subject to the fractures used to fit it. Witherspoon et al. (1980) overestimates the permeability by a factor of ~42. Like the ACL, Witherspoon et al. (1980) does not account for the contribution from the matrix in the permeability computation.

Table 5.4: Summary of permeability measurements and fracture permeability estimates.

Method	Permeability Estimate
Permeability (matrix and Fracture)	$4.1767 \times 10^{-10} \text{ (m}^{-2}\text{)}$
Alternative Cubic Law	$2.874 \times 10^{-08} \text{ (m}^{-2}\text{)}$
Witherspoon et al. (1980)	$1.7526 \times 10^{-08} \text{ (m}^{-2}\text{)}$
Zhang et al. (1996)	$6.1837 \times 10^{-10} \text{ (m}^{-2}\text{)}$
Eker and Akin (2006)	$0.1489 \text{ (m}^{-2}\text{)}$
Zimmerman and Bodvarsson (1996)	$1.7728 \times 10^{-08} \text{ (m}^{-2}\text{)}$

Zhang et al. (1996) underestimates the permeability by a factor of 1.5 with a fitted exponent of $\beta = 2.85$ ($k_f \sim \bar{h}^\beta$). Zhang et al. (1996) stimulated fluid flow in a fracture with impermeable walls, thus their estimate of permeability cannot be compared with the matrix-fracture simulated in this work. Eker and Akin (2006) proposed the β used in Zhang et al. (1996) as a linear function of the fractal dimension, D, ($\beta = 4.8065D - 6.4154$). While their function for β fits their results for different fractal dimensions, it does not fit the results of Zhang et al. (1996) or the results in this work. The correlation

by Eker and Akin (2006) overestimates permeability by several orders of magnitude. Hence we can assume that a linear function of β determined from fractal dimensions alone will not provide accurate results.

Zimmerman and Bodvarsson (1996) derived their fracture permeability estimates from semi-analytical correlations. The fracture permeability correlation is derived from Reynold's lubrication equation and it is applicable given the viscous forces dominate inertia forces. The permeability estimate of Zimmerman and Bodvarsson (1996) is applicable to fractures in impermeable rock, hence it will not correctly predict the permeability in the polyethylene sample used in this work. The correlation overestimates permeability in the polyethylene by 42.4. The Palabos permeability takes into account contributions from both the matrix and fracture.

Landry and Karpyn (2012) estimated the full pore permeability in a 520 x 520 x 800 voxel³ of the polyethylene as 3232.27 D, which is almost 8 times the value computed from our 250 x 250 x 300 voxel³ sample.

CONCLUSION

The fracture created and used in Landry and Karpyn (2012) was analyzed using image analysis (3DMA), and flow simulation tools (LSMPQS and Palabos). The single rough fracture was propagated along the axis of a porous polyethylene rod and imaged using x-ray computed microtomography. The CDF of tortuosity in the sample was found to be about the same in the x- and y- directions. The sample has a mean aperture of 0.5766 mm, with a range of 0.1289 – 2.1182 mm. The permeability in the polyethylene sample was found to be 423.21 D with a porosity of 44.54%. The permeability estimate

was compared with those in Landry and Karpyn (2012) as well as estimates from a variety of previous investigations; all of these estimates assume an impermeable fracture wall. Landry and Karpyn (2012) estimated the matrix and fracture (full pore) permeability as $3.19\text{E-}09\text{m}^2$ (3232.27 D). The ACL computes fracture permeability and overestimated permeability in this sample by two orders of magnitude. The ACL does not account for fracture roughness, tortuosity, asperities and aperture distribution, and has been widely accepted to grossly overestimate the fracture permeability. Zhang et al. (1996) suggest that permeability is a power function of mean aperture and a fitted power factor β . While their correlation provides a good estimate of permeability for a value of β that fits the fracture flow measurements, it has no power of prediction without a function for β dependent on fracture characteristics. Eker and Akin (2006) proposed a linear function for β dependent on the fractal dimension of the fracture wall roughness, however their prediction for β did not fit the results of Zhang et al. (1996), Landry and Karpyn (2012), or this work. Hence, a linear function for β dependent only on the fracture wall fractal dimension is inadequate. Zimmerman and Bodvarsson (1996) derived a semi-analytical prediction of fracture permeability dependent on the mean fracture aperture, fracture aperture deviation, and fractional contact area from the Reynold's lubrication equation. The permeability predicted by this function overestimated fracture permeability 22.8 times, indicating tortuosity and roughness are determining factors in the estimation of fracture permeability.

Lattice Boltzmann methods and other pore-scale models provide insight into fluid flow through permeable porous media at the micron scale, particularly in rough walled

fractured permeable media. The following chapters investigate flow in rough walled natural fractures with impermeable walls.

Chapter 6: Torridonian Sandstone

SAMPLE DESCRIPTION

Torridonian sandstone is a collective informal term for sandstones of the Late Proterozoic Torridon Group, NW Scotland (Ellis et al., 2012). For this study, I analyzed a partially cemented fracture, collected by Ellis (2012), from the Applecross Formation of the Torridon Group, exposed in the foreland of the Moine Thrust Belt, south of Dundonnell, Wester Ross (Figures 6.1 and 6.2). With a matrix porosity of ~4% (this study) and partially cemented fractures, Torridonian sandstone can be considered an outcrop analog for unconventional fractured oil and gas sandstone reservoirs. Fractures of the Torridonian sandstone are frequently partially cemented with quartz lining the fracture walls, and creating a complex fracture-porosity geometry (Ellis, 2012). The sampled core is a compositionally and texturally immature lithic arkose with framework grain composition of quartz, feldspar and lithic fragments of $Q_{58}F_{22}L_{20}$.



Figure 6.1: Torridonian sandstone from the Moine Thrust Belt, NW Scotland (Photograph by Peter Eichhubl).

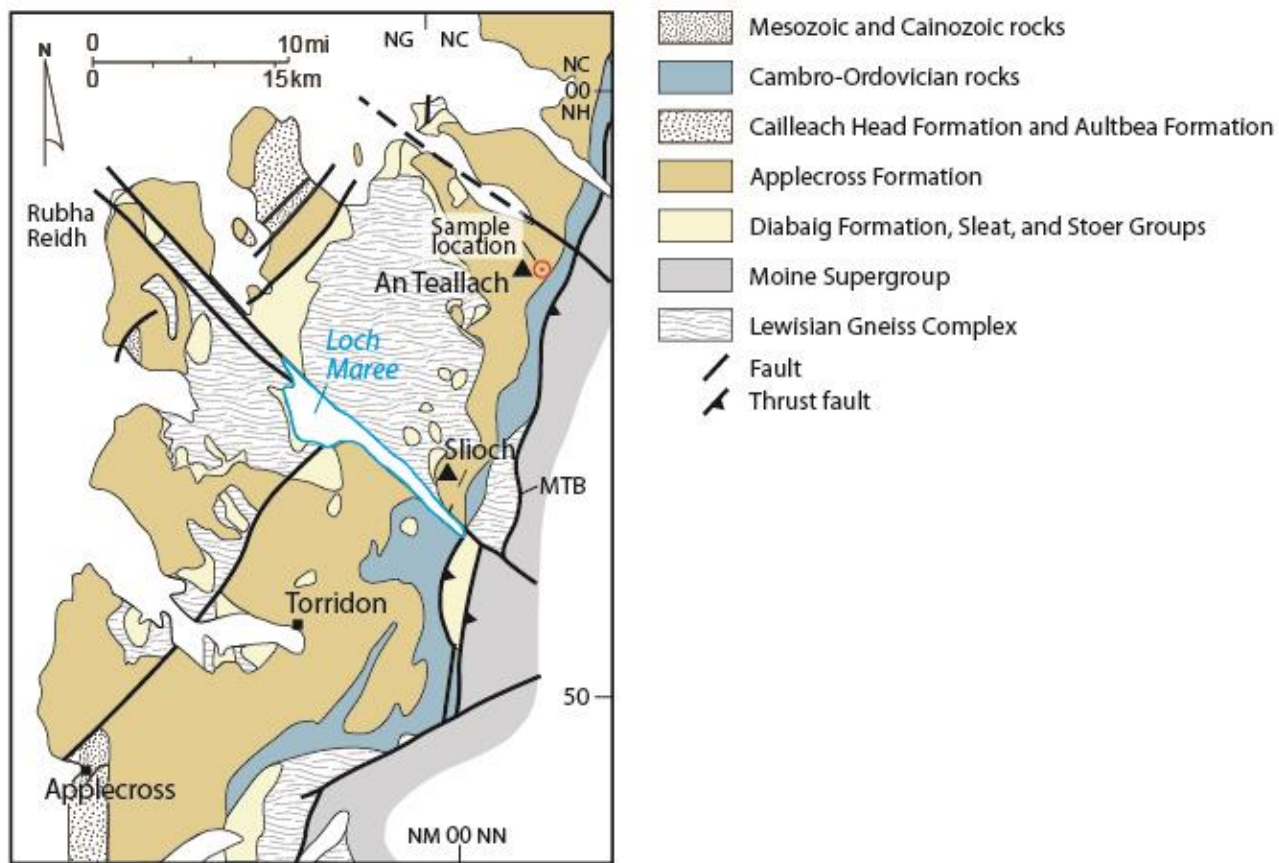


Figure 6.2: Map of Applecross Formation (Torridon Group) exposures in NW Scotland (modified from Ellis et al., 2012).

PETROGRAPHY

An accurate interpretation of the spatial distribution of grains and porosity is important in the understanding and predicting of petroleum reservoir performance. Relating the petrology of a reservoir to geophysical and petrophysical data provides an improved assessment of reservoir quality. Petrography involves qualitative interpretation and quantitative description of rock properties at the microscopic scale with the use of thin sections. It is the most fundamentally qualitative field of rock study and it depends highly on the experience of the observer (Milliken et al., 2007).

This section begins with a visual inspection of the thin section and a description of the method used in the analysis. It also discusses the petrographical analysis of a single thin section (Tor1ba) of the Torridonian sample, as well as the different analyses done to qualitatively and quantitatively describe the thin section. It concludes with a brief section summarizing the results of the analyses.

Visual inspection of the thin section

Holding up the thin-section of the sample to the light, there is a visible fracture that cuts the sample length-wise and contains open porosity. There is some homogeneity within the fracture. There is no visible porosity outside of the fracture. The grains appear to be uniformly distributed and there might be matrix or cement in the sample. The sample was cut too thick and this may make grain identification difficult. The thin-section was polished and there was no coverslip. The sample was not stained, and this may make the identification of the feldspars difficult.

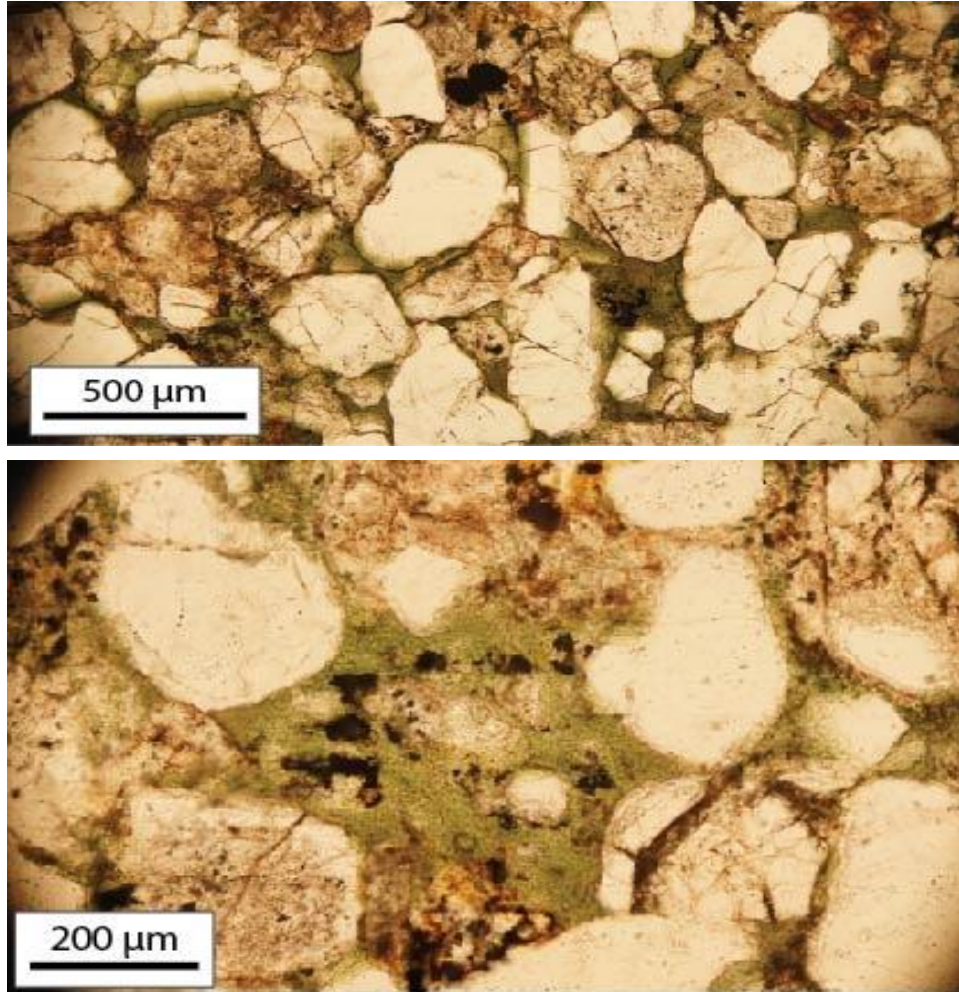


Figure 6.3: Sample showing the abundance of chlorite between the grains (PPL).

The sample was viewed under the light microscope with cross-polarized light (XPL) and plain polarized light (PPL). From the microscope, copious amounts of chlorite were found in the sample (figure 6.3). As a consequence of the chlorite, quartz cement was not very visible. There are lots of lithic fragments of different origin. There are lots of feldspars; however, due to the lack of stains, it is hard to distinguish between albite

and orthoclase, hence in this report, they are classified as untwinned feldspars. There appears to be some calcite grain replacement as well as chlorite in the lithic fragments.

Method

The thin section specimen was examined in plane-polarized light (PPL) and cross-polarized transmitted light (XPL) using a conventional transmitted light petrographic microscope. This was used to identify the different grains, heavy minerals, cements, etc. that are present in the specimen. The gypsum plate was used in the identification of some of the sandstone components.

Point count data was collected using a swift stage and following the methods described in the Sandstone Petrology Tutorial (Milliken et al., 2007) and by Folk (1980). The Gazzi-Dickinson method was used i.e. If the cross-hairs lands on any crystal larger than 62 μ m, the grain is counted as if it were a monocrystalline grain regardless of whether it is in a lithic fragment or not. If the cross-hairs lands on a component (less than 62 μ m) within a lithic fragment (or clast); then the component is classified as a lithic fragment.

Photographic images were taken using the camera (Sony Handy cam) attached to the microscope (Zeiss Axioskop 40). Using the image analysis software, JMicrovision (Roudit, 2007), calibrated to the image scale, the grain shapes from the images were traced and the grain size data were exported to Excel, for analysis. Descriptive statistics were computed and will be discussed in the data analysis section.

Point Count

The relative abundance of the quartz, feldspar and lithics (QFL) based on the Gazzi-Dickinson point counts are summarized in Table 6.1. Figure 6.4 shows the normalized QFL representation of the sandstone composition. A total of 1027 points were counted; Table 6.2 provides a summary of the different grain types and their relative abundance in the sample. Figure 6.5 shows the 95% confidence limits on the counted points.

Table 6.1: QFL composition in the sample.

Quartz	58
Feldspar	22
Lithic	20

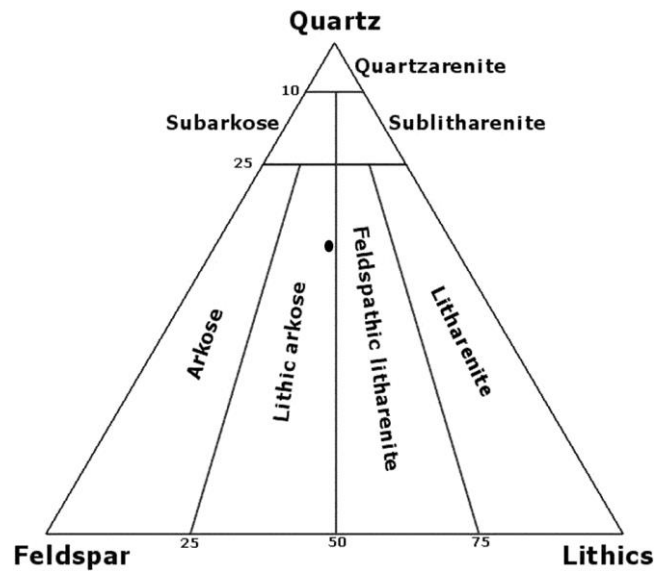


Figure 6.4: Normalized representation of sandstone composition (QFL).

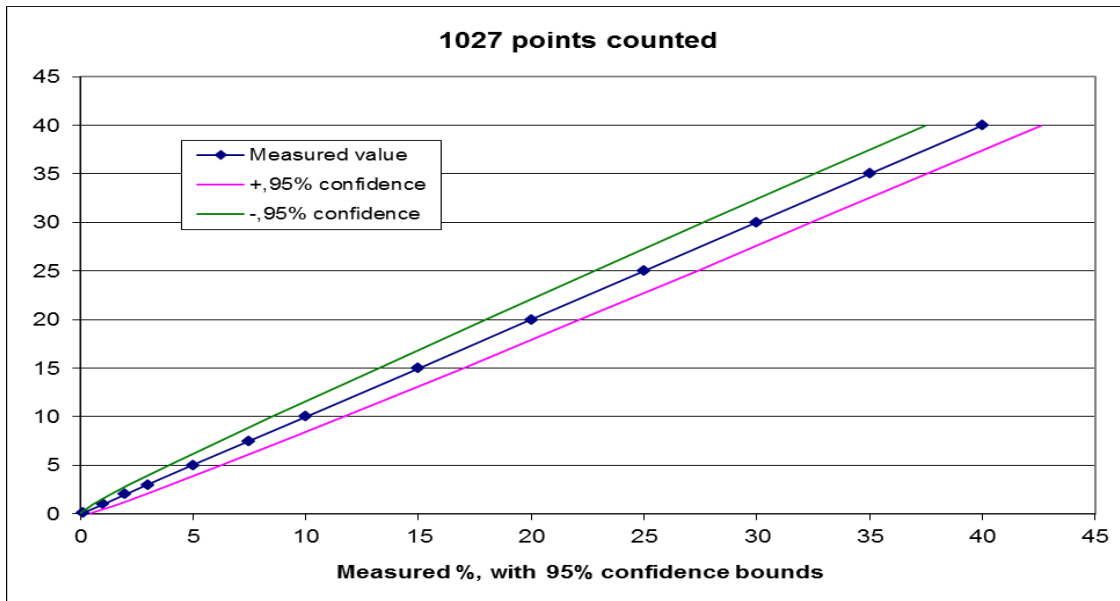


Figure 6.5: Errors from the point count based on a 95% confidence interval following Howarth (1998).

The sample is a lithic arkose with a composition of $Q_{58}F_{22}L_{20}$. The sandstone composition from point count as a % of the whole rock is show in Table 6.2 below. It should be noted that Table 6.2 is not a complete representation of the sandstone composition. The fracture was excluded in the point count.

Porosity

The sample shows less than 5% visible porosity outside of the fracture. The intergranular volume (IGV), primary porosity (φ_{prim}), and secondary porosity (φ_{sec}) calculated from the point count are 1.9%, 0% and 1.95% respectively. The original porosity loss due to compaction (COPL) and cementation (CEPL) are 36.9% and 3.1% respectively (based on an assumed initial porosity of 40%).

Table 6.2: Sandstone composition from point count (% of whole rock).

Component	% Composition
Monocrystalline quartz	36.7
Lithic quartz	8.0
Microcline	3.0
Untwinned feldspars	4.0
Polysynthetic twining	2.6
Altered feldspar	7.1
Intragranular porosity	1.9
Secondary porosity	1.9
Quartz cement	3.4
Clasts (pseudo matrix)	5.1
Clay cement	1.6
Chlorite	14.5
Chert	0.6
Other Lithics	9.6

Table 6.3: Point count estimated porosity and porosity losses.

Φ_j	φ_{prim}	φ_{sec}	φ_{total}	IGV	COPL	CEPL
40	0	1.95	1.95	1.9	36.9	3.1

Grain types and Distribution

The sample (Figure 6.6) is a compositionally and texturally immature, lithic arkose with a framework grain composition of quartz, feldspar and lithic fragments of $Q_{58}F_{22}L_{20}$.

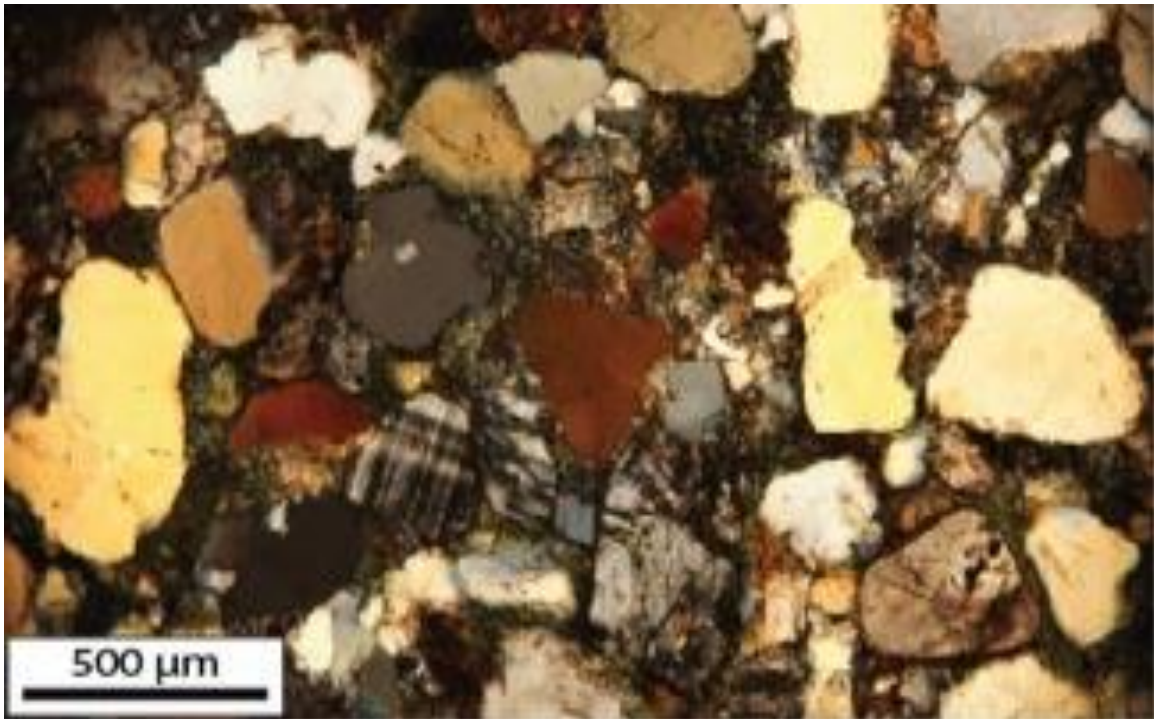


Figure 6.6: Sample showing the abundance of quartz and feldspars (XPL).

Quartz

Quartz appears as both monocrystalline grains and polycrystalline lithic grains. Quartz is present as overgrowth, fracture fill, and intergranular cement. Quartz represents about 60% of the grains in the sample, with the monocrystalline grains making up about

82% of the total quartz population. The grains are rounded and sub-rounded (Figure 6.7).

Quartz grains are large, euhedral, and abundant in the sample.

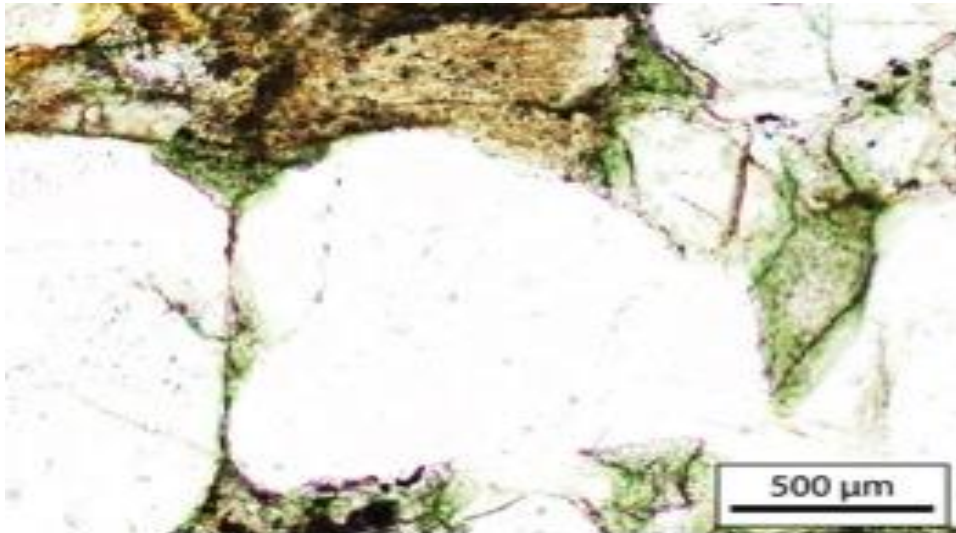


Figure 6.7: Sub-rounded beta quartz grain (PPL).

Feldspars

Potassium feldspar and K-feldspar-dominated granitic grains are common (~3% in composition), in addition to polysynthetic twinned and untwined feldspars. Potassium feldspar occurs as microcline, rarely with perthitic texture; other feldspars lack twinning and show partial albitization/sericitization (Figure 6.8) as well as some secondary porosity.

Lithic Fragments

Lithic fragments in the sample include chert and argillaceous sedimentary rock fragments, metamorphic rock fragments, and probable volcanic and plutonic rock

fragments. Most of the metamorphic rock fragments form as pseudomatrix, which appear to be penetratively deformed between harder framework grains, and contain some chlorite. Some rock fragments include mica books, usually muscovite, as well as unidentifiable heavy minerals (Figure 6.9).

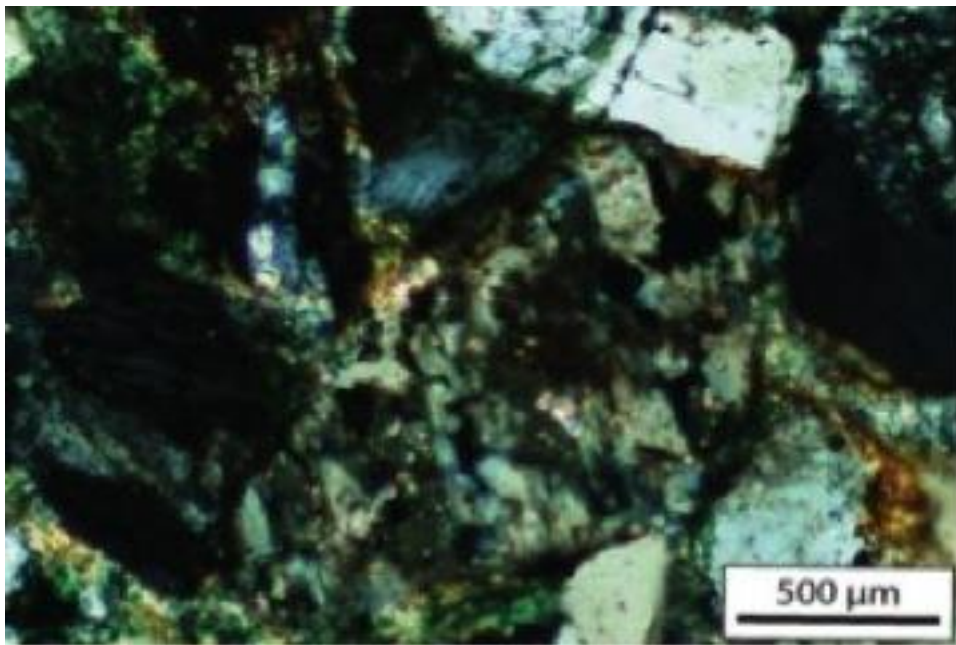


Figure 6.8: Sericitization of feldspar (XPL).

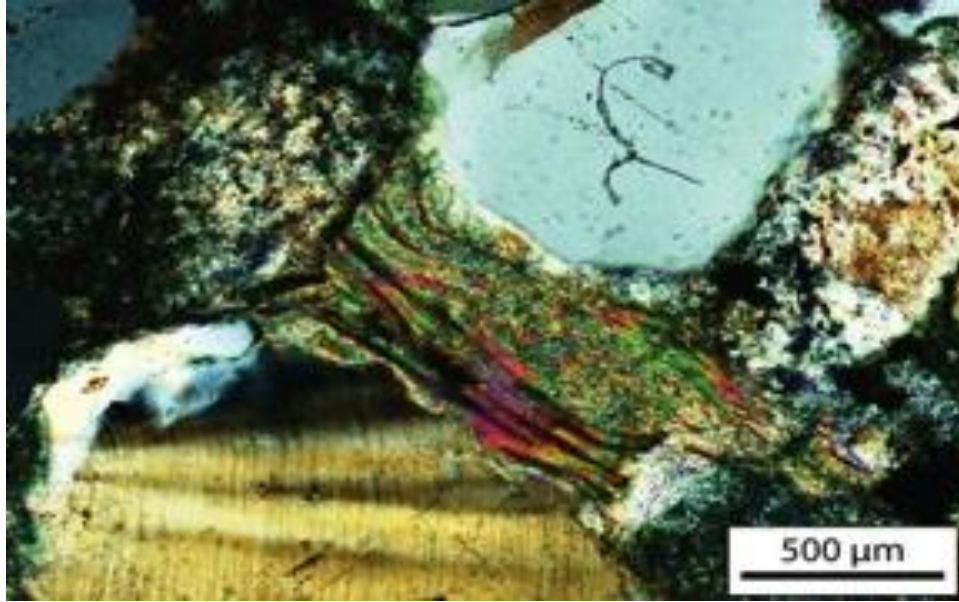


Figure 6.9: Muscovite contained within lithic fragments (XPL).

Cement

The sample shows low (~1.9%) intergranular volume due to compaction. The most prevalent cement is chlorite. Little quartz cement is seen due to compaction, feldspar dissolution and temperature. Lots of quartz present in the fracture, however, the fracture was not included in the point count. Lithic fragments contain abundant chlorite. Pore-bridging, clay mineral cements occur parallel and perpendicular to some framework grains. Detrital chlorite, calcite grain replacements and altered pseudomatrix are also observed (Figure 6.10). Minor syntaxial potassium feldspar and albite cement are present. Trace authigenic minerals include chlorite and muscovite. There is no visible intergranular or intragranular porosity, except in the fracture.

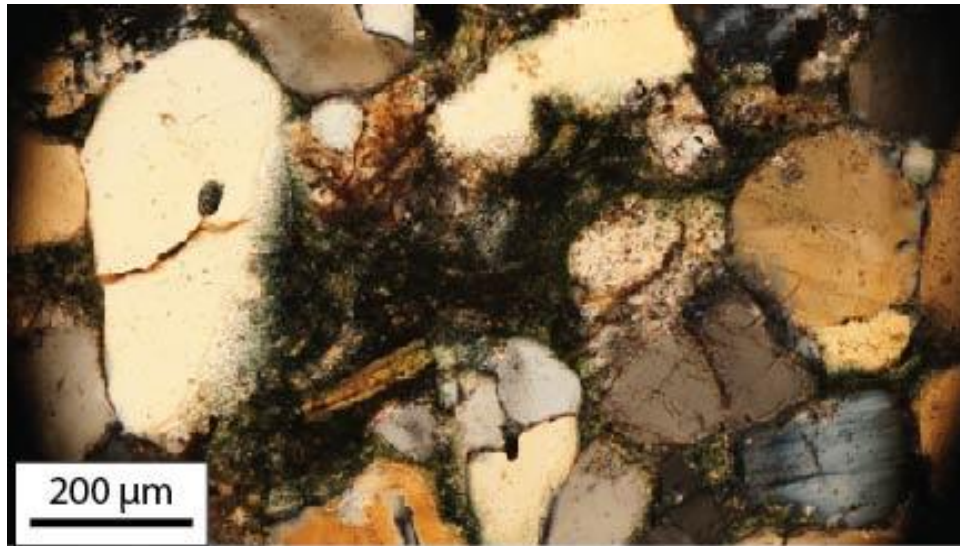


Figure 6.10: Detrital chlorite in the lithic fragments (XPL).

Other Grains

Detrital chlorite, muscovite, magnetite, zircon, and tourmaline occur in minor quantities. Dominantly quartz and feldspar granitic lithics (Figure 6.11) also occur in the sample.

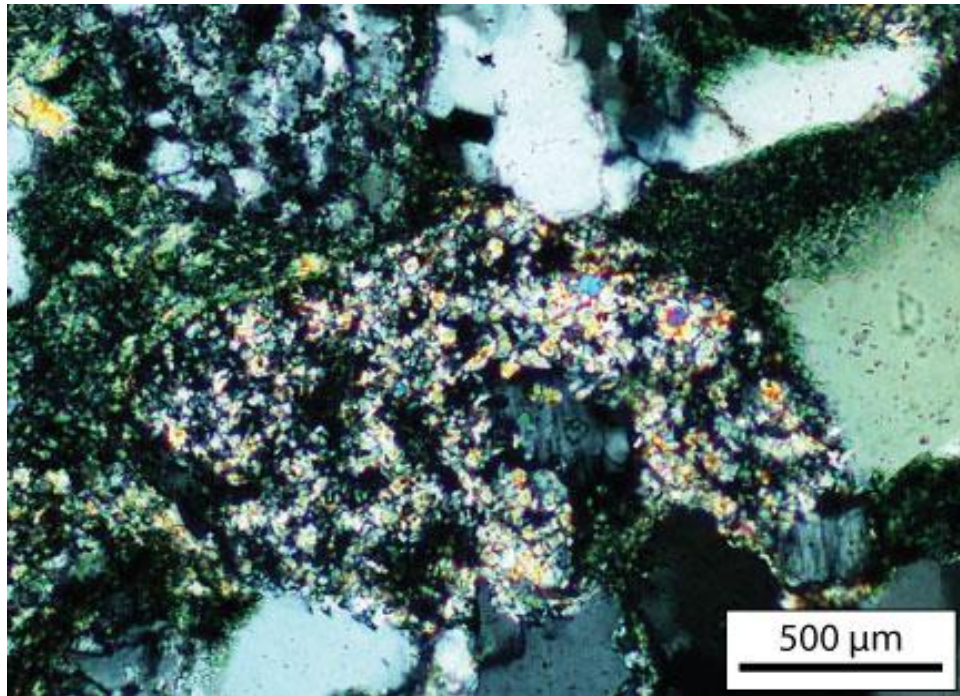


Figure 6.11: Granitic lithic with altered feldspar (XPL).

Fracture

The fracture is an opening mode fracture with crack-seal texture marking the concurrent opening and precipitation of quartz (Figure 6.12). The quartz cement in the fracture is blocky, euhedral, commonly with euhedral crystals present and locally facing traces of open pore space and in optical continuity with the host quartz (Figure 6.13). The fracture contains pores ranging from 0.49-1.83mm. These pores are interpreted to represent residual fracture porosity after incomplete quartz fracture cementation..



Figure 6.12: Opening mode fracture containing blocky quartz and locally preserved porosity (PPL).



Figure 6.13: Fracture containing blocky quartz and secondary pores (PPL).

Diagenetic mineral phases

Diagenesis altered the original pore type and geometry of the sample, ultimately controlling its total porosity and permeability. Evidence of diagenesis include: mechanical and chemical burial compaction, pre-compaction cements, grain fracturing and dissolution. Mechanical compaction is the pervasive cause of grain deformation and fracturing in the sample. Chlorite precipitation, grain-coating clay-mineral cements, and compaction of ductile lithic grains occurred early, followed by alteration of pseudomatrix (partly by chlorite), incipient feldspar dissolution, precipitation of quartz and feldspar syntaxial cements, and clay-mineral reactions. Chlorite and clay mineral cement growth as well as albitization and sericitization of feldspars largely predate the formation of the opening-mode fractures. Quartz-cement precipitation accompanied the formation of the fracture and may have continued during later burial history. Some feldspar dissolution and chlorite deposition occurred late, possibly after the formation of the fracture.

Statistical Analysis

The cumulative distribution functions (cdf) and histograms of the grain sizes (diameters) measured in mm and ϕ are shown in Figures 6.14 and 6.15. Figure 6.15 provides the distribution of the grain diameters contained in the sample as heights of column. A normal distribution fit (frequency curve) is overlain on the histogram. The frequency curve provides a better representation of the data than the histogram, as it is independent of bin sizes. The cumulative distribution function plots show the cumulative weight (in fractions) of the grain sizes, starting with the coarsest size class. The grain

sizes are finely skewed, according to Folk's "inclusive graphic Skewness" (1980), and moderately well sorted.

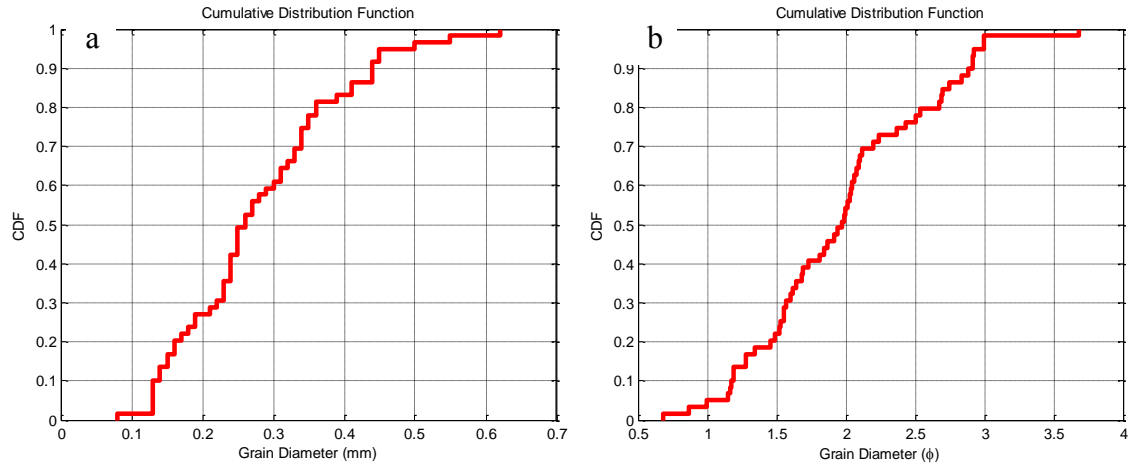


Figure 6.14: Cumulative distribution function (cdf) of grain diameter in (a) mm (b) phi scale (ϕ).

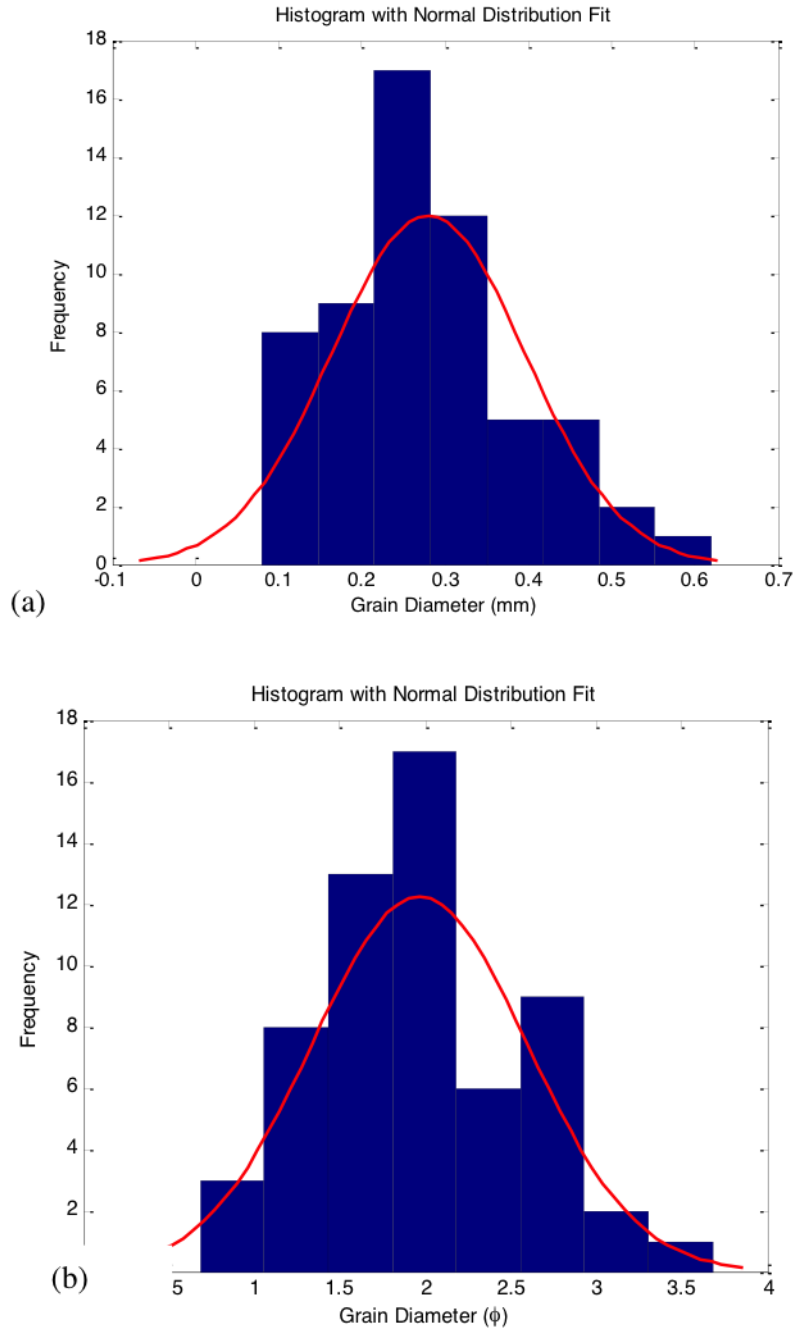


Figure 6.15: Grain size histogram with normal distribution fit overlain (a) mm (b) phi scale (ϕ). The Skewness shows that the grains are moderately well sorted in both the mm and phi scales. The average grain size is 0.28 mm with a standard deviation of 0.12 mm and a range between 0.08 – 0.62 mm.

Statistical parameters of the sample were also computed. Table 6.4 shows the measures of central tendency and other statistical parameters. The sample has a mean grain diameter of 0.28 mm, median of 0.26 mm, a mode of 0.30 mm, a standard deviation of 0.12mm and a range between 0.08-0.62 mm. Table 6.4 provides a summary of the statistical analysis.

The abundance of feldspars (F) in the sample was compared to quartz (Q). Table 6.5 shows a summary of the comparisons. About 58% of the feldspars in the sample were unaltered (UF) while the remaining 42% have been altered (AF) via different mechanical and chemical processes. Untwinned feldspars are the most abundant of the feldspars, and are about 24% of the feldspar population. The feldspars are about 27% of the feldspar-quartz population while the quartz matrix (Q_m) makes up about 82% of the total quartz (Q_t) population.

Table 6.4: Summary of Statistical Analysis.

Data Analysis	
Mean (mm)	0.28
Median (mm)	0.26
Mode (mm)	0.30
Standard deviation (mm)	0.12
Standard deviation (ϕ)	0.63
Skewness (mm)	0.65
Skewness (ϕ)	0.34
Kurtosis (ϕ)	0.06
Minimum (mm)	0.08
Maximum (mm)	0.62

From the point count data, the grain size distribution of the feldspars was also estimated using JMicroVision (2007) and a summary is shown in Table 6.6 below. The

data in Tables 6.5 and 6.6 may not be a complete representation of the entire sample, but they give an idea of the relative abundance of the feldspars to quartz. The data shows that the feldspar and quartz grains are moderately well sorted with the feldspars symmetrically skewed and quartz strongly positively skewed.

Table 6.5: Summary of feldspar and quartz comparisons.

F/(Q+F)	UF/F	AF/F	Q _m /Q _t
0.27	0.58	0.42	0.82

Table 6.6: Summary of Data Analysis of the feldspar and quartz in the sample as measured from JMicroVision.

Data Analysis	Feldspar	Quartz
Mean (mm)	0.29	0.30
Median (mm)	0.25	0.29
Mode (mm)	0.20	0.30
Standard deviation (mm)	0.16	0.12
Standard deviation (φ)	0.76	0.63
Skewness (mm)	1.29	0.54
Skewness (φ)	0.02	0.38
Kurtosis (φ)	0.74	-0.36
Minimum (mm)	0.11	0.11
Maximum (mm)	0.60	0.57

IMAGE CHARACTERIZATION

Microtomography image scans were taken at the mid-length of the core at two different resolutions, 6.31 μm (scan A) and 3.16 μm (scan B). Tomographic data for Samples A and B are shown in Figure 6.16(a) and 6.16(b) respectively. Since there is almost no pore space within the matrix resolved in the images, I isolated fracture space in each image and also upscaled it twice, ultimately to images of sizes (450x200x200) for Sample A (upscaled voxel length 12.62 μm) and (285 x 135 x 270) for Sample B (upscaled voxel length 6.32 μm). I analyzed the fracture space for both samples using 3DMA-Rock software. The first step is segmentation, i.e. deciding where pore space (phase 0) and solid space voxels (phase 1) are. The surface between the two spaces is shown in Figure 6.17(a). Figure 6.17(b) shows the pore space thinned down to the medial axis skeleton. The coloring reveals the distance to the closest grain voxel (i.e. red is the closest while purple is furthest).

Segmented images can be post-processed to find the aperture in the z direction. The aperture field spatial distribution for scan A is shown in Figure 6.18(a), whereas the histogram comparison for both scans is shown in Figure 6.18(b). Note that one voxel length is the minimum aperture that can be found (12.62 μm and 6.32 μm , respectively).

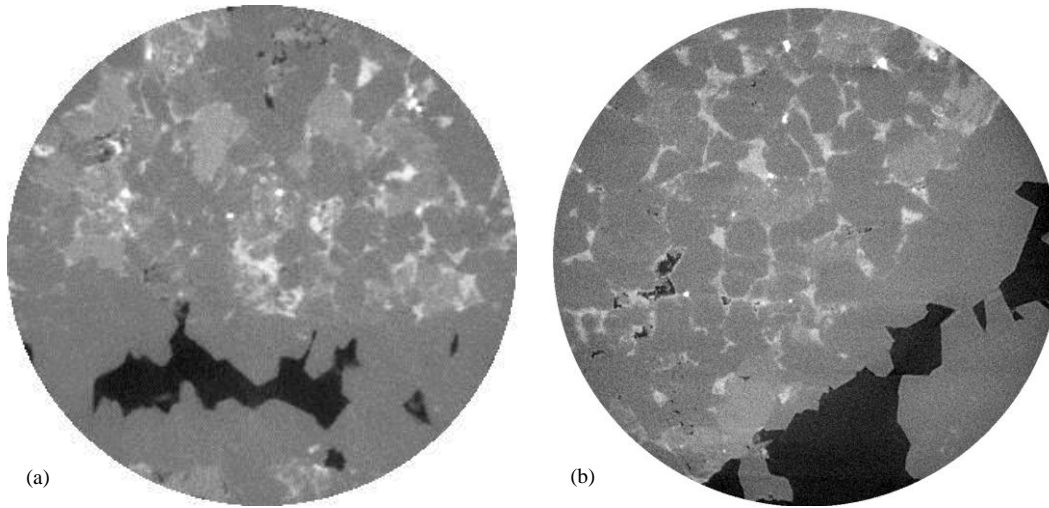


Figure 6.16: Microtomographic slice of (a) scan A – voxel length 6.31 μm (b) voxel length 3.16 μm . Images are 5.2 mm in diameter.

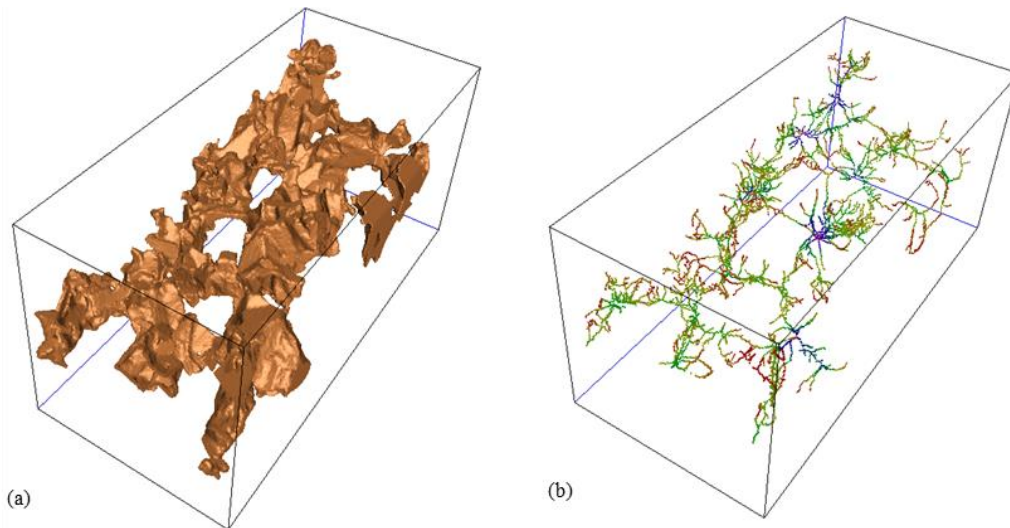


Figure 6.17: (a) Pore-grain surface and (b) medial axis (pore space skeleton) (450x200x200 voxels). The medial axis is colored according to their distance to the grain surface.

Fluid configurations

I use segmented fracture pore space as input for the LSMPQS simulation. Inlet/outlet volume sides are aligned with x-directions and all others are sealed. The curvature-saturation relationships are shown in Figure 6.19(a). If capillary pressure is

needed, curvature can be scaled with measured surface-tension according to the Young-Laplace equation. The LSMPQS method allows for the periodic checking of the trapped non-wetting phase. Figures 6.19(a) and 6.19(b) show wetting and non-wetting fluid configuration at the end of drainage and imbibition. The wetting phase is either in small nooks and crevices of the pore space (small green blobs), or occupying bypassed parts of the pore space (larger green blobs). The disconnected non-wetting fluid surface is shown in blue and mostly occupies the middle of the pore space.

Figure 6.20(a) shows the comparison of the drainage and imbibition curvature/saturation plots for both scans. While percolation thresholds during drainage are similar, the qualitative shift in curves is mainly the result of bypassed wetting phase (see Figure 6.20(a)) that causes large residual wetting phase in drainage of scan A. Figure 6.20(b) shows tortuosity of NW phase during drainage and imbibition. NW phase is somewhat more tortuous during imbibition (during lower curvatures between W and NW phase), than during drainage. The behavior is, however, binary in nature: Once the NW phase percolates, tortuosity is between 1.6 and 1.8, and when it does not, the value is of course 0.

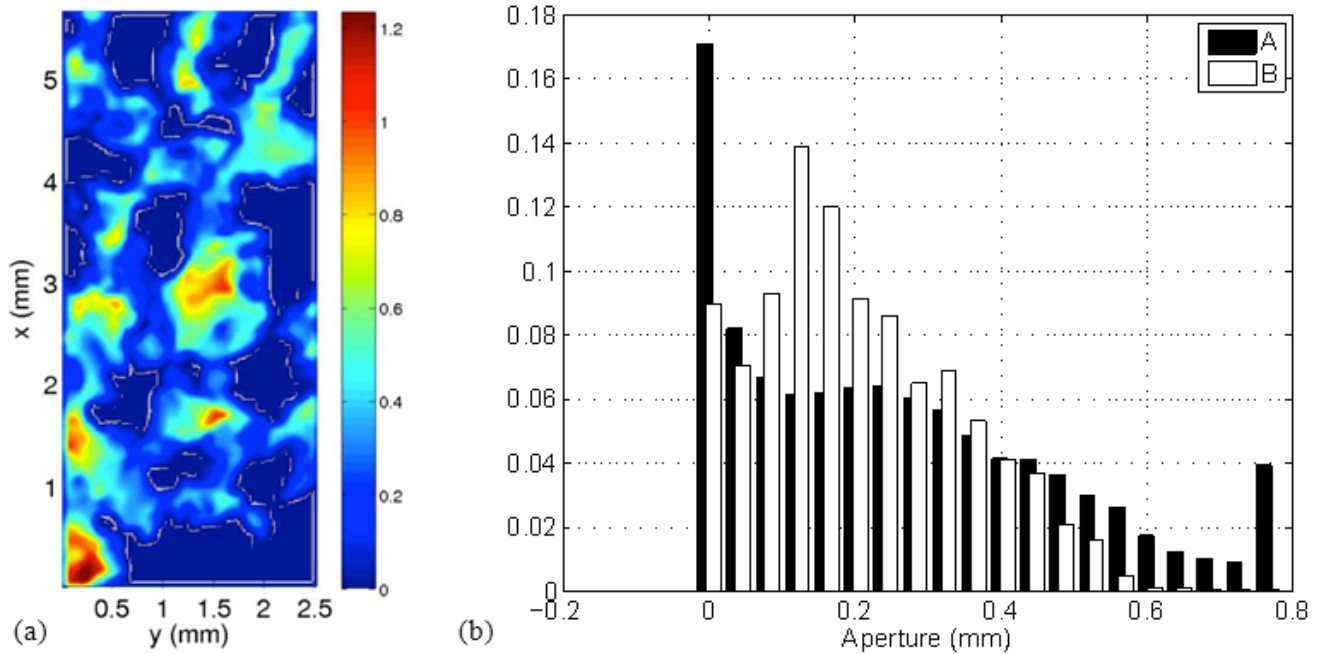


Figure 6.18: (a) Scan A aperture field distribution (measured in z-direction). (b) Probability density function (based on imaged data) of apertures for both scans. Note that only positive apertures are shown, Median and average values (for the positive values) of aperture are 0.2576mm and 0.2021mm for scan B. As expected, with increased resolution, the smallest bin frequency reduces.

As suggested by medial axis shown for scan A in Figure 6.16(b), pathways across the sample are few. Thus, the cumulative distribution of all possible paths in scan A is one of the narrowest shown in Figure 6.21. Furthermore, the Torridonian is compared with a wide variety of porous or fractured media available in literature (summarized in Table 6.1). The fractures have the narrowest distribution of the data set and thus provide the most direct path across the sample (Figure 6.21(a)). Consolidated media and carbonate samples show the widest distribution. Among fractures, however, the

Torrignonian fracture has the widest distribution, overlapping with that of granular media.

Finally, cementation increases tortuosity as shown in Figure 6.21(b).

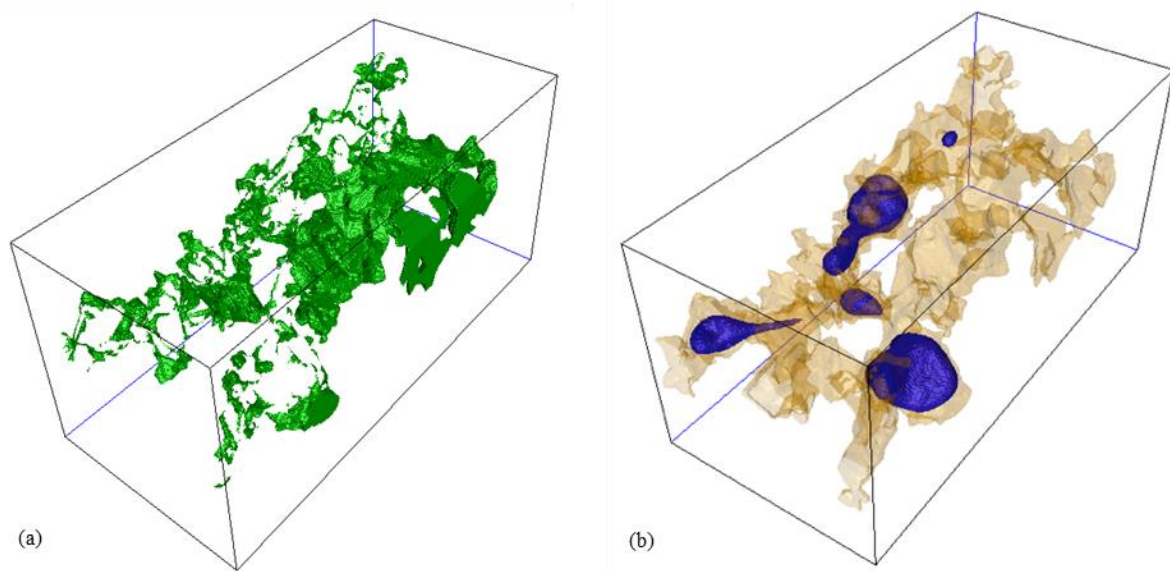


Figure 6.19: (a) Residual water configuration surface at the drainage end point for scan A. (b) Scan A at the end of imbibition. The pore/grain surface of the Torrignonian pore is shown as transparent, and the trapped non-wetting phase (blue) in the pore space.

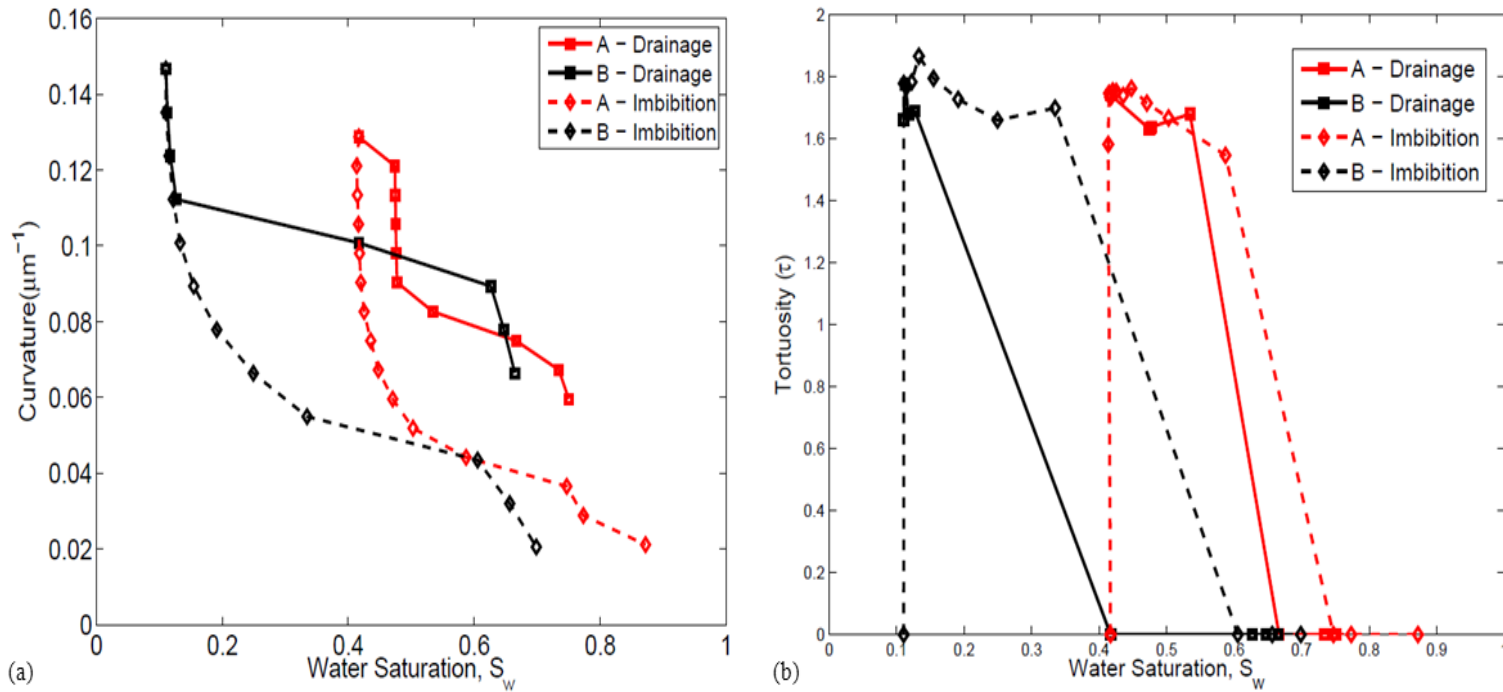


Figure 6.20: (a) Curvature-saturation plots for drainage and imbibition for both Torrionian scans. (b) Matching tortuosity saturation curves for NW phase during drainage and imbibition.

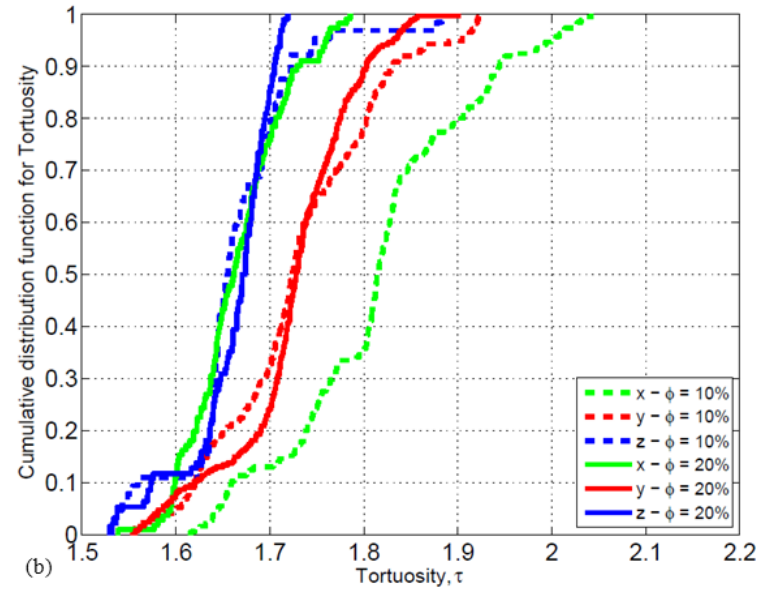
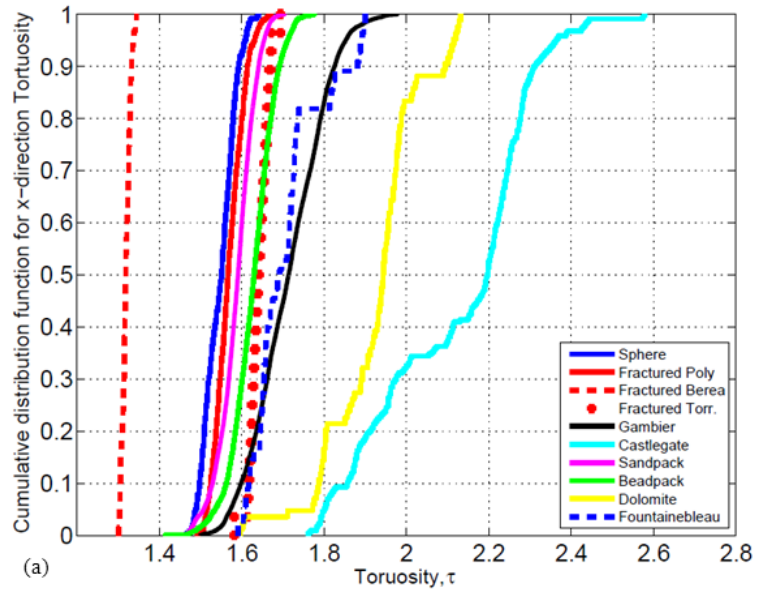


Figure 6.21: (a) Cumulative distribution function of x-direction tortuosity in different media (see Table 6.1). (b) Influence of cementation on tortuosity. Cement was numerically added to all grain surfaces of Castlegate sandstone until porosity reduced to 10%.

Table 6.7: Porosity and the sizes of the different media shown in Figure 6.21.

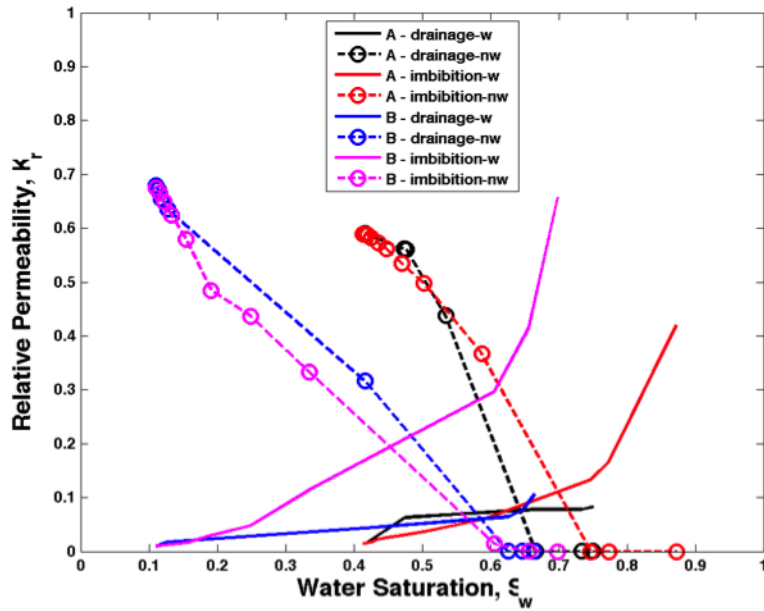
	Porosity (ϕ)	Sample Size	Voxel Size
Granular media:			
Monodisperse model “sphere” (Finney, 1970)	36%	512^3	
Imaged spheres “beadpack”*	37.9%	512^3	17.472 μm
Unconsolidated fluvial “sandpack”*	36.3%	512^3	9.184 μm
Consolidated media:			
Castlegate Sandstone*	20.6%	512^3	5.6 μm
Gambier Limestone*	43.6%	512^3	3.024 μm
Dolomite (Rodriquez et al., 2012)	18.9%	512^3	3.5 μm
Fractured media:			
Polyethylene (Landry et al., 2011)		1024x1024x800	13.606 x 13.606 x 12.405 μm^3
Berea Sandstone (Prodanović et al., 2010)			
Torrionian Sandstone (Ellis et al. 2012)		954^3	6.31 μm / 3.16 μm

* Available from http://xct.anu.edu.au/network_comparison/#data_sets

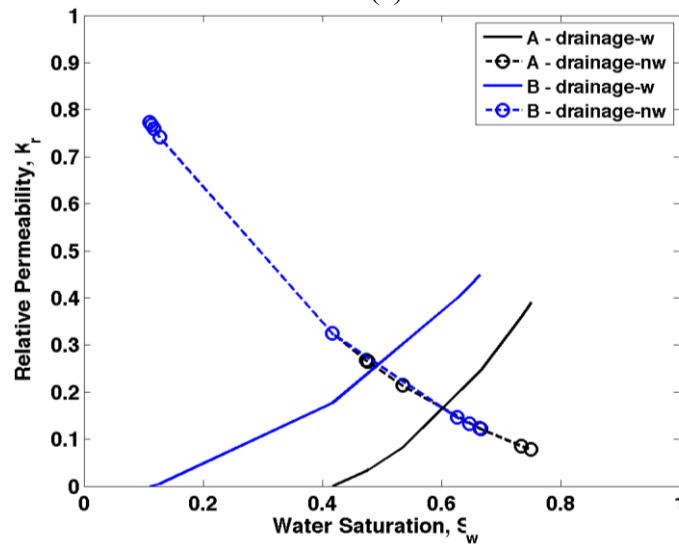
Permeability

The absolute permeability computed with Palabos software is 0.561 mD for scan A and 0.153 mD for scan B. If we compute the permeability using the cubic law and average apertures of 0.2576 mm and 0.2021 mm for scans A and B, estimated permeabilities are 5603 D and 3448.8 D, respectively. This discrepancy indicates that a parallel plate model poorly represents these partially cemented fractures because of large variations in aperture

The relative permeability of the fluid configurations were then computed (Figure 6.22(a)). Note that trapped/bypassed water at drainage (shown in Figure 6.20(a)) is causing low relative permeability for drainage in scan A. The relative permeability shows a monotonic behavior, whereas tortuosity of the non-wetting (NW) phase does not (see Figure 6.20(b)). Hence, I conclude that tortuosity of NW phase cannot be correlated well with its relative permeability. I compared our simulation to the values obtained using Chen and Horne's (2006) correlation for drainage in rough walled fractures using the saturation values from our simulation (Figure 6.22(b)). I observe no similarity between the two correlations because of differences in fracture geometry. Rough walled fractures in Chen and Horne's work did not have any asperities (and thus no trapped water phase at the end of drainage), and were manufactured with a mean aperture of 0.24 mm and standard deviation of 0.05 mm.



(a)



(b)

Figure 6.22: (a) Relative permeability curves for drainage and imbibition of the two Torridonian scans. (b) Relative permeability curves computed based on correlations from Chen and Horne (2006).

CONCLUSION

Effectively predicting sandstone reservoir quality depends on accurately predicting diagenetic history as a product of depositional environments, sediment composition, and fluid migration patterns. The Torridonian sample has undergone chemical and mechanical compaction with lots of grain dissolution and fracturing. The IGV of the sample is very low (about 1.9%), and there is no visible primary matrix porosity. Porosity loss due to compaction (COPL) of 36.9% dominates over porosity loss by cementation (CEPL) of 3.1%. The Torridonian sample is a compositionally and texturally immature, lithic arkose with a framework grain composition of quartz, feldspar and lithic fragments of $Q_{58}F_{22}L_{20}$.

The partially cemented fractures of the Torridonian Sandstone were found to be constricted, with quartz bridging across the fracture while maintaining connected residual fracture porosity open to flow. This constricted pore space causes trapping of fluids during drainage and imbibition akin to that in sandstone pore space. The adjacent matrix, however, is almost completely cemented leaving only fractures open to flow. I compare the tortuosity distribution in the Torridonian fractures with those in other porous media. I found that the fractures have considerably narrower tortuosity distribution when compared to other porous materials, and despite cements provide the most direct path across the material. Consolidated media and carbonate samples have the widest distribution. In addition, I find that the tortuosity in both consolidated porous media and partially cemented fractures increases with an increase in the amount of carbonate or quartz overgrowth cement.

Chapter 7: A comparative analysis of fracture fluid-flow properties of Torridonian and Travis Peak sandstones

This chapter evaluates fracture fluid-flow properties such as geometric tortuosity, porosity, permeability, relative permeability from two distinct sandstones: a core sample, of Travis Peak Sandstone and an outcrop of Torridonian sandstone. Although the Torridonian and Travis Peak sandstones differ in composition, diagenesis, and age, they are both tightly quartz cemented sandstones. Both sandstones have undergone compaction and extensive cementation during their burial history, resulting in low porosity and permeability (Dutton et al., 1991; Ellis et al., 2012). Torridonian rocks experience a largely unknown late Proterozoic tectonic burial and uplift history (Ellis et al., 2012).

The details of the work done on the Torridonian are discussed in Chapter 6 as well as in Tokan-Lawal et al (2013). This chapter focuses on the analysis done on the Travis Peak Sandstone, as well as a discussion on the similarities and differences in the simulation-computed fluid properties of the Torridonian and Travis Peak sandstones.

GEOLOGIC SETTING

The samples used in this work are sandstones from Torridonian (Chapter 6) and Travis Peak formations. The sample referred to here as Torridonian sandstone is an outcrop sample of the Late Proterozoic Applecross Formation of the Torridon Group, exposed in the foreland of the Moine Thrust Belt, NW Scotland (see Chapter 6 for more details on composition and diagenesis). The Travis Peak sample is from the Ashland SFOT No. 1 Well (depth 10,105 ft) in the Lower Cretaceous Travis Peak Formation of east Texas

(Figure 7.1).

The Travis Peak Formation was deposited ~ 140 to 115 m.y. ago in East Texas (Braunstein et al., 1988); it is equivalent to the Hosston Formation of Louisiana, Arkansas, and Mississippi (Dutton et al., 1991). The East Texas Basin formed during Late Triassic rifting (Buffler et al., 1980). Deposition of the Travis Peak Formation and underlying Cotton Valley Group represents the first major progradation of terrigenous clastics into East Texas after the opening of the Gulf of Mexico in the Jurassic (Seni and Jackson, 1983). Deposition occurred on stretched continental crust that was undergoing cooling-induced subsidence (Jackson, 1981).

The formation dips to the west and southwest off the western flank of the Sabine Uplift; in the South, the top of the Travis Peak is at 9,400 ft (2,745 m) below sea level (Dutton et al., 1991). The Travis Peak Formation is approximately 1,800 to 2,200 ft (550 to 670 m) thick in the area where the sample was cored.

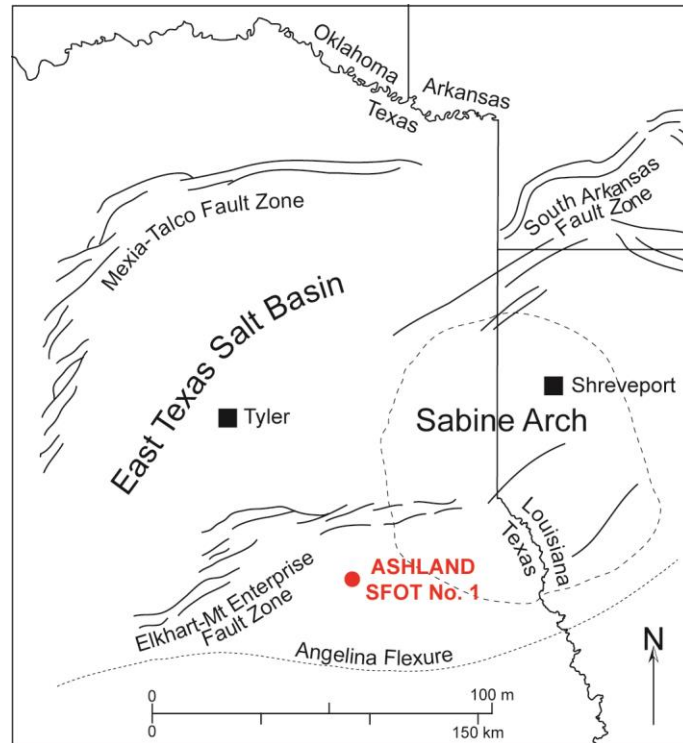


Figure 7.1: Map showing the location of the Travis Peak Ashland SFOT No. 1 well (modified from Becker *et al.*, 2010)

The Travis Peak formation is composed of fine-grained to very fine-grained sandstone, silty sandstone, muddy sandstone, and sandy mudstone (Dutton *et al.*, 1991). The sandstones in the Travis Peak are quartzarenites and subarkoses with an average composition of $Q_{95}F_4L_1$ (Dutton, 1987). Sandstones have undergone compaction and extensive cementation during their burial history, resulting in low porosity and permeability (Dutton *et al.*, 1991). Although a few thin zones near the top of the Travis Peak in east Texas have permeability greater than 90 mD, most of the Travis Peak has permeability of less than 0.1 mD (Dutton *et al.*, 1991). Porosity in these sandstones ranges from 3 to 17% but is mostly less than 8 % (Dutton & Finley, 1988). Precipitation

of authigenic quartz, ankerite, dolomite, illite, and chlorite, as well as the introduction of reservoir bitumen, are the most important causes of occlusion of primary porosity and reduction of permeability (Dutton & Land, 1988).

PETROGRAPHY

The Travis Peak sample investigated for this study contains a macroscopic fracture that is partly cemented with quartz cement bridges leaving residual fracture porosity (Figure 7.2). A thin section of fracture cement and host rock was imaged under the transmitted light microscope and using Scanning-electron-microscope-based-cathodoluminescence (SEM-CL) to determine the composition of fracture cement and host rock and textural relationships between fracture cement and pore cement in the host rock. Imaging was performed on an Oxford XL30 SEM with an Oxford monoCL detector. SEM machine was operated at 15kV and 30nA with a spot size of 6.3 μm , 100 dual time with a working distance of 11.4. A blue-filtered SEM-CL image is shown in Figure 7.2. The fracture contains euhedral quartz crystals. Lateral cement grows on the crack seal bridge.

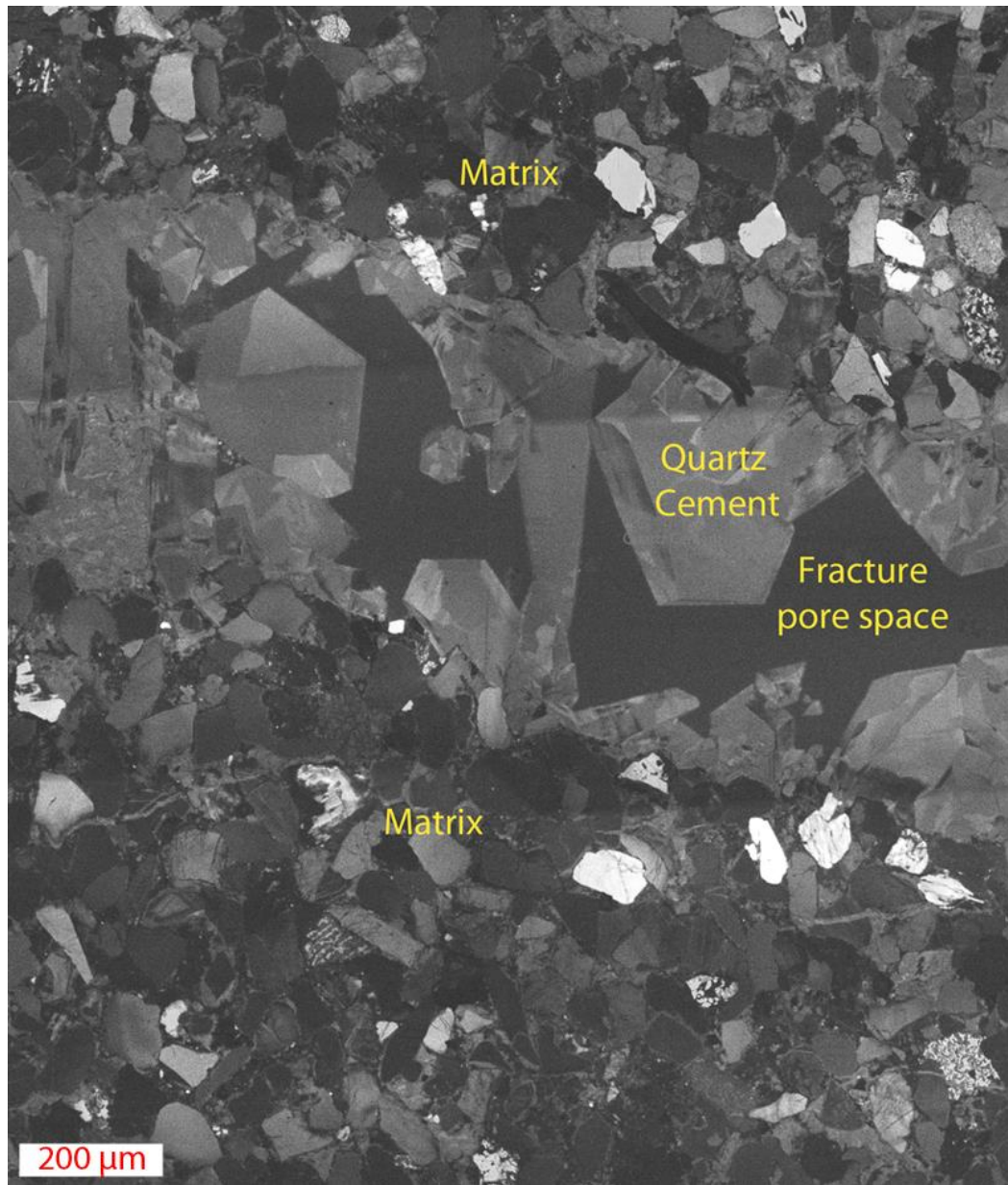


Figure 7.2: Scanning-electron-microscope-based-cathodoluminescence (SEM-CL) image (with a UV-blue filter) of the Travis Peak sample. The fracture contains euhedral quartz crystals. Lateral cement grows on the crack seal bridge. Presence of transgranular micro-fractures relating to the crack seal

The host rock is composed of mostly quartz, feldspar lithic fragments of varying origin, and diagenetic mineral phases such as clay, and carbonate (Figures 7.3 and 7.4).

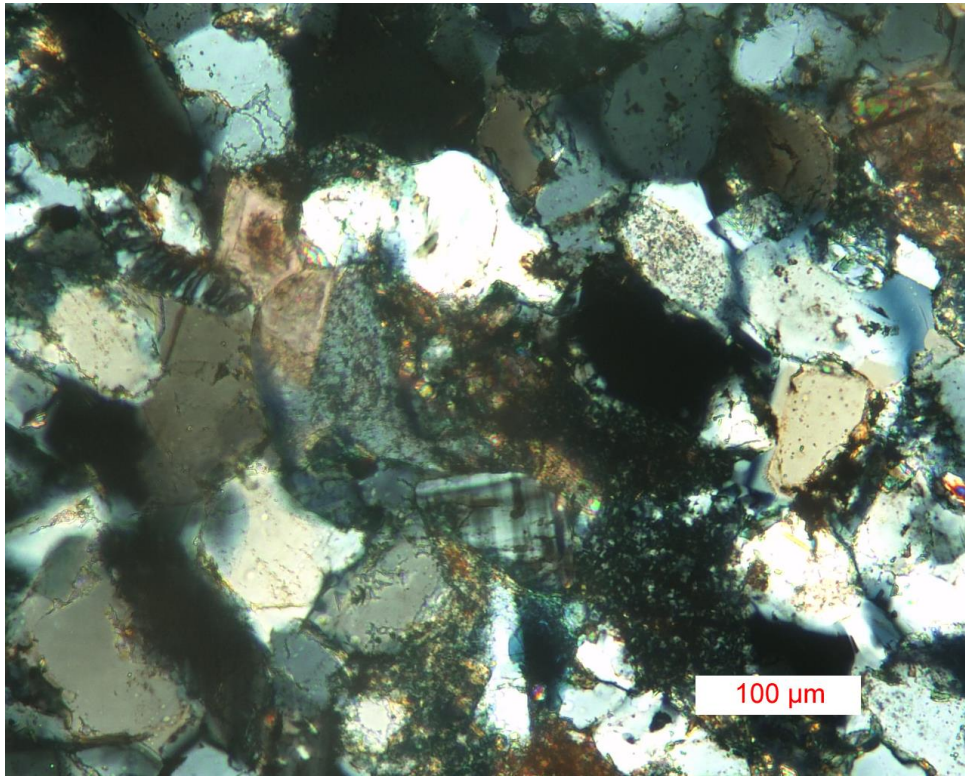


Figure 7.3: Sample showing the abundance of quartz and feldspars, and evidence of grain dissolution in the Travis Peak (XPL)

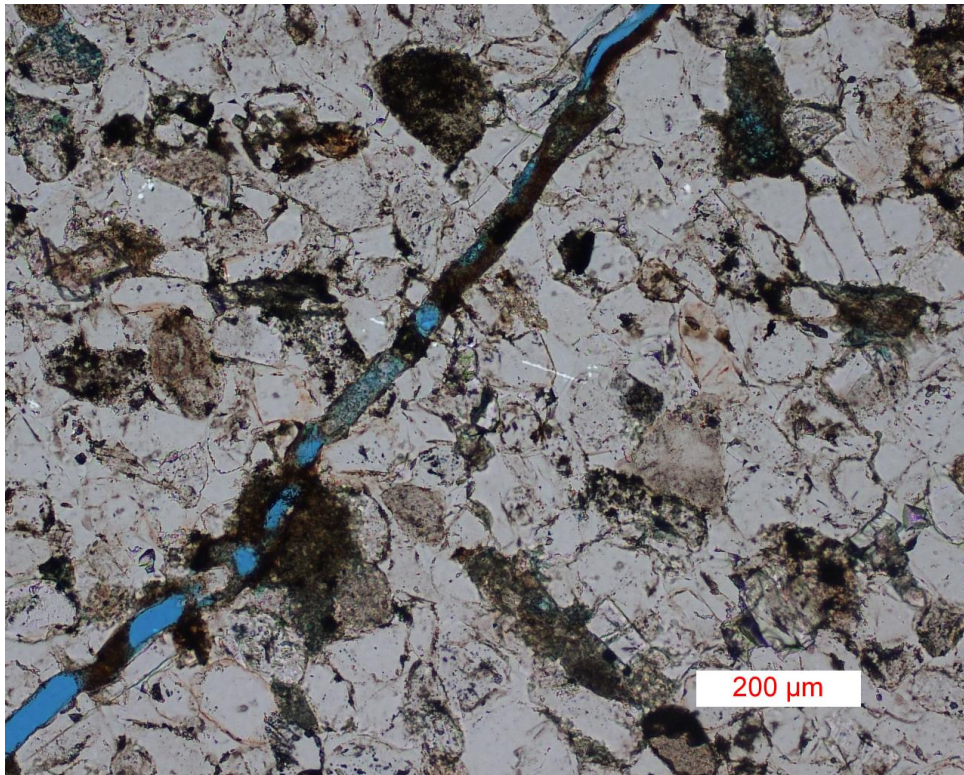


Figure 7.4: Sample showing the presence of carbonate cement in the fracture space, lithic fragments and grain dissolution (PPL).

IMAGE CHARACTERIZATION

The matrix of the Travis Peak sample contains no porosity that is resolvable using micro-CT scanning techniques (resolution limit about 3 μm). Hence, imaging and modeling addressed flow only through the fracture pore space. Microtomography image scans were taken at the mid-length of a 3 mm thick and 10 mm long core plug at a resolution of 5.97 μm . The scans were split into two data sets: TP1 and TP2, representing the top and bottom halves of the core plug, respectively, and sized to boxes of 400x400x175 voxel around the fractures. I used standard median filter to remove noise in the tomographic images before segmenting them. The pore spaces non-interacting with the main fractures were then removed from the images.

The CT scans were analyzed using Image-J and 3DMA-Rock software (Figure 7.5). The first step in fracture space analysis is segmentation, i.e. deciding where pore space (phase 0) and solid space voxels (phase 1) are. The surface between the two spaces is shown in Figure 7.6. TP1 has a similar fracture-grain structure to the Torridonian fracture. The fracture space in TP2, on the other hand, is more connected.

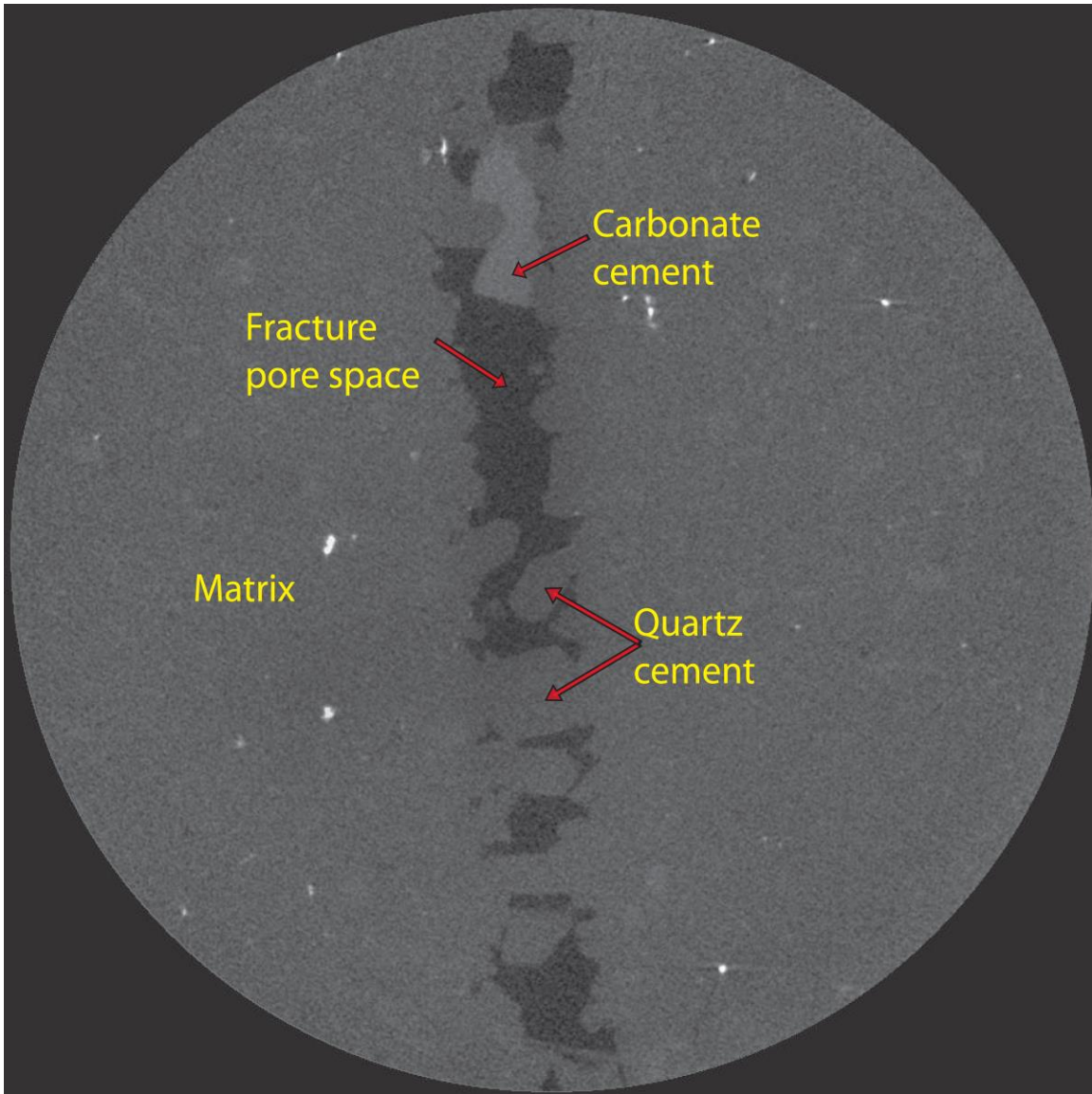
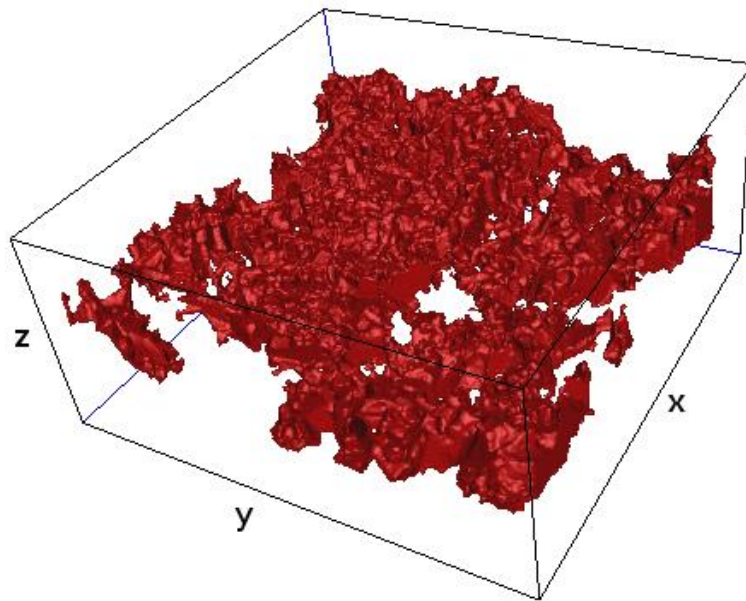
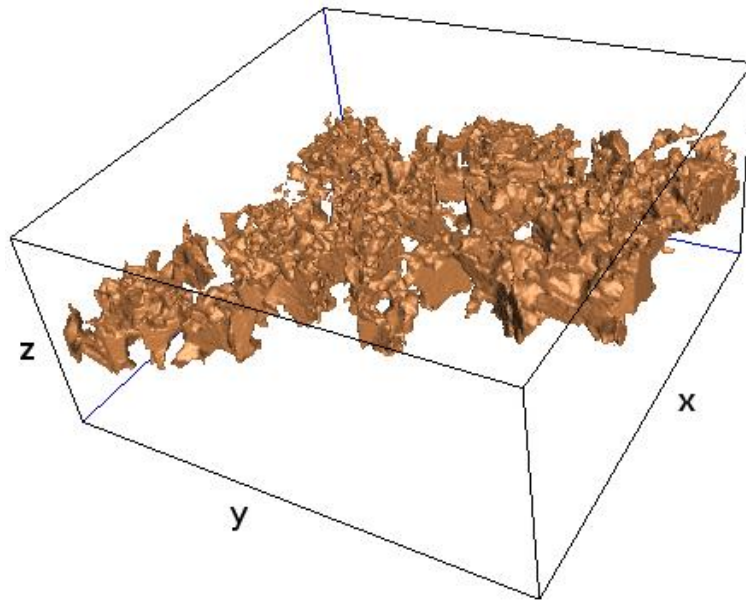


Figure 7.5: Microtomographic slice of Travis Peak sample. Voxel length = 5.97 μm . Image is $\sim 4.2\text{mm}$ in diameter. Fracture pore contains quartz and carbonate cement bridges.



(a)



(b)

Figure 7.6: Fracture-grain surface for (a) TP1 (b) TP2. TP1 has a similar structure to the Torridonian fracture described in Chapter 6 and in Tokan-Lawal et al. (2013). In comparison, TP2 fracture space is more connected.

The segmented images were post-processed to find the aperture in the z direction (Figure 7.7; note that the image has been rotated so the z direction is the aperture

direction just like is shown in Figure 7.6). Probability distribution function (pdf) of the apertures in TP1 and TP2, shown in Figure 7.8, display wider apertures in TP2 (with a mean of 0.1214mm) than those in TP1 (mean 0.0863)). Figure 7.9 shows the pore space thinned down to the medial axis skeleton. The coloring reveals the distance from the pore to the closest grain voxel (red is the closest while purple is furthest). Tortuosities are computed from the medial axis. Figure 7.10 shows the cumulative distribution function of x-direction tortuosity for both samples, whereas the histogram comparison for both samples is shown in Figure 8b. Note that one voxel length is the minimum aperture that can be found (i.e. 5.97 μm). TP1 (mean tortuosity = 2.4190) is more tortuous than TP2 (mean tortuosity = 1.8582). The apertures in TP1 appear to be smaller than those in TP2. All of the above is consistent with the TP1 section being more cemented than the TP2 section.

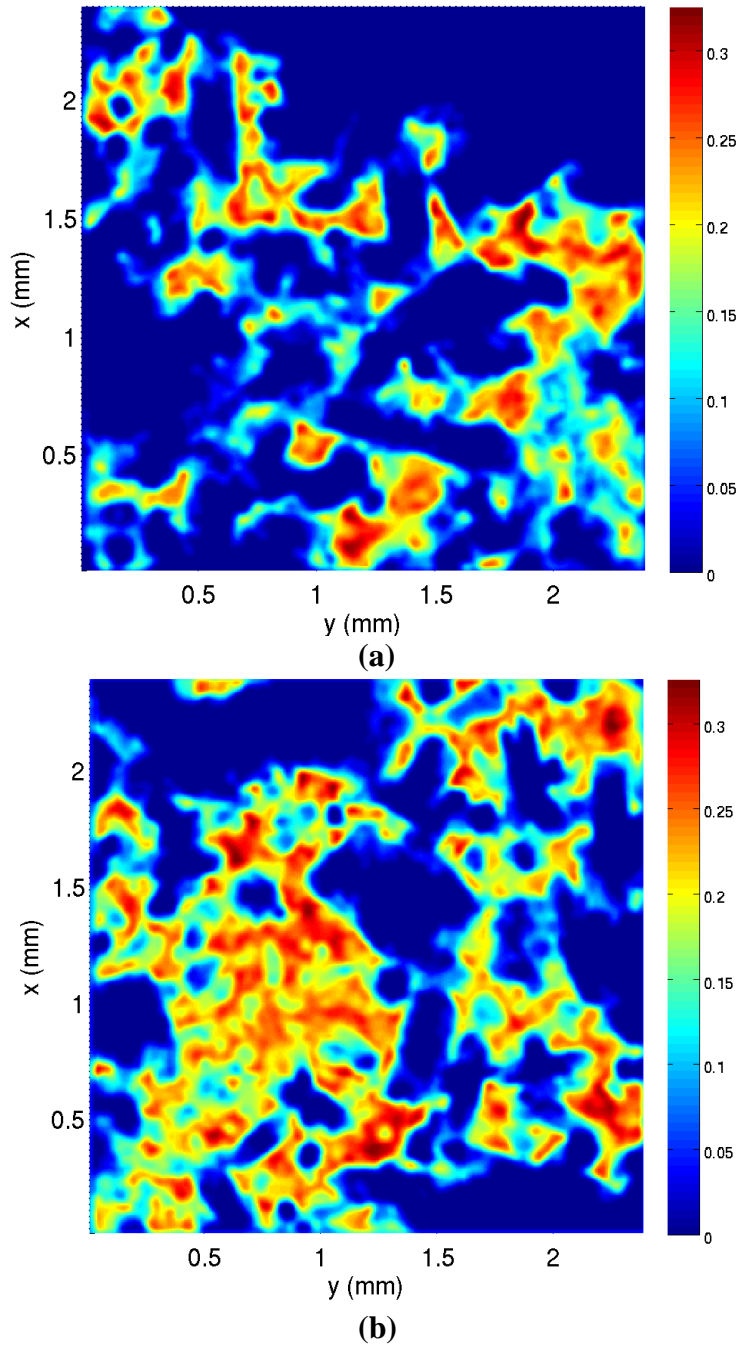


Figure 7.7: Aperture field distribution (measured in z-direction): (a) TP1 (b) TP2. The apertures in TP2 are wider (with a mean of 0.1214 mm) than those in TP1 (mean 0.0863 mm)

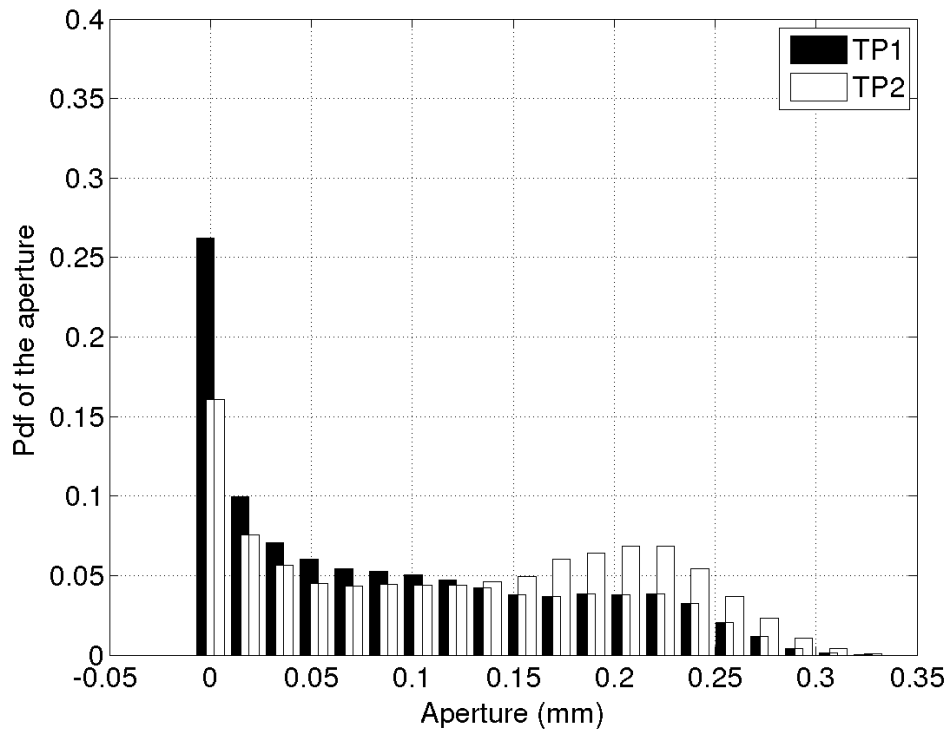


Figure 7.8: Probability distribution function of aperture for TP1 and TP2. The apertures in TP2 are wider (with a mean of 0.1214 mm) than those in TP1 (mean 0.0863 mm).

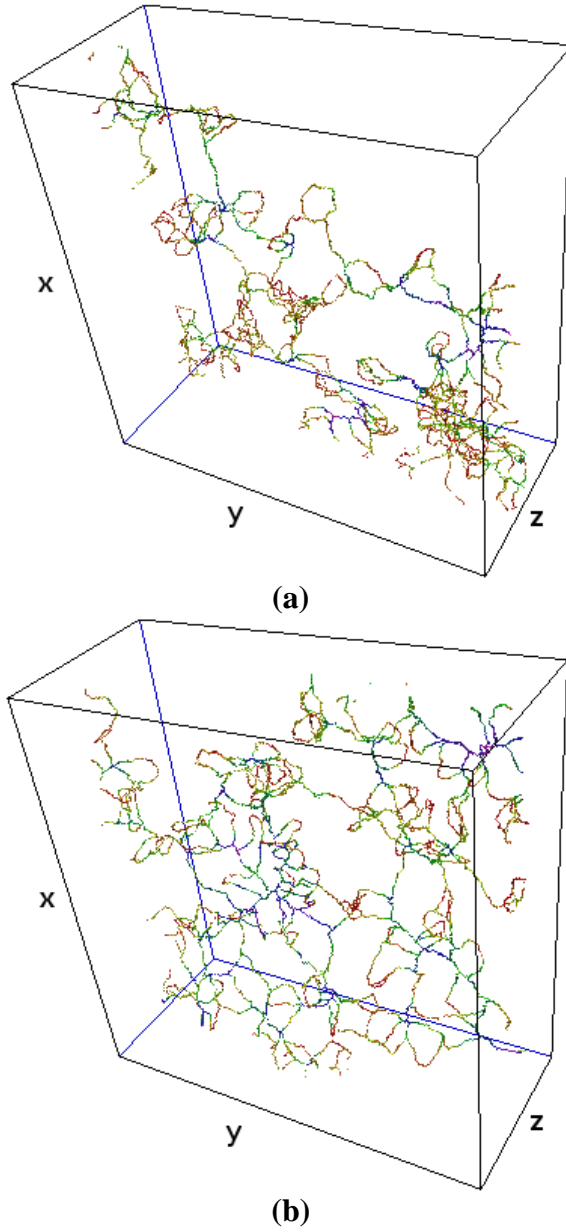


Figure 7.9: Medial axis (pore space skeleton) for (a) TP1 and (b) TP2. The medial axis voxels are colored according to the distance of the pore to the grain surface (red is the closest, and purple is the furthest). Both samples contain 400x400x175 voxels.

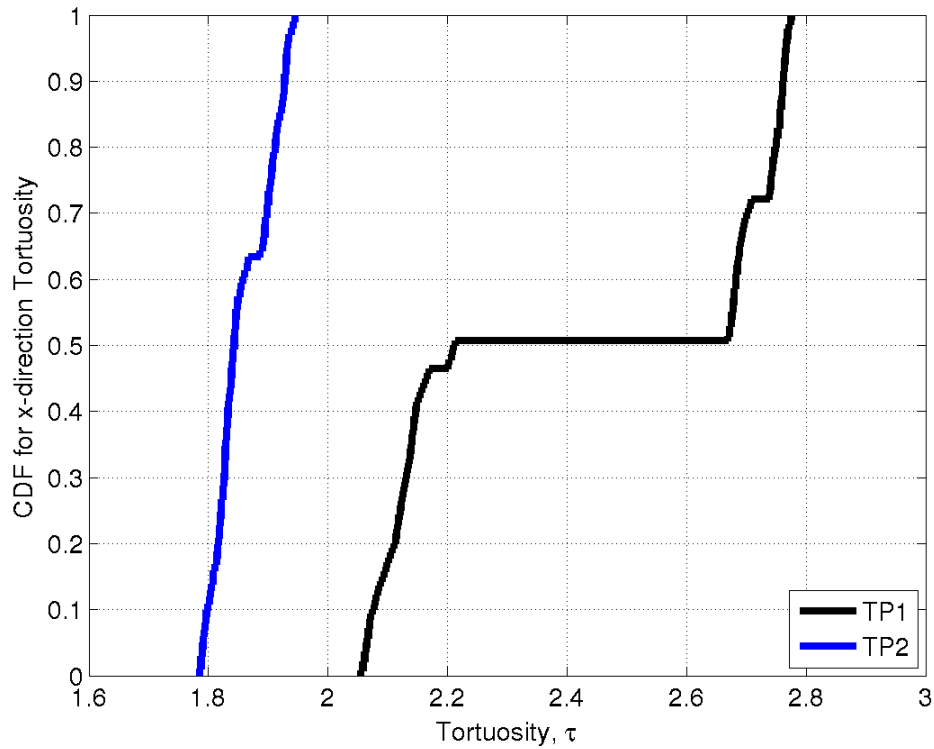


Figure 7.10: Cumulative distribution function (CDF) of x-direction tortuosity for samples TP1 and TP2. The paths in TP1 (mean tortuosity = 2.4190) are more tortuous than those in TP2 (mean tortuosity = 1.8582).

Fluid configurations

The segmented fracture pore space was used as input for the LSMPQS simulation. Inlet/outlet volume sides are aligned with x-directions and all others are sealed. The curvature-saturation relationships are shown in Figure 7.11. This method allows for the periodic checking of the trapped non-wetting phase. Figure 7.12(a) and 7.12(b) show the wetting and non-wetting fluid configuration at the end of drainage and imbibition for TP1. The wetting phase is either in small nooks and crevices of the pore space (small green blobs), or occupies bypassed parts of the pore space (larger green

blobs). The disconnected non-wetting fluid surface is shown in blue and mostly occupies the middle of the pore space.

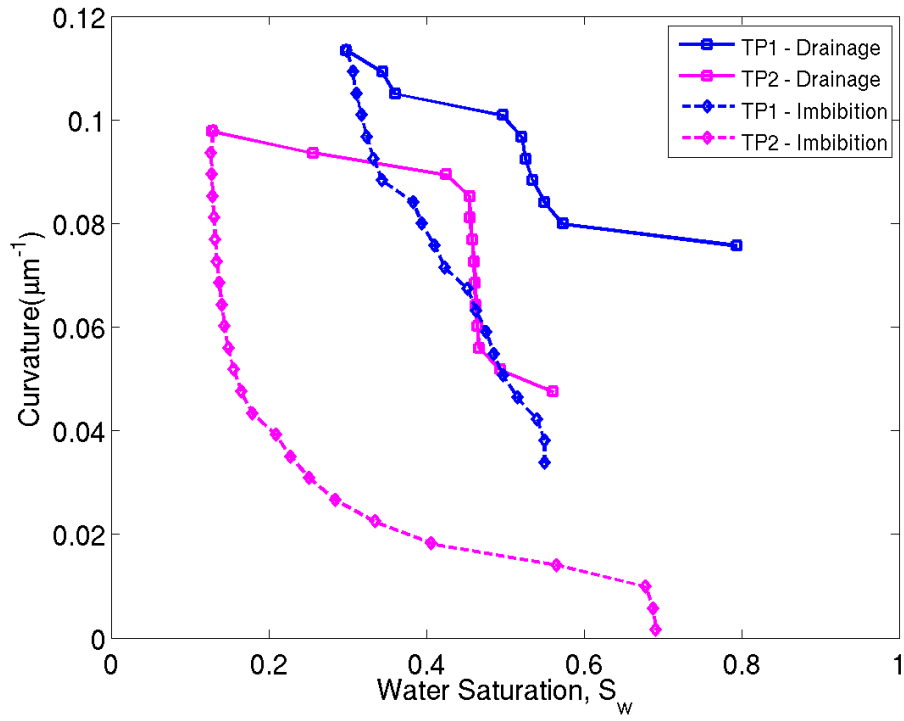
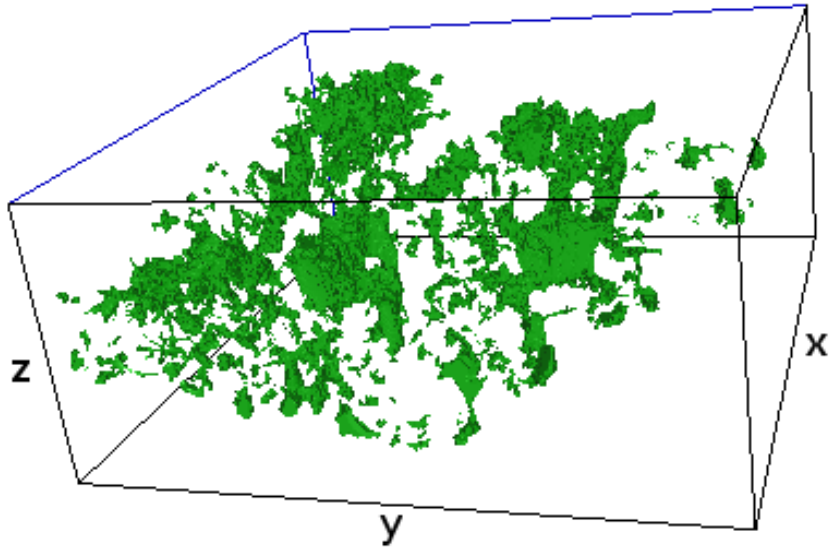
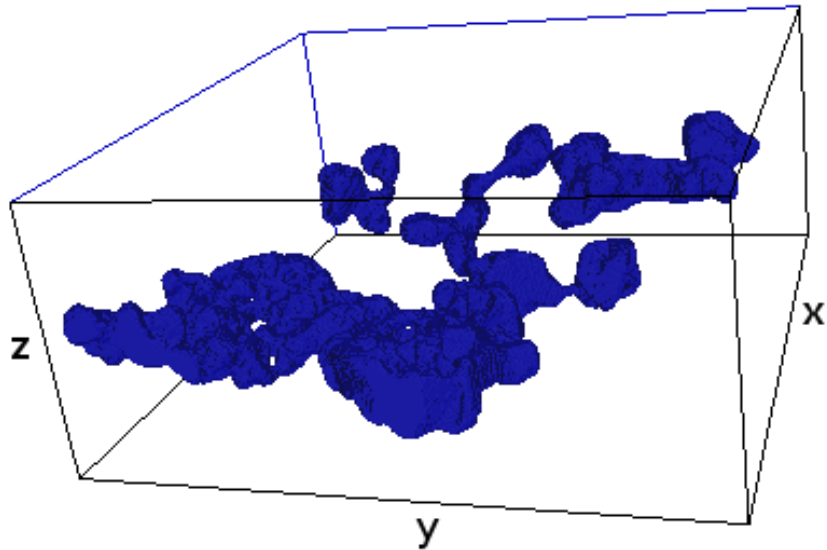


Figure 7.11: Curvature-Saturation plots for the Travis Peak sandstones.



(a)



(b)

Figure 7.12: (a) Residual wetting phase at the drainage end point for TP1 (b) Trapped non-wetting phase of TP1 at the end of imbibition. TP1 has more trapped either phase and is shown here; TP2 shows less trapping but the configurations are similar and thus not shown.

While percolation thresholds during drainage are similar, the qualitative shift in curves is mainly the result of bypassed wetting phase (see Figure 7.11) that causes larger residual wetting phase in drainage of TP2. The shift in the curvature of both curves shows the difference in aperture, with TP2 having a larger aperture and thus a lower curve. The shift in the residual saturation in TP1 shows more constricted geometry, i.e. narrower pathways causing bypasses during drainage and imbibition.

Permeability

The absolute permeabilities computed with Palabos software are 9.610 mD and 11.794 mD for TP1 and TP2, respectively. For comparison, permeabilities for TP1 and TP2 computed using the cubic law are 628.86 D and 1244.44 D, respectively. This discrepancy indicates that a parallel plate model poorly represents these partially cemented fractures, and large variations in aperture are certainly partly to blame. The relative permeabilities of the fluid configurations were also computed using Palabos (Figure 7.13). Both samples show low relative permeabilities for the non-wetting phase at saturations between 25-80% for both phases. Note that trapped/bypassed water during drainage (shown in Figure 7.11) is causing low relative permeabilities in both samples. The simulation results were compared to the values obtained using Chen and Horne's (2006) correlation for drainage in rough walled fractures using the saturation values computed from my (LSMPQS) simulation (Figure 7.14). Figures 7.13 and 7.14 show no similarities likely because of differences in fracture geometry. Rough-walled fractures in Chen and Horne's work did not have any asperities and thus no trapped water phase at

the end of drainage, and were manufactured with a mean aperture of 0.24 mm and standard deviation of 0.05 mm.

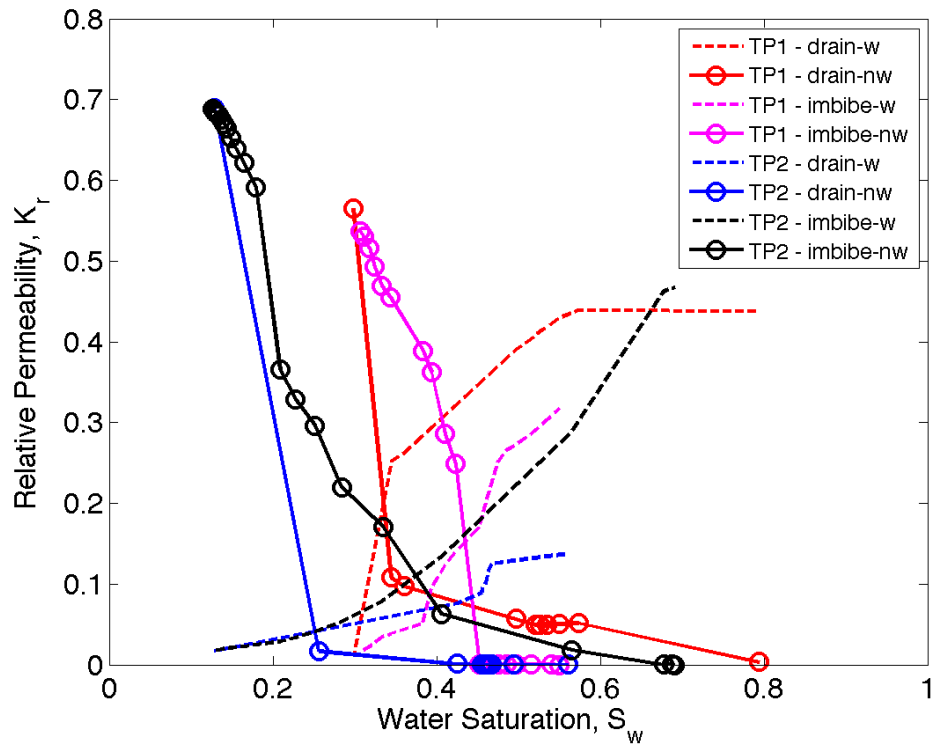


Figure 7.13: Drainage and imbibition relative permeability plots for the Travis peak samples. Drain-nw: drainage of non-wetting fluid, drain-w: drainage of wetting fluid, imbibe-w: imbibition of wetting fluid and imbibe-nw: imbibition of non-wetting fluid.

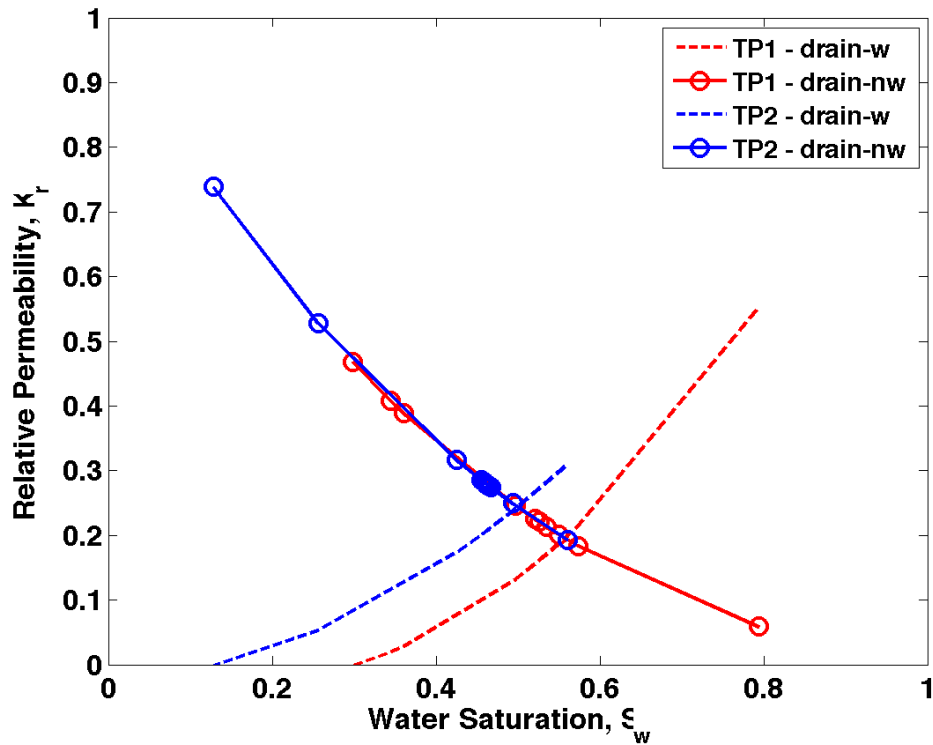


Figure 7.14: Relative permeability curves (drainage) computed based on correlations from Chen and Horne (2006). Drain-nw: drainage of non-wetting fluid, drain-w: drainage of wetting fluid.

DISCUSSION

Comparison to published fracture flow models

A summary of the pore space geometry and fracture characteristics for the Travis Peak is shown in Table 7.1 while Table 7.2 shows a summary of the computed fracture permeability, as well as those from correlations by Witherspoon et al. (1980), Zhang et al. (1996), Eker and Akin (2006), Zimmerman and Bodvarsson (1996) and the Alternate Cubic Law (ACL). These correlations all consider only fracture permeability and hence, are comparable to this work. ACL determines an estimate of permeability from aperture

only, ignoring the influence of fracture geometry. It overestimates the fracture permeability by a factor of 384.

Witherspoon et al. (1980) overestimates the permeability by a factor of 234. Zhang et al. (1996) suggested that permeability is a power function of mean aperture and a fitted factor, β (*i. e.* $k_f \sim \bar{h}^\beta$). In their work, they stimulated fluid flow in a fracture with impermeable walls, the correlation overestimates the permeability by 1.62 with a fitted exponent of $\beta = 2.85$. Eker and Akin (2006) proposed the fitted factor in Zhang et al. (1996) as a linear function of the fractal dimension, D , ($\beta = 4.8065D - 6.4154$). While their function for β fits their results for different fractal dimensions, it does not fit the results of Zhang et al. (1996) or the results in this work. The correlation by Eker and Akin (2006) overestimates permeability by several orders of magnitude. Hence, I can assume that a linear function of β determined from fractal dimensions alone will not provide accurate results.

Comparison of fracture flow between Travis Peak and Torridonian sandstones

Fracture characteristics, pore space geometry, and the permeability estimation using different correlations for the Torridonian sandstone are summarized in Tables 7.1 and 7.2. Like in the Travis Peak, all the correlations overestimate the permeability in both Torridonian samples by several orders of magnitude. The ACL overestimates the fracture permeability in scans A and B by a factor of 93 and 290 respectively; Witherspoon et al (1980), overestimates the permeabilities in the samples by a factor of ~56 and ~180. The Zhang et al (1996) correlation provides the closest estimates with permeabilities values

about ~1 and ~3 times the value calculated by Palabos. Eker and Akin (2006) overestimates the permeability values by 9 orders of magnitude. Figure 7.15 shows a graphical comparison of the computed permeabilities (correlation equations and Palabos simulations) versus porosity for Travis Peak and Torridonian samples.

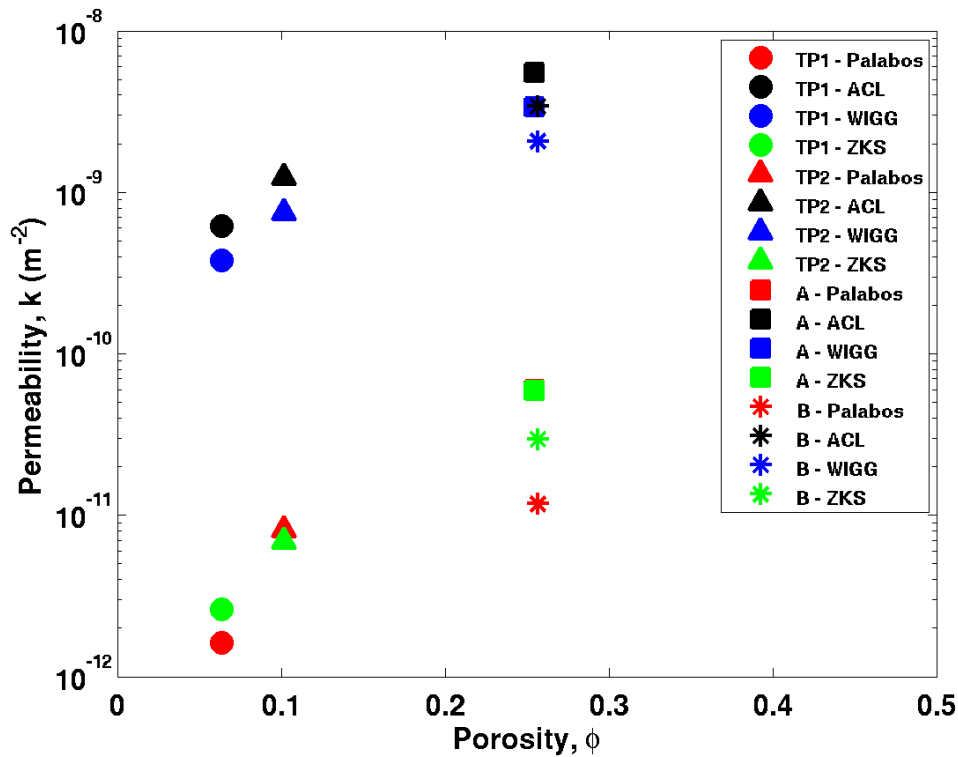


Figure 7.15: Plot of permeability vs porosity for the Torridonian and Travis Peak samples. ACL = Alternate Cubic Law; WIGG = Witherspoon et al. (1980) and ZKS = Zhang et al. (1996).

Table 7.1: Summary of pore space geometry and fracture characteristics for the Travis Peak and Torridonian sandstones

Characteristic(s)	Travis Peak		Torridonian	
	TP1	TP2	A	B
Average Fracture aperture (\bar{h})	0.0863 [mm]	0.1214 [mm]	0.2576 [mm]	0.2021 [mm]
Fracture tortuosity (τ)	2.4190	1.8582	1.6017	1.9033
Fracture aperture standard deviation (σ_h)	0.0836 [mm]	0.0902 [mm]	0.2293 [mm]	0.1390 [mm]
Fracture porosity (ϕ)	0.06394	0.10173	0.25473	0.25664

Table 7.2: Summary of permeability measurements and fracture permeability estimates for the Travis Peak and Torridonian sandstones.

Method	Travis Peak sandstone		Torridonian sandstone	
	TP1	TP2	A	B
Fracture Permeability	$1.61475 \times 10^{-12} \text{ (m}^{-2}\text{)}$	$8.1463 \times 10^{-12} \text{ (m}^{-2}\text{)}$	$5.9992 \times 10^{-11} \text{ (m}^{-2}\text{)}$	$1.1740 \times 10^{-11} \text{ (m}^{-2}\text{)}$
Alternate Cubic Law (ACL)	$6.2064 \times 10^{-10} \text{ (m}^{-2}\text{)}$	$1.2282 \times 10^{-09} \text{ (m}^{-2}\text{)}$	$5.5298 \times 10^{-09} \text{ (m}^{-2}\text{)}$	$3.4037 \times 10^{-09} \text{ (m}^{-2}\text{)}$
Witherspoon et al. (1980)	$3.7844 \times 10^{-10} \text{ (m}^{-2}\text{)}$	$7.4888 \times 10^{-10} \text{ (m}^{-2}\text{)}$	$3.3718 \times 10^{-09} \text{ (m}^{-2}\text{)}$	$2.0754 \times 10^{-09} \text{ (m}^{-2}\text{)}$
Zhang et al. (1996)	$2.6160 \times 10^{-12} \text{ (m}^{-2}\text{)}$	$6.9187 \times 10^{-12} \text{ (m}^{-2}\text{)}$	$5.9047 \times 10^{-11} \text{ (m}^{-2}\text{)}$	$2.9571 \times 10^{-11} \text{ (m}^{-2}\text{)}$
Eker and Akin (2006)	$0.0911 \text{ (m}^{-2}\text{)}$	$0.0994 \text{ (m}^{-2}\text{)}$	$0.1205 \text{ (m}^{-2}\text{)}$	$0.1133 \text{ (m}^{-2}\text{)}$

In comparison with the Travis Peak, the apertures in the Torridonian are wider (Figure 7.16), while the tortuosity of the Torridonian sandstone scans are significantly lower (Figure 7.17), reflecting less constricted geometry. Figure 7.18 shows the curvature-water saturation plot of the Travis Peak and Torridonian sandstones. Torridonian A, TP1 and TP2 show bypassed fluid phases during drainage and imbibition due to constricted geometry caused by the presence of cement bridges.

In Torridonian scan B was clearly a higher resolution image of a more open section of scan A. In Travis Peak, however, TP1 and TP2 were two sections, one more constricted than the other of the same sample along the main flow path (x-direction). It is interesting that scan A and TP1 (more constricted samples) and sample B and TP2 (more open samples) exhibit similar flow behavior. I essentially sampled both y and z (aperture) direction entirely. Thus any larger fracture would consist of sections such as TP1 and TP2 series, and the permeability would overall be limited by the minimum of the two. These examples are thus fairly representative, in terms of individual fractures; of course, the question remains how connected they are on larger scales, which is a question that cannot be answered by microtomography imaging.

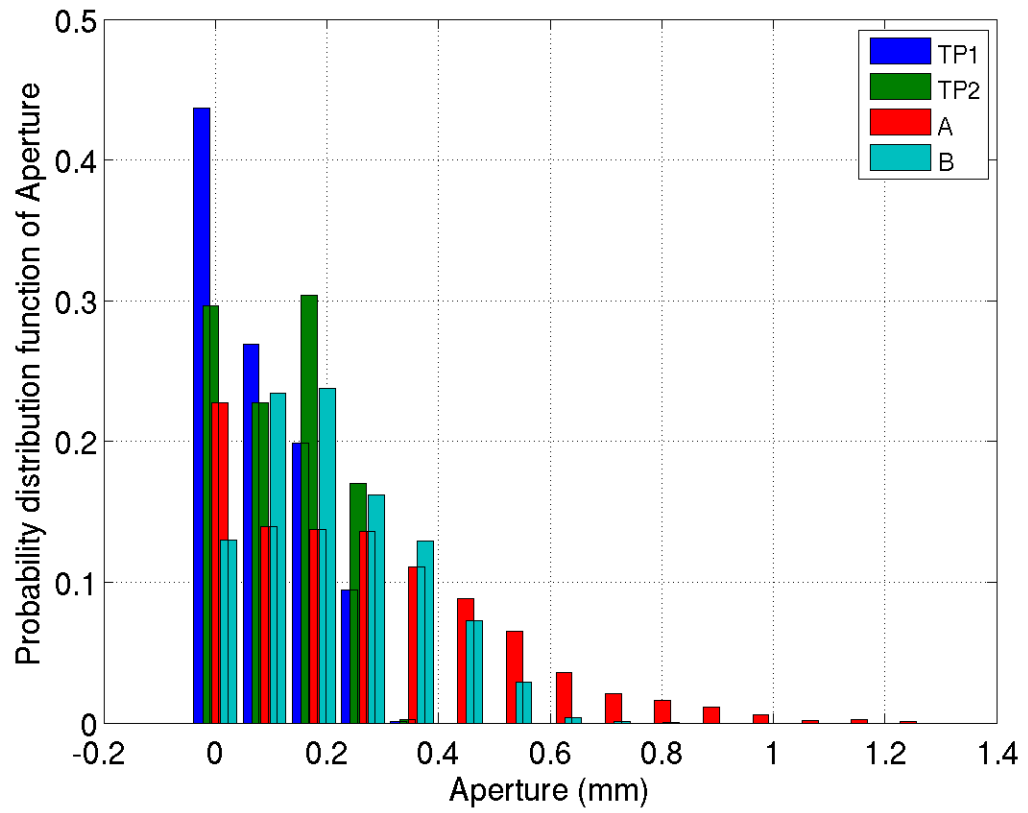


Figure 7.16: Probability distribution function (PDF) of the aperture in the Travis Peak and Torridonian sandstones. The aperture in the sandstones decreases with increasing depth with the Torridonian having average apertures of 0.2576 mm (A) and 0.2021 mm (B).

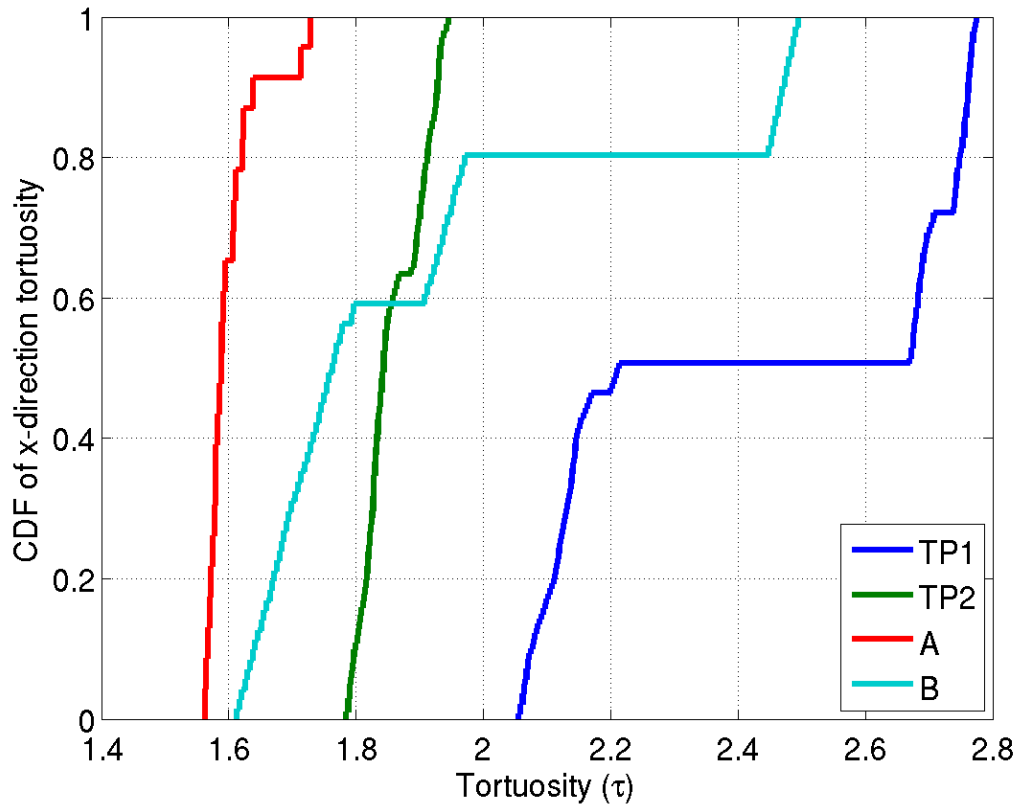


Figure 7.17: Cumulative distribution function (CDF) of the x-direction tortuosity in the Torridonian and Travis Peak. The Torridonian A and B have narrower tortuosities than TP1 and TP2 due to less cement constrictions.

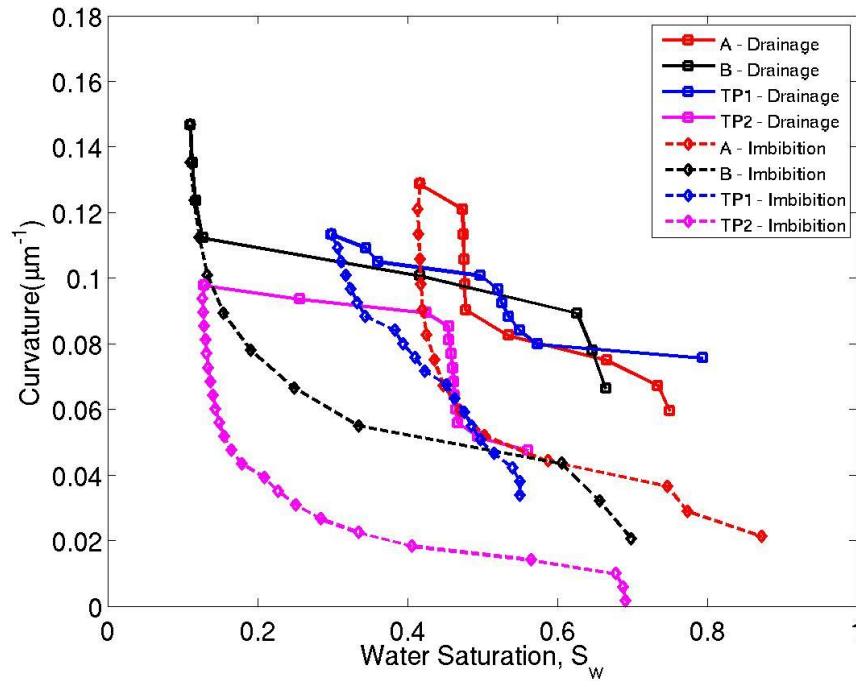


Figure 7.18: Curvature-Water Saturation plot of the Travis Peak and Torridonian sandstones. Torridonian A and TP1 show bypassed fluid phases during drainage and imbibition due to constricted geometry.

CONCLUSION

The partially cemented fractures of the Travis Peak and Torridonian sandstones are lined with quartz and carbonate cement but preserving residual connected fracture porosity open to flow. Large variations in fracture aperture result in constricted pore space geometry that causes trapping of fluids during drainage and imbibition akin to that in sandstone pore space. When compared with the Travis Peak, Torridonian scans have higher permeability, porosity and tortuosity. Permeability estimates in the Travis Peak and Torridonian vary by several orders of magnitude when using different correlations, which I attribute to the constricted fracture pore geometry of cement-lined or partially

cemented fractures that is not accounted for by previously published fracture aperture--
flow correlations.

Chapter 8: Niobrara Carbonate

SAMPLE DESCRIPTION

The fracture imaged in this study was cored from an outcrop sample of the Niobrara Formation (Figure 8.1a), collected near Lyons, Colorado. The host rock is a dense micrite with no matrix porosity visible in thin section. The fracture is lined with euhedral to blocky calcite (Figure 8.2). Microtomography image scans were taken at the mid-length of the core with a voxel resolution of $29.69\ \mu\text{m}$ (Figure 8.1b).

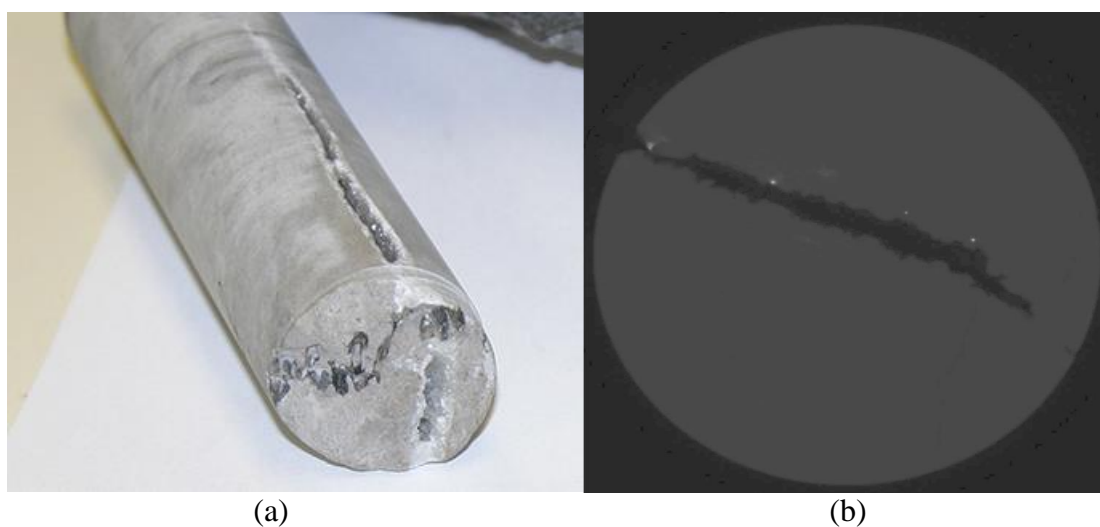


Figure 8.1: (a) Core plug containing a partially cemented fracture in limestone of the Niobrara Formation, Lyons, Colorado. Core plug is 1 inch (2.5 cm) in diameter (b) Tomographic image slice, 1 inch (2.5 cm) in diameter, imaged at UTCT with voxel length = $29.69\ \mu\text{m}$

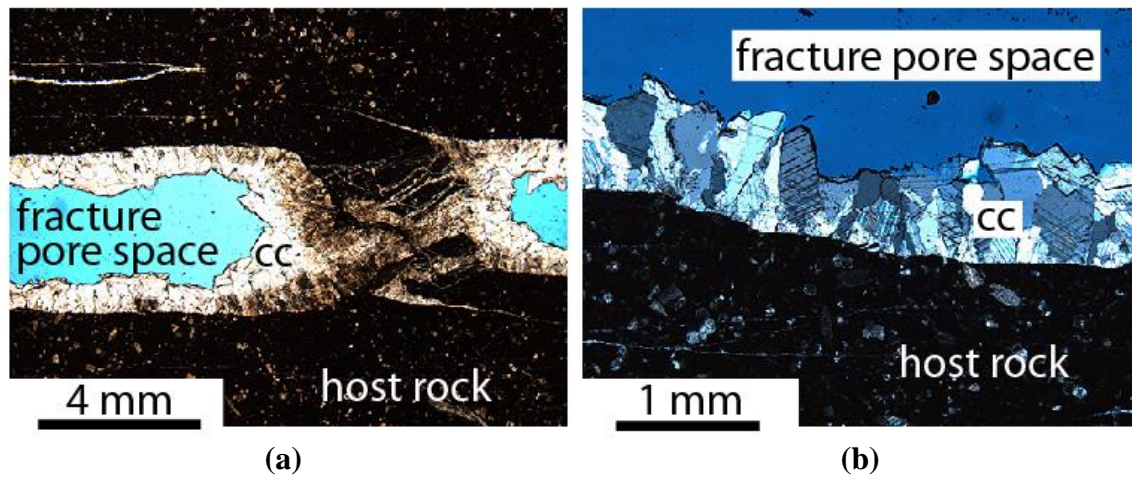


Figure 8.2: Transmitted light petrographic images of partially calcite-cemented (cc) fracture in Niobrara Formation. Host rock composed of micritic carbonate. (a) Plain-polarized, (b) cross-polarized image of twinned calcite growing into residual fracture pore space

IMAGE CHARACTERIZATION AND MANIPULATION

The matrix of the Niobrara sample contains no visible pore space that is resolved in the CT scan; I thus limited image characterization and flow modeling to the fracture pore space. The image was resized to a bounding box of 600x730x170 voxels around the fracture. I used standard median filter to remove noise in the tomographic image before segmentation. The contrast between gray-scale values of two different phases allowed simple thresholding segmentation. The pore space non-interacting with the main fracture was then removed from the image. The final fracture/solid surface is shown in Figure 8.3.

Cement was numerically grown in the fracture pore space of the imaged sample to simulate the effect of cement precipitation on fracture pore space connectivity, permeability, and multiphase flow properties. Fracture cement was added numerically on the imaged fracture, on top of the natural fracture cement, in ~ 0.1 mm increments, thus stepwise occluding the residual fracture pore space (Figure 8.4). For the remainder of this

chapter I will refer to the fracture geometry with 0.5 mm of numerically added cement thickness as “numerically cemented” when compared to the imaged naturally cemented sample, referred to as the “original sample”. The medial axis of original sample and the fracture-solid surface of both samples are show in Figure 8.3, while the aperture-field visualization and distributions for both samples are shown in Figure 8.5.

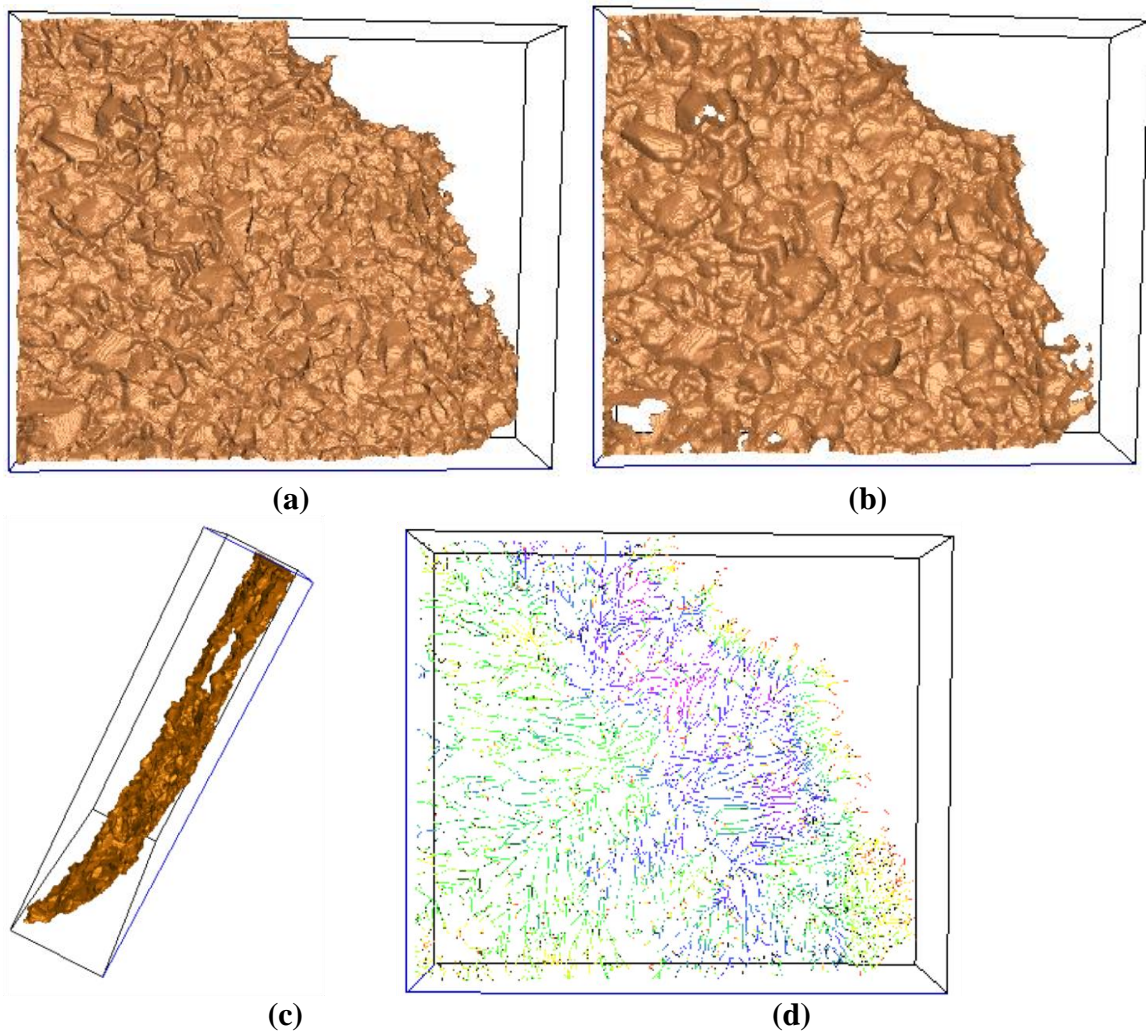
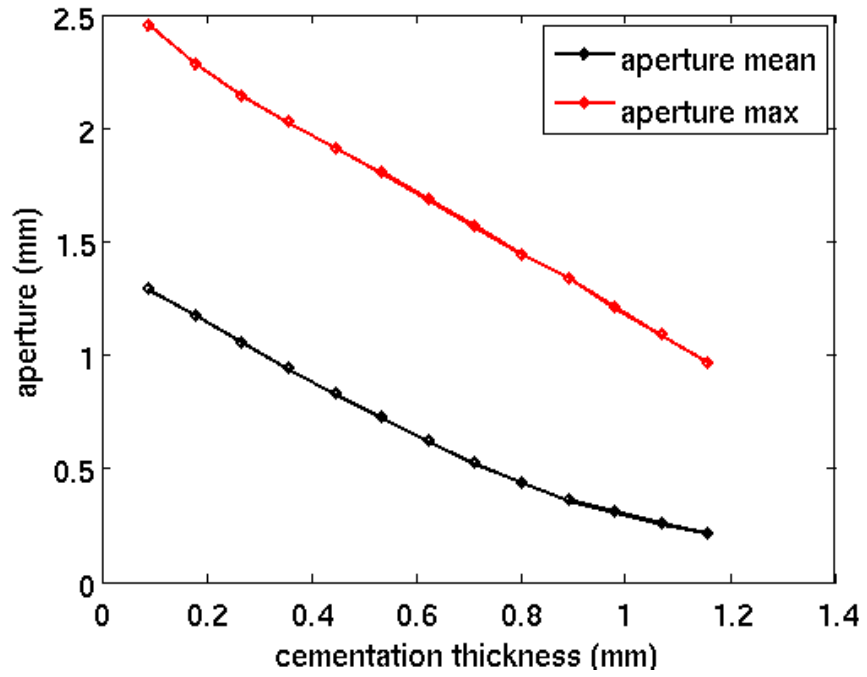
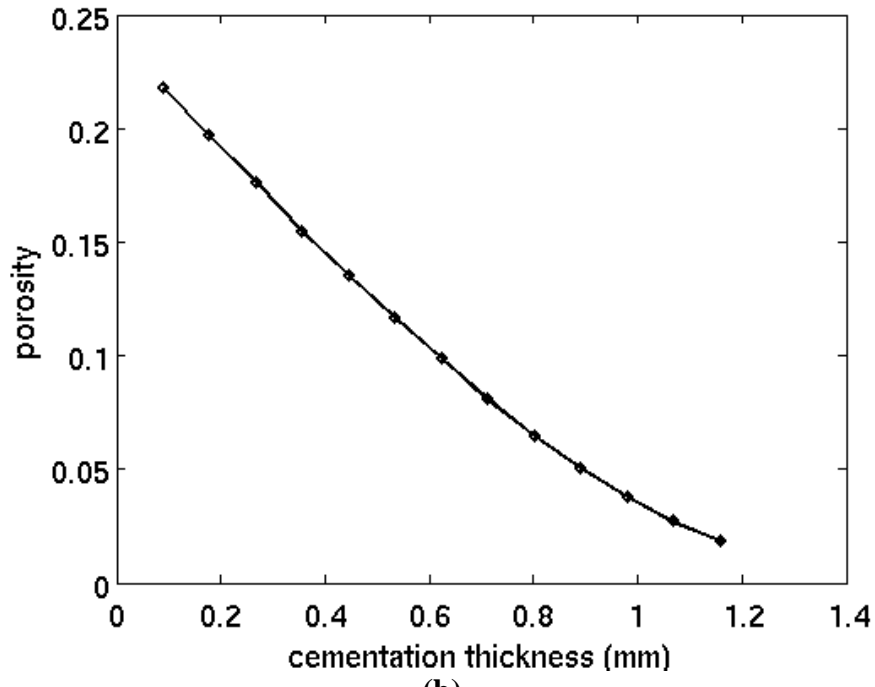


Figure 8.3: (a) Fracture-solid surface of the imaged fracture before numerical cementation (b) fracture-solid surface after numerical cementation (c) side/aperture view of the fracture surface (d) the fracture pore space thinned down to the medial axis skeleton. The coloring reveals the distance to the closest grain voxel, i.e. red is the closest while blue is farthest from the closest grain voxel.



(a)



(b)

Figure 8.4: Change in aperture (a) and porosity (b) during simulated fracture cement growth in ~ 0.1 mm increments on the imaged fracture pore space.

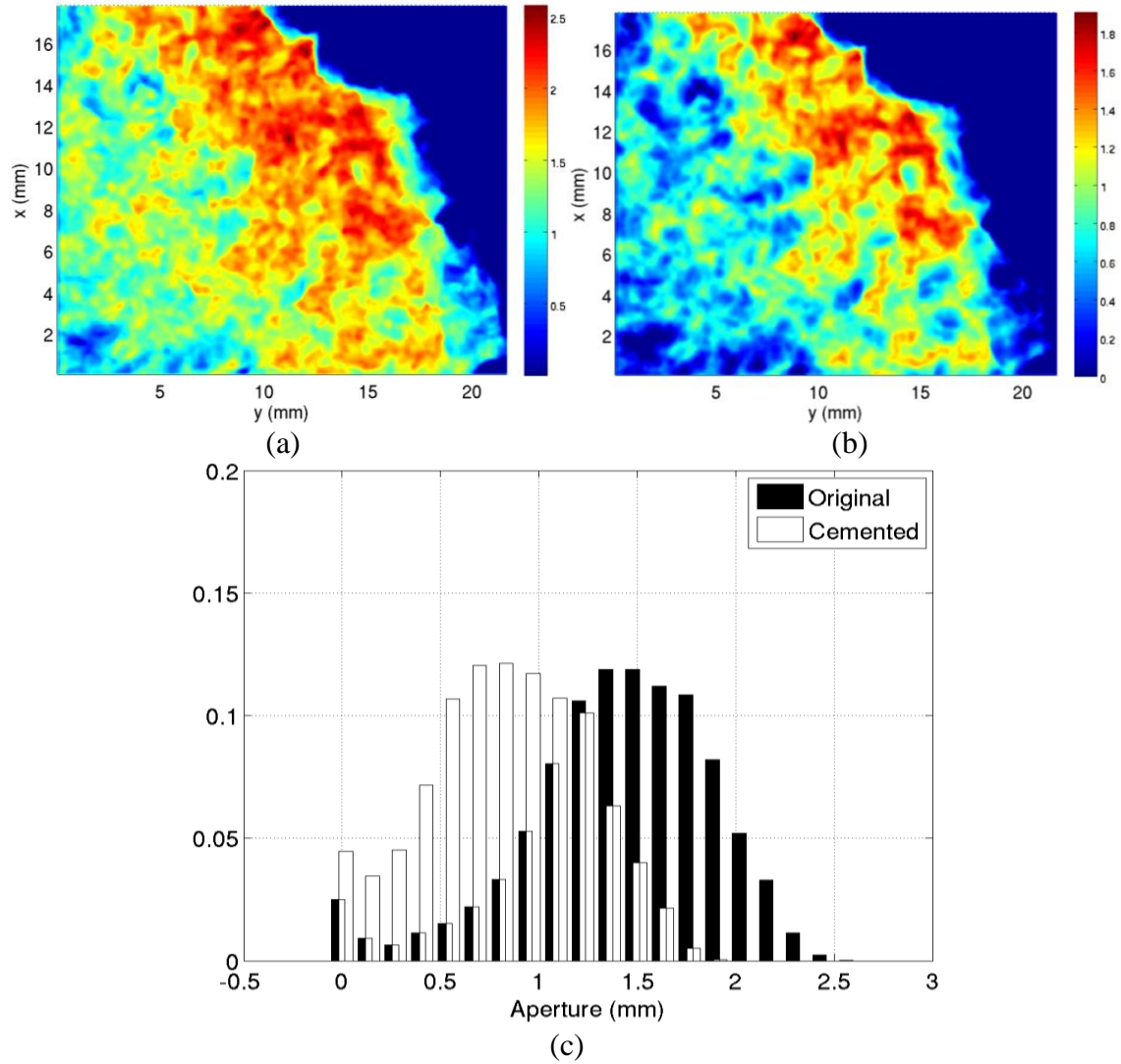


Figure 8.5: Aperture field for (a) the imaged fracture, $h_{\max}=2.32$ mm, $h_{\text{ave}}=1.26$ mm and (b) the fracture after numerically adding 0.5 mm of cement. Note large white/blue islands indicating contact areas that appear after cementation. (c) Probability Density Function (PDF) of z-direction aperture for the original and cemented samples. PDF shows that the aperture distribution in the Niobrara shifts to the left after cementation.

Absolute Permeability

The absolute and relative permeabilities for the samples were computed with Palabos software. Computing permeability using the cubic law and average apertures for the samples yields values that are several orders of magnitude higher than those obtained from the simulation (see Table 8.1). This discrepancy indicates that the parallel plate model poorly represents the fractures. I have previously found that different correlations that depend on (average) aperture yield permeability estimates that extend over several orders of magnitude (Chapter 6 and Tokan-Lawal et al. 2013).

Table 8.1: Summary of the mean aperture, porosity and permeability values for the Niobrara samples

Sample	Porosity (%)	Permeability (Darcy)	Min/Mean/Max Aperture (mm)	Cubic Law Permeability (Darcy)
Original	22.72	5.33	0/ 1.41/ 2.58	166302.32
Cemented	12.88	0.44	0/ 0.83/ 1.91	57735.29

Fluid Configurations and Relative Permeability

I used the segmented fracture pore space as input for the LSMPQS drainage simulation. Inlet/outlet volume sides are aligned with x-directions and all others are sealed. The cemented sample shows a higher curvature-saturation plot than the original “imaged naturally cemented sample”. This is because a higher capillary pressure is required for the fluid to move through the fractured pore spaces, thus yielding a lower permeability in the cemented sample. The curvature-saturation relationship of the drainage in both samples is compared in Figure 8.6 (a) while the matching tortuosity-saturation curves, during drainage, are shown in Figure 8.6 (b).

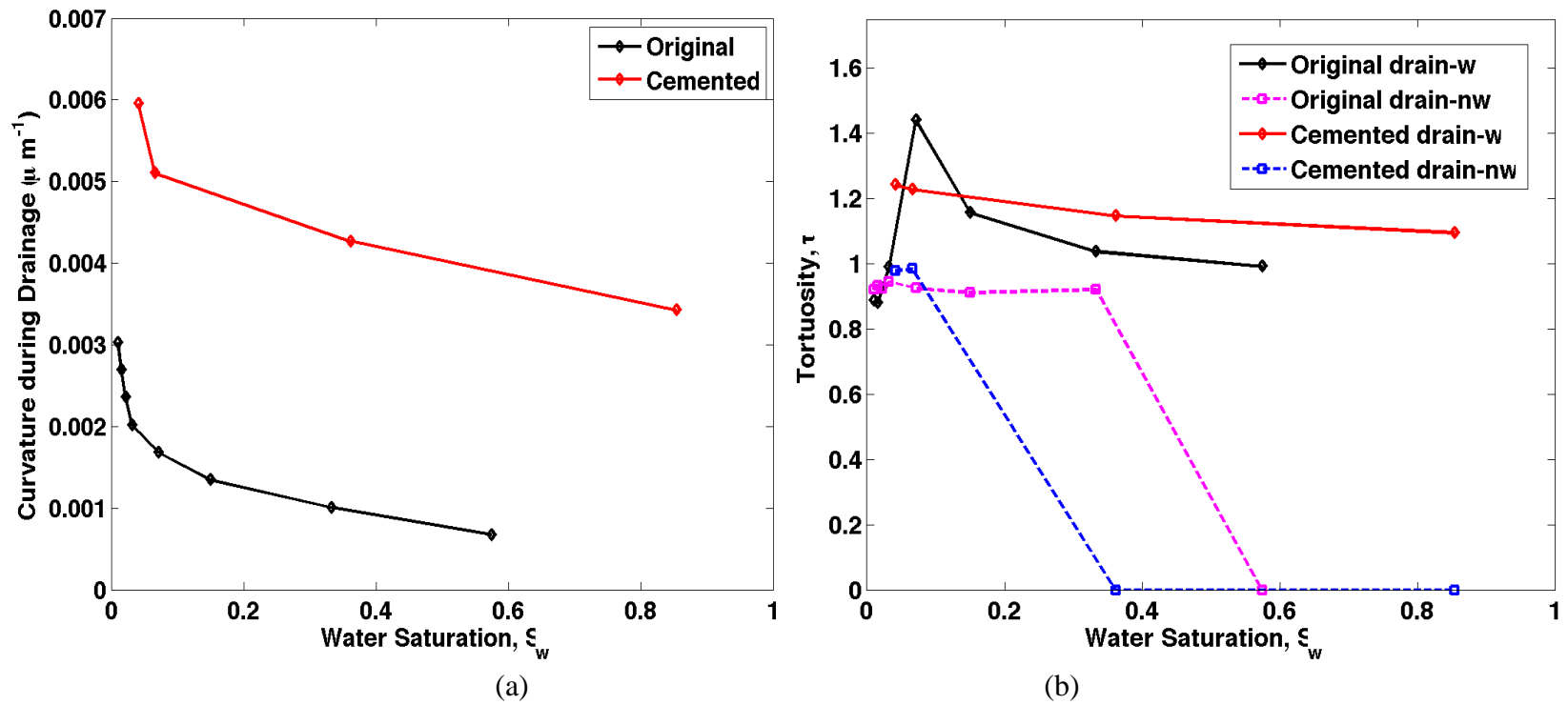


Figure 8.6: (a) Curvature-saturation curves for drainage for the original and numerically cemented Niobrara fracture. (b) Matching tortuosity saturation curves for the non-wetting (nw) phase during drainage. Tortuosity values have been divided by the average tortuosity values shown in Table 8.1.

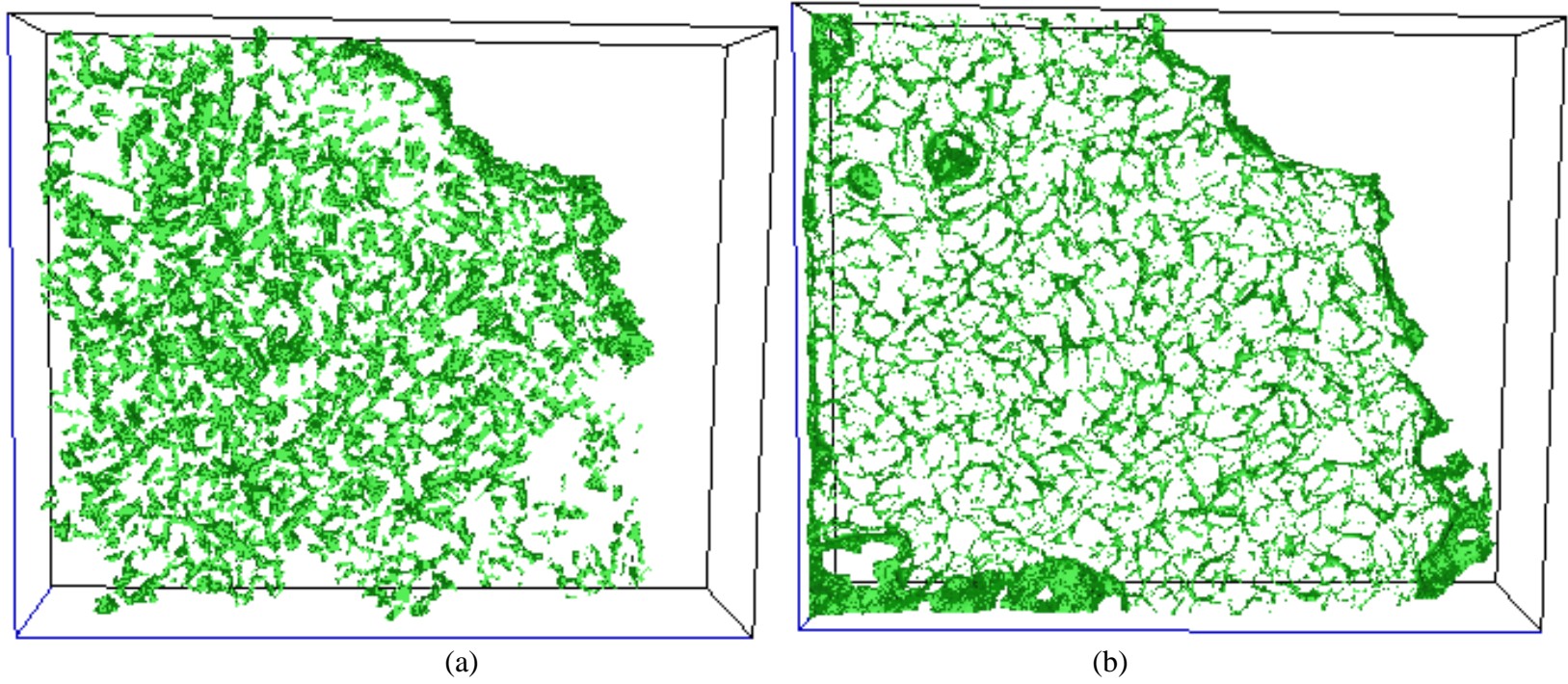
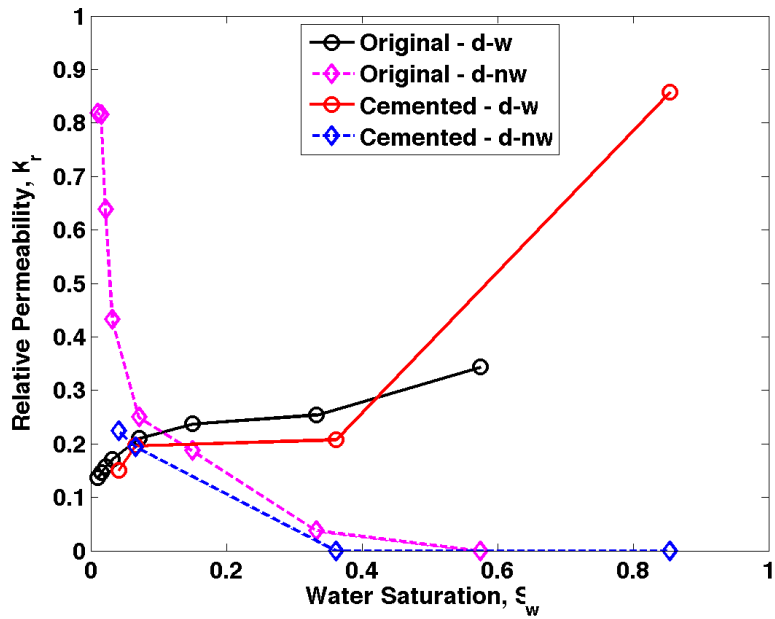


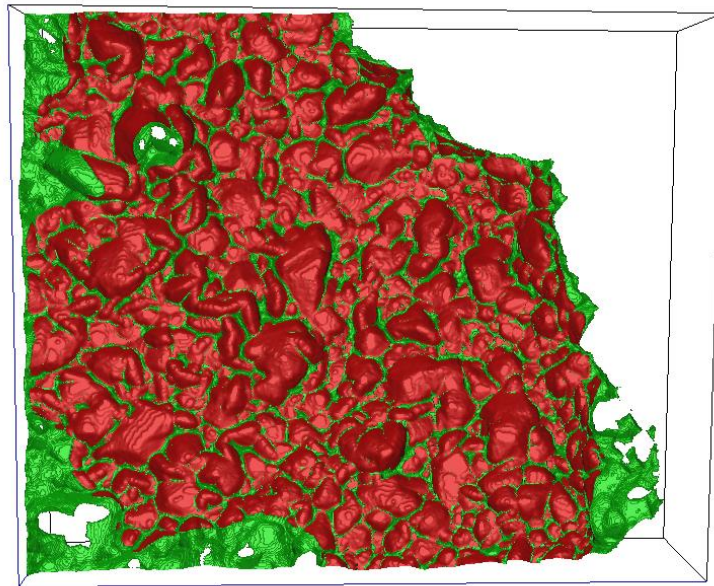
Figure 8.7: Trapped wetting phase at the end of drainage for (a) the original (b) cemented Niobrara fracture.

I analyzed differences between the original and cemented sample a bit further. In Figure 8.6(a), I see a higher curvature (overall, higher capillary pressure due to the presence of cement and hence smaller pore throats for the fluids to move through) in the cemented sample than in the original sample. I see higher endpoint water saturation in the cemented sample owing to the presence of smaller apertures and corners for the wetting phase to reside. This is visually confirmed when comparing Figure 8.7(a) and 8.7(b). Figure 8.6(b) shows that the wetting phase has fairly tortuous paths (since residing in corners), while the non-wetting fluid has relative tortuosity of about 0.9-1, when it percolates and zero otherwise.

In terms of relative permeability, the non-wetting fluid has overall higher relative permeability than the cemented sample for the same saturation (Figure 8.8). The relative permeability (Figure 8(a)) and relative tortuosity (Figure 8.6(b)) plots, when compared, do not show any correlations, contrary to what is expected per the Carman-Kozeny equation.



(a)



(b)

Figure 8.8: (a) Drainage relative permeability plots for the original and cemented fractures. D-nw: drainage of non-wetting fluid, d-w: drainage of wetting fluid. (b) Non-wetting (in red) and wetting (in green) fluid configurations for cemented sample for the third drainage step. Interlocked configuration reduces relative permeability to both fluids.

DISCUSSION

At the end of drainage, the wetting phase (the fluid, which adheres more readily to the solid surface) tends to reside in the smallest areas of the pore space such as small pores (small green blobs), the corners of larger pores as well as connected films residing in the roughness of the solid surface (Figure 8.7). Conversely, the non-wetting phase, which adheres less easily, resides in the largest areas of the pore space, principally around local maxima of apertures. The wetting phase covers the walls of the pores (apertures) and flows along the walls through thin liquid pathways, hence most of the residual wetting phase is either in small nooks and crevices of the pore space (small green blobs), or occupying bypassed parts of the pore space (larger green blobs). In the cemented sample, Figure 8.7(b), I see a block of water in lower left that appears bypassed due to the tightened apertures around it.

The relative permeability of the non-wetting fluid is lower, overall, in the numerically cemented sample than the original for the same saturation. This phenomenon exists because the newly created cement bridges lead to an increased number of pockets of disconnected water. In contrast to the non-wetting phase, the wetting phase initially has a higher permeability in the numerically cemented than in the original sample (for the same saturation). At lower saturation, the fluid phases impede each other in more intricate ways, and the wetting fluid behavior reverses. Based on the Carman-Kozeny relationship, I expect that the relative tortuosity and relative permeability will be inversely proportional. Other than both being zero when the fluid does not percolate, however, I see no clear relationship between relative tortuosity and relative permeability. In addition, the taper in fracture aperture toward the fracture tip line provides a continuous path for wetting fluid, which never gets completely disconnected, and relative permeability never goes to zero.

The cumulative distribution functions of the x-direction geometric tortuosity in the Niobrara, Torridonian (Chapter 6), and Travis Peak (Chapter 7) are shown in Figure 8.9. The Niobrara samples contain more cement; however the absence of mineral bridges makes them less constricted than the Travis Peak and Torridonian samples. The geometric tortuosity values for the samples fall between 1.25 and 2.5. Although cemented, the fractures in the samples are still open to flow. While the Niobrara fractures are more cemented than the sandstones, the presence of mineral bridges in the Travis Peak make them more constricted.

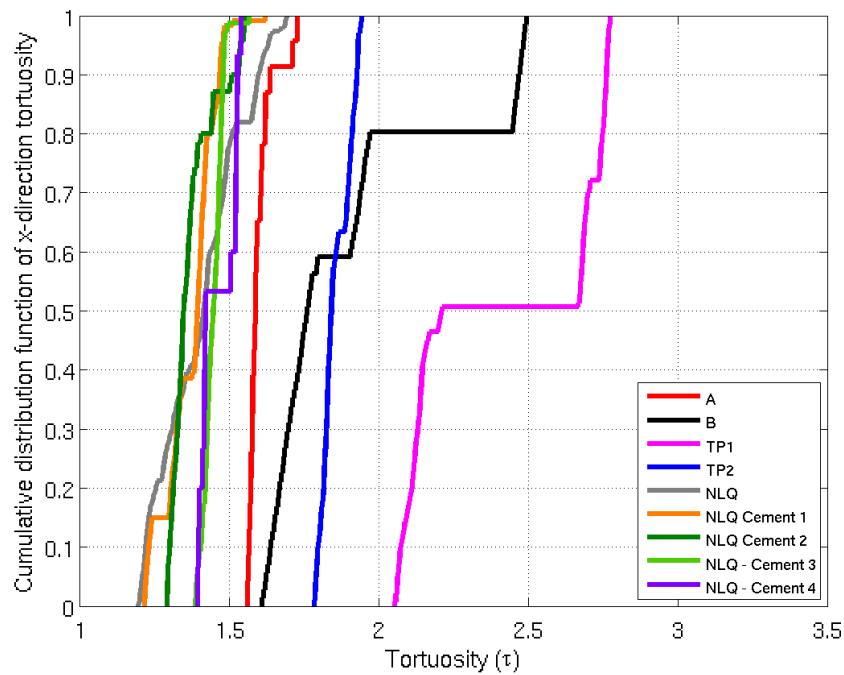


Figure 8.9: CDF of the x-direction tortuosity in the Torridonian and Travis Peak.

Finally, the imaged fracture analyzed in this work is much smaller than the fracture that exists in the drilled sample. Hence there might be some size limitations and

the calculated properties will have to be scaled up to accurately represent the drilled sample.

CONCLUSION

Residual porosity in the partially cemented fracture of the Niobrara Formation provides a connected and thus efficient fluid pathway through otherwise very tight carbonate rock. I compared the curvature, tortuosity, permeability and relative permeability of the imaged fracture geometry with a fracture geometry that contained additional numerically generated fracture cement. The curvature in the numerically cemented fracture is twice that of the imaged fracture, showing that increasing cementation requires a higher capillary pressure to percolate fluid. While there are no cement contact points or bridges in the CT-scanned fracture volume, numerical fracture cementation creates unevenly distributed apertures and cement contact points. This, in turn, causes the wetting and non-wetting fluids to impede each other, with no consistent trends in relative permeability with increasing saturation for the cemented fracture. Wetting fluid remains connected at all saturations along the fracture tip line. Contrary to my expectation, the relative tortuosity of either wetting or non-wetting phase and their respective relative permeabilities show no clear correlation to relative permeability.

Chapter 9: Summary

Fractures exist at all scales from microcracks to km-scale faults, and this makes it challenging to define average flow properties of fracture networks. In this thesis, I attempted to extend the understanding of flow at the pore (micrometer) scale in fractured porous media using x-ray microtomography images as input into models. This scale is below seismic image resolution, and thus often overlooked, yet in tight reservoirs it is relatively important.

Chapters 1 through 4 introduce the topic and review relevant literature and methodology used in this work.

In Chapter 5, an artificial fracture, created by Landry and Karpyn (2012) was used to understand fluid flow characteristics in a fracture at the pore scale. In addition, the permeability estimate was compared with those in Landry and Karpyn (2012) as well as estimates from a variety of previous investigations. All of the permeability estimates assume an impermeable fracture wall, and overestimate the permeability by varying orders of magnitude. Lattice Boltzmann methods, and other pore-scale models provide insight into fluid flow through permeable porous media at micron scale; particularly in rough walled fractured permeable media.

The focus of Chapter 6 was to correlate permeability with geometric tortuosity of both pore (fracture) space and individual fluid phases for fractured Torridonian sandstone, an outcrop analog for tight sandstone reservoirs. The partially cemented fractures of the Torridonian sandstone were found to be very constricted, with many crystals bridging across the fracture but keeping large portions open to flow. The adjacent

matrix, however, was almost completely cemented. The tortuosity distribution in the Torridonian sandstone was compared with those in other porous media. It was found that fractures have considerably narrower tortuosity distribution when compared to other porous materials. Despite their cement lining, these fractures provide the most direct path across the material. In addition, I found that tortuosity in both consolidated porous media and partially cemented fractures increases with an increase in the amount of carbonate or quartz overgrowth cement. When analyzing tortuosity of different fluid phases, there is a very weak correlation between fluid phase tortuosity and relative permeability. Relative permeability correlations and capillary pressure curves found here can be used in reservoir simulators to model recovery of hydrocarbons in fractured tight reservoirs.

In Chapter 7, the influence of fluid flow was studied in naturally fractured Travis Peak Sandstone taken from depth of 10000ft. The simulation-measured fluid properties of the Travis Peak were compared to those of the Torridonian. Both sandstones are tight with excessive compaction and quartz cementation. Overall, permeability, and porosity decrease with increasing depth while tortuosity increases with increasing depth.

In Chapter 8, I continued my investigation of fluid flow in naturally fractured tight reservoirs. I computed permeability and geometric tortuosity of both pore (fracture) space and individual fluid phases for fractured Niobrara carbonate. I further investigated the change in all parameters (geometric tortuosity, curvature, permeability and relative permeability) with a layer of numerically applied uniform cement. The partially cemented fractures in the Niobrara provide a sizeable fluid pathway through otherwise very tight carbonate rock. I successfully grew numerical cement in the fracture space and compared

the curvature, tortuosity, permeability and relative permeability of the cemented and original fractures. The curvature in the cemented fracture was twice that of the original fracture, showing that a higher capillary pressure is needed to percolate fluid than in the original fracture. While there was no cement contact points or bridges in the CT-scanned fracture volume, numerical fracture cementation created unevenly distributed apertures and cement contact points. This, in turn, caused the wetting and non-wetting fluids to impede each other, with no consistent trends in relative permeability with increasing saturation for the cemented fracture. Wetting fluid remains connected at all saturations along the fracture tip line. Contrary to my expectation, the tortuosity of either wetting or non-wetting phase and their respective relative permeabilities show no clear correlation.

Overall, pore scale methods provide an insight to flow characteristics in rough walled fractures at micron scale. This scale is often overlooked for fractures, yet important/dominant for tight reservoirs. The method employed in this study, initially developed for flow in porous media, is demonstrated here to predict flow in natural cement-lined or partially cemented fractures. Natural fractures have considerably narrower tortuosity distribution when compared to other porous materials. They also provide the most direct path across the sample, even in the presence of cements. The presence of cement reduces porosity and permeability, thus hindering flow by creating unevenly distributed apertures and cement contact points.

Appendix A: Methods

This section describes how to run 3DMA, LSMPQ and Palabos simulations.

IMAGE CHARACTERIZATION

Segmentation in ImageJ

Segmentation is the most crucial step in image analysis, since all further characterization, modeling input and/or any conclusions made about the porous material are dependent on the segmentation output. X-ray computed microtomography (XCMT) scans are input for Segmentation. It is the process of simplifying and/or changing the representation of an image into something that is more meaningful and easier to analyze. Several options exist for the segmentation process: simple (global) thresholding, statistical (e.g. k-means clustering), indicator kriging, etc. I used indicator kriging implemented 3DMA-Rock (Oh and Lindquist, 1999). The indicator kriging method requires input of two thresholds, T_0 and T_1 . T_0 (T_1) establishes a lower (upper) limit below (above) which any voxel can reasonable be identified as phase 0 (1). For all other voxels, indicator kriging determines the probability of belonging to phase 0 utilizing the local two-point correlation function (Figure A.1). I use ImageJ (Fiji) to manipulate the data, plot histogram and ultimately find the two thresholds to be used for segmentation in 3DMA-Rock. The image sequence (XMT jpeg images) was imported via: *File -> Import -> Image Sequence* (Figure A.2).

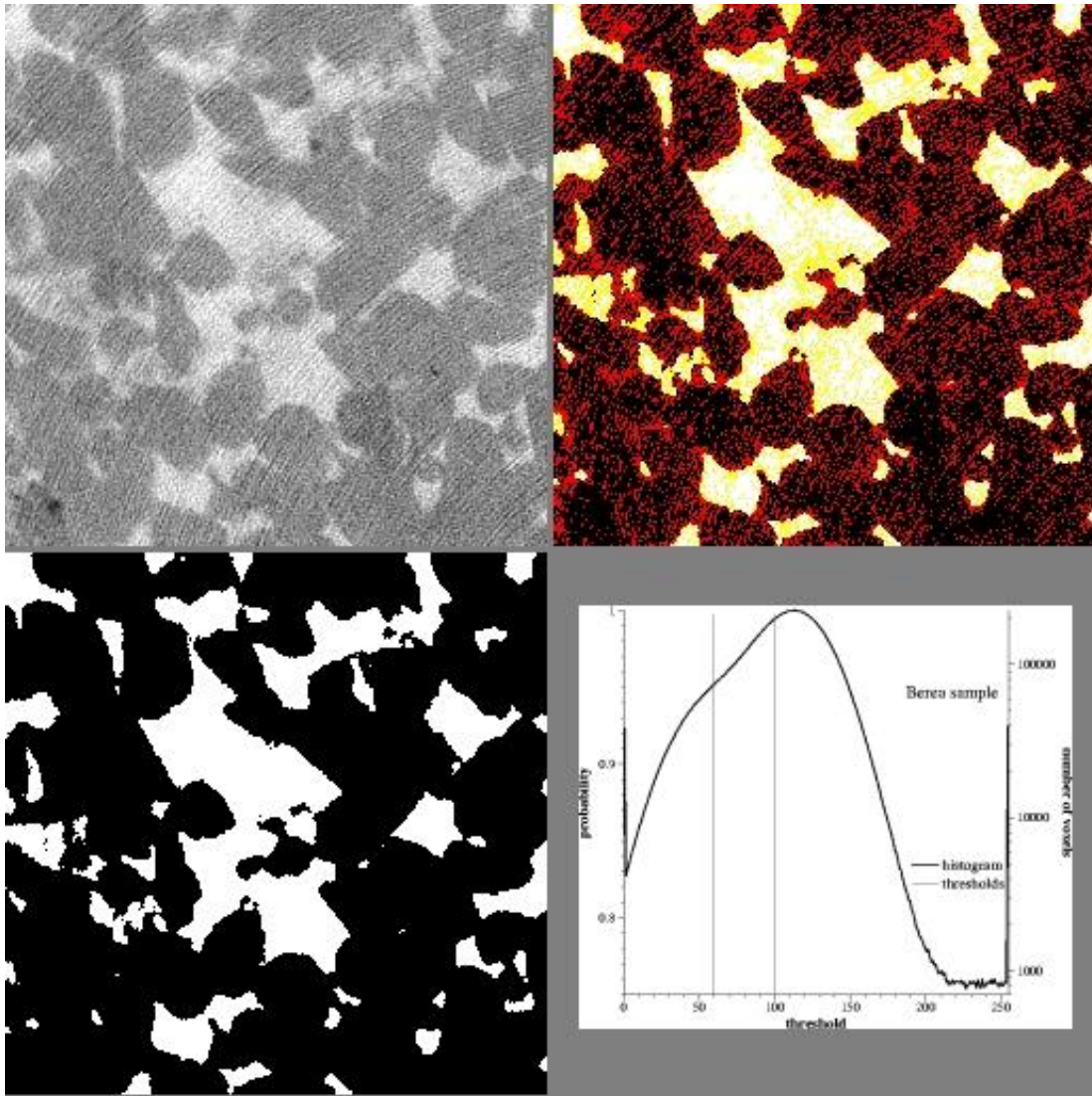


Figure A.1: (Top left) Tomographic image – slice of Berea sandstone. (Top right) White (black) voxels are identified as phase 0 (1) through the threshold T_0 (T_1). Yellow (red) voxels are identified as phase 0 (1) via kriging. (Bottom left) result after the indicator kriging segmentation. (Bottom Right) Histogram with superimposed attenuation coefficient. Indicator kriging thresholds are indicated as light vertical lines (3DMA-ROCK website - http://www.ams.sunysb.edu/~lindquis/3dma/3dma_rock/3dma_rock_05_primer/primer.html)

After successfully importing the data, one needs to select the area of interest. Since my work involved understanding flow in fractures with impermeable walls, I select

the region that includes the fracture (Figure A.3); then clear the outside of the selected box (*Edit -> Clear Outside*) to remove the unwanted matrix voxels before producing a histogram (Figure A.4). ImageJ->Analyze->Histogram will produce a histogram (Figure 5). Picking two thresholds from the valley between the two humps; we can set T_0 and T_1 . Save the images as a .raw file (*File->Save As -> Raw Data....*)

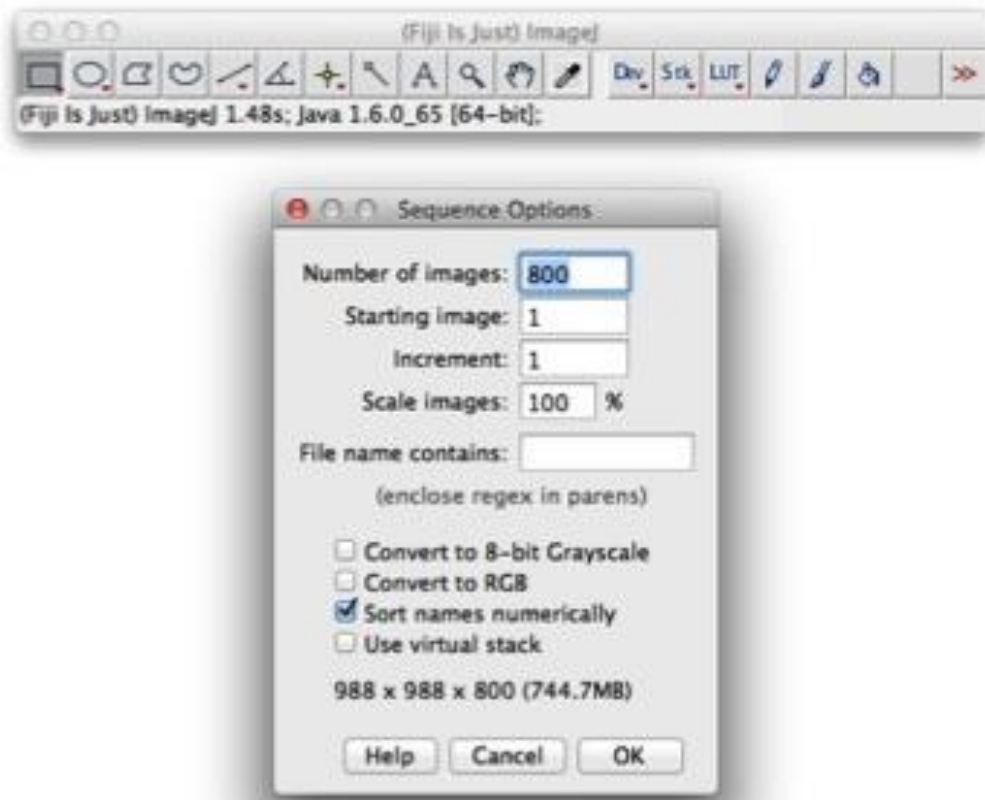


Figure A.2: Importing the image sequence

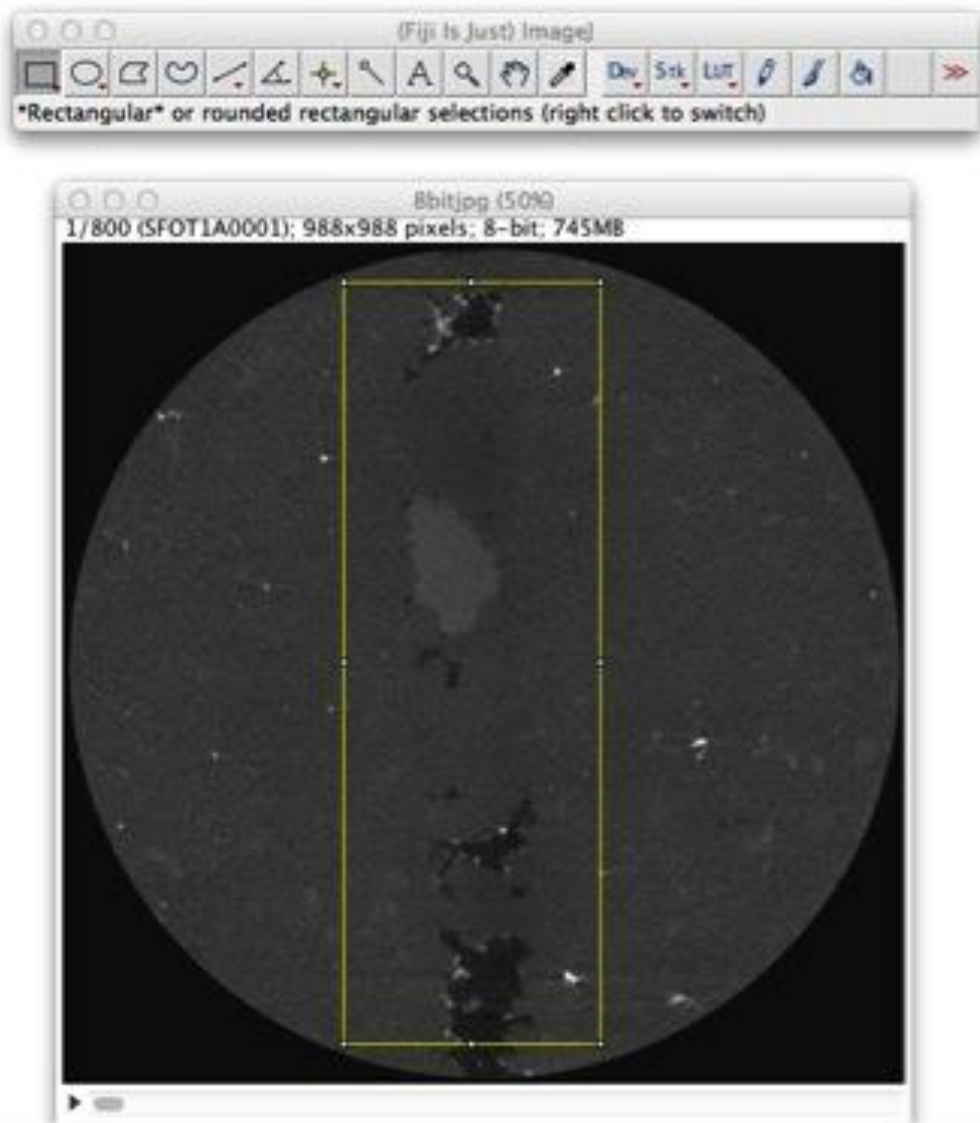


Figure A.3: Selecting the region of interest using the rectangular selection (yellow)

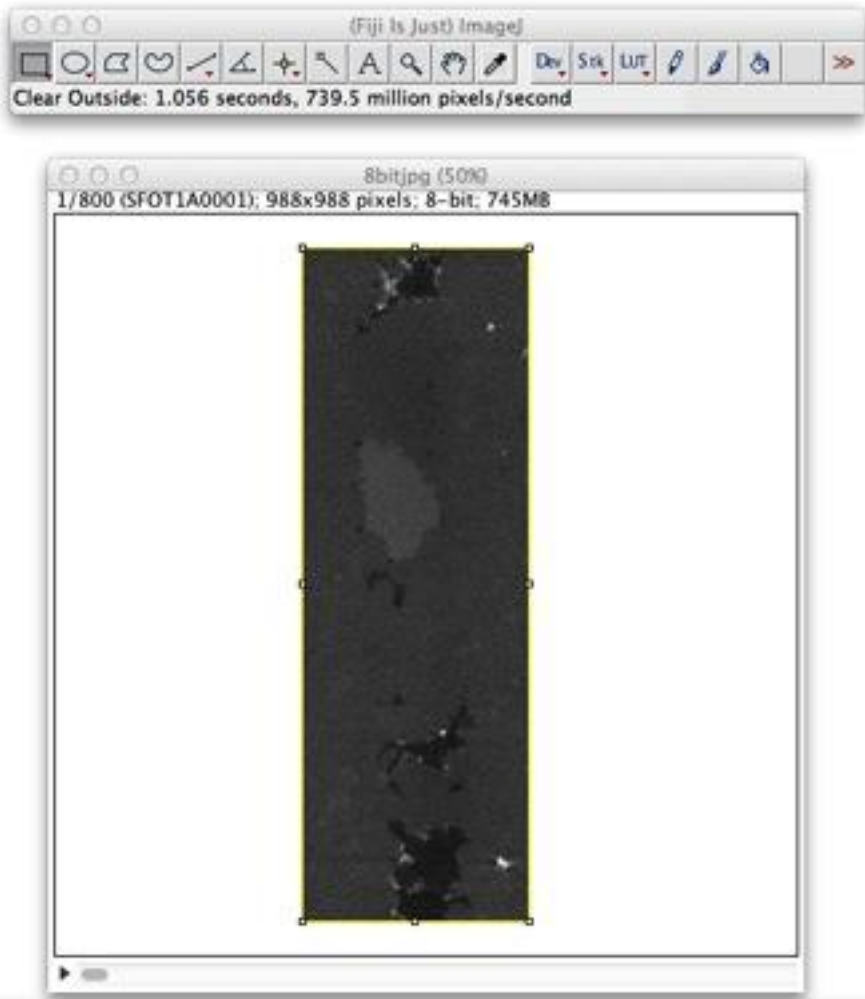


Figure A.4: Image slice after the unwanted voxels have been cleared out.

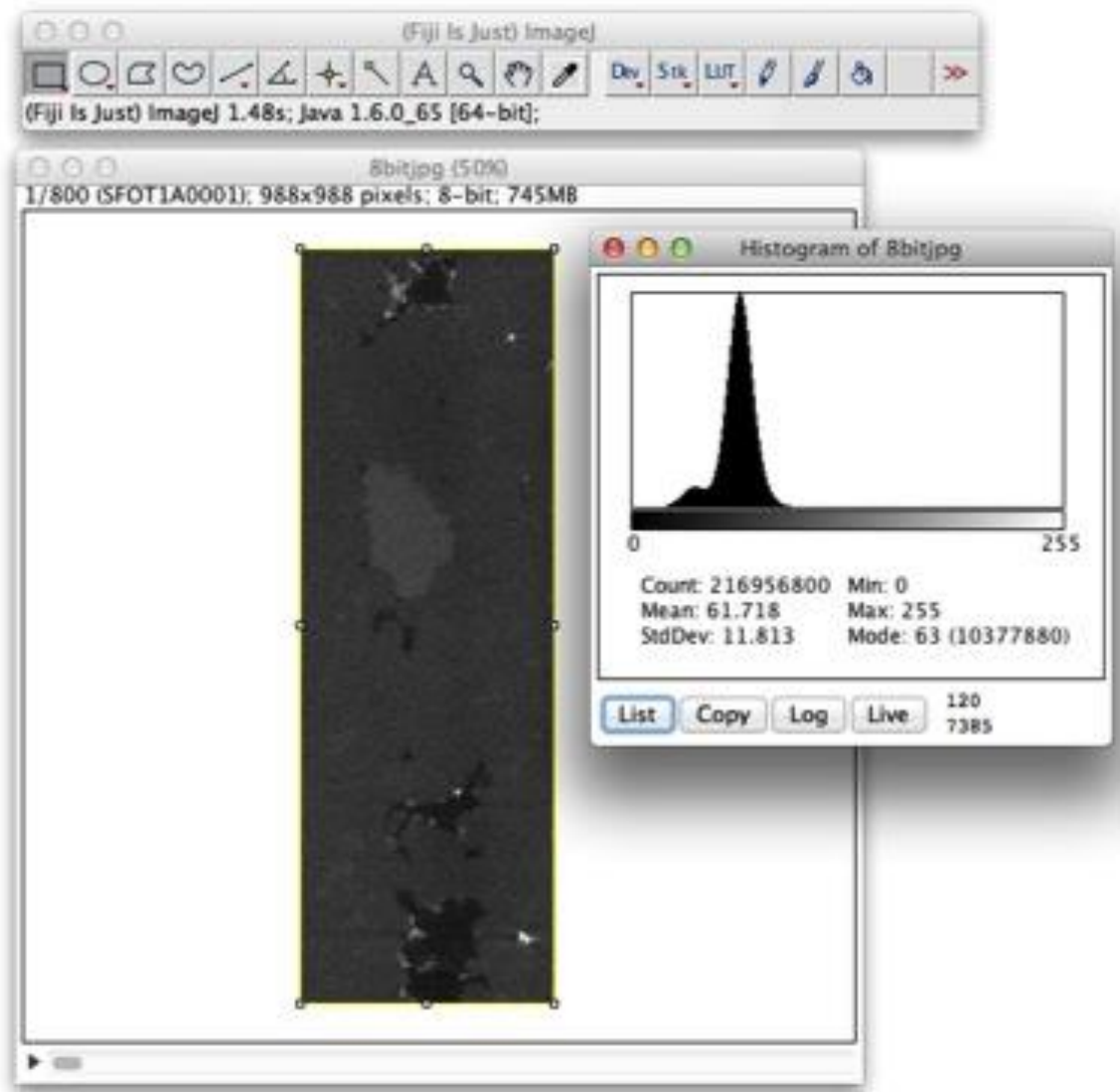


Figure A.5: Histogram of the 800 image slices.

Medial axis extraction and tortuosity analysis in 3DMA-Rock

3DMA-Rock is a command-line based software package for analyzing the pore space in three- (and two-) dimensional X-ray computed microtomographic (XCMT) images of rock. With the indicator kriging thresholds from Imagej, we can proceed with the segmentation. Below is a sample input file used in 3DMA:

Case 1.5: Image segmentation via kriging:

Input Data Options

- tomographic data (1)
- segmented data (2)
- burn data (3)
- medial axis data (4)
- throat data (5)
- pore-throat network data (6)
- fluid data (7)
- lattice Boltzmann simulation (8)

Enter choice: 1

Data Processing Options

- plot image (1)
- intensity dist'n (pdf), cdf, binormal fit (2)
- resize tomographic data (3)
- generate circular fiducial polygon (4)
- segment data (5)
- image magnification (6)

Enter choice: 5

Segment by

- simple threshold (smpl)
- anisotropic diffusion (dfn)
- indicator kriging (krig)
- Mardia-Hainsworth (mh)
- color values (hls)

Enter choice: krig

The tomographic data file is a

- raw data file (raw)
- partially diffused data file (dfn)

Enter choice: raw

Tomographic data slices are contained in
separate files (slc)
a single file (vol)

Enter file type (slc,vol): vol

Recognized tomographic data file types are

ascii integer array (ai)
binary integer array (bi)
swapped binary integer array (sbi)
binary short integer array (bs)
swapped binary short array (sbs)
binary unsigned char array (ubc)
bmp (bmp)
Bio-Rad pic files (pic)
IDL(CFD_V1) files (cfd1)
IDL(CFD_V2) files (cfd2)
multi-tiff (mtif)

Enter data type (ai,bi,sbi,bs,sbs,ubc,bmp,pic,cfd1,cfd2,mtif,re): ubc

Tomographic file has header? (y,n(dflt)): n

Enter basename for tomographic file(s): ../tomog/resized.raw

Are file(s) compressed? [y,n]: n

Enter first and last slice of data to use: 1 471

Slice size of data, (nx,ny): 320 320

Fiducial polygon generation

NONE (N)

MANUALLY set (M)

Enter method: N

Select computational dimension

3d (by volume) (v)

2d (by slice) (s)

Enter choice [v,s(dflt)]: v

Enter basename for segmented file(s): ../seg/data

covariance/semivariogram information

Available methods for estimating data correlations

Classical semivariogram (v)

Classical covariance (c)
Moving window semivariogram (m)
Enter choice (v,c,m): m

Available directions for estimating correlations
vertical (v)
horizontal (h)
isotropic (i)
Enter choice (v,h,i): h

Available correlation output formats
covariance (c)
semi_variogram (v)
Enter choice (c,v): v

Available methods for thresholding data are by
Entropy function (e)
Binormal mixing (m)
User specified (u)
Enter choice (e,m,u): u

Enter void and material cut-off values: 80 100

Merge histogram files of variogram image (y,n(dflt)): n

Enter the title for histogram: blah

Enter the data label for histogram: blah

Prepare raster files of kriging action on image (y,n(dflt)): y

Prepare raster files of final segmented image (y,n(dflt)): n

Enter voxel length in physical units: 3.16

No segmentation is perfect, hence some clean up is necessary after running case1.5. To remove small isolate phase blobs, case 2.3 and 2.4 are needed. Case 2.3 provides a text printout of the distribution of isolated blob sizes. Note that in the output of case 2.3, the word “pore” refers to phase 0 voxels, while the word “grain” refers to phase

1. In case 2.4, all isolated rock and pore blobs are converted to the opposite phase. While isolated pore spaces may be real in some rocks, they are unimportant in this work because they certainly cut off from fluid flow.

Case 2.3: post-segmentation clean up (1):

Input Data Options

- tomographic data (1)
- segmented data (2)
- burn data (3)
- medial axis data (4)
- throat data (5)
- pore-throat network data (6)
- fluid data (7)
- lattice Boltzmann simulation (8)

Enter choice: 2

Data Processing Options

- plot image (1)
- resize data (2)
- disconnected volume distribution (3)
- clean up segmented files (4)
- burn and compute LKC medial axis/surface (5)
- moment of inertia of disconnected components (6)
- convert data to/from ascii format (7)
- 2-point covariance function (8)
- tomographic/segmented data covariance comparison (9)
- set fiducial polygon exterior to grain phase (10)
- overlay segmented and tomographic images (11)
- pore erosion connectivity analysis (12)
- directional erosion connectivity analysis (13)
- seal image volume (14)
- convert to/from segmented slice/volume file formats (15)
- image magnification/coarsening (16)
- create hexagonal sphere pack segmented image (17)
- L2 distance based burn (18)
- estimate shifted overlay of seg images (19)
- estimate rotated overlay of seg images (20)
- segmented files intersection (21)
- convert ubc seg'd data to/from 3DMA format (22)
- pointwise porosity variation (23)

Enter choice: 3

There are two methods of obtaining disconnected volumes
erosion (smaller memory requirement, does both phases) (e)
tree search (faster, does one phase only) (t)

Enter choice [e(dflt),t]: e

Enter basename for segmented volume file(s): ../seg/data_resize

Are file(s) compressed? [y,n]: y

Enter first and last slice of data to use: 1 471

Input data can be inverted to compute burn/medial axis of
grain space rather than void space.

Invert data (y,n(dflt))?: n

Fiducial polygon generation methods

NONE (N)

MANUAL (M)

AUTOMATIC (A)

Enter method: N

Enter basename for disconnected volumes histogram file(s): /tmp/trash

Enter title for histogram: k

Ignore components that touch the exterior? (y,n(dflt)): n

Case 2.4, also provides the ability to “smooth” the void/grain interfaces by reducing the number of dead-ends that may result from small interface irregularities, and the elimination of “1-voxel wide pore channels” running between grains that may result from segmentation/digitization artifacts.

Case 2.4: post-segmentation clean up (2):

Input Data Options

tomographic data (1)

segmented data (2)

burn data (3)

medial axis data (4)

throat data (5)

pore-throat network data (6)
fluid data (7)
lattice Boltzmann simulation (8)
Enter choice: 2

Data Processing Options

plot image (1)
resize data (2)
disconnected volume distribution (3)
clean up segmented files (4)
burn and compute LKC medial axis/surface (5)
moment of inertia of disconnected components (6)
convert data to/from ascii format (7)
2-point covariance function (8)
tomographic/segmented data covariance comparison (9)
set fiducial polygon exterior to grain phase (10)
overlay segmented and tomographic images (11)
pore erosion connectivity analysis (12)
directional erosion connectivity analysis (13)
seal image volume (14)
convert to/from segmented slice/volume file formats (15)
image magnification/coarsening (16)
create hexagonal sphere pack segmented image (17)
L2 distance based burn (18)
estimate shifted overlay of seg images (19)
estimate rotated overlay of seg images (20)
segmented files intersection (21)
convert ubc seg'd data to/from 3DMA format (22)
pointwise porosity variation (23)

Enter choice: 4

Enter basename for input segmented volume file(s): ../seg/data

Are file(s) compressed? [y,n]: y

Enter first and last slice of data to use: 1 471

Input data can be inverted to compute burn/medial axis of
grain space rather than void space.

Invert data (y,n(dflt))?: n

Apply morphological closure operation to grain space? (y,n(dflt)): n

Fiducial polygon generation methods

NONE (N)

MANUAL (M)
AUTOMATIC (A)
Enter method: N

Correct for ring artifacts? (y,n(dflt)): n

The material/void boundary can be lightly smoothed.

Available options are

0) no conversion

or convert those boundary voxels having

1) exactly one neighbor of the same type

2) less than a majority of neighbors of the same type

Enter choice (0(dflt),1,2): 0

Isolated clusters of grain and/or pore voxels up to a specified size
can be assumed to be misidentified and converted to the opposite material type.

Convert isolated grain clusters? (y,n): y

Enter maximum allowed size (number of voxels)

for convertible isolated grain cluster: 1000

Convert isolated pore clusters? (y,n): y

Enter maximum allowed size (number of voxels)

for convertible isolated pore cluster: 120000

Enter basename for output segmented file(s): ../c_seg/data

Are file(s) to be compressed? [y,n]: y

Prepare raster files of corrected segmented image (y,n(dflt)): n

We can construct medial axis in case 2.5. Processed segmented files from case 2.4 are used to compute the medial axis of the pore space using the LKC algorithm (Lee, Kashyap and Chu, 1994). Additionally, a “burn” or “erosion” number (i.e. an integer distance value) is associated with each pore voxel. The burn number is the maximum norm distance from the pore voxel to the closest grain voxel in units of voxel (for instance, a pore voxel sharing a face with a grain voxel has a burn number of 1 while the layer of grain voxel bordering the pore space have a burn number of 0).

Case 2.5: Medial axis construction:

Input Data Options

- tomographic data (1)
- segmented data (2)
- burn data (3)
- medial axis data (4)
- throat data (5)
- pore-throat network data (6)
- fluid data (7)
- lattice Boltzmann simulation (8)

Enter choice: 2

Data Processing Options

- plot image (1)
- resize data (2)
- disconnected volume distribution (3)
- clean up segmented files (4)
- burn and compute LKC medial axis/surface (5)
- moment of inertia of disconnected components (6)
- convert data to/from ascii format (7)
- 2-point covariance function (8)
- tomographic/segmented data covariance comparison (9)
- set fiducial polygon exterior to grain phase (10)
- overlay segmented and tomographic images (11)
- pore erosion connectivity analysis (12)
- directional erosion connectivity analysis (13)
- seal image volume (14)
- convert to/from segmented slice/volume file formats (15)
- image magnification/coarsening (16)
- create hexagonal sphere pack segmented image (17)
- L2 distance based burn (18)
- estimate shifted overlay of seg images (19)
- estimate rotated overlay of seg images (20)
- segmented files intersection (21)
- convert ubc seg'd data to/from 3DMA format (22)
- pointwise porosity variation (23)

Enter choice: 5

LKC computation of

- 0) medial axis
- 1) medial surface

Specify request (0,1): 0

Methods for handling the medial surface/axis computation at the fiducial polygon or volume edges. We recognize two possibilities for the region exterior to the edge, either i) it is of material type opposite to that for which we are constructing the medial axis or ii) the composition of the exterior is unknowable. For case ii) edges we implement `absorbing' boundary conditions.

Current options for treating edges are

- 0) all edges are case i) [original LKC algorithm]
- 1) all edges are case ii)
- 2) top/bottom slice are case ii), all other edges are case i)

Specify choice [0,1,2]: 1

Methods for examining/deleting voxels during erosion

- 1) examine/delete during each of the six directional sweeps
[original LKC algorithm].
- 2) delete only after all six directional examination sweeps done.

Specify choice [1,2]: 1

Specify thinning connectivity [6,26(dflt)]: 26

Enter basename for segmented volume file(s): ../c_seg/data_rotated

Are file(s) compressed? [y,n]: y

Enter first and last slice of data to use: 1 285

The material/void boundary can be lightly smoothed.

Available options are

- 0) no conversion

or convert those boundary voxels having

- 1) exactly one neighbor of the same type
- 2) less than a majority of neighbors of the same type

Enter choice (0(dflt),1,2): 0

Isolated clusters of grain and/or pore voxels up to a specified size can be assumed to be misidentified and converted to the opposite material type.

Convert isolated grain clusters? (y,n): n

Convert isolated pore clusters? (y,n): n

Input data can be inverted to compute burn/medial axis of grain space rather than void space.

Invert data (y,n(dflt))?: n

Exclude the first or last slices to compensate for lack of information beyond the end slices?

[(n)one, (f)irst, (l)ast, (b)oth]: n

Enter basename for burned file(s): ../burn/data
Are file(s) to be compressed? [y,n]: y

Fiducial polygon generation methods

NONE (N)
MANUAL (M)
AUTOMATIC (A)

Enter method: N

Using the medial axis, we can compute the tortuosity of the pore space pathways

(as described by medial axis), however the medial axis needs to be trimmed first. The medial axis algorithm is sensitive to surface noise, which results in dead-end paths that have no relevance to the geometrical features being investigated. The dead end paths have to be removed before the axis is used for the tortuosity computation. Case 4.10 is used for trimming the medial axis.

Case 4.10: Medial axis trimming:

Input Data Options

tomographic data (1)
segmented data (2)
burn data (3)
medial axis data (4)
throat data (5)
pore-throat network data (6)
fluid data (7)
lattice Boltzmann simulation (8)

Enter choice: 4

Data Processing Options

plot MA (1)
plot MA with MS (2)
convert MS files to segmented file type (3)
histogram and fit pore MA burn data (4)
embed search tree(s) (5)
shortest paths (6)
min cut/max flow (7)
convert data to/from ascii format (8)
convert MA list to/from node/path formats (9)

modify MA (10)
histogram MA info (11)
throat calculation (12)
convert to graph format (13)
reconstruct burn layers (14)
MA path curvature and torsion (15)
maximal balls algorithm (16)
unpad MA cluster/path files (17)

Enter choice: 10

Files assumed to be labelled `basename.ext`,
`basename` is limited to 255 characters maximum,
`ext` is a numerical designator lying between 000 and 999
It is assumed that the files have consecutively numbered extensions
ie. 000 -> 056, or 021 -> 049

Enter basename for Medial structure file(s): `../ma/data`
Are file(s) compressed? [y,n]: y

Enter basename for burn file(s): `../burn/data`
Are file(s) compressed? [y,n]: y

Resize information selection.
NOTE, row and column numbers begin from 0

For each slice,
enter first and last column of data to use (x-dir): 0 284
enter first and last row of data to use (y-dir): 0 149

enter first and last slice of data to use (z-dir): 1 285
Trim medial structure voxels on volume edges? (y,n(dflt)): n

Medial axis clean up control menu

Maximum burn number on medial axis is 36

Remove isolated voxels (y,n(dflt)): y
Remove isolated voxels having burn number less than: 30

Remove isolated paths (y,n(dflt)): y
Remove isolated paths having length less than: 1000

Remove branch-leaf paths (y,n(dflt)): y

Retain branch-leaf paths exiting through boundary? (y,n(dflt)): y

branch-leaf path removal criteria

Remove path if length less than
maximum cluster burn number (auto)
user specified tolerance (user)

Enter choice [a(dflt),u]: u

Enter tolerance length: 1000

Remove needle-eye paths (y,n(dflt)): y

needle-eye path removal criteria

Remove path if length less than
maximum cluster burn number (auto)
user specified tolerance (user)

Enter choice [a(dflt),u]: u

Enter tolerance length: 1000

Surface Remnant clean up

Reduce surface remnant structure where possible (y,n(dflt)): y

Enter voxel length in physical units: 3.16

Specify output medial axis data format

voxel location list only (v)
cluster/path format (cp)
graph node/path format (g)

Enter format (v,cp,g): cp

Merge close clusters? (y,n(dflt)): y

Select the criterion for merging clusters.

Two clusters will be merged if they are separated by a path

- a) having length (measured in voxels) less than the maximum burn number at either end of the path + 2
- b) having minimum interior burn number greater than or equal to the minimum burn number at either end
- c) having length (measured in voxels) less than a value specified by the user.

OR

- d) Merge clusters according to maximal ball criteria.
(Silin/Patzek, 2003., SPE paper 84296)

Specify criterion (a(dflt),b,c,d): a

Enter basename for singlet loc/burn file(s): ../ma_t/cp_sngl
Enter basename for cluster/path loc/burn file(s): ../ma_t/cp_loc
Enter basename for cluster/path structure file(s): ../ma_t/cp_struct
Are file(s) to be compressed? [y,n]: y

Once the trimming is successfully completed, the medial axis can be plotted. Case

4.1 plots the medial axis in color. The color spectrum provides information on the burn number distribution along the medial axis with small burn numbers being red and large burn numbers being blue/violet (for the absolute value in terms of voxel lengths that corresponds to these colors, one can refer to the case 4.10 output file). I use Geomview (<http://www.geomview.org>) for plotting hence case 4.1 the 3D Geomview option.

Case 4.1: Medial axis plotting:

Input Data Options

- tomographic data (1)
- segmented data (2)
- burn data (3)
- medial axis data (4)
- throat data (5)
- pore-throat network data (6)
- fluid data (7)
- lattice Boltzmann simulation (8)

Enter choice: 4

Data Processing Options

- plot MA (1)
- plot MA with MS (2)
- convert MS files to segmented file type (3)
- histogram and fit pore MA burn data (4)
- embed search tree(s) (5)
- shortest paths (6)
- min cut/max flow (7)
- convert data to/from ascii format (8)
- convert MA list to/from node/path formats (9)
- modify MA (10)
- histogram MA info (11)
- throat calculation (12)
- convert to graph format (13)

reconstruct burn layers (14)
MA path curvature and torsion (15)
maximal balls algorithm (16)
unpad MA cluster/path files (17)

Enter choice: 1

Image format options

SUN rasterfile(2D) (1)
Inventor(3D) (2)
Geomview(3D) (3)
Open_GL(3D) (4)
IBM Explorer(3D) (5)
Bio-Rad (3D) (6)

Enter choice: 3

Medial Axis Geomview output options

complete axis (ma)
branch clusters (cl)

Enter choice: ma

Specify input medial axis data format

voxel location list only (v)
cluster/path format (cp)

Enter format (v,cp): cp

Enter basename for singlet loc/burn file(s): ../ma_t/cp_sngl

Enter basename for cluster/path loc/burn file(s): ../ma_t/cp_loc

Are file(s) compressed? [y,n]: y

Enter beginning and ending file numbers (zs,ze) used to produce the medial axis:

1 320

Resize information selection.

NOTE, row and column numbers begin from 0

For each slice,

enter first and last column of data to use (x-dir): 0 470

enter first and last row of data to use (y-dir): 0 199

enter first and last slice of data to use (z-dir): 1 320

Trim medial axis voxels on volume edges? (y,n(dflt)): y

Add grains? (y,n): n

Enter basename for burn file(s): ../burn/data

Are file(s) compressed? [y,n]: y

10799 ma voxels in the sample
601 pma voxels removed due to trimming
burn numbers encountered, min 1 max 36

A rainbow colormap may be used for coloring MA voxels according to their burn numbers.

Use rainbow coloring? (y/n(dflt)): y
Enter basename for Geomview file(s): ../plots/ma

After computing (and trimming) the medial axis for the pore space inside a rectangular bounding box, we can compute the tortuosity of the paths through the medial axis. However, since the medial axis was computed in cluster/path format in case 4.1, we need to convert the medial axis list to/from node/path format using case 4.9.

Case 4.9: Conversion from cluster-path to voxel-based medial axis file formats:

Input Data Options

- tomographic data (1)
- segmented data (2)
- burn data (3)
- medial axis data (4)
- throat data (5)
- pore-throat network data (6)
- fluid data (7)
- lattice Boltzmann simulation (8)

Enter choice: 4

Data Processing Options

- plot MA (1)
- plot MA with MS (2)
- convert MS files to segmented file type (3)
- histogram and fit pore MA burn data (4)
- embed search tree(s) (5)
- shortest paths (6)
- min cut/max flow (7)
- convert data to/from ascii format (8)
- convert MA list to/from node/path formats (9)

modify MA (10)
histogram MA info (11)
throat calculation (12)
convert to graph format (13)
reconstruct burn layers (14)
MA path curvature and torsion (15)
maximal balls algorithm (16)
unpad MA cluster/path files (17)
Enter choice: 9

Specify input medial axis data format
voxel location list only (v)
cluster/path format (cp)
Enter format (v,cp): cp

Enter basename for singlet loc/burn file(s): ../ma_t/cp_sngl
Enter basename for cluster/path loc/burn file(s): ../ma_t/cp_loc
Are file(s) compressed? [y,n]: y

Enter beginning and ending file numbers used to produce the medial axis (zs,ze):
1 320
Enter basename for voxel location list style file(s): ../ma_t/data
Are file(s) to be compressed? [y,n]: y

Finally, we can compute the geometric tortuosity in the x-, y- and z- direction
between all possible entrance/exit voxel pairs on the medial axis network.

Case4.6: Geometrical tortuosity for shortest paths through the medial axis:

Input Data Options
tomographic data (1)
segmented data (2)
burn data (3)
medial axis data (4)
throat data (5)
pore-throat network data (6)
fluid data (7)
lattice Boltzmann simulation (8)
Enter choice: 4

Data Processing Options
plot MA (1)

plot MA with MS (2)
convert MS files to segmented file type (3)
histogram and fit pore MA burn data (4)
embed search tree(s) (5)
shortest paths (6)
min cut/max flow (7)
convert data to/from ascii format (8)
convert MA list to/from node/path formats (9)
modify MA (10)
histogram MA info (11)
throat calculation (12)
convert to graph format (13)
reconstruct burn layers (14)
MA path curvature and torsion (15)
maximal balls algorithm (16)
unpad MA cluster/path files (17)

Enter choice: 6

Files assumed to be labelled `basename.ext`,
`basename` is limited to 255 characters maximum,
`ext` is a numerical designator lying between 000 and 999
It is assumed that the files have consecutively numbered extensions
ie. 000 -> 056, or 021 -> 049

Enter basename for voxel location list file(s): `../ma_t/data`
Are file(s) compressed? [y,n]: y

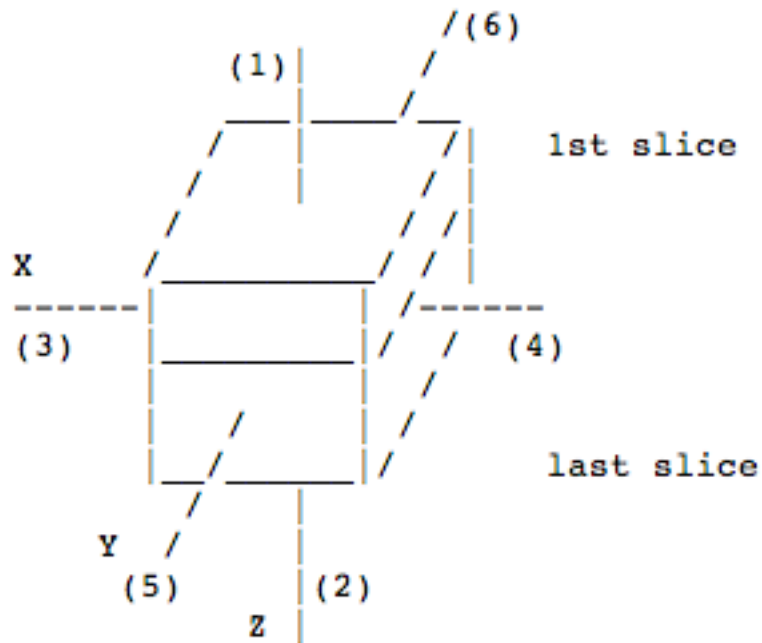
Resize information selection.
NOTE, row and column numbers begin from 0

For each slice,
enter first and last column of data to use (x-dir): 0 470
enter first and last row of data to use (y-dir): 0 199

enter first and last slice of data to use (z-dir): 1 320
Number of voxels in volume 377055312
Number of medial axis voxels 10799

Do you want to trim the data? (y,n(dflt)): n
Do you want 6 or 26 connectivity: 26

Dijkstra shortest path computations
Labelling of cube faces



Enter start face (1 -> 6): 3

Enter end face (1 -> 6, except 3): 4

5 Starting side 1 MA locations

478 Ending side 2 MA locations

By default all nodes on starting face are used in the Dijkstra calculation.
If only a subrange of nodes are to be used, enter `r':

Viewing options

Print information on NBHD_LIST (l)

Print Geomview data for viewing (g)

Print jgraph data for viewing (2-D data only) (j)

Print as medial axis data file (r)

None of above (n)

Enter choice? (l,g,v,j,r,n): g

Request magnification of the view of the shortest paths in the X direction?
(y,n(dflt)): n

Enter basename for writing absolute shortest path for Geomview file(s):
../plots/tort_x_abs

Enter basename for writing all shortest paths for Geomview file(s):
../plots/tort_x_all
Enter basename for face-to-face tortuosity distribution file(s): ../results/tort_x
Enter data identifier for all histograms: Torridonian sample

Set binning for tortuosity histogram
number of bins (c)
bin width (w)
Enter choice: w

Specify bin width to be used: 0.05

With the computed geometrical tortuosities, I plot the cumulative distribution function (cdf) plot of the shortest paths.

MODELING OF FLUID FLOW IN IMAGED POROUS MEDIA

Capillary dominated fluid displacement in LSMPQS

With the segmented 3DMA data files, we can simulate capillary dominated (drainage and imbibition) flow through the medium. The cleaned segmented file from case2.4 serves as the input for LSMPQS. Since we simulating flow through the fracture, the segmented file needs to be rotated so that the z-direction becomes x-direction (LSMPQS is developed to simulate flow in the x-direction). This can be done with:

```
rotate_data_array s data_in data_out 0
```

Below is a sample input file for drainage:

```
email adenike@utexas.edu % Email address for notifications
geom_type seg_data % Geometry type
geom_fname ../c_seg/data_rotated.gz % File name and location
dx 0.05 % x-direction grid spacing
a 0.05 % Motion in the normal direction
b 0.05 % Motion by mean curvature
ic_pos 30 % Position of the initial condition
compute_a_entry 0 % Compute entry pressure, 1 or not, 0
vol_frac_target 0.5 % Volume fraction for constant
%compressible model
do_seal 1 % Seal volume sides – all, 2, orthogonal to
%flow, 1, or none, 0.
narrow_band 1 %apply narrow banding, 1, or not, 0.
dc 0.5 %curvature increment (or decrement, if
% negative) by 0.5
stop_touch 0 %stop when opposite boundary is touched,
% 1, or not, 0.
tmax 200 % Maximum run time allowed
do_trap_w 1 % Enable Wetting phase trapping, 1, or
% not, 0
checkpoint 1 % Output data files at every step,
% necessary for re-starting runs.
```

The file can be executed by typing the following on the Linux command prompt:

➤ *drain input_file_name*

Once the drainage run is completed, we can start the imbibition run. The imbibition input file is set up to start from the end (last step) of drainage. Below is a sample input file:

email	adenike@utexas.edu	
dx	0.05	% x-direction grid spacing, should be % be the same as in drainage
b	0.05	% Motion by mean curvature
narrow_band	1	% Apply narrow banding, 1, or not, 0
dc	-0.16	% Curvature decrement
tmax	200	% Maximum run time allowed
init_trap_w	1	% Initiate trapped wetting phase % from file, 1, or not, 0.
trap_w_phase_fname	data_step8_trap_w.gz	% Trapped wetting phase input data
do_trap_nw	1	% Enable Non-wetting phase % trapping 1, or not, 0.
checkpoint	1	% Output data files at every step, % necessary for re-starting runs.

The file can be executed with:

> *imbibe input_imbibe_filename*

Once the simulation is complete, several binary data files will be created in the directory: mask.gz (masking level set function), data_init.gz (initial non-wetting phase), and data_stepSTEP_ID.gz (non-wetting phase for each step of the simulation, one dimensional data arrays: a.gz, curvature.gz, vol_frac.gz that contain pressure term (a), curvature (a/b) and volume fraction of the non-wetting phase (relative to the available pore space) for each step of the simulation; and a text file, out_file containing information about the simulation (options, grid information and the log for each step).

For more details on LSMPQS and the visualization functions, see the LSMPQS software manual (Prodanović, 2009).

Tortuosity of fluid phases in 3DMA

In addition to computing the tortuosity of the pore space, I also studied the tortuosity of the individual fluid phases. I did this by calculating the geometric tortuosity of each of the drainage and imbibition steps. Using a perl scripts:

For the *Non-wetting phase*:

```
# File: create_MA_files_simulation.pl
# To run:
# perl create_MA_files_simulation.pl
#     # Or change file to executable ('chmod +x') and run like
#     # ./create_MA_files_simulation.pl
#
# Converts simulation data files (NW phase) to segmented type and runs
# 3DMA medial axis code on it.
# Knowledge of NX, NY, NZ (array size) for input data is required beforehand.
# Requires 'rpl'

# Run from the simulation directory. Subdirectory ma/ is created.

# Visualization is done in Geomview, available in ma/Geomview/.

##### Modify information here:
$start_step = 1;
$end_step = 14;
$NX = 306;
$NY = 206;
$NZ = 306;
$email_address = "adenike.tokanlawal@gmail.com";

$target_directory =
"/disk1/tadenike/Data/PeterEichhubl/Monterey_new/Tortuosity/drainage/NonWetting";
#$lsmpqs_vis_dir =
"/disk1/tadenike/Data/PeterEichhubl/NLQ/100/LsmpqsData/permeability/imbibition";
```

```

$lmpqs_data = "/disk1/tadenike/Data/PeterEichhubl/Monterey_new/LsmpqsData/";
$templates_directory = "/disk1/tadenike/Data/Scripts/Template/medial_axis";

####

$NX1 = $NX - 1;
$NY1 = $NY - 1;

system "cd $target_directory";
system "mkdir $target_directory/ma";
system "mkdir $target_directory/ma/Geomview";

for ($num_step=$start_step; $num_step <=$end_step; $num_step++)
{
  # create a separate directory for this step
  system "cd $target_directory/ma; mkdir $target_directory/ma/step$num_step";

  # create subdirectories to keep 3DMA files in order
  system "cd $target_directory/ma/step$num_step; mkdir burn cases seg ma ma_t results
plots";

  # convert NW phase to segmented data
  system          "data_array2seg          $lmpqs_data/data_step$num_step.gz
$target_directory/ma/step$num_step/seg/data";

  # copy 3DMA input file templates
  system "cp $templates_directory/case*in $target_directory/ma/step$num_step/cases/.";
  system "rpl NX1 $NX1 $target_directory/ma/step$num_step/cases/case*in";
  system "rpl NY1 $NY1 $target_directory/ma/step$num_step/cases/case*in";
  system "rpl NZ $NZ $target_directory/ma/step$num_step/cases/case*in";

  #run 3DMA
  system "cd $target_directory/ma/step$num_step/cases/; runcases linux 2.5 4.10 4.1 4.9
4.6x";

  #move files to visualization directory
  #system "mv ma/step$num_step/ma_t/ma.list ma/geomview/ma_step$num_step.list";
  #system          "cp          $lmpqs_vis_dir/geomview_templates/template.list
ma/geomview/view_d$num_step.list";
  #system "rpl tmp1 ma_step$num_step ma/geomview/view_d$num_step.list";
}

```

```
#send an email that all is done...
system "pwd > email.txt";
system "mail -s medial-axis-done $email_address < email.txt";
system "/bin/rm -f email.txt";
```

For the *Wetting Phase*:

```
# File: create_MA_files_simulation_wetting.pl
# Author(s): Adenike Tokan-Lawal
#
# To run:
# perl create_MA_files_simulation_wetting.pl
# Or change file to executable ('chmod +x') and run like
./create_MA_files_simulation.pl
#
# Converts simulation data files (W phase) to segmented type and runs
# 3DMA medial axis code on it.
# Knowledge of NX, NY, NZ (array size) for input data is required beforehand.
# Requires 'rpl'

# Run from the simulation directory. Subdirectory ma/ is created.

# Visualization is done in Geomview, available in ma/Geomview/.

#### Modify information here:
$start_step = 1;
$end_step = 22;
$NX = 250;
$NY = 250;
$NZ = 300;
$email_address = "adenike.tokanlawal@gmail.com";

$send_nw_zip = ".gz";
$send_w_zip = "_w.gz";
$send_w = "_w";

$target_directory =
"/disk1/tadenike/Data/Fracture/Fracture_xyz/Lsmpqsdata/tortuosity/drainage";
$simulation_directory = "/disk1/tadenike/Data/Fracture/Fracture_xyz/Lsmpqsdata";
#$lsmpqs_vis_dir = "/home/masha/svn/lsmpqs/trunk/src/visualization/";
#$templates_directory = "/home/masha/Code/3dma_rock/template/";
$templates_directory = "/disk1/tadenike/Data/Scripts/Template/medial_axis";
```



```

####

$NX1 = $NX - 1;
$NY1 = $NY - 1;

system "cd $target_directory";
system "pwd";
system "mkdir $target_directory/ma_w";
system "mkdir $target_directory/ma_w/geomview";

for ($num_step=$start_step; $num_step <=$end_step; $num_step++)
{
    # create a separate directory for this step
    system "mkdir $target_directory/ma_w/step$num_step";

    # create subdirectories to keep 3DMA files in order
    system "cd $target_directory/ma_w/step$num_step; mkdir burn cases seg ma ma_t
results plots";

    # create W phase file
    system "cd $target_directory/ma_w/step$num_step; reverse_phases
$simulation_directory/data_step$num_step$end_nw_zip tmp
$simulation_directory/mask.gz";

    # resize and convert W phase to segmented data
    system "cd $target_directory/ma_w/step$num_step; resize_data_array
$target_directory/ma_w/step$num_step/tmp.gz 3 252 3 252 3 302
$target_directory/ma_w/step$num_step/tmp1";
    system "data_array2seg $target_directory/ma_w/step$num_step/tmp1.gz
$target_directory/ma_w/step$num_step/seg/data";

    # copy 3DMA input file templates
    system "cp $templates_directory/case*in
$target_directory/ma_w/step$num_step/cases/";
    system "rpl NX1 $NX1 $target_directory/ma_w/step$num_step/cases/case*in";
    system "rpl NY1 $NY1 $target_directory/ma_w/step$num_step/cases/case*in";
    system "rpl NZ $NZ $target_directory/ma_w/step$num_step/cases/case*in";
    system "rpl SEGDATA './seg/data'
$target_directory/ma_w/step$num_step/cases/case*in";

    #run 3DMA

```

```
system "cd $target_directory/ma_w/step$num_step/cases/; runcases linux 2.5 4.10 4.1
4.9 4.6x";
```

```
#move files to visualization directory
#system "mv ma_w/step$num_step/ma_t/ma.list
ma_w/geomview/ma_step$num_step.list";
#system "cp $lsmpqs_vis_dir/geomview_templates/template.list
ma_w/geomview/view_d$num_step.list";
#system "rpl tmp1 ma_step$num_step ma/geomview/view_d$num_step.list";
}
```

```
#send an email that all is done...
system "pwd > email.txt";
system "mail -s medial-axis-done $email_address < email.txt";
system "/bin/rm -f email.txt";
system "/bin/rm -f tmp.gz"
```

With the generated case 4.6 output files, one can compute the CDF and statistics on the tortuosity.

Permeability computation with Palabos

First of all, the Palabos software has to be downloaded and installed from the Palabos (2013) website. The permeability code assumes that the input files are .bmp files, hence we will need to convert our segmented data files to something readable by the code. For that, I use matlab scripts. The LSMPQ data are first converted to binary arrays with: *readDataArray.m*

```
%%%%%%%%%%%%%%%%%%%%%%%%%%%%%%%%%%%%%%%%%%%%%%%%%%%%%%%%%%
%%%%%%%%%%%%%%%%%%%%%%%%%%%%%%%%%%%%%%%%%%%%%%%%%%%%%%%%%%
%
% Author: Masa Prodanović
% Copyright: (c) 2009 The University of Texas at Austin. All rights reserved.
%
%%%%%%%%%%%%%%%%%%%%%%%%%%%%%%%%%%%%%%%%%%%%%%%%%%%%%%%%%%
%%%%%%%%%%%%%%%%%%%%%%%%%%%%%%%%%%%%%%%%%%%%%%%%%%%%%%%%%%
%
```

```

% function [data,nx,ny,nz] = readDataArray(filename)
%
% Reads a binary data file which contains 3 binary integers nx, ny, nz
% indicating sizes of the array in each dimension, followed by an array
% of nx*ny*nz single precision real numbers.
%
% Arguments:
% filename - file name
%
% Returns
% data    - data array read from the file
% nx,ny,nz - array dimensions
%
%%%%%%%%%%%%%%%%%%%%%%%%%%%%%%%%%%%%%%%%%%%%%%%%%%%%%%%%%%%%%%%%%%%%%%%%
%%%%%%%%%%%%%%%%%%%%%%%%%%%%%%%%%%%%%%%%%%%%%%%%%%%%%%%%%%%%%%%%%%%%%%%%

function [data,nx,ny,nz] = readDataArray(filename)

data = [];
nx = 0; ny = 0; nz = 0;

[zip,filename1] = checkUnzipFile(filename);

if( exist(filename1,'file') )
    fid = fopen(filename1,'r');
    nx = fread(fid,1,'int');
    ny = fread(fid,1,'int');
    nz = fread(fid,1,'int');

    data = fread(fid,nx*ny*nz,'float');
    data = reshape(data,[nx ny nz]);
    fclose(fid);

    if(zip)
        gzip(filename1); delete(filename1);
    end;
else
    data = [];
    nx = 0; ny = 0; nz = 0;
end

return

```

The absolute permeability can be computed with the *mask.gz*. First, the *mask.gz* needs to be rotated (linux command-line code, part of the LSMPQS/3DMA package) by with:

```
>rotate_data_array mask.gz mask_new 2
```

Once the *mask.gz* is rotated, to flip the x and z directions, we can convert the file to something readable by Palabos:

```
%%%%%%%%%%%%%%%%%%%%%%%%%%%%%%%%%%%%%%%%%%%%%%%%%%%%%%%%%%
%%%%%%%%%%%%%%%%%%%%%%%%%%%%%%%%%%%%%%%%%%%%%%%%%%%%%%%%%%
%
% Author: Adenike Tokan-Lawal
% Copyright: (c) 2014 The University of Texas at Austin. All rights reserved.
%
%%%%%%%%%%%%%%%%%%%%%%%%%%%%%%%%%%%%%%%%%%%%%%%%%%%%%%%%%%
%%%%%%%%%%%%%%%%%%%%%%%%%%%%%%%%%%%%%%%%%%%%%%%%%%%%%%%%%%
%
%function [ raw_filename, dat_outputfilename] = PalabosPermDataFile(mask_filename)
%
% Reads in the mask data, and converts it to a raw file (readable by
% imagej) and a .dat file readable by Palabos
%
% Arguments:
%mask_filename - mask.gz, rotated binary array file from LSMPQS
%
% Returns
% raw_filename - raw data file readable by imagej
% dat_outputfilename - .dat file readable by Palabos
%
%%%%%%%%%%%%%%%%%%%%%%%%%%%%%%%%%%%%%%%%%%%%%%%%%%%%%%%%%%
%%%%%%%%%%%%%%%%%%%%%%%%%%%%%%%%%%%%%%%%%%%%%%%%%%%%%%%%%%
function [ raw_filename, dat_outputfilename] = test_perm(mask_filename)

clear all;
clc;
close all;

if(nargin <1)
```

```

    mask_filename = 'mask.gz';
end
[mask,nx,ny,nz] = readDataArray(mask_filename); %Get the mask data

%data0 = +(mask>0);
%data = +(data1<0);
data0 = +(ceil(mask)) ;
%data0 = data1;

%set default file names for the output
if (nargout<2)
    raw_filename = 'mask_rotated.raw';
    baseOutput = 'mask.dat';
else
    baseOutput = dat_outputfilename;
end

%% Generate raw
fid = fopen(raw_filename, 'w');
fwrite(fid,255*data0,'uint8');
fclose(fid);

%% plot isosurface
p = patch(isosurface(data0,0));
isonormals(data0,p)
set(p,'FaceColor','blue','EdgeColor','none');
daspect([1,1,1])
view(3); axis tight
camlight
lighting gouraud
xlabel('X');
ylabel('Y');
zlabel('Z');

fid = fopen(baseOutput, 'w+');

for i=1:nz

    data_input = data0(:, :, i) ;
    data_input ((data_input==1))=2;

    [data_image]=grow_edge_outward(data_input);

```

```

    if(mod(i,10) ==0)
        figure
        image(30*data_image)
        colorbar
    end

    fprintf(fid, '%i\n', data_image);
end

fclose(fid);
close all

```

With the drainage and imbibition zipped (*.gz) files, we can compute the relative permeability. But first, the files need to be rotated to flip the x- and z- direction. I wrote a Perl script to help with the rotation:

```

##
## Copyright (c) 2014, The University of Texas at Austin. All rights reserved.
##
#
#! /usr/bin/perl
#
# File: rotate_files_Palabos.pl
# Author: Adenike Tokan-Lawal
#
# To run:
# perl rotate_files_Palabos.pl
# Or change file to executable ('chmod +x') and run like ./rotate_files_Palabos.pl
#
# Rotates drainage and imbibition step files from x-y-z
# Rotated files are needed so that Palabos simulation of flow is done in the x-direction
# Requires 'rpl'

##### Modify information here:
$start_step = 2;
$end_step = 14;

$email_address = "adenike.tokanlawal@gmail.com";

$lsmpqs_data

```

=

```

"/disk1/tadenike/Data/PeterEichhubl/NLQ/Cementation/Data9/LsmpqsData/imbibe14_co
rrected";
$target_directory
"/disk1/tadenike/Data/PeterEichhubl/NLQ/Cementation/Data9/LsmpqsData/rotated/imbi
be";

####

for ($num_step=$start_step; $num_step <=$end_step; $num_step++)
{
  # convert NW phase to segmented data
  system "rotate_data_array $lsmpqs_data/data_step$num_step.gz
$target_directory/data_step$num_step 2";
}

#send an email that all is done...
system "pwd > email.txt";
system "mail -s medial-axis-done $email_address < email.txt";
system "/bin/rm -f email.txt";

```

Next, I used a Matlab file to generate the .dat files for Palabos computation:

generate_relperm.m

```

%%%%%%%%%%
%%%%%%%%%%
%
% Author: Adenike Tokan-Lawal
% Copyright: (c) 2014 The University of Texas at Austin. All rights reserved.
%
%%%%%%%%%%
%%%%%%%%%%
%
% function generate_relperm(drainagePath, imbibitionPath, baseInput, numdrainSteps,
numimbibeSteps)
%
% Reads the drainage and imbibition .gz step files, and them to .dat files
% for Palabos processing
%
% Arguments:
% drainagePath - path where the drainage step files are located
% imbibitionPath - path where the imbibition step files are located

```



```

%close all
fprintf('Drainage non-wetting phase step %d completed.\n', j);

data0 = +((mask_data <=0) & (data1 >=0) );
data_w = 1-data0;
baseOutput = strrep(baseInput, '.gz', '_w.dat');
fid = fopen(baseOutput, 'w+');

%% wetting
for i=1:nz
    data_input = data_w(:, :, i) ;
    data_input ((data_input==1))=2;
    [data_image]=grow_edge_outward(data_input);
    fprintf(fid, '%i\n', data_image);
end
fprintf('Drainage wetting phase step %d completed.\n', j);

    fclose(fid);
    num = num2str(j);
    num1 = num2str(j+1);
    baseInput = strrep(baseInput , num, num1);
    close all
end %end for j

fprintf('Drainage runs completed.\n');

%% Imbibition
cd(imbibitionPath);
num = num2str(1);
num1 = num2str(2);
%num1 = num2str(15);
baseInput_imbibe = strrep(baseInput_imbibe , num, num1);

fprintf('beginning imbibition runs....\n');

for j=2:numimbibeSteps
    %% non-wetting
    [data1,nx,ny,nz] = readDataArray(baseInput_imbibe);
    baseOutput = strrep(baseInput_imbibe, '.gz', '_nw.dat');
    fid = fopen(baseOutput, 'w+');
    data = +((mask_data <= 0) & (data1 < 0)) ;
    data0 = 1-data;

```

```

%% non-wetting phase
for i=1:nz
    data_input = data0(:, :, i) ;
    data_input ((data_input==1))=2;
    [data_image]=grow_edge_outward(data_input);
    fprintf(fid, '%i\n', data_image);
end
fclose(fid);
fprintf('Imbibition non-wetting phase step %d completed.\n', j);

%% wetting phase
baseInput_trap_nw = strrep(baseInput_imbibe, '.gz', '_trap_nw.gz');

if exist(baseInput_trap_nw,'file')
    [trap_nw,nx,ny,nz] = readDataArray(baseInput_trap_nw);
    data2 = +((mask_data <= 0) & (data1 >= 0) &(trap_nw >= 0));
    data_w = 1-data2;
    % data_w = data1;
else
    data2 = +((mask_data <=0) & (data1 >=0) );
    data_w = 1-data2;
    %data_w = data1;
end

baseOutput = strrep(baseInput_imbibe, '.gz', '_w.dat');
baseRawOutput = strrep(baseInput_imbibe, '.gz', '_w.raw');
fid = fopen(baseOutput, 'w+');

for i=1:nz
    data_input = data_w(:, :, i) ;
    data_input ((data_input==1))=2;
    [data_image]=grow_edge_outward(data_input);
    fprintf(fid, '%i\n', data_image);
end
fclose(fid);
fprintf('Imbibition wetting phase step %d completed.\n', j);
num = num2str(j);
num1 = num2str(j+1);
baseInput_imbibe = strrep(baseInput_imbibe, num, num1);
close all
end %end for j

```

With the input files ready, the Palabos script file can now be set up. I installed

Palabos on one of the *parallel* high-performance systems at TACC, Lonestar. Lonestar works with batch scripts, and below is a sample one I wrote:

```
#!/bin/bash
#$ -V
#$ -cwd                # Start job in submission directory
#$ -N JobName          # Job Name
#$ -e y                # stderr and stout options
#$ -o $JOB_NAME.o$JOB_ID # Name of the output file (eg. myMPI.oJobID)
#$ -pe 12way 24        # Requests 12 tasks/node, 24` cores total
#$ -q normal           # Queue name normal
#$ -l h_rt=24:00:00    # Run time (hh:mm:ss)
#$ -M adenike@utexas.edu # Address for email notification
#$ -m be               # Email at Begin and End of job
#$ -A pge-fracture
set -x                 # Echo commands, use set echo with csh
ibrun PALABOS_DIR DAT_DIR VIS_DIR NX NY NZ deltaP
```

Where,

PALABOS_DIR = Directory where Palabos' permeability.cpp code is located

DAT_DIR = full path of the .dat file

VIS_DIR = Directory where output files should be place

deltaP = Pressure gradient

Table A.1: Location of data files used in this thesis

Sample	Simulation	Machine	File Location
Fractured	3DMA	Vooga	/disk1/tadenike/Data/Fracture/Fracture_xyz
Polyethylene	LSMPQS	Vooga	/disk1/tadenike/Data/Fracture/Fracture_xyz/Lsmpqsdata
	LBM	Lonestar	/work/02059/tadenike/Workspace/Fracture/xyz
Torridonian (Tor1bA)	3DMA	Vooga	/disk1/tadenike/Data/PeterEichhubl/Torridonian/tor1ba/tor1ba_cleaner
	LSMPQS	Vooga	/disk1/tadenike/Data/PeterEichhubl/Torridonian/tor1ba/tor1ba_cleaner/Lsmpqsdata
	LBM	Lonestar	/work/02059/tadenike/Workspace/Torridonian/tor1ba
Torridonian (Tor1bB)	3DMA	Vooga	/disk1/tadenike/Data/PeterEichhubl/Torridonian/tor1bb/tor1bb_tighter
	LSMPQS	Vooga	/disk1/tadenike/Data/PeterEichhubl/Torridonian/tor1bb/tor1bb_tighter/Lsmpqsdata
	LBM	Lonestar	/work/02059/tadenike/Workspace/Torridonian/tor1bb
Travis Peak (TP1)	3DMA	Frattura	/home/tadenike/Data/TravisPeak/TP1
	LSMPQS	Frattura	/home/tadenike/Data/TravisPeak/TP1/LsmpqsData
	LBM	Lonestar	/work/02059/tadenike/Workspace/TravisPeak/TP1
Travis Peak (TP2)	3DMA	Frattura	/home/tadenike/Data/TravisPeak/TP2
	LSMPQS	Frattura	/home/tadenike/Data/TravisPeak/TP2/LsmpqsData

	LBM	Lonestar	/work/02059/tadenike/Workspace/TravisPeak/TP2
Niobrara (Original)	3DMA	Vooga	/disk1/tadenike/Data/PeterEichhubl/NLQ/nx600ny730nz170
	LSMPQS	Vooga	/disk1/tadenike/Data/PeterEichhubl/NLQ/nx600ny730nz170/LsmpqsData
	LBM	Lonestar	/work/02059/tadenike/Workspace/NLQ/Original
Niobrara (Cement 1)	3DMA	Vooga	/disk1/tadenike/Data/PeterEichhubl/NLQ/Cementation/Data5
	LSMPQS	Vooga	/disk1/tadenike/Data/PeterEichhubl/NLQ/Cementation/Data5/LsmpqsData
	LBM	Lonestar	/work/02059/tadenike/Workspace/NLQ/Data5
Niobrara (Cement 2)	3DMA	Vooga	/disk1/tadenike/Data/PeterEichhubl/NLQ/Cementation/Data7
	LSMPQS	Vooga	/disk1/tadenike/Data/PeterEichhubl/NLQ/Cementation/Data7/LsmpqsData
	LBM	Lonestar	/work/02059/tadenike/Workspace/NLQ/Data7
Niobrara (Cement 3)	3DMA	Vooga	/disk1/tadenike/Data/PeterEichhubl/NLQ/Cementation/Data9
	LSMPQS	Vooga	/disk1/tadenike/Data/PeterEichhubl/NLQ/Cementation/Data9/LsmpqsData
	LBM	Lonestar	/work/02059/tadenike/Workspace/NLQ/Data9
Matlab Script files (Vooga): /disk1/tadenike/Data/Scripts			
(Frattura): /home/tadenike/Data/Scripts			

Appendix B: Subsampling in the Niobrara

The Niobrara original sample (Chapter 8) was split into 4 subsamples (i.e. 000, 010, 100 and 110), to see the variation of tortuosity, fluid flow and permeability in the different regions of the sample. The aperture distributions in the subsamples vary with samples 000 and 100 having wider distributions (lesser solid spaces) than 010 and 110 (Figures B.1 - B.4). Zero (0) aperture represents the solid space.

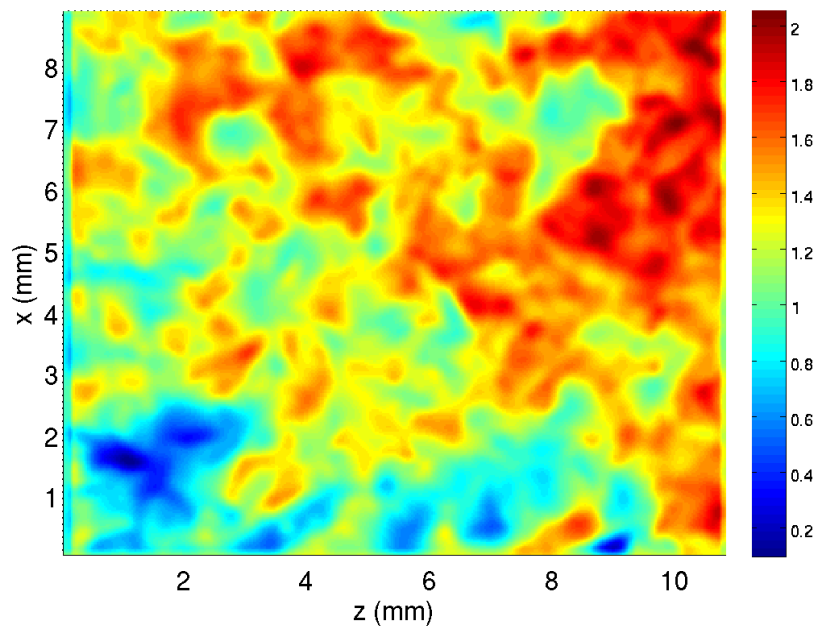


Figure B.1: Aperture field distribution (measured in y-direction) of the 000 Niobrara subsample. The aperture ranges from 0.0990 mm to 2.0550 mm.

The cumulative distribution functions of the Niobrara subsamples are shown in Figure B.5. The tortuosities of the 4 samples are all within the same range, 1-15 – 1.7.

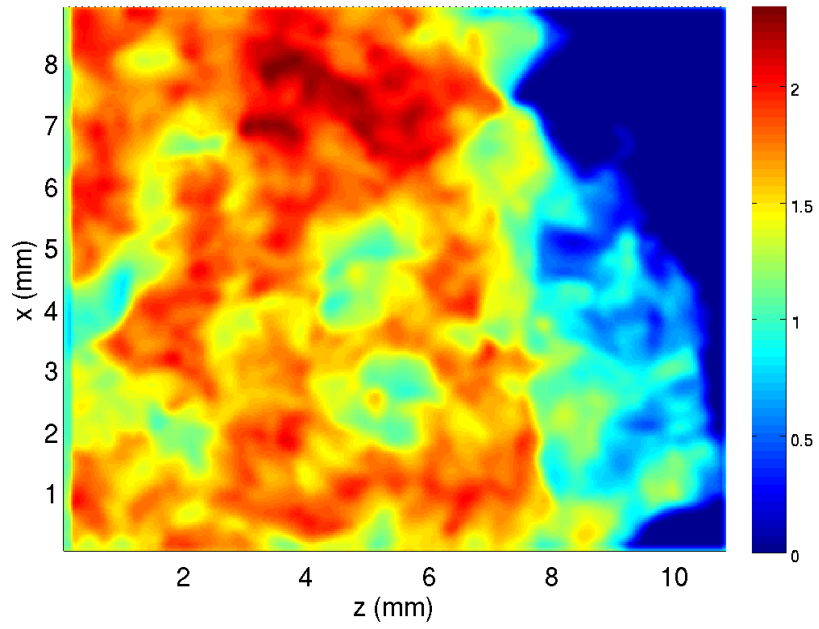


Figure B.2: Aperture field distribution (measured in y-direction) of the 010 Niobrara subsample. The aperture ranges from 0 mm to 2.3456 mm.

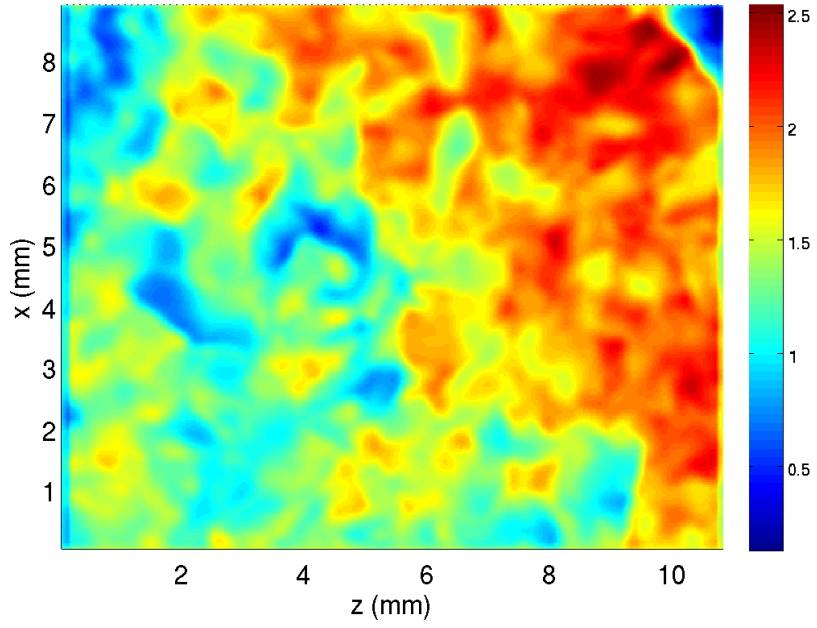


Figure B.3: Aperture field distribution (measured in y-direction) of the 100 Niobrara subsample. The aperture ranges from 0.1303 mm to 2.3456 mm.

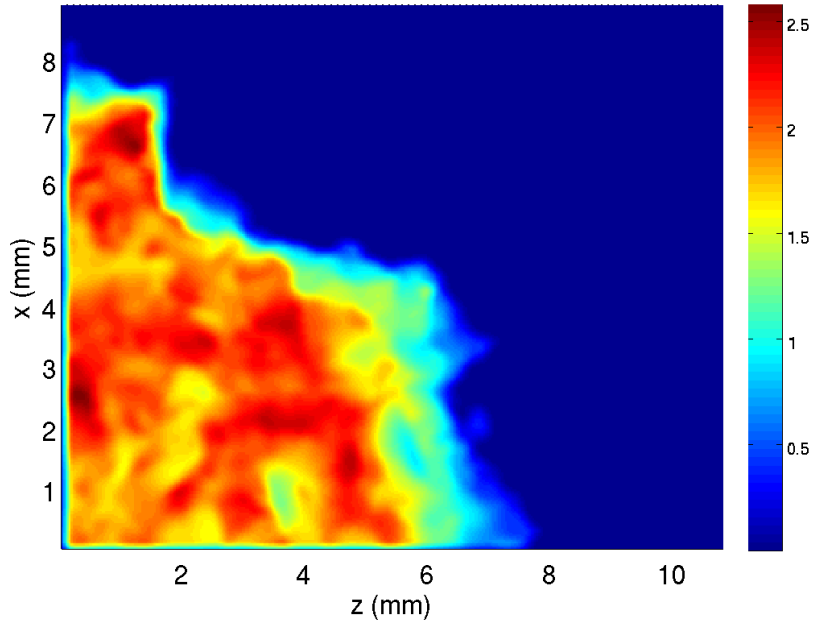


Figure B.4: Aperture field distribution (measured in y-direction) of the 100 Niobrara subsample. The aperture ranges from 0 mm to 2.5816 mm.

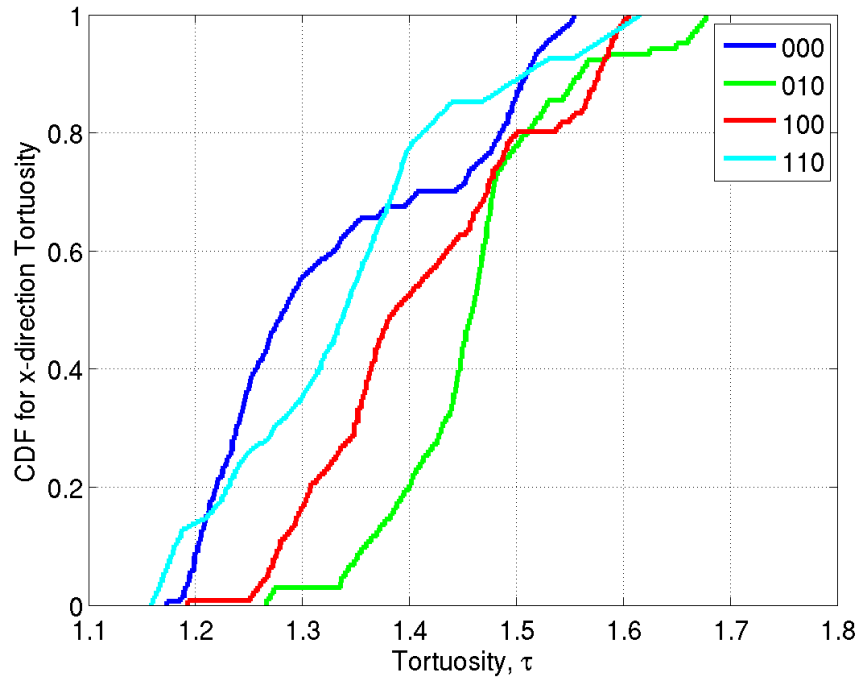


Figure B.5: CDF of x-direction tortuosity in the 4 Niobrara subsamples.

The capillary-dominated flow properties were studied in subsamples (see Figure B.7). The percolation thresholds are observed to be similar in all 4 subsamples. Further, all but sample 100 show that the imbibition starts off following the path of the drainage. In sample 100, the deviation is due to the bypassed wetting phase.

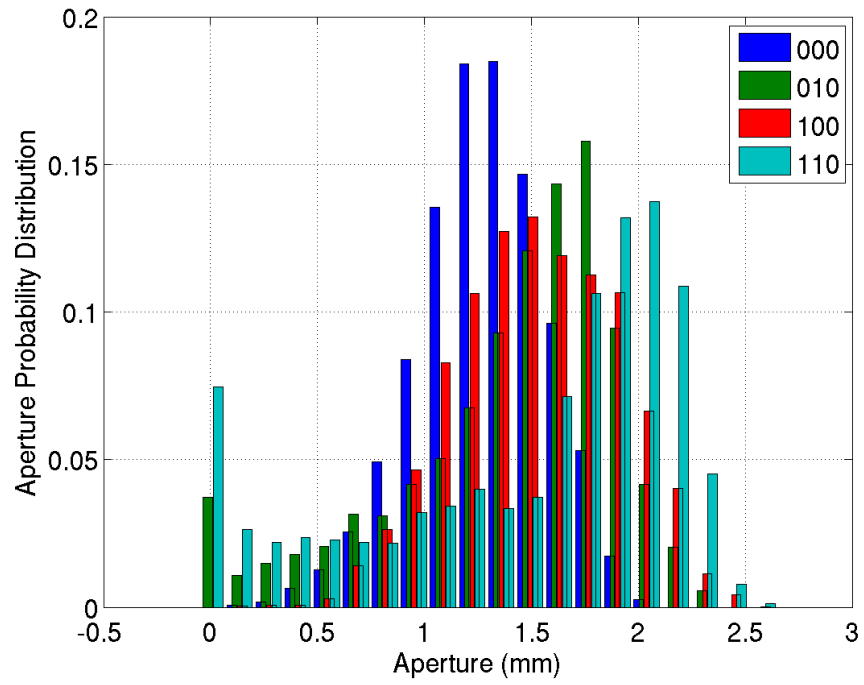


Figure B.6: Aperture distribution in the 4 subsamples.

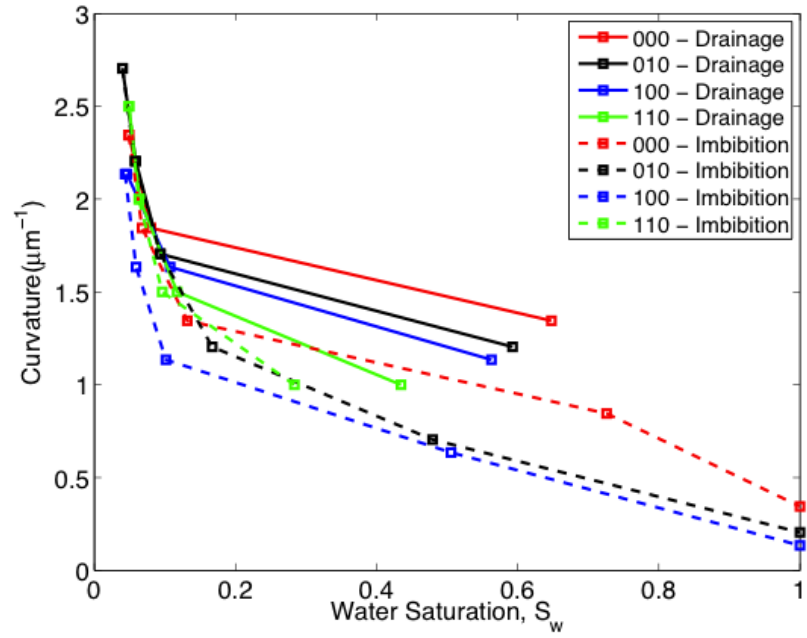


Figure B.7: Curvature – Saturation plot for the 4 Niobrara subsamples

Appendix C: Monterey

A sample from the Monterey outcrop sample was trimmed and imaged at 36.41 micron resolution using X-ray microtomography (XMT) at the UTCT.



Figure C.1: Monterey sample showing the fracture with pores and calcite cement.

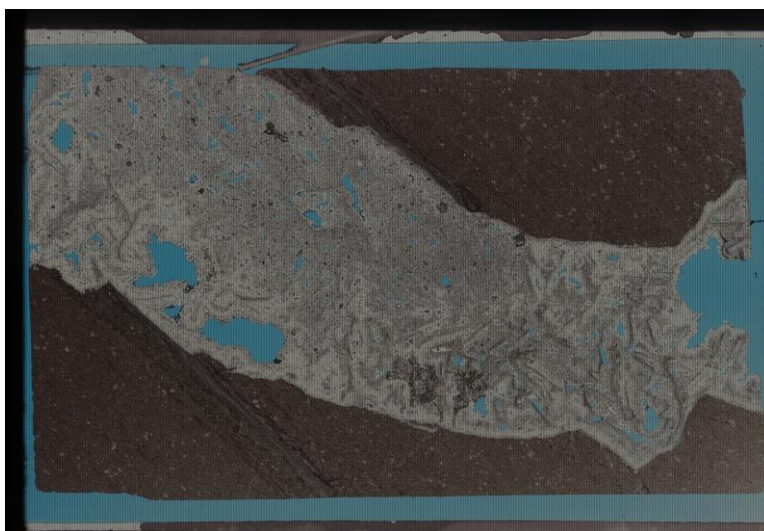


Figure C.2: Full scan of the thin-section of the Monterey sample. Scan shows the matrix as well as the fracture containing mineral cements and pores.

PETROLOGY

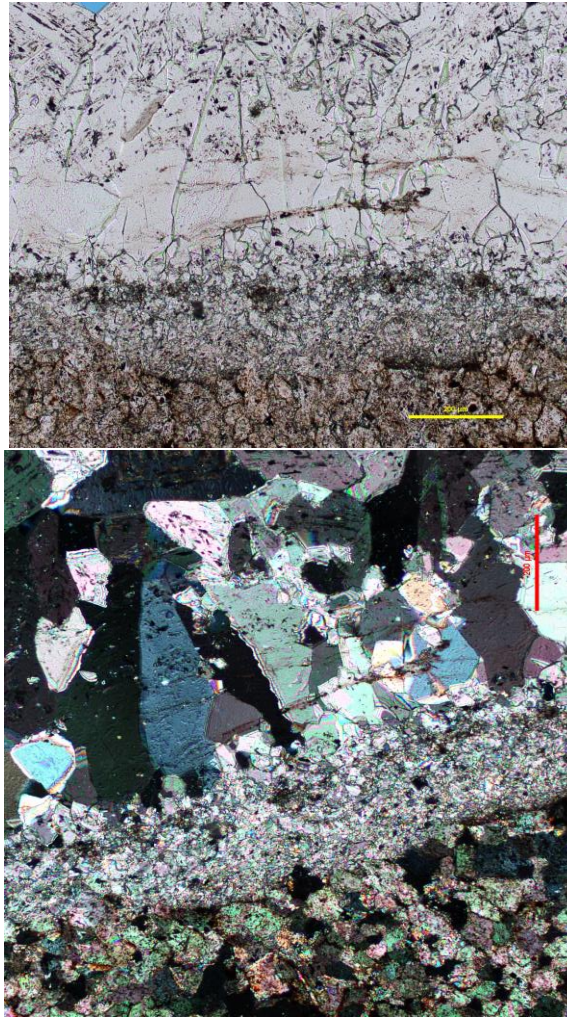


Figure C.3: The matrix-fracture boundary in the Monterey sample. Scale bars (yellow and red respectively) are 200 microns in both images. Top: Plain polarized light (PPL) image: boundary shows two types of calcite in the matrix, which appears to be a mixture of oxidized and non-oxidized calcite. Bottom: The cross-polarized image (XPL; of a similar region) confirms existence of the “calcite mixture” boundary and shows different quartz cements on top of it

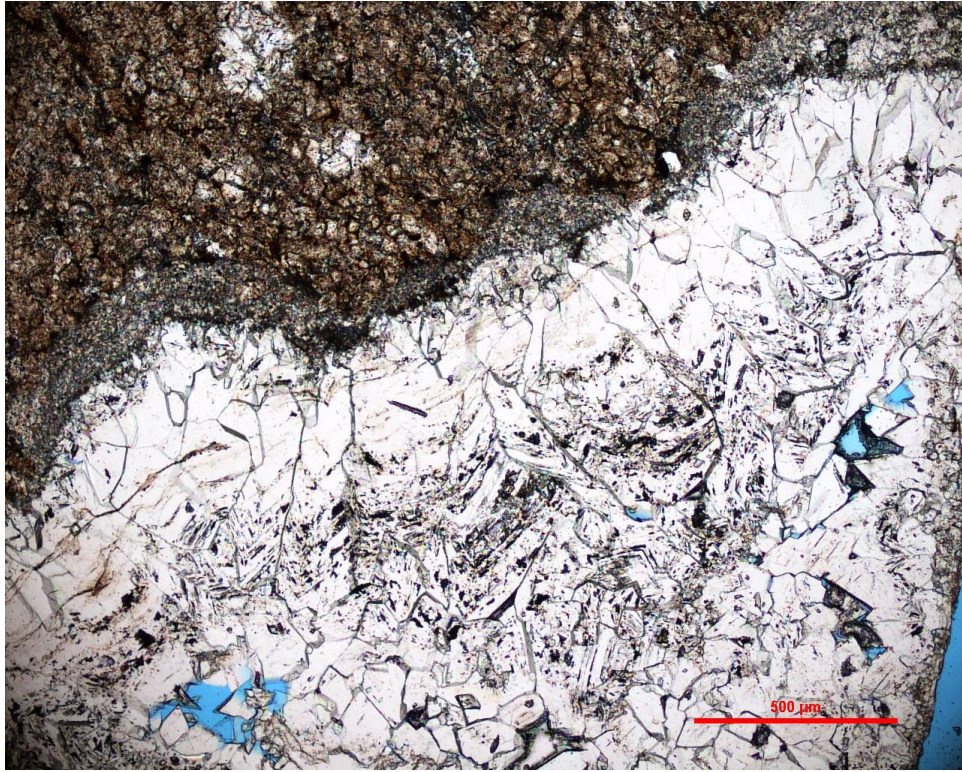


Figure C.4: The non-oxidized calcite along the matrix-fracture boundary shows varying thickness. The scale bar is 500 microns.

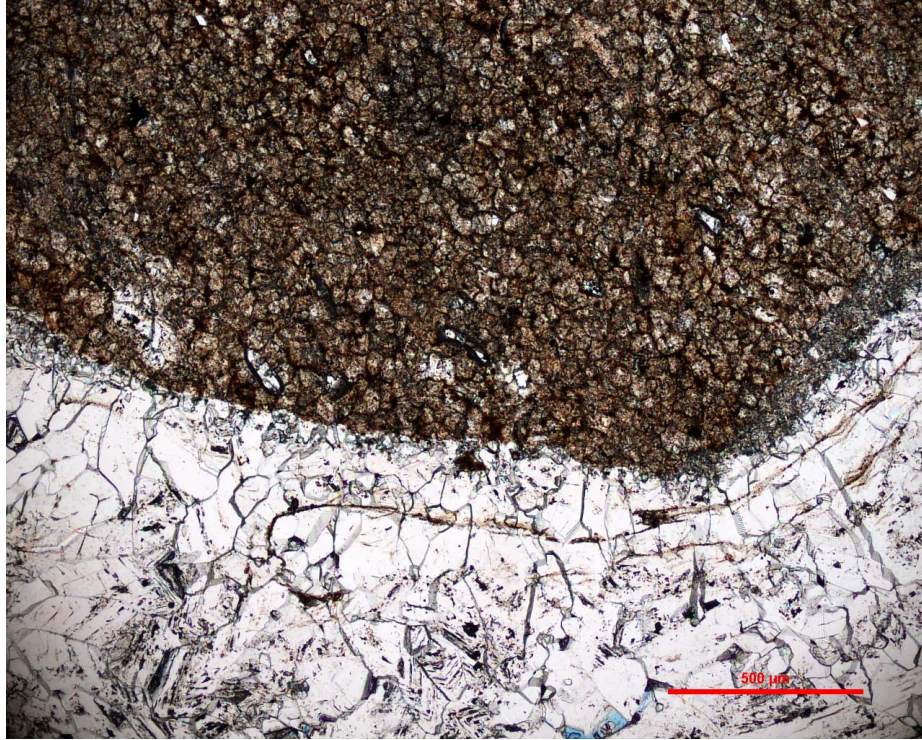


Figure C.5: The presence of calcite along the matrix-fracture boundary is not continuous (PPL). The scale bar is 500 microns.

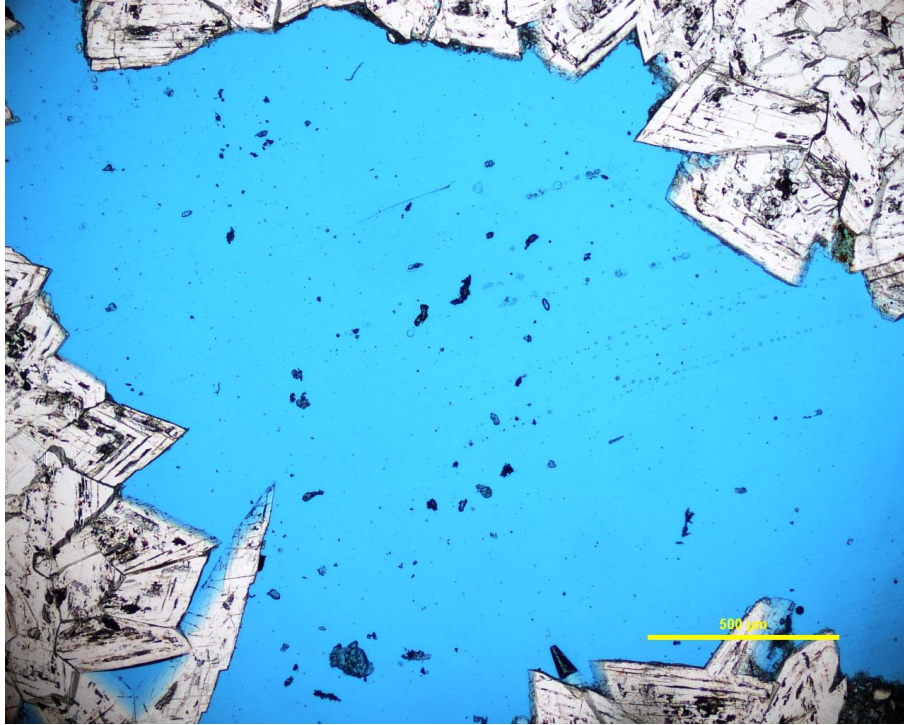


Figure C.6: PPL image of fracture pore space with quartz bridges. The scale bar is 500 microns.

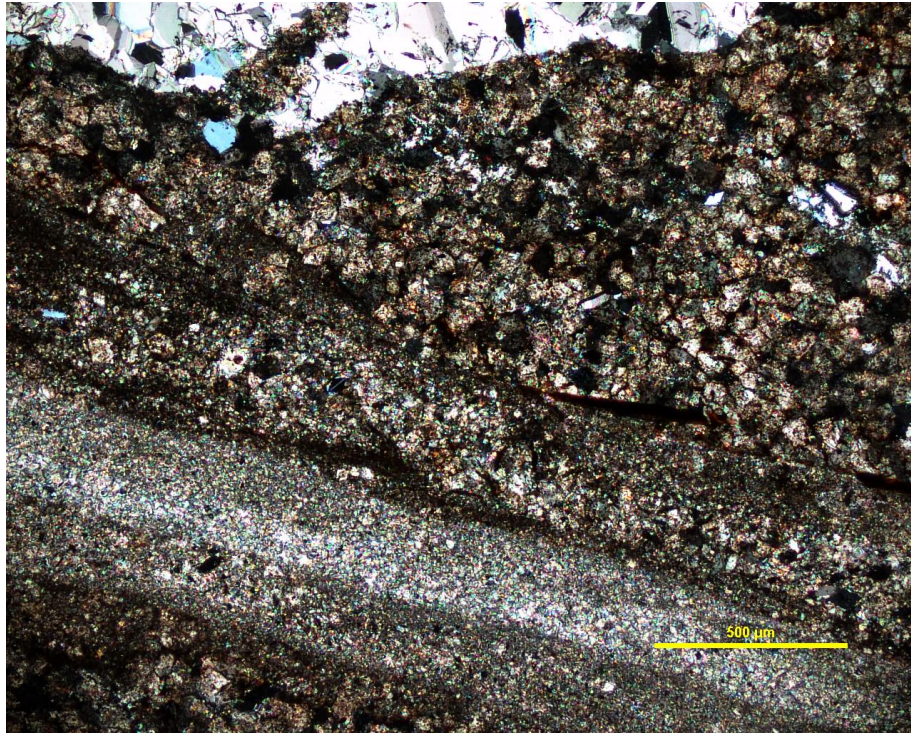


Figure C.7: XPL image of a matrix/fracture boundary showing microfractures in between different layers with some variation in composition. This indicates different timing for different layers. The scale bar is 500 microns

ANALYSIS OF THE FRACTURE SPACE

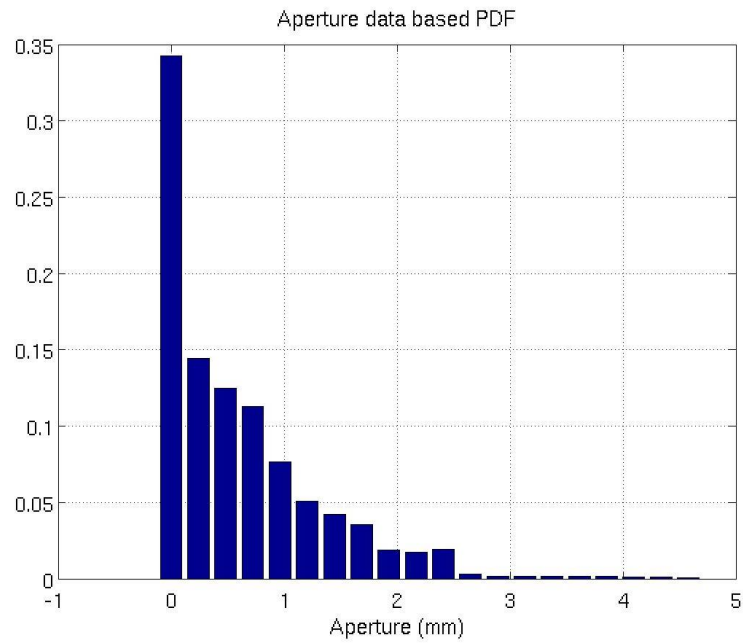


Figure C.8: Probability distribution function (PDF) of the fracture aperture. Aperture in the fracture ranges from 0 to ~4.8mm

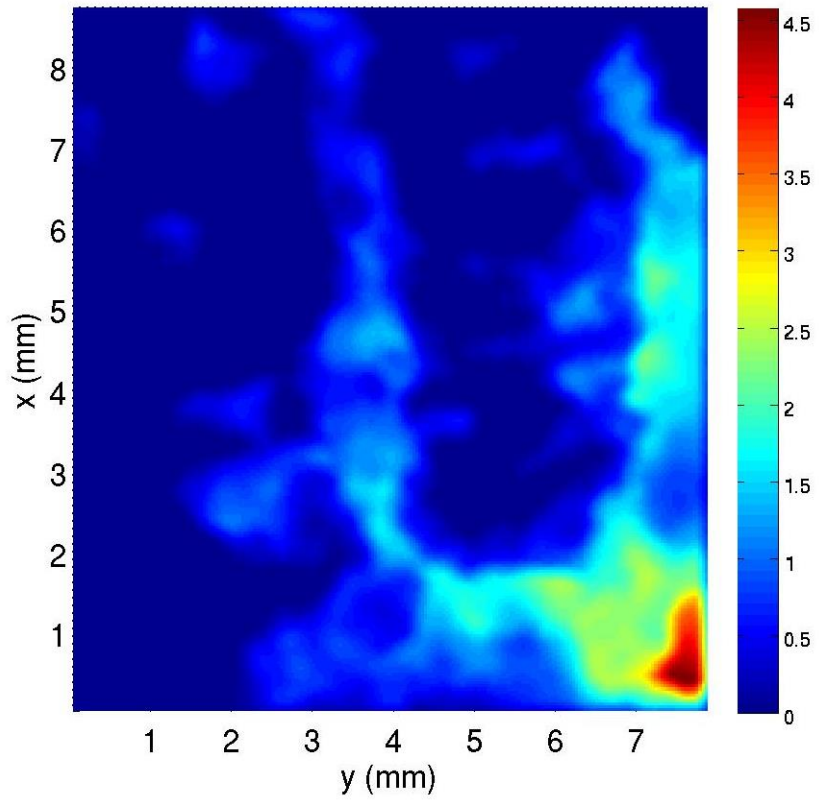


Figure C.9: Z-direction of the fracture aperture showing the distribution

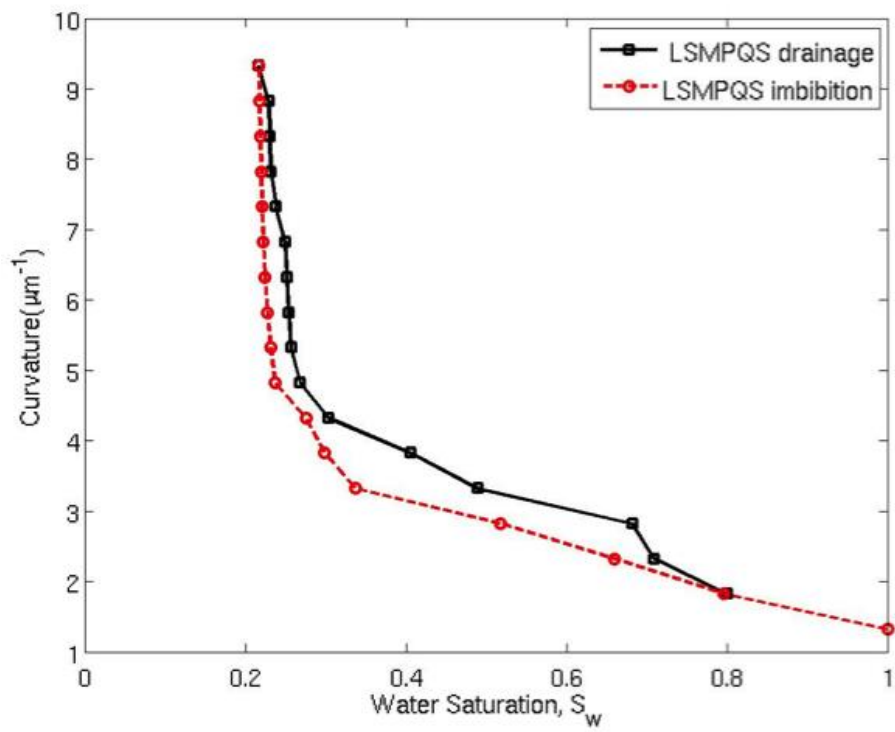


Figure C.10: Curvature – Saturation plot for drainage and imbibition.

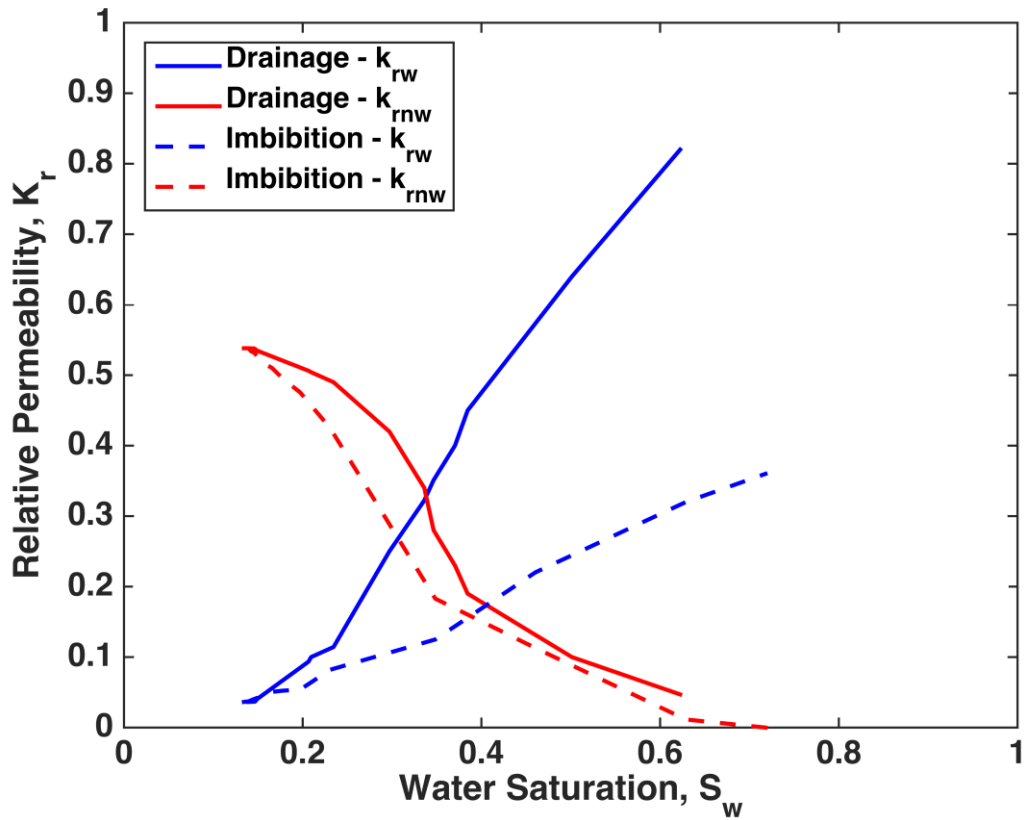


Figure C.11: Relative permeability curves for drainage and imbibition.

CEMENTATION IN THE MONTEREY

Numerical cement was grown in the Monterey sample, to understand its influence on the fracture space connectivity. The interface is the fracture-grain surface in a porous medium that moves into the fracture space (i.e., the grain space effectively grows, the fracture space effectively shrinks) as cement is deposited on the surface. The cementation

was done in multiple steps; each step represented a 1mm increase in the cement thickness (i.e. a fractional decrease in the initial fracture porosity). The influence of cementation on porosity and aperture in the samples was then studied. Porosity decreases (exponentially) as cementation thickness increases (Figure C.11).

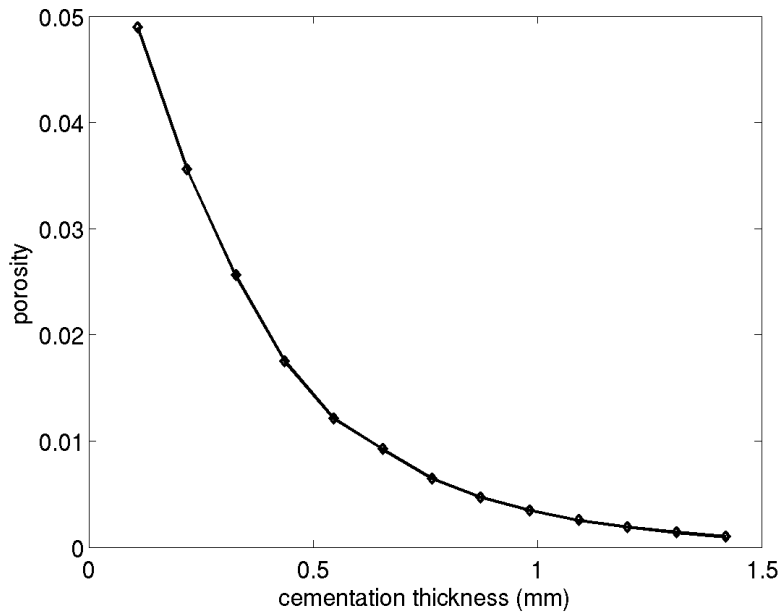


Figure C.12: Porosity vs. Cement thickness in the Monterey.

Aperture on the other hand, has a linear relationship with cementation thickness. The mean aperture is relatively constant while the maximum aperture decreases linearly with increasing cementation thickness (Figure C.12).

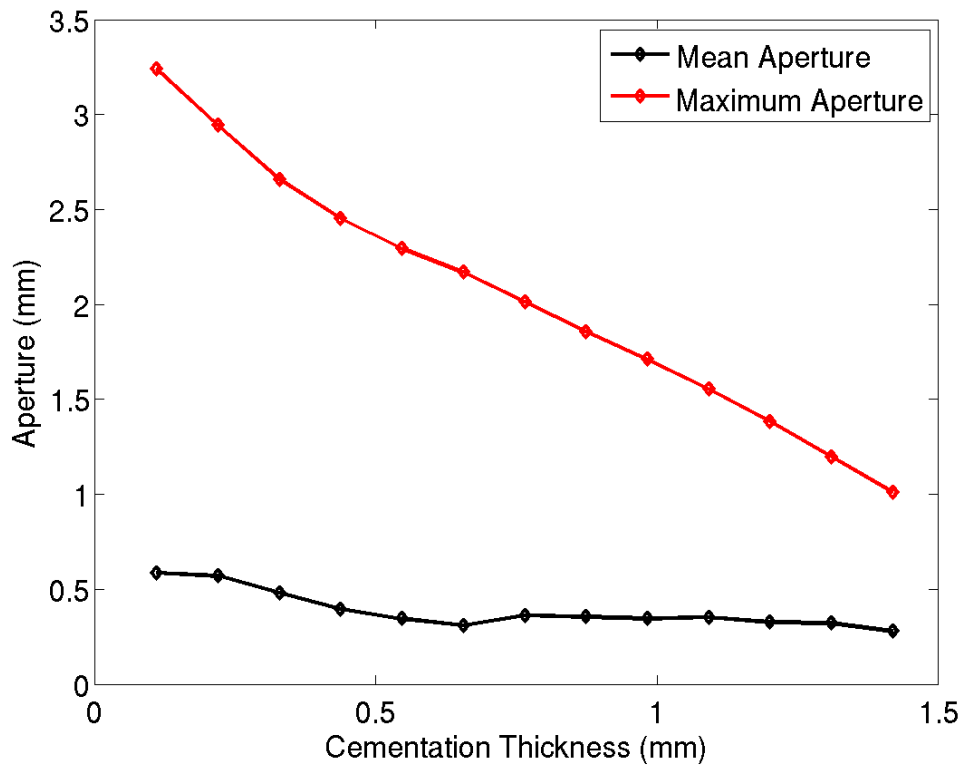


Figure C.13: Aperture vs. Cementation thickness in the Monterey.

The Monterey sample has most of the fracture filled with mineral cement (calcite), hence there is a small pore space open to flow. After numerically growing 5mm thick cement, the pore spaces reduced drastically with porosity reducing from about 5% to 1% (Figure C.13). There is a leftward shift in the histogram of the aperture in the original sample (Figure C.9), after 5mm thick cement (Figure C.14) has been added. This is in relation to the reduced fracture pore space. The probability distribution function

(PDF) of aperture after cementation in the Monterey is shown in Figure C.15 showing reduced aperture.

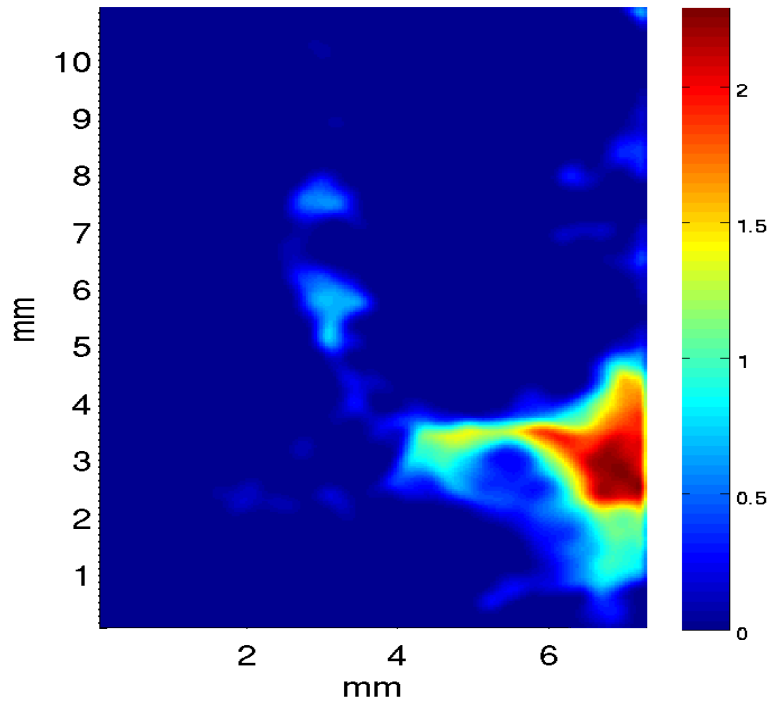


Figure C.14: Aperture distribution field after 5mm of cement has been numerically added to the fracture space.

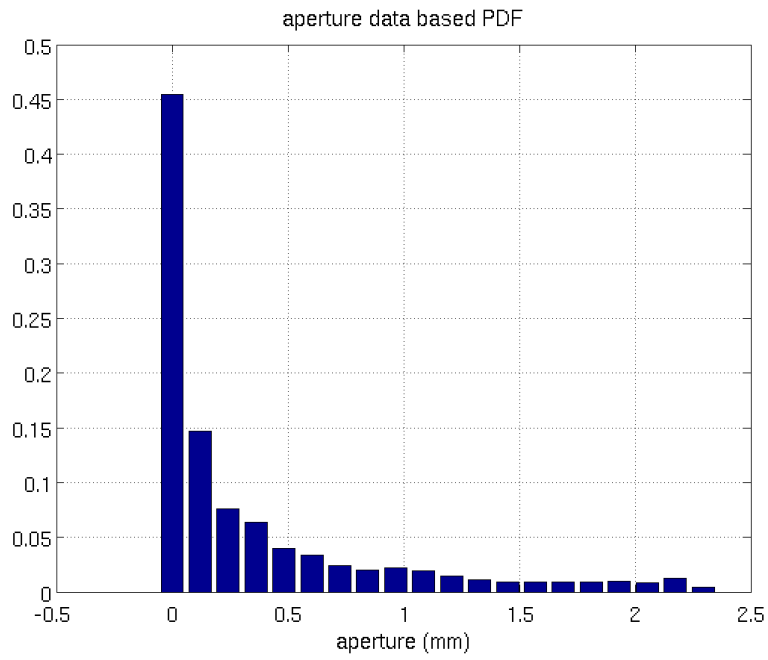


Figure C.15: Probability distribution function of the aperture in the cemented Monterey sample after the addition of 5mm thick cement.

References

- Adler, P. M., 1992, Porous media: Geometry and transports. Butterworth–Heinemann, Stoneham, MA
- Agosta, F., Alessandrini, M., Antonellini, M., Tondi, E., and Giorgioni, M., 2010, From fractures to flow: a field-based quantitative analysis of an outcropping carbonate reservoir. *Tectonophysics*, vol. 490, no. 3, pp. 197-213.
- Aguilera, R., 1980, Naturally Fractured Reservoirs, Petroleum, Tulsa, OK
- Aidun, C. K., and Clausen, J. R., 2010, Lattice-Boltzmann method for complex flows. *Annual Review of Fluid Mechanics*, vol. 42, pp. 439-472
- Al-Omari, A., and Masad, E., 2004, Three dimensional simulation of fluid flow in X-ray CT images of porous media. *International Journal of Numerical Analysis Methods Geomech*, vol. 28, no. 13, pp. 1327–1360
- Archie, G. E., 1950, Introduction to petrophysics of reservoir rocks. *AAPG Bulletin*, vol. 34, no. 5, pp. 943-961.
- Arns, C.H., Knackstedt, M.A., Pinczewski, W.V., and Martys, N.S., 2004, Virtual permeametry on Microtomographic images. *Journal Petroleum Science and Engineering* vol. 45, no. 1–2, pp. 41–46
- Benzi, R., Succi, S., and Vergassola, M., 1992, The lattice Boltzmann equation: theory and applications. *Physics Reports*, vol. 222, no. 3, pp. 145-197.
- Berkowitz, B., 2002, Characterizing flow and transport in fractured geological media: a review. *Advanced Water Resources* vol. 25, no. 8–12, pp. 861–884
- Ball, B.C., 1981, Modeling of soil pores as tubes using gas permeabilities, gas diffusivities and water release. *Journal of Soil Science* vol. 32, pp. 465-481
- Bear, J., 1972, *Dynamics of Fluids in Porous Media*, New York: American Elsevier, pp. 764,
- Becker, S.P., Eichhubl, P., Laubach, S.E., Reed, R.M., Lander, R.H., and Bodnar, R.J., 2010, A 48 m.y. history of fracture opening, temperature, and fluid pressure: Cretaceous Travis Peak Formation, East Texas basin: *Geological Society of America Bulletin*, v. 122, p. 1081-1093.
- Bjørlykke, K., Ramm, M., and Saigal, G. C., 1989, Sandstone diagenesis and porosity modification during basin evolution. *Geologische Rundschau*, vol. 78, no. 1, pp. 243-268.
- Boles, J. R., Eichhubl, Peter, Garven, G., and Chen, J., 2004, Evolution of a hydrocarbon migration pathway along basin-bounding faults: evidence from fault cement: *AAPG Bulletin*, v. 88, no. 7, p. 947–970.
- Bratton, T., Canh, D. V., Van Que, N., Duc, N. V., Gillespie, P., Hunt, D., and Sonneland, L., 2006, The nature of naturally fractured reservoirs. *Oilfield Review*, 18(2), 4-23.
- Braunstein, J., Huddles ton, P., McLemore, W., and Biel, R., 1988, Gulf Coast Province regional correlation chart: American Association of Petroleum Geologists Correlation Chart Series

- Brown, S. R., and Scholz, C. H., 1985, Broad bandwidth study of the topography of natural rock surfaces, *Journal of Geophysical Research*, vol. 90, no. B14, pp. 12575–12582, doi:10.1029/JB090iB14p12575.
- Brown, S. R., 1987, Fluid flow through rock joints: The effect of surface roughness, *Journal of Geophysical Resources*, vol. 92, no. B2, pp. 1337–1347, doi:10.1029/JB092iB02p01337.
- Brown, S.R., 1989, Transport of fluid and electric current through a single fracture. *Journal of Geophysical Resources* vol. 94, no. B7, pp. 9429–9438
- Brown, S.R., 1995, Simple mathematical model of a rough fracture. *Journal of Geophysical Research* vol. 100, no. B4, pp. 5941–5952
- Brown, S.R., Stockman, H.W., and Reeves, S.J., 1995, Applicability of the Reynolds equation for modeling fluid flow between rough surfaces. *Geophysical Research Letters*, vol. 22, no. 18, pp. 2537–2540
- Carman, P. C., 1937, Fluid flow through granular beds: *Transactions of the Institute of Chemical Engineers*, vol. 15, pp.150 – 166
- Carman, P. C. 1956, *Flow of Gases through Porous Media*. Butterworths Scientific Publication, London
- Chen, S., and Doolen, G. D., 1998, Lattice Boltzmann method for fluid flows. *Annual review of fluid mechanics*, vol. 30, no. 1, pp. 329-364.
- Chen, C. Y., Horne, R. N., and Fourar, M., 2004, Experimental study of liquid-gas flow structure effects on relative permeabilities in a fracture. *Water Resources Research*, vol. 40, no. 8.
- Chen, C. and Horne, R., 2006, Two-phase flow in rough-walled fractures: Experiments and a flow structure model. *Water Resources Research*, vol. 42, no. 3, W03430, doi:10.1029/2004WR003837
- Childs, E. C., 1969, *An introduction to the physical basis of soil water phenomena*, Wiley-Interscience, New York
- Clark, Norman J., 1960, *Elements of Petroleum Reservoirs*, Henry L. Doherty Series, Society of Petroleum Engineers of AIME, Dallas.
- Clennell, M. B., 1997, Tortuosity: A guide through the maze. In: M.A. Lovell and P.K. Harvey, editors, *Development in petrophysics*. Geological Society, London, pp. 299-344,
- Coleman, S.W., and Vassilicos, J.C., 2008, Transport properties of saturated and unsaturated porous fractal materials. *Physical Review Letters*. 100:035504. doi:10.1103/PhysRevLett.100.035504
- Collins, R. E., 1976, *Flow of fluids through porous materials*, Research & Engineering Consultants Inc.
- Cooke, M. L., 1997, Fracture localization along faults with spatially varying friction. *Journal of Geophysical Research: Solid Earth (1978–2012)*, vol. 102, no. B10, pp. 22425-22434.
- Crandall, D., Bromhal, G., and Karpyn, Z. T., 2010, Numerical simulations examining the relationship between wall-roughness and fluid flow in rock fractures.

- International Journal of Rock Mechanics and Mining Science Vol. 47, pp. 784–796
- Currie, J.A., 1960, Gaseous diffusion in porous media: II. Dry granular materials. *Br. J. Appl. Phys.* 11:318–324. doi:10.1088/0508-3443/11
- Dahi Taleghani, A., and Olson, J. E., 2013, How Natural Fractures Could Affect Hydraulic-Fracture Geometry. *SPE Journal*, (Preprint).
- Darcy, H. 1956. *Les fontaines publiques de la ville de Dijon*. Paris: Victor Dalmont.
- Davies, D.K., B.P.J. Williams, and R.K. Vessel, 1993, Reservoir geometry and internal permeability distribution in fluvial, tight gas sandstones, Travis Peak Formation, Texas: *SPE Reservoir Engineering*, February, 1993, p. 7-12.
- De, S., Nagendra, K., and Lakshminisha, K. N., 2009, Simulation of laminar flow in a three-dimensional lid-driven cavity by lattice Boltzmann method. *International Journal of Numerical Methods for Heat & Fluid Flow*, vol. 19, no. 6, pp. 790-815.
- De Gennes, P. G., 1985, Wetting: statics and dynamics. *Reviews of modern physics*, vol. 57, no. 3, p. 827.
- Dickinson, W. W., and Milliken, K. L., 1995, The diagenetic role of brittle deformation in compaction and pressure solution, Etjo sandstone, Namibia. *The Journal of Geology*, pp. 339-347.
- Dijk, P.E., and Berkowitz, B., 1999, Three-dimensional flow measurements in rock fractures. *Water Resources Research* vol. 35, no. 12, pp. 3955–3959
- Dullien, F.A.L., 1979, *Porous media: Fluid transport and pore structure*. Academic Press, San Diego
- Durham, W. B., 1997, Laboratory observations of the hydraulic behavior of a permeable fracture from 3800 m depth in the KTB pilot hole. *Journal of Geophysical Research*, vol. 102, pp.18405-18416
- Dutton, S. P., and Finley, R. J., 1988, Controls on Reservoir Quality in Tight Sandstones of the Travis Peak Formation, East Texas. *Society of Petroleum Engineers*. doi:10.2118/15220-PA
- Dutton, S. P., and Land, L. S., 1988, Cementation and burial history of a low-permeability quartzarenite, Lower Cretaceous Travis Peak Formation, East Texas: *Geological Society of America Bulletin*, v. 100, pp. 1271-1282.
- Dutton, S. P., Laubach, S.E., Tye, R. S., Herrington, K. L., and Diggs, T. N., 1991, Geological analysis of the Travis Peak Formation and Cotton Valley Sandstone, in Peterson, R. E., ed., *SFE No. 3 Comprehensive Well Report: CER Corporation and S. A. Holditch and Associates, Inc.*, topical report no. GRI-91/0048 prepared for the Gas Research Institute under contract no. 5090-211-1940, pp. 27-66
- Dyke, C., 1995, How sensitive is natural fracture permeability at depth to variation in effective stress. *Fractured and Jointed Rock Masses*, pp. 81-88.
- Ehrenberg, S. N., 1989, Assessing the relative importance of compaction processes and cementation to reduction of porosity in sandstones: Discussion; Compaction and porosity evolution of Pliocene sandstones, Ventura Basin, California: Discussion. *AAPG Bulletin*, vol. 73, no. 10, pp. 1274-1276.

- Ellis, M. A., Laubach, S. E., Eichhubl, P., Olson, J. E., and Hargrove, P., 2012, Fracture development and diagenesis of Torridon Group Applecross Formation, near An Teallach, NW Scotland: millennia of brittle deformation resilience?, *Journal Geological Society*, vol. 169, no. 3, pp. 297-310.
- Epstein, N., 1989, On tortuosity and the tortuosity factor in flow and diffusion through porous media. *Chem. Eng. Sci.* 44:777-779. doi:10.1016/0009-2509(89)85053-5
- Eker, E., and Akin, S., 2006, Lattice Boltzmann simulation of fluid flow in synthetic fractures. *Transport in Porous Media* vol. 65, no. 3, pp. 363-384
- Engelder, T., and Scholz, C. H., 1981, Fluid flow along very smooth joints at effective pressures up to 200 megapascals, in: *Mechanical Behavior of Crustal Rocks, The Handin Volume*, American Geophysical Union Monograph 24, pp. 147-152
- Faris, S. R., Gournay, S., Lipson, L.B., and Webb, T.S., 1954, Verification of Tortuosity Equations, *AAPG Bulletin*, vol. 38, pp. 2226-2232.
- Fatt, I., and Klikoff, W. A., 1959, "Effect of Fractional Wettability on Multiphase Flow through Porous Media", *Petroleum Transactions of AIME*, vol. 216, pp. 426-432.
- Finney, J. L., 1970, Random packings and the structure of simple liquids, I. The geometry of random close packing. *Proceedings of the Royal Society*, vol. 319, no. 479, pp. 479-493
- Fossen, H., Schultz, R. A., Shipton, Z. K., and Mair, K., 2007, Deformation bands in sandstone: a review. *Journal of the Geological Society*, vol. 164, no. 4, pp. 755-769.
- Gale, J. E., and Raven, K. G., 1980, Effects of sample size on the stress—permeability relationship for natural fractures, Lawrence Berkeley Laboratory Report, LBL-11865 (SAC-48), Berkeley, California
- Gale, J. F., Reed, R. M., and Holder, J., 2007, Natural fractures in the Barnett Shale and their importance for hydraulic fracture treatments, *AAPG Bulletin*, vol. 91, no. 4, pp 603-622
- Gangi, A. F., 1978, Variation of whole and fractured porous rock permeability with confining pressure *International Journal of Rock Mechanics & Mining*, vol. 15, no 5, pp. 249-257
- Ghanbarian, B., Hunt, A. G., Ewing, R. P., and Sahimi, M., 2013, Tortuosity in Porous Media: A Critical Review. *Soil Sci. Soc. Am. J.* 77:1461-1477. doi:10.2136/sssaj2012.0435
- Golf-Racht, T. D., 1982, *Fundamentals of fractured reservoir engineering*. Amsterdam: Elsevier.
- Good, R. J., 1992, Contact angle, wetting, and adhesion: a critical review. *Journal of adhesion science and technology*, vol. 6, no. 12, pp. 1269-1302.
- Gudmundsson, A., 2011, *Rock Fractures in Geological Processes*, Cambridge University Press
- Guo, Z., Zheng, C., and Shi, B. (2002). An extrapolation method for boundary conditions in lattice Boltzmann method. *Physics of Fluids (1994-present)*, vol. 14, no. 6, pp. 2007-2010
- Greenkorn, R.A., 1983, *Flow phenomena in porous media*. Marcel Dekker, NY.

- Hartmann, D. J., Beaumont, E. A., and Coalson, E., 2000, Predicting Sandstone Reservoir System Quality and Example of Petrophysical Evaluation. Search and discovery, 40005.
- Hakami, E., and Larsson, E., 1996, Aperture measurements and flow experiments on a single natural fracture: International Journal of Rock Mechanics and Mining Sciences & Geomechanics Abstracts, vol. 33, pp. 395-404.
- Hayes J. B., 1979, Sandstone diagenesis-the hole truth. In Aspects of Diagenesis (eds. P. A. Scholle and P. R. Schluger). Society for Sedimentary Research Special Publication vol. 26, pp. 127-140
- He, X., Zou, Q., Luo, L. S., and Dembo, M., 1997, Analytic solutions of simple flows and analysis of nonslip boundary conditions for the lattice Boltzmann BGK model. Journal of Statistical Physics, vol. 87, pp. 115-136.
- Hillel, D., 2004, Introduction to environmental soil physics. Academic Press, San Diego
- Houseknecht, D. W., 1987, Assessing the relative importance of compaction processes and cementation to reduction of porosity in sandstones: AAPG Bulletin vol. 71, pp. 633-642
- Iassonov, P., Gebrenegus, T., and Tuller, M., 2009, Segmentation of X-Ray Computed Tomography Images of Porous Materials: A Crucial Step for Characterization and Quantitative Analysis of Pore Structures. Water Resources Research vol. 45, no. 9. doi:10.1029/2009WR008087.
- Iwai, K., 1976, Fundamentals of fluid flow through a single fracture, Ph.D. thesis, Berkeley, University of California.
- Jackson, M. P. A., 1981, Tectonic environment during early infilling of the East Texas Basin, in Kreitler, C. W., and others, Geology and geohydrology of the East Texas Basin, a report on the progress of nuclear waste isolation feasibility studies (1980): The University of Texas at Austin, Bureau of Economic Geology Geological Circular vol. 81 no. 7, pp. 7-It.
- Jolley, S. J., Barr, D., Walsh, J. J., and Knipe, R. J., 2007, Structurally complex reservoirs: an introduction. Geological Society, London, Special Publications, 292(1), 1-24.
- Kalantari-Dahaghi, A., and Mohaghegh, S. D., 2009, Top-Down Intelligent Reservoir Modeling of New Albany Shale. SPE paper presented at the 2009 SPE Eastern Regional Meeting held in Charleston, West Virginia, USA, 23–25 September
- Kang, Q., Lichtner, P., Viswanathan, H., and Abdel-Fattah, A., 2009, Pore Scale Modeling of Reactive Transport Involved in Geologic CO₂ Sequestration. Transport in Porous Media vol. 82 (July), pp. 197–213. doi:10.1007/s11242-009-9443-9.
- Ketcham, R.A., and Carlson, W.D., 2001, Acquisition, optimization and interpretation of X-ray computed tomographic imagery: applications to the geosciences. Computational Geoscience vol. 27, pp. 381–400
- Khan, F., Enzmann, F., Kersten, M., Wiegmann, A., and Steiner, K., 2011, 3D simulation of the permeability tensor in a soil aggregate on basis of nanotomographic imaging and LBE solver. Journal of Soils Sedimentation 1–11

- Kim, I., Lindquist, W.B., and Durham, W.B., 2003, Fracture flow simulation using a finite-difference lattice Boltzmann method. *Physical Review E* 67(4), 46708
- Klimczak, C., Schultz, R. A., Parashar, R., and Reeves, D. M., 2010, Cubic law with aperture-length correlation: implications for network scale fluid flow. *Hydrogeology Journal*, vol. 18, no. 4, pp. 851-862
- Kirkham, M. B., 2005, Principles of soil and plant water relations. Elsevier Academic Press, Burlington, MA.
- Kranz, R. L., Frankel, A. D., Engelder, T., and Scholz, C. H., 1979, The permeability of whole and jointed Barre granite, *International Journal of Rock Mechanics and Mining Sciences & Geomechanics Abstracts* vol. 16, pp. 225–234
- Ladd, A. J. C., 1994, Numerical simulations of particulate suspensions via a discretized Boltzmann equation. Part 1. Theoretical foundation *Journal of Fluid Mechanics*. pp. 271-285
- Landry, C. J. and Karpyn, Z., 2012, Single-phase lattice Boltzmann simulations of pore-scale flow in fractured permeable media: *International Journal of Oil, Gas and Coal Technology*, vol. 5, no. 2/3, pp. 182-206.
- Laubach, S. E., 2003, Practical approaches to identifying sealed and open fractures, *AAPG Bulletin*, vol. 87, no. 4, pp. 561-579.
- Laubach, S.E., Olson, J. E., and Gross, M.R., 2009, Mechanical and fracture stratigraphy: *AAPG Bulletin*, vol. 93, no. 11
- Laubach, S.E., Reed, R.M., Olson, J.E., Lander, R.H., and Bonnell, L.M., 2004, Coevolution of crack-seal texture and fracture porosity in sedimentary rocks; cathodoluminescence observations of regional fractures: *Journal of Structural Geology*, vol. 26, pp. 967-982.
- Laubach, S. E., Olson, J. E., Eichhubl, P., Fomel, S. B., and Marrett, R. A., 2010, Natural fractures from the perspective of diagenesis, in *CSEG Recorder*, pp. 26-31
- Lee, C. H., and Farmer, I. W., 1993, Fluid flow in discontinuous rocks. London: Chapman and Hall.
- Lee, Kashyap, and Chu, 1994, Building Skeleton Models via 3-D Medial Surface Axis Thinning Algorithms CVGIP: Graphical Models and Image Processing vol. 56, no. 6, pp. 462–478. doi:10.1006/cgip..1042
- Lenormand, R., Zarcone, C., and Sarr, A., 1983, Mechanisms of the displacement of one fluid by another in a network of capillary ducts. *Journal of Fluid Mechanics*, vol. 135, pp. 337-353.
- Lindquist, W.B., and Venkatarangan, A.B., 1999, Investigating 3D geometry of porous media from high-resolution images. *Physics and Chemistry of the Earth A* vol. 25, pp. 593–599
- Lindquist, W. B., 2010, 3DMA-Rock, a software package for automated analysis of rock pore structure in 3D computed microtomography images. http://www.ams.sunysb.edu/~lindquis/3dma/3dma_rock/3dma_rock.html.
- Lomize, G. M., 1951, Flow in Fractured Rocks (in Russian). Gosenergoizdat, Moscow
- Lorenz, P. B., 1961, Tortuosity in porous media. *Nature* 189:386-387. Doi:10.1038/189386a0 1961.

- Louis, C., 1967, Strömungsvorgänge in klüftigen Medien und ihre Wirkung auf die Standsicherheit von Bauwerken und Böschungen im Fels. Technische Hochschule Karlsruhe (1967)
- Matyka, M., Khalili, A., and Koza, Z., 2008, Tortuosity-porosity relations in porous media flow. *Physic review E* 78:026306.doi:10.1103/PhysRevE.78.026306.
- McBride, E. F., 1989, Quartz cement in sandstones: a review. *Earth-Science Reviews*, vol. 26, no. 1, pp. 69-112.
- Meredith, R.E., and Tobias, C.W., 1962, Conduction in heterogeneous systems. In: Tobias, C.W. (ed.) *Advances in Electrochemistry and Electrochemical Engineering 2*, Interscience Publishers, New York
- Méheust, Y., and Schmittbuhl, J., 2001, Geometrical heterogeneities and permeability anisotropy of rough fractures. *Journal of Geophysical Research* vol. 106(B2), pp. 2089–2102
- Méheust, Y., and Schmittbuhl, J., 2003, Scale effects related to flow in rough fractures. *Pure Applied Geophysics* vol. 160 no. 5, pp. 1023–1050
- Moreno, L., and Tsang, C. F., 1994, Flow channeling in strongly heterogeneous porous media: a numerical study. *Water Resources Research* vol. 30, no. 5, pp. 1421–1430
- Mourzenko, V., Thovert, J.F., and Adler, P. 1995. Permeability of a single fracture; validity of the Reynolds equation. *Journal of Physics II* vol. 5, no. 3, pp. 465–482
- Moldrup, P., Olesen, T., Gamst, J., Schjonning, P., and Rolston, D.E., 2001, Tortuosity, diffusivity, and permeability in the soil liquid and gaseous phases. *Soil Science Society America Journal* 64:94-100. Doi:10.2136/sssaj2003.0041
- Morrow, N. R., 1970, Physics and thermodynamics of capillary action in porous media. *Industrial and Engineering Chemistry*, vol. 62, no. 6, pp. 32-56.
- Morrow, N.R., Brower, K.R., Ma, S., and Buckley, J. S., 1990, Fluid Flow in Healed Tectonic Fractures: *Journal of Petroleum Technology*, vol. 42, pp. 1310-1318.
- Motealleh, S. and Bryant, S. L., 2009, Quantitative Mechanism for Permeability Reduction by Small Water Saturation in Tight-Gas Sandstones: SPEJ. doi:10.2118/107950-PA, June
- Mousavi, M. A. and Bryant, S. L., 2007, Geometric models of porosity reduction mechanisms in tight gas sands, SPE Rocky Mountain Oil and Gas Technology Symposium, April 16-18, Denver, Colorado
- Naar, J., Wygal, R. J., and Henderson, J. H., 1962, Imbibition relative permeability in unconsolidated porous media. *Society of Petroleum Engineers Journal*, vol. 2, no. 1, pp. 13-17.
- Narr, W., Schechter, D. W., and Thompson, L. B., 2006, *Naturally Fractured Reservoir Characterization*, Text book Series, SPE, Richardson, Texas, USA
- Narváez, A., Zauner, T., Raischel, F., Hilfer, R., and Harting, J., 2010, Quantitative analysis of numerical estimates for the permeability of porous media from lattice-Boltzmann simulations. arXiv 1005, 1.0
- Nelson, R.A. 1985. *Geological Analysis of Naturally Fractured Reservoirs*: Houston, Gulf Publishing Co, 320 p.

- Nelson, R.A. 2001. Geological Analysis of Naturally Fractured Reservoirs, second edition: Houston, Gulf Publishing Co.
- Neuville, A., Toussaint, R., and Schmittbuhl, J., 2010, Hydrothermal coupling in a self-affine rough fracture. *Physical Review E* vol. 82 no. 3
- Neuville, A., Toussaint, R., and Schmittbuhl, J., 2011, Hydraulic transmissivity and heat exchange efficiency of open fractures: a model based on lowpass filtered apertures. *Geophysical Journal International*
- Ogilvie, S. R., Isakov, E., and Glover, P. W. J., 2006, Fluid flow through rough fractures in rocks. II: a new matching model for rough rock fractures. *Earth Planetary Science Letters*. vol. 241, pp. 454–465
- Oh, W. and Lindquist, W. B., 1999, Image thresholding by indicator kriging. *IEEE Transport Pattern Analysis Machine Intelligence* vol. 21 pp. 590-602.
- Olson, J. E., 2008, Multi-fracture propagation modeling: Applications to hydraulic fracturing in shales and tight gas sands. In *The 42nd US rock mechanics symposium (USRMS)*. American Rock Mechanics Association
- Olson, J. E., Laubach, S. E., and Lander, R. H., 2009, Natural fracture characterization in tight gas sandstones: Integrating mechanics and diagenesis. *AAPG Bulletin*, vol. 93, no. 11, pp. 1535-1549.
- Oron, A.P., and Berkowitz, B., 1998, Flow in rock fractures: the local cubic law assumption reexamined. *Water Resources Research* vol. 34, no. 11, pp. 2811–2825
- Owens, W.W. and Archer, D.L., 1971, The Effect of Rock Wettability on Oil-Water Relative Permeability Relationships. *Journal Petroleum Technology* vol. 23 no. 7 pp. 873-878. SPE-3034-PA. <http://dx.doi.org/10.2118/3034-PA>
- Øren, P. E., and Bakke, S., 2003, Reconstruction of Berea sandstone and pore-scale modeling of wettability effects. *Journal of Petroleum Science and Engineering* vol. 39, np. 3–4, pp. 177–199
- Øren, P. E., Bakke, S., and Held, R., 2007, Direct pore-scale computation of material and transport properties for North Sea reservoir rocks: *Water Resources Research* vol. 43, no. 11
- Palabos, 2013, Fluid Flow at your fingertips. Retrieved from <http://www.palabos.org>. Website last accessed May 31, 2013.
- Pan, C., Luo, L.S., and Miller, C.T., 2006, An evaluation of lattice Boltzmann schemes for porous medium flow simulation. *Computational Fluids* vol. 35, no. 8–9, pp. 898–909
- Philip, Z.G., Jennings, J.W., Olson, J.E., Laubach, S.E., and Holder, J., 2005, Modeling Coupled Fracture-Matrix Fluid Flow in Geomechanically Simulated Fracture Networks: *SPE Reservoir Evaluation and Engineering*, vol. 8, pp. 300-309.
- Phillips, O. M., 1991, *Flow and reactions in permeable rocks*. Cambridge University Press.
- Pieters, D.A., and Graves, R.M., 1994, Fracture Relative Permeability: Linear or Non-Linear function of Saturation. SPE paper presented at the International Petroleum Conference and Exhibition of Mexico in Veracruz, 10-13 October

- Prodanović, M., and Bryant, S., 2006, A level set method for computing critical curvatures for drainage and imbibition: *Journal of Colloid and Interface Science*, vol. 304, pp. 442-458
- Prodanović, M., Lindquist, W. B., and Seright, R. S., 2007, 3D image-based characterization of fluid displacement in a Berea core. *Advances in Water Resources*, vol. 30, pp. 214–226.
- Prodanović, M., Bryant, S., and Karpyn, Z., 2010, Investigating matrix/fracture transfer via a level set method for drainage and imbibition: *SPE Journal* vol. 15, pp. 125-136
- Prodanović, M., Bryant, S. and Davis, S., 2013, Numerical Simulation of Diagenetic Alteration and Its Effect on Residual Gas in Tight Gas Sandstones: *Transport in Porous Media* vol. 96, no. 1, pp. 39–62. doi:10.1007/s11242-012-0072-3.
- Pyrak-Nolte, L. J., Myer, L. R., Cook, N. G. W., and Witherspoon, P.A., 1987, Hydraulic and mechanical properties of natural fractures in low permeability rock, in: *Proceedings, International Society for Rock Mechanics, 6th International Congress on Rock Mechanics*, Montreal, Canada, August, 1, pp. 225–231, A. A. Balkema, Rotterdam.
- Pyrak-Nolte, L. J., Cook, N.G.W., and Nolte, D. D., 1988, Fluid percolation through single fractures. *Geophysical Research Letters* vol. 15, no. 11, pp. 1247–1250
- Pyrak-Nolte, L. J., Nolte, D. D., and Cook, N. G., 1995, Hierarchical cascades and the single fracture. In *Fractals in Petroleum Geology and Earth Processes*, pp. 143-178, Springer US.
- Rodriquez, E., Prodanović, M. and Bryant, S.L., 2012, Contact Line Extraction and Length Measurements in Model Sediments and Sedimentary Rocks: *Journal of Colloid and Interface Science* vol. 368, pp. 558-577
- Sahimi, M., 1993, Flow phenomena in rocks: From continuum models to fractals, percolation, cellular automata, and simulated annealing. *Reviews of Modern Physics* vol. 65 pp. 1393–1534. doi:10.1103/RevModPhys.65.1393
- Sahimi, M., 2011, *Flow and transport in porous media and fractured rock*. 2nd ed. Wiley-VCH, Weinheim, Germany.
- Salathiel, R. A., 1973, Oil Recovery by Surface Film Drainage in Mixed-Wettability Rocks. *Journal of Petroleum Technology* vol. 25, no. 10, pp. 1216–1224. SPE-4104-PA.
- Satterfield, C.N., and T.K. Sherwood., 1963, *The role of diffusion in catalysis*. Addison-Wesley, Reading, MA.
- Scheidegger, A.E., 1974, *The physics of flow through porous media*. 3rd ed. University of Toronto Press, Toronto.
- Scherer, M., 1987, Parameters influencing porosity in sandstones: a model for sandstone porosity prediction. *AAPG bulletin*, vol. 71, no. 5, pp. 485-491.
- Schopper, J. R., 1966, A theoretical investigation on the formation factor/permeability/porosity relationship using a network model. *Geophysical Prospect.* 14:301-341.doi:10.1111/j.1365-2478.1966.tb01763.x

- Seni, S. J., and Jackson, M.P.A., 1983, Evolution of salt structures, East Texas diaper province, Part 1: Sedimentary record of halokinesis: *American Association of Petroleum Geologists Bulletin*, vol. 67, no. 8, pp. 1219-1244.
- Shan, X., and Chen, H., 1993, Lattice Boltzmann model for simulating flows with multiple phases and components. *Physical Review E*, vol., 47, no. 3, p. 1815.
- Shen, L., and Chen, Z. 2007. Critical review of the Impact of tortuosity on diffusion. *Chemical Engineering Science* 62:3748-3755.doi:10.1016/j.ces.2007.03.041
- Singhal, B. B. S., and Gupta, R. P., 2010, Fractures and discontinuities. In *Applied Hydrogeology of Fractured Rocks* (pp. 13-33). Springer Netherlands.
- Snow, D. T. 1969. Anisotropic Permeability of Fractured Media: *Water Resources Research*, vol. 5, no. 6, pp. 1273–1289, doi:10.1029/WR005i006p01273.
- Sukop, M. C. and Thorne, D. T. J., 2006, *Lattice Boltzmann Modeling*. Springer, Heidelberg
- Tartakovsky, A. M., Meakin, P., Scheibe, T., and Eichler West, R., 2007, Simulations of Reactive Transport and Precipitation with Smoothed Particle Hydrodynamics: *Journal of Computational Physics* vol. 222 no. 2, pp. 654–72. doi:10.1016/j.jcp.2006.08.013.
- Tindall, J. A., Kindel, J. R., and Anderson, D. E., 1999, *Unsaturated zone hydrology for scientists and engineers*. Prentice Hall, Englewood Cliff, NJ.
- Torskaya, T., Jin, G., and Torres-Verdin, C., 2007, Pore-level analysis of the relationship between porosity, irreducible water saturation, and permeability of clastic rocks, in: *Proceedings of SPE Annual Technical Conference and Exhibition*
- Tokan-Lawal, A., Prodanović M., and Eichhubl, P., 2013, Image-Based Modeling of Flow in Natural Partially Cemented Fractures, SPE paper 168805–MS presented at the 2013 Unconventional Resources Technology Conference (UrTec), Denver, Colorado, USA.
- Tokan-Lawal, A., Prodanovic, M., Landry, C. J., and Eichhubl, P., 2014, Understanding Tortuosity and Permeability variations in Naturally Fractured Reservoirs: Niobrara Formation, SPE paper 1922870 presented at the 2014 Unconventional Resources Technology Conference (UrTec), Denver, Colorado, USA.
- Tsang, Y. W., 1984, The effect of tortuosity on fluid flow through a single fracture, *Water Resources Research* Vol. 20, pp. 1209–1215
- Tsang, Y.W, and Tsang, C. F., 1987, Channel Model of Flow Through Fractured Media, *Water Resources Research*, vol. 23, no. 3 pp. 467-479
- Vogel, H. J., 1997, Morphological determination of pore connectivity as a function of pore size using serial sections. *European Journal of Soil Science*, vol. 48, no. 3, pp. 365-377.
- Walsh, J. B., 1981, Effect of pore pressure and confining pressure on fracture permeability, *International Journal of Rock Mechanics and Mining Sciences & Geomechanics Abstracts* vol. 18, pp. 429–435
- Walsh, J.B., and Brace, W.F., 1984, The effect of pressure on porosity and the transport properties of rock. *Journal Geophysical Resources* vol. 89, no. B11, pp. 9425–9431

- Walton, I., and McLennan, J., 2013, The Role of Natural Fractures in Shale Gas Production. In *ISRM International Conference for Effective and Sustainable Hydraulic Fracturing*. International Society for Rock Mechanics.
- Wang, J.G., Leung, C.F., and Chow, Y.K., 2003, Numerical solutions for flow in porous media. *International Journal Numerical Analytical Methods Geomechanics* vol. 27, no. 7, pp. 565–583
- Watson, R.W, and Boukadi, F.H., 1991, The Effects of clay matrix, carbonate cement and quartz overgrowth on wettability, porosity, residual oil saturation, tortuosity and rock surface area of Berea. SPE paper presented at the CIM/OSTRA technical conference in Banff, 21-24 April
- Warpinski, N. R. and Lorenz, J. C., 2005, Analysis of the Multiwell Experiment Data and Results: Implications for the Basin-centered Gas Model, in *Understanding, Exploring, and Developing Tight-Gas Sands---2005 Vail Hedberg Conference*, S. P. Cumella, K. W. Shanley, and W. K. Camp, Eds. Tulsa, Oklahoma, U.S.A.: AAPG Bulletin, pp. 157-176, 2008.
- Warren, J.E. and Root, P.J., 1963, The behavior of Naturally Fractured Reservoirs. *SPE J.* vol. 3 no. 3, pp. 245–255. SPE-426-PA. .
- Wildenschild, D., Vaz, C. M., Rivers, M. L., Rikard, D., Christensen, B. S. B., 2002, Using X-ray computed tomography in hydrology: systems, resolutions, and limitations. *Journal of Hydrology* vol. 267, no. 3–4, pp. 285–297
- Wildenschild, D, and Sheppard, A. P., 2013, X-ray Imaging and Analysis Techniques for Quantifying Pore-scale Structure and Processes in Subsurface Porous Medium Systems: *Advances in Water Resources*, vol. 51, pp. 217–246. doi:10.1016/j.advwatres.2012.07.018.
- Witherspoon, P. A., Wang, J. S. Y., Iwai, K., and Gale, J. E., 1980, Validity of cubic law for fluid in a deformable rock fracture: *Water Resources Research*, vol. 16, no. 6, pp. 1016-1024
- Wong, P., 1999, Conductivity, permeability and electrokinetics. In: P. Wong, editor, *Methods in the physics of porous media*. Academic Press, London. pp. 115–159.
- Worden, R. H., and Burley, S. D., 2003, Sandstone diagenesis: the evolution of sand to stone. *Sandstone Diagenesis: Recent and Ancient*, pp. 1-44.
- Wyllie, M. R. J., 1957, *The fundamentals of electric log interpretation*. Academic Press, New York
- Yang, Z., Niemi, A., Fagerlund, F., and Illangasekare, T., 2013, Two-phase flow in rough-walled fractures: Comparison of continuum and invasion-percolation models: *Water Resources Research*, vol. 49, pp. 993-1002.
- Yuan, Y., and Lee, T. R., 2013, Contact angle and wetting properties. In *Surface Science Techniques* (pp. 3-34). Springer Berlin Heidelberg.
- Yang, C., Tartaglino, U., Persson, B., 2006, Influence of surface roughness on superhydrophobicity. *Physical Review Letters* vol. 97 no. 11
- Zhang, X., Knackstedt, M.A. and Sahimi, M., 1996, Fluid flow across mass fractals and self-affine surfaces, *Physica A: Statistical Mechanics and its Applications*, vol. 233, nos. 3/4, pp.835–847.

- Ziegler, D. P., 1993, Boundary conditions for lattice Boltzmann simulations. *Journal of Statistical Physics*, vol. 71, pp. 1171-1177.
- Zimmerman, R. W., Chen, G., Hadgu, T., and Bodvarsson, G. S., 1992, A dual porosity model with an improved coupling term, presented at 17th Stanford Geothermal Reservoir Engineering Workshop, Stanford, Calif., Jan. 29–31
- Zimmerman, R.W., and Bodvarsson, G. S., 1996, Hydraulic conductivity of rock fractures. *Transport in Porous Media* vol. 23 no. 1, pp. 1–30

Vita

Adenike O. Tokan-Lawal was born in Lagos, Nigeria. After completing her schoolwork at Queen's College Yaba Lagos in 1999, Adenike enrolled at the University of Kentucky in Lexington, Kentucky from 2000 to 2002. During the summers of 2001 and 2002, she attended the University of British Columbia, Vancouver, Canada and University of Houston, Texas respectively. Adenike received Bachelor of Science degrees in Electrical Engineering and Computer Science Engineering from University of Texas at Arlington, Texas, in May 2005. During the following year, Adenike worked as a Control Systems Engineer for Praxair Inc. and as a Design Engineer for Texas Instruments Inc. In August 2006, she enrolled in Graduate School at Texas A&M University, College Station, where she obtained her Master of Science in Petroleum Engineering in December 2008. After gaining some work experience in the oil and gas industry, Adenike re-enrolled in Graduate School at the University of Texas at Austin. Upon graduation, Adenike will begin work at the Shell Technology Center, Houston, TX.

Permanent address (or email): adenike.tokanlawal@gmail.com

This thesis was typed by: Adenike Tokan-Lawal